Crystalline, Amorphous, and Liquid Metal-Organic Frameworks at Non-Ambient Conditions

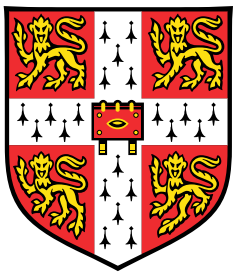

Remo N. Widmer

Department of Earth Sciences
University of Cambridge

This dissertation is submitted for the degree of
Doctor of Philosophy

Jesus College July 2019

Declaration

This dissertation is the result of my own work and includes nothing which is the outcome of work done in collaboration except where specifically indicated in the text. This work has not been submitted in whole or part towards any other qualification at this, or any other university. The total length does not exceed the 275 numbered page limit prescribed by the Department of Earth Sciences Degree Committee, including 225 pages of text, illustrations and bibliography.

Parts of this dissertation have been previously reported as papers published in the peer reviewed literature by the candidate:

1) Widmer R. N., Lampronti G. I., Kunz B., Battaglia C., Shepherd J. H., Redfern S. A. T., et al. Manufacturing Macroporous Monoliths of Microporous Metal–Organic Frameworks. *ACS Appl Nano Mater* **1,** 497–500 (2018).

2) Widmer R. N., Lampronti G. I., Anzellini S., Gaillac R., Farsang S., Zhou C., et al. Pressure Promoted Low-Temperature Melting of Metal-Organic Frameworks. *Nature Materials* **18,** 370–376 (2019).

3) Widmer R. N., Lampronti G. I., Casati, P. M. , Farsang, S., Bennett, T. D., Redfern S. A. T. X-ray radiation-induced amorphization of metal-organic frameworks. *Physical Chemistry Chemical Physics* **21,** 12389–12395 (2019).

4) Widmer R. N., Lampronti, G. I., Chibani, S., Wilson, C. W., Anzellini, S., Farsang, S., et al. Polymorphism of a Metal-Organic Framework in Pressure–Temperature Space. *Journal of the American Chemical Society* **141**, 9330–9337 (2019).

Remo N. Widmer
July 2019

Abstract

Crystalline, Amorphous, and Liquid Metal-Organic Frameworks at Non-Ambient Conditions

Remo N. Widmer

Metal-organic frameworks (MOFs), in the traditional sense, are crystalline and microporous materials. MOFs are of incessant scientific interest due to their enormous potential as host structures for a range of chemical process applications, including molecular separation, catalytic reaction, and gas storage. In the course of investigating their physical and chemical properties, it was soon discovered how diverse the structural responses of these low-density materials are when, for example, heated or compressed. Such structural changes range from the simple loss of pore-occupying solvent molecules to intricate sequences of structural phase transitions. Some MOFs are also capable of forming glasses, *i.e.* dense amorphous structures, with chemical composition and short-range order that is reminiscent of their crystalline precursor. This generated a new area of research within the MOF discipline at the interface of glass science, supramolecular chemistry, and condensed matter physics.

Here, two isotopological zeolitic imidazolate frameworks, ZIF-4 and ZIF-62, have been studied under the influence of a range of physical variables. Pressure- and temperature-induced crystalline–amorphous and crystalline–crystalline phase transitions have been investigated using *in-situ* high-pressure/high-temperature powder X-ray diffraction and Raman spectroscopy. Furthermore, these transitions were also studied as a function of varying chemical composition of the ZIFs, as well as of dynamic variables such as heating- and compression-rate. The two ZIFs were shown to be related by a continuous solid solution and this chemical substitution was found to systematically control the high-temperature behaviour. Moreover, simultaneous heating and compression of the endmember compositions ZIF-4 and ZIF-62 up to 600 °C and 8 GPa resulted in strikingly different pressure-temperature phase diagrams. For ZIF-4, four, previously unknown, high-pressure-temperature polymorphs were found. The crystal structures of two new phases were solved by powder diffraction methods.

The other two new phases could be assigned with a unit cell and space group. In contrast, the crystalline starting phase of ZIF-62 undergoes pressure- and temperature-induced amorphisation without subsequent recrystallisation. Importantly, it was found that the melting temperature of ZIF-62 decreases with increasing pressure. Furthermore, based on the topology of the two phase diagrams, it could be concluded that the respective pressure- and temperature-amorphous phases of ZIF-4 and ZIF-62 must be different from each other – density contrasts and observations on the reversibility of the crystalline–amorphous transitions clearly indicate the polyamorphic character of these phases.

The use of a pressure-assisted sintering techniques allowed for the production of macroporous crystalline, dense amorphous, and dense recrystallised monoliths of ZIF-4, in accordance with the previously established phase diagrams. The results from mechanical testing and microstructural analysis of the monoliths correlate well, which establishes useful materials characteristics for potential industrial applications. The interconnected porosity of the macroporous crystalline material provides an immense interface for gas–solid interaction, while the dense amorphous and recrystallised monoliths have distinct mechanical robustness.

The structural collapse of of the ZIFs was also studied as a result of the interaction of these materials with X-rays. The underlying mechanisms were investigated by kinetic analysis of the crystalline-amorphous transformation at ambient and elevated temperature. It was found that the ZIFs display a rare example of transient effects which lead to increasing local Avrami exponents in the course of amorphisation. This was attributed to the structural complexity and the density contrast between the crystalline and the amorphous forms of the frameworks. These findings have essential practical implications - any synchrotron-based experiments on MOFs should ideally be preceded by an assessment of their stability in the beam.

Acknowledgements

I thank my supervisors Prof. Simon Redfern and Dr. Thomas Bennett for their trust, guidance, and motivation. Special thanks goes to Dr. Giulio Lampronti for many stimulating discussion and his incessant interest in my work. I want to express my particular appreciation to Giulio for going beyond his official role on many occasions and becoming the friend he is. I thank the Engineering and Physical Sciences Research Council (EPSRC) for a full scholarship. I thank all my past and present collaborators at Diamond Light Source, Swiss Light Source, and Empa for providing their facilities and sharing their expertise. Furthermore, I would like to recognise and thank Prof. Thomas Armbruster, Dr. Martin Fisch, and Dr. Frank Gfeller, of the former Mineralogical Crystallography group at University of Bern, for their lasting influence on my scientific mindset. Finally, I am eternally grateful to my family and to my fiancée Garance.

Table of contents

Chapter 1

Introduction

In this introductory chapter, metal-organic frameworks (MOFs), an emerging class of synthetic, microporous materials, are introduced from a broad and multidisciplinary perspective. A brief review of the development and current directions of research on MOFs is presented, in the context of both fundamental and applied sciences. This is followed by an introduction to zeolitic imidazolate frameworks (ZIFs), the particular group of MOFs on which this thesis focuses. Emphasis is then given to the phenomenology of amorphous, i.e. glassy, ZIFs, including the known routes of their formation from crystalline precursors. An introduction to structural phase transformations, including the formation of amorphous phases, provides a theoretical context. Finally, the motivation and aims for this thesis are outlined in a discussion of the limitations of traditional approaches and questions that consequently remain open in the field of MOF research.

1.1 Metal-Organic Frameworks and their applications

Metal-organic frameworks, commonly abbreviated to MOFs, are synthetic materials based on networks of metal ions interlinked by organic molecules. By definition, MOFs are a subclass of coordination polymers with the potential for micro-porosity[1]. Such micro-porosity, i.e. crystal-structural voids up to 20 Å in diameter [2], stems from the three-dimensional periodic arrangement of the metal-centres and interconnecting linkers which act as struts. This class of materials is also known by alternative terms, including porous coordination polymers (PCPs), porous coordination networks (PCNs), or microporous coordination polymers (MCPs), although their use is discouraged by the IUPAC.

Materials with intrinsic porosity have been known for at least 100 years[3], most prominently as purely inorganic, aluminosilicate zeolites. Such zeolites have an important industrial

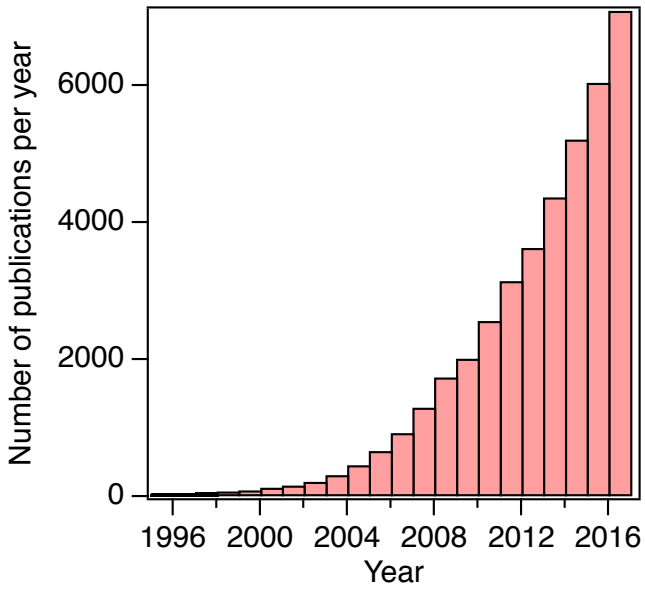

Figure 1.1 Number of publications on the topic of metal-organic frameworks, retrieved from Web of Knowledge, May 2017

.

and economic role as they are used in catalysis (e.g. petrochemical cracking), ion-exchange (e.g. water softening), and molecular sieving (e.g. purification), amongst other applications. Zeolites are suitable for these tasks due to their distinct pore and channel geometries and charge-balancing extra-framework cations. Yet their chemical and structural variability is mostly limited to interlinked tetrahedral SiO_4 and AlO_4 building blocks. In view of applications in catalysis, for instance, one major difficulty is the incorporation of catalytically active transition metals into the frameworks of zeolites [4]. The chemical diversity of organic molecules which can act as framework builders and linkers in MOFs presents a seemingly unlimited resource of building blocks for novel framework structures. It is therefore unsurprising that a growing library of over 60,000 MOF and coordination polymer compounds is available to date[5]. The term "metal-organic framework" was coined in 1995[6] and has since then generated tremendous interest within numerous branches of science (Figure 1.1). Since their discovery, the relatively young MOFs have quickly evolved into a potentially relevant industrial and economic resource and their applications are therefore the focal point of a growing body of research. Many specialist fields have contributed to their study as illustrated in Figure 1.2. While contributions from chemical sciences are predominant, with somewhat more than 50%, the fields of material sciences, crystallography, and physics are not far behind.

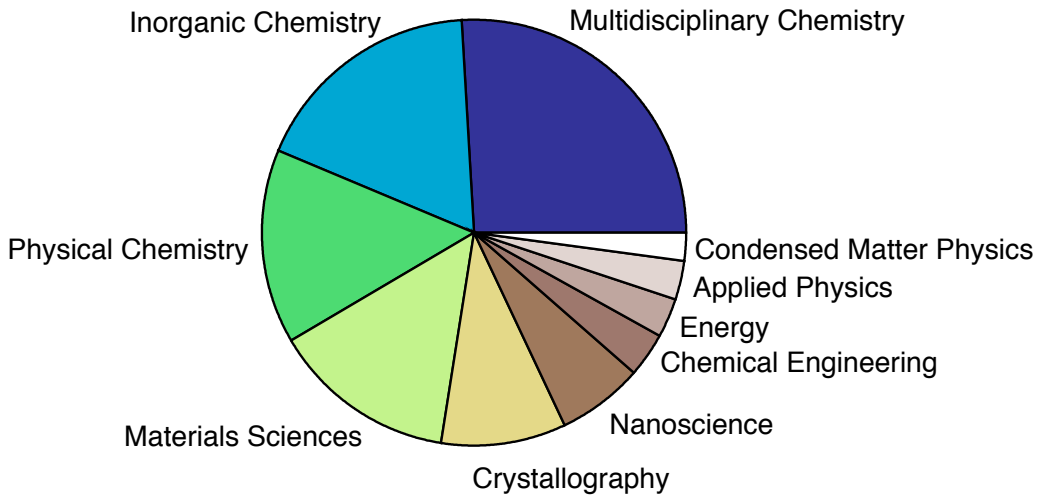

Figure 1.2 Relative abundance of articles on the topic of metal-organic frameworks sorted by their main category on *Web of Science*. The data are based on roughly 43,000 entries, with a minimum of 1000 articles per group. Date: May 2017

Application-oriented research, mainly targeting the chemical functionalities of MOFs, generally treats synthesis, composition, and morphology as the main variables of interest. This has resulted in the development of MOFs for an exceptional breadth of potential uses. Proposed applications include, for example, gas storage and separation[7–10], catalysis[11–14], drug delivery[15–17], water harvesting[18], sensing[19, 20], energy storage [21, 22], and electrical conductivity and dielectrics [23–26].

Fundamental research on the other hand is fuelled by interest in the underlying microscopic foundations of the macroscopic physical properties of MOFs. This has produced abundant reports of unusual physical properties and stimuli-responsive behaviour[27]. Examples include structural flexibility[28] and breathing[29], negative gas adsorption[30], and temperature-[31] and pressure-induced[32] phase transitions.

1.2 Zeolitic Imidazolate Frameworks: A special group of MOFs

Zeolitic imidazolate frameworks (ZIFs) are a subgroup of MOFs. To date more than one hundred ZIF compounds, with distinct chemical and structural characteristics, have

been reported[33]. In ZIFs, tetrahedral $M^{2+}N_4$ units (M=transition metal) interlinked with imidazolate-derived ligands (Figure 1.3) form periodic low-density frameworks. The structures of ZIFs are analogous to those of natural zeolites, which form low-density frameworks of interlinked tetrahedral SiO_4 and AlO_4 units. Much like the related zeolites, ZIFs have attracted significant interest due to their promising performance as molecular adsorbers. At the same time, they also display remarkable thermal, chemical, and mechanical stability[34–36]. In the context of fundamental structural studies, polymorphic phase transitions such as breathing and gate-opening have been identified as responsible for much of the adsorption potential in ZIFs[37–40]. However, a recent review established that ZIFs have only a limited volumetric adsorption performance in comparison with the currently best-performing MOFs[41]. Yet, the separation performance and selectivity of ZIFs, alongside their exceptional thermal and chemical stabilities, remain remarkable. Thus ZIFs remain good candidates for membrane separation, catalysis, sensing, and drug delivery[33].

The traditional role envisaged for MOFs has clearly been based on their adsorption functionality. But there is growing recognition that the family of ZIFs (and MOFs in general) have other unusual physical properties. Considerable interest has resulted from the behaviour of their initially porous and crystalline frameworks under the influence of pressure and/or temperature, when they were observed to recrystallise to denser states[42], amorphise[43, 44], as well as melt[45]. What might generally first be considered as a limit of their structural stability and hence a problem for the potential use of ZIFs in chemical processes such as retention or separation of guest molecules, in fact, deserves attention as a fascinating interplay between thermodynamic forces and kinetic barriers. The fundamental study of such transitions in ZIFs not only adds to our understanding of the condensed-matter physics of such ‘soft’ crystals, it has also the potential to facilitate the prediction and the control of phase stability limits of ZIFs for applications at non-ambient conditions. Moreover, new types of applications for these chemically highly versatile systems have emerge through such observations, as will be described in the following section.

1.3 Amorphous ZIFs

Functional *amorphous* ZIFs represent an important extension of the applications of MOF materials[47, 48]. Relatively recent advances in solid-state amorphisation, melting, and melt-quenched ZIF glasses have spearheaded not only new types of potential application for MOFs, for instance due to their particular mechanical, optical, and conductive properties,

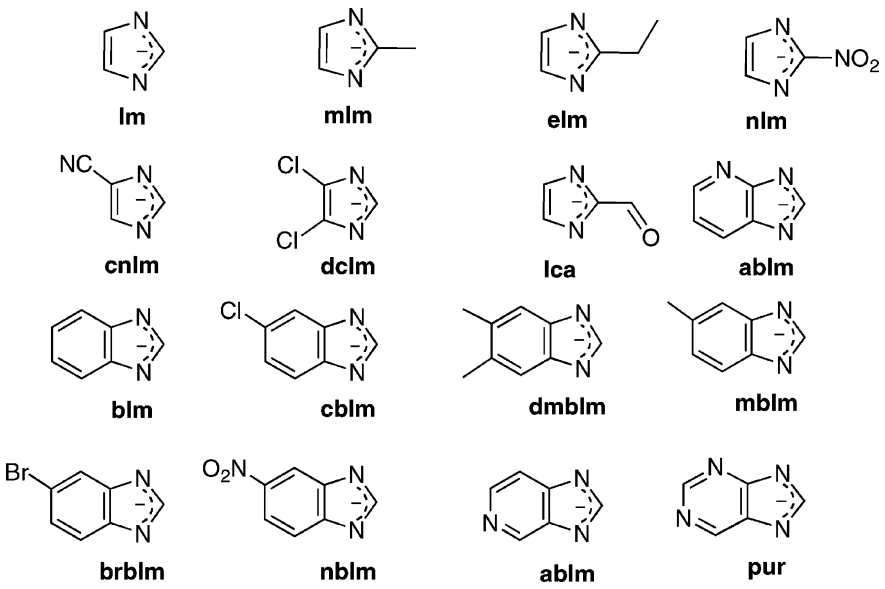

Figure 1.3 A selection of imidazolate-derived molecules used to synthesise ZIFs. From Phan et al. 2010[46].

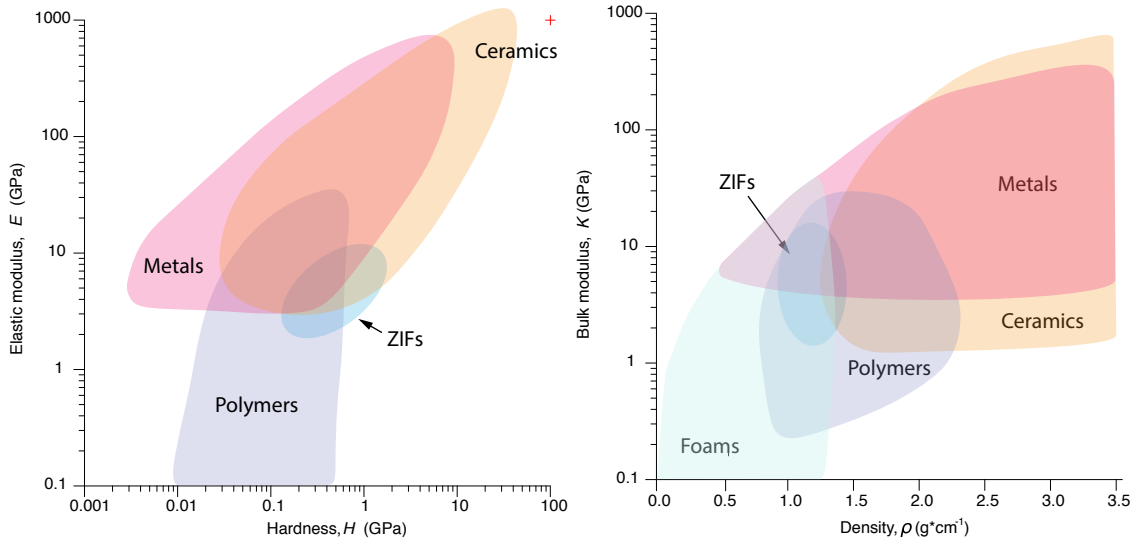

Figure 1.4 Left: Elastic modulus versus Hardness of major material classes and ZIFs, Right: Bulk modulus versus density of major material classes and ZIFs. From Tan et al. 2010[35].

but also defined an entirely new class of glassy materials[45, 49]. These are distinct from existing inorganic non-metallic, organic, and metallic categories[50].

Conventional glass has found broad use in our every-day lives, for example, as window panes and tableware. The most familiar glasses (and historically the first to be fabricated) are composed of approximately three quarters SiO_2, and a mixture of Na_2O,Na_2CO_3, and CaO. However, technologically relevant glasses are not limited to these ubiquitous soda-lime-glasses, as is demonstrated by non-oxide compositions such as metal-fluoride-, aluminate- and aluminosilicate-, phosphate-, borate-, and chalcogenide-glasses. Their primary use is in lenses, optical fibres, and optoelectronic components, that require particular transmission characteristics [51]. Pure metallic glasses, on the other hand, have superior mechanical properties compared to crystalline metals due to the absence of grain boundaries and dislocations in the glass[52]. However, the extremly rapid quenching of temperature, required to prevent crystallisation in the metal, limits the production of metallic glasses to thin layers.

ZIF glasses, on the other hand, have been reported to have very high glass-forming ability (avoidance of crystallisation on cooling) and very high glass transition temperature relative to the melting temperature[53]. In addition they have very high Poisson's ratios and high viscosities in the molten state[53]. All these properties are attributed to the unique structure of the ZIF melts. The mechanical properties of ZIFs and ZIF glasses in relation to other major material classes are shown in Figure 1.4. Importantly, experiments and simulations of the properties of some ZIF glasses have revealed that they retain the characteristic connectivity of the crystalline precursor, though in a continuously random arrangement, both upon melting and after supercooling from the liquid state[45, 54].

1.4 Technological applications of amorphous ZIFs

The potential applications of MOF-glasses have been detailed in reviews by Tao et al. 2017 and Bennett et al. 2018[49, 55]. Their findings are summarised here.

Gas separation and adsorption Accessible porosity in amorphous MOFs is a recent discovery. While the micro-porosity of crystalline counterparts will probably always outperform that of amorphous MOFs, it has been shown that the latter have several other material-specific advantages. Porous amorphous MOFs' main strength is the ease of processing and mechanical stability[56].

Ion Conduction Crystalline MOFs have been successfully optimised to conduct H^+, Li^+, and Na^+[57], but their polycrystalline nature have inherent conduction limitations

due to grain boundaries. Bulk parts and thin films manufactured from melt-quenched MOFs, on the other hand, have (at least theoretically) no such limitations.

Waste Storage Conventional separation and sequestration of hazardous molecules and ions requires the trapping of these species in host structures and irreversible occlusion in an often glassy matrix. Porous MOFs in general can capture toxic or radioactive waste atoms and molecules and the conversion of such saturated sorbent material into a glassy state may present a direct pathway to encapsulation of the previously adsorbed waste [58–60]. ZIFs have been shown, for example, to adsorb radioactive iodine. Amorphisation of the iodine-loaded MOF resulted in enhanced retention of the iodine at elevated temperatures.

Medical Applications The delivery of drugs to the human body from MOF carriers is an important topic [15]. However, the relatively fast diffusion of guest species in crystalline MOFs leads to a fast, uncontrolled release. On the other hand, amorphous MOF-drug complexes have been shown to significantly slow down the release kinetics[61], allowing for the timed delivery of a drug.

Shock Absorber On a gravimetric basis, the process of amorphisation due to compression (see 1.5.2) was shown to absorb energy through bond breakage equal in magnitude to the energy released by typical explosives[62]. It has thus been envisaged to employ amorphisable MOFs as mechanical energy absorbers for hydrostatic and shock compression.

1.5 Formation of amorphous ZIFs

The preparation of bulk amorphous materials in general has been explored in various ways. Most commonly, they are formed through melting and subsequent vitrification, i.e fast enough cooling of a melt to prevent recrystallization. Alternatively, though hardly industrial, solid-amorphous substances can be produced from bombardment of a crystal by α rays, electron beams, intense neutron fluxes, mechanical grinding, decompression of high-pressure polymorphs to ambient pressure, or chemical reactions [63]. A relatively late discovery made in 1984 by Mishima et al. [64] revealed the possibility to directly transform crystalline H_2O ice to an amorphous solid by pressurizing it to 1 GPa under hydrostatic conditions at 77 K. The formation of ZIF glasses has been studied by adaption of some of theses methods, the most important of which are described in the next section.

1.5.1 Thermal amorphisation and melting

The first thermally-amorphised MOF to be investigated in detail, and, in fact, the first amorphous MOF in general, was produced by heating the crystalline precursor ZIF-4 [$Zn(Im)_2$] to above 300 °C [65] (Figure 1.5). This is possible due to the fact that this ZIF transforms to an amorphous phase at temperatures well below its decomposition temperature, in contrast to most other MOFs that readily decompose upon heating. The resulting material was termed *a*-ZIF. The generality of this name takes into account the fact that all thermally amorphised ZIF-4 polymorphs are structurally indistinguishable from each other after loss of their crystallinity[42]. Upon further heating to 400 °C, *a*-ZIF recrystallises to the dense ZIF-*zni*. The fact that the amorphous phase recrystallised to a phase with the same stoichiometry as the ZIF-4 precursor was taken as evidence that no alteration in chemical composition occurs during the intermediate amorphisation. To probe the structure of the amorphous *a*-ZIF with the know chemical composition, neutron total scattering data was recorded and used as a basis for reverse Monte Carlo refinement of an atomistic model. Most strikingly, it was found that the pair distribution functions (PDFs, Fourier transforms of the total scattering data), and thus the short-range structures, of all three phases, ZIF-4, *a*-ZIF-4, and ZIF-*zni*, and, as shown later on also amorphous ZIF-4 from ball-milling[66], appear to be identical up to interatomic distance of approximately 6 Å (Figure 1.6)[65]. This was a first confirmation that the linkers, their tetrahedral coordination of Zn, and the interlinkage of these tetrahedral units are virtually identical in the crystalline and amorphous structures. However, in modelling the long-range structure, attempts to use the connectivity (i.e. topology) of either the crystalline ZIF-4 or ZIF-*zni* did not result in a satisfactory fit to the total scattering data. The network of interlinked $Zn(Im)_4$ units was eventually satisfactorily modelled as a continuous random network, analogous to that of amorphous SiO_2[67]. This implies that the classification of the crystalline-amorphous-crystalline transformations during the heating of ZIF-4 should be regarded as reconstructive transitions.

Motivated by the remarkable characteristics of the pure imidazole ZIF-4, Bennett et al. (2016) [45] probed the high-temperature behaviour of the partially benzimidazole substituted ZIF-62. Similar to ZIF-4, ZIF-62 also amorphises around 300 °C, but, in contrast, ZIF-62 does not recrystallise to a denser form. However, both ZIF-4 and ZIF-62 were not only found to amorphise in the solid state upon heating, but ultimately also to congruently melt to a liquid with a chemical composition identical to the starting phase[45]. Quenching of this liquid under the appropriate conditions yields transparent glasses with very high recrystallisation resistance[53]. Gaillac et al. (2017)[54] were the first to investigate the melting of ZIF-4, and the structure of this melt, by molecular dynamics simulations. For these

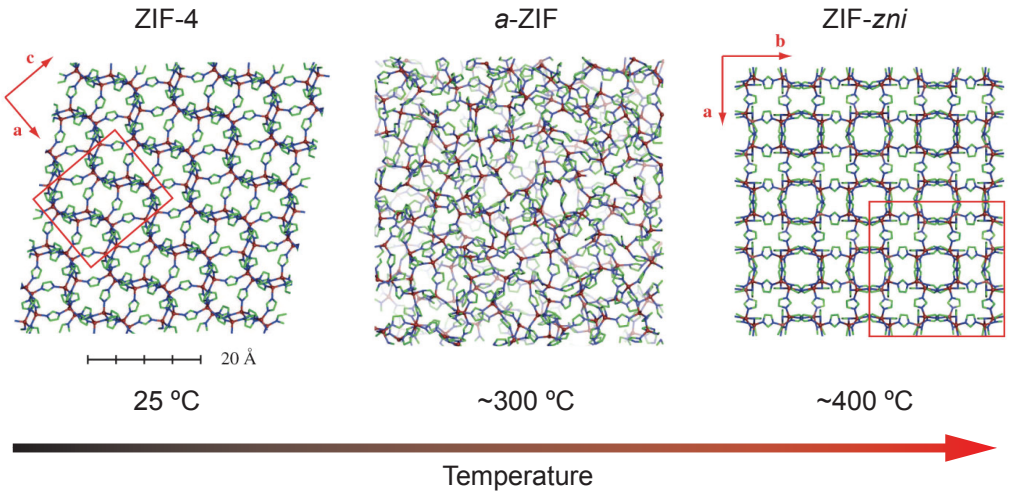

Figure 1.5 Crystal structural models of ZIF-4, amorphous *a*-ZIF-4, and recrystallised ZIF-*zni*. From Bennett et al. (2010)[65].

short-timed simulations to yield statistical relevant results, they had to be run at extremely high temperatures. Although these temperatures do not match the conditions of experimental observations, they nevertheless provide a good relative scale for the succession of events. They found that (1) the main contribution to the surmounting of the free energy barrier for melting is energetic in nature, as opposed to entropic, that (2) the microscopic mechanism responsible for melting is that of Zn–N bond breaking with an Arrhenian behaviour, and that (3) the structure of the melt retains some porosity of the crystalline precursor.

1.5.2 Pressure amorphisation

Pressure-induced amorphisation of ZIFs under hydrostatic conditions is usually investigated by *in-situ* techniques using diamond anvil cells (see Chapter 2). Amorphisation under non-hydrostatic conditions is also possible, mainly under uniaxial compression[62, 68]. The latter, however, is much more difficult to model and understand due to the predominance of shear forces. Amorphisation pressures depend on a multitude of experimental variables, particularly when investigating porous framework structures. Amongst the most important factors are the presence or absence of pore-occupying guest molecules in the material under consideration; whether the sample is a large single crystal or a fine powder; the nature of the pressure transmitting medium, i.e. whether it is penetrating or non-penetrating; and the hydrostatic

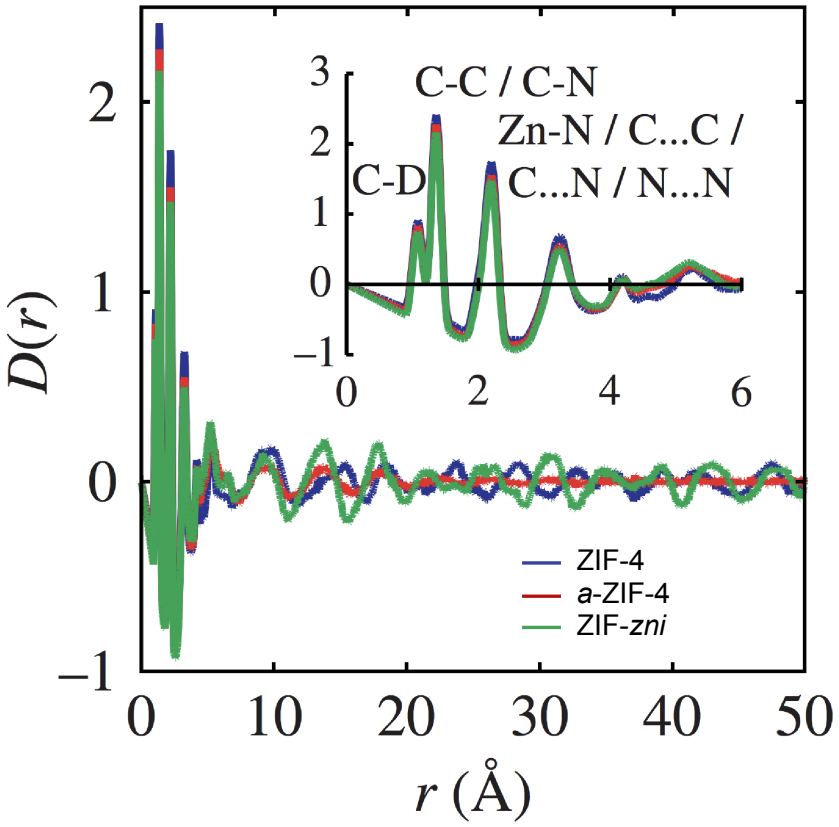

Figure 1.6 Neutron differential correlation functions *D(r)* of crystalline ZIF-4 (blue), amorphous *a*-ZIF (red), and recrystallised ZIF-*zni* (green). The inset illustrates the practically identical local structure of all phases up to approximately 6 Å. Atom-pairs corresponding to individual peaks are indicated at the top. From Bennett et al. (2010)[65].

limits of the pressure transmitting media. A summary of experimental parameters and resulting amorphisation conditions for all ZIFs reported in this context is given in Table 1.1. Generally speaking, guest occupation of the MOF framework increases the stability of its crystalline structure, as does the use of a penetrating pressure medium[36]. This is due to a decrease in compressibility and an increase in shear stability when the pores are filled[69]. Evacuated ZIF-8 powder, (Zn(2-methylimidazole)$_2$), was the first ZIF shown to undergo irreversible pressure-induced amorphisation following compression beyond 0.34 GPa using a non-penetrating pressure transmitting fluid[70]. Under comparable conditions, ZIF-4 was later shown to amorphise in a similar pressure range from 0.35-0.98 GPa. Remarkably however, amorphisation of ZIF-4 was found to be reversible upon decompression, if the maximal applied pressure did not significantly exceed the initial amorphisation pressure[71]. Consequently, it can be assumed that pressure-induced amorphisation in ZIF-4 does not change the medium range connectivity, as opposed to the thermal amorphisation described in the previous section. Therefore, the structure of pressure-amorphised ZIF-4 cannot be randomly continuous as in the case of thermally-amorphised ZIF-4, and it remains unclear. ZIF-7 also undergoes pressure-induced amorphisation at similar pressures to those found for ZIF-4[36].

Table 1.1 Compilation of experimental conditions and resulting pressure of amorphisation ($P_{amorph.}$) and bulk moduli (K_0) for pressure amorphisable ZIFs in literature.

Material	Method	PTM	Solvent	$P_{amorph.}$ /GPa	K_0 /GPa	Ref.
ZIF-8	Powder	FC	empty	0.3 GPa	6.5(4)	[70]
ZIF-4	Single crystal	ME	DMF	5.0 – 6.5	n.a.	[43]
ZIF-4	Powder	ME	DMF	2.0 – 4.5	n.a.	[43]
ZIF-4	Powder	DO	DMF	2.6 – 6.4	7.7(8)	[43]
ZIF-4	Powder	ME	empty	1.5 – 4.5	n.a.	[43]
ZIF-4	Powder	DO	empty	0.4 – 1.0	2.6(1)	[43]
ZIF-4	Powder	FC	empty	1	1.4	[71]
ZIF-7	Powder	DMF	DMF	n.a.	23.3(5)	[36]
ZIF-7	Powder	FC	DMF	3.5	13(1)	[36]
ZIF-7	Powder	ME	ME	5.7	21.1(7)	[36]
ZIF-9	Single crystal	ME	DMF	n.a.	13.4(5)	[36]

1.5.3 Amorphisation by ball milling

Ball milling (i.e. mechano-synthetic methods) to synthesise materials is of special interest due to the ease of the procedures, the absence of organic solvents, and its scalability. The

use of ball milling to fabricate amorphous ZIFs was reported by Bennett et al. 2011[72] and Baxter et al. 2016[73]. These authors report that crystalline ZIF-4, and its polymorphs ZIF-1, ZIF-3, and ZIF-*zni*, can be transformed into mutually indistinguishable amorphous phases (*a*-ZIF) after 30 min grinding time. However, the attempt to form *a*-ZIF from a mixture of the precursors, imidazole and Zn-salt, was not successful. Depending on the presence or absence of DMF solvent, respectively, either crystalline ZIF-4 or ZIF-*zni* was obtained. Interestingly, ball milling is also capable of producing amorphous ZIF-8 with a continuous random network topology, and yet this is unattainable through thermal amorphisation[74].

1.6 Theoretical context

The behaviour of ZIFs at non-ambient conditions, and the formation of amorphous ZIFs from crystalline precursors, can in principle be understood in terms of thermodynamic stability and energy minimisation through structural transformations. Frequently, however, to match experimental observations, kinetic factors have to be considered, as will be shown throughout this thesis. A brief introduction to thermodynamic classification, and kinetic implications of structural phase transitions, including glass formation, follows.

1.6.1 Phase transitions

Structural phase transitions are processes that change the atomic structure of a substance while its chemical composition remains unaltered. Such structural changes are usually caused by a change in either temperature or pressure, and the resulting thermodynamic force that drives the free energy of the system to a minimum. As a consequence, phase transitions bring about changes in both intensive and extensive physical properties, and can encompass crystalline-crystalline, crystalline-amorphous, and solid-liquid transitions.

From a thermodynamic perspective, phase transitions can be categorised into first-order and second-order processes, depending on whether or not the Gibbs free energy G evolves smoothly across the critical pressure or temperature. This behaviour and the corresponding evolution of entropy S, volume V, enthalpy H, and heat capacity C_p is summarised in Figure 1.7.

On the other hand, from a structural perspective, phase transition can be displacive, reconstructive, or order-disorder in nature.

Displacive transitions constitute relatively small structural adjustments such as the tilting and rotating of structural units caused by the distortion of bonds. These types of

transitions are generally fast and readily reversible, and can be of either thermodynamic first- or second-order character.

Reconstructive transitions involve the breaking and reformation of bonds and are always thermodynamically first-order. Due to high activation energies, such transitions are typically slow and thermally-activated, and the resulting polymorphs can often be recovered in a meta-stable state at ambient conditions.

Order-disorder transitions are mainly observed in minerals comprised of mixed cations over multiple crystallographic sites. Here, the long-range symmetry of a polymorph can be increased by statistically random distribution of the initially ordered cation sites.

Experimental methods to study phase transitions include structural studies and thermochemical measurements. Structural studies include X-ray, electron, and neutron diffraction methods on polycrystalline powders or single-crystals. Measurements can be performed *ex-situ* on samples rapidly quenched from non-ambient conditions in expectation of a kinetically stabilised transformation; or *in-situ* at high-pressure and -temperature. On the other hand, thermochemical measurements cover a range of techniques to measure heat capacities and enthalpies. Techniques to measure heat capacities include adiabatic calorimetry, differential scanning calorimetry, and drop calorimetry. Indirectly, the heat capacity can also be calculated from the integrated phonon density as measured by inelastic neutron scattering experiments. Enthalpies can be directly measured by heat of solution calorimetry.

Departing from experimental methods, thermodynamic properties of substances can also be computed with ever increasing sophistication given the continuous rise of computing power. *Static lattice energy calculation* models the sum of the interatomic interactions of a set of atoms based on their mutual attractive and repulsive forces, which gives the overall potential energy. These interactions can include Coulombic and van der Waals terms, and the influence of polarization of electron densities. These calculations assume a temperature of 0 K and thus exclude vibrational energy. *Lattice dynamics calculations* take the static model a step further by including the thermal vibration of atoms from their equilibrium positions. To account for temperature, calculations are done with varying lattice dimensions, simulating varying interatomic distances. *Molecular dynamics simulations* start from a volume of atoms and the forces between these atoms. Classical mechanics calculations are then carried out for the entire assembly at sequential time steps. The kinetic energy accounts directly for the influence of temperature. A major advantage is that it is possible to include anharmonic interactions between atoms responsible for thermal expansion; temperature

dependent elastic constants; temperature dependent phonon frequencies; and ultimately structural phase transitions. Furthermore, molecular dynamics simulations can be carried out for both crystalline and amorphous phases.

1.6.2 Melting and amorphous solids

In contrast to solid state phase transitions from one crystalline state to another, the process of melting, by definition, entails the breakdown of structural periodicity and is a transition to a different state of matter. Melting is categorised as a first-order, reconstructive, transition. Two widely cited conditions for melting, and, in fact, the first ones to be proposed in the early 20th century, are the Lindemann[76] and the Born[77] criteria. The Lindemann criterion explains melting as a result of vibrational instability when, due to thermal vibration, the atomic displacement exceeds the nearest-neighbour distances by more than 10%. According to the Born criterion, thermal expansion leads to collapse and melting of a crystal due to the reduction to zero of the shear strength as the interatomic distances increase. However, while these two explanations give intuitive reasons for the phenomena of melting, their ability to quantitatively predict experimental results are limited due to their overly simple assumptions that, for example, structures are solely closed-packed spheres, and interatomic forces are purely harmonic[78]. Moving on from theories based only on lattice-instabilities, more recent work on microscopic mechanisms of melting has consolidated more advanced theories such as surface melting[79] or melting based on point defects[80, 81].

Glasses are materials trapped in meta-stable states due to the fact that activation energies are too high for crystal nucleation and growth to proceed. This kinetic control on the stability of a glass phase is exemplified, for example, by the process of super-cooling. On cooling a melt, its viscosity increases, which makes it progressively more difficult for atomic species to diffuse. This has been explained by the "freezing in" of thermal motions of the chemical constituents[82]. Below the so-called glass transition temperature (T_g), the atomic configuration is trapped, preventing subsequent periodic ordering. T_g is defined by the on-set of a rapid increase of specific heat capacity (C_p) when a solid glass is heated at 10 K/min. This increase of C_p is also accompanied by a macroscopic softening of the glass. The increase of C_p is attributed to the sudden increase in kinetically accessible degrees of freedom within the system[83]. Irrespective of bonding type, it generally occurs at around two thirds of the temperature of the melting point.

To illustrate the theoretical and experimental complexity of the glass transition in glass—liquid systems, three separate temperature regimes can be defined as shown in Figure 1.8[84].

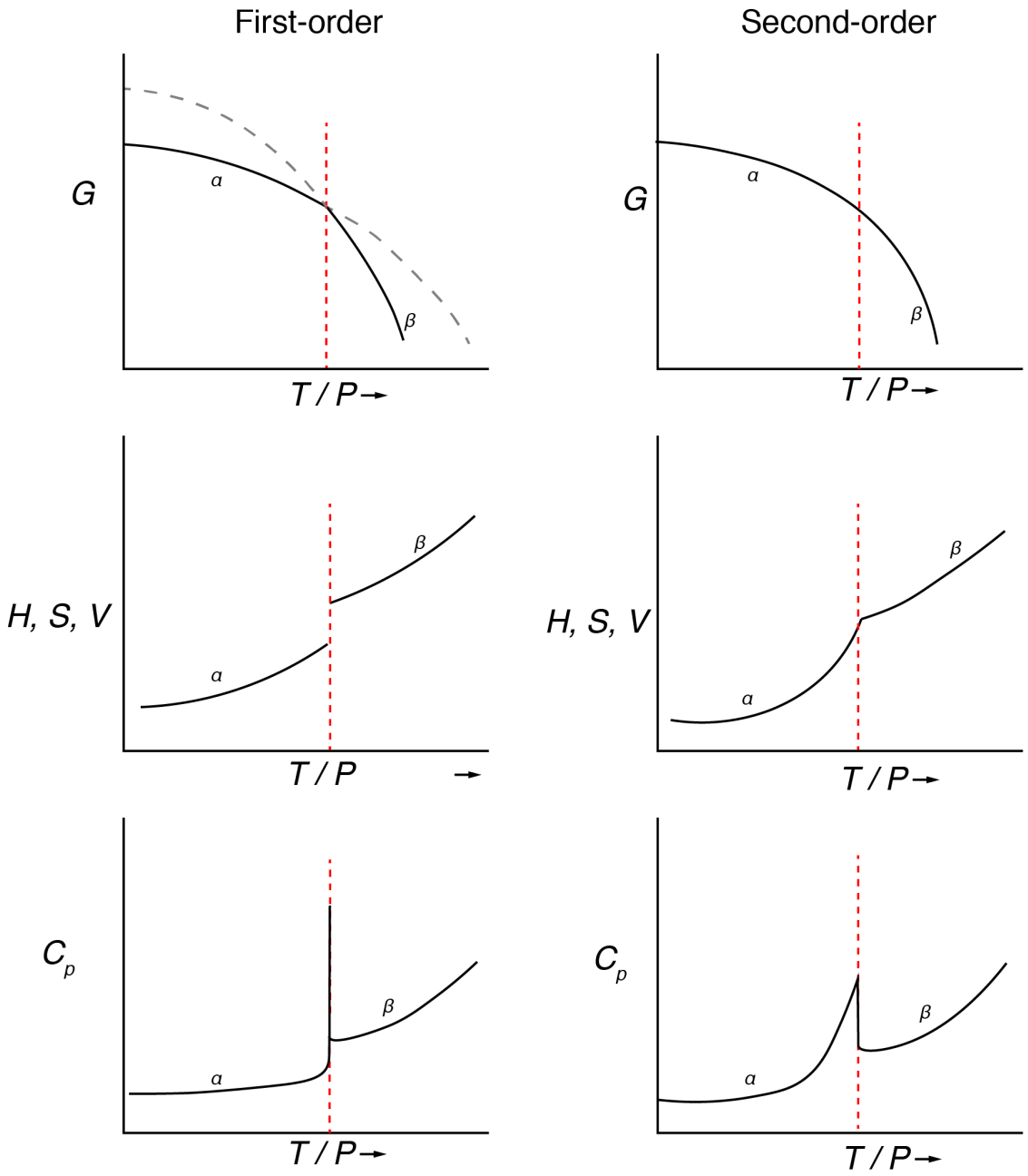

Figure 1.7 Evolution of free energy G, enthalpy H, entropy S, volume V, and heat capacity C_P as a function of pressure or temperature for first-order (left), and second-order (right) phase transitions after Putnis 1992[75].

In region A, the properties of the liquid are fully reversible and not dependent on the thermal history, neither annealing nor varying heating rates. In region B, however, properties not only depend on the thermal history but also on the duration of the observation. This is due to continuous relaxation processes (annealing) that are active in this temperature range. Glasses in region C show, again, reversible behaviour, however, with a dependency on the thermal history or whatever other mechanism led to the amorphous state.

The microscopic and energetic reasons for this behaviour can generally be described as "a falling out of equilibrium of a kind that inevitably happens to any system cooled faster than its temperature-dependent internal equilibration time"; and it has been suggested that the key to understanding this lies in the successful explanation of the temperature-dependent viscosity of the liquid just above T_g[85]. An Arrhenian behaviour controlled by thermal activation is to be expected, but it is observed, for the vast majority of materials, that the temperature dependent-viscosity increases much faster upon cooling.

A further complication in the prediction of the behaviour of glass systems arises from the so-called Kauzmann paradox which extrapolates the decrease in entropy of a liquid on cooling[86]. A monotonic extrapolation suggests that the entropy of the super-cooled liquid will fall below that of a corresponding glass or crystalline state, and in addition the entropy will be negative above 0 K. Thermodynamic laws prohibit all three consequences. This hypothetical extrapolation would be futile if the glass transition were a genuine structural phase transition, because the entropy-evolution would be non-continuous. However, it is observed to be continuous[85]. One possible explanation that would resolve this is that of a liquid-liquid phase transition occurring close to T_g. Such polyamorphic transitions have been experimentally described for a number of systems[87, 88], including ice, silicon, the Y_2O_3-Al_2O_3 system, and the metal-organic framework ZIF-4[89]. Such transitions result in, or at least approach, ‘perfect’ glasses. This state is termed ‘perfect’, or ‘ideal’, because it accesses a lower minimum of configurational potential energy in the complex energy landscape of amorphous phases [85].

Similarly challenging to conceptualise is the solid-state transition of a material from a crystal to a glass without going through a liquid state, which has been observed both upon heating and compressing crystalline materials. A widely cited article, and, in fact, the first to report pressure-induced amorphisation of a crystalline substance, is that of Mishima et al. (1984), which describes the ‘melting’ of ice at 77 K when pressurised to 10 kbar[64]. For solid-state amorphisation upon increasing pressure to be spontaneous, and thus an energetically favourable transition, a negative volume change ΔV must occur upon amorphisation. However, a disordered material is unlikely to be denser than a (hypothetically) crystalline

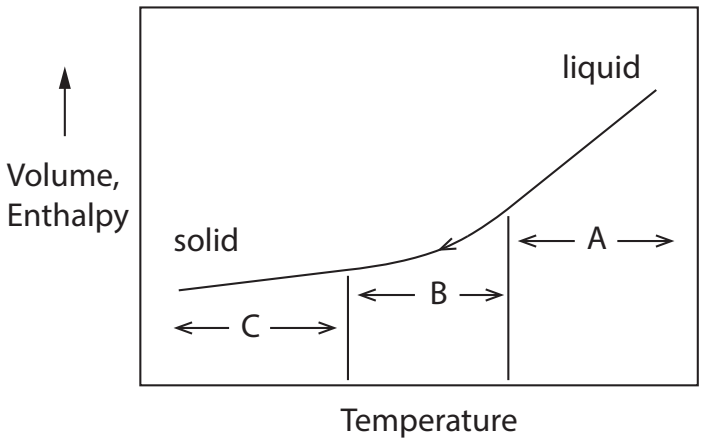

Figure 1.8 The three regions of glass-formation based on the variation with temperature of the extensive thermodynamic properties volume and enthalpy during heating and cooling without annealing. After Angell et al. 2000[90].

counterpart, given that the theoretically densest packing of equal spheres is that of a periodic closed-packed structure. It is also unlikely to represent the energetically most favourable structure given the high conformational entropy of a disordered phase. Consequently, solid state amorphisation is observed when a crystalline-to-crystalline transformation to a denser polymorph is kinetically hindered and the amorphous state presents itself as an energetically intermediate conformation[91]. Interatomic forces become more and more repulsive under compression, increasing the potential barrier for necessary diffusion for a reconstructive transition[92]. In relation to the Clapeyron equation $\delta P/\delta T = \Delta S/\Delta V$, where ΔV and ΔS are, respectively, the changes in molar volume and entropy between the crystal and the liquid, a negative volume change ΔV signifies a melting curve with negative Clapeyron slope. Therefore, pressure-induced amorphisation may also be regarded as a kinetically-controlled melting event at significantly lower temperatures compared to thermal melting at ambient pressure[93]. Intriguingly, the resulting amorphous solid may still transform to a liquid, i.e. melt, at higher temperatures. Similarly, the solid-state amorphisation observed when a crystalline phase is heated[42], is likely to represent an intermediate state, kinetically hindered to recrystallise.

Although all of the previously mentioned phenomena (the glass transition, the Kauzmann paradox, and the solid-state amorphisation) appear to be processes that are intuitively understood, they nevertheless have posed some major unsolved problems in solid state theory[94].

Alternative explanations, experiments, and computational modelling which aim to reconcile these, and other phenomena are the subject of ongoing debate[84, 95, 96].

1.7 The present thesis

1.7.1 Motivation and Aims

The majority of studies on MOFs aim to establish, or follow, so-called principles of "rational design"[97], as opposed to the blind screening of properties. Synthesis procedures and chemical composition are usually treated as the most important variables. These relentless adjustments of formulations to create new and better performing materials have undoubtedly led to numerous MOFs with exceptional performance. However, it has also resulted in many properties of MOFs being overlooked. Some properties of MOFs are strongly dependent on, or are only triggered by, the variation of thermodynamic variables such as pressure and temperature at a fixed composition. Yet, the influence of such external stimuli is often ignored. Furthermore, the field of interest has been narrowed down to purely crystalline materials and the first signs of amorphisation are usually treated as deleterious. It is only in the last few years that the amorphous counterparts of MOFs have received due attention. Indeed, MOFs have found an important new field of potential applications based on the combination of the specific technical advantages of glasses over crystalline materials and some of the unique characteristics of MOF glasses. Importantly, almost all MOF glasses to date are formed from crystalline starting materials, which provide the chemical connectivity inherited by the amorphous products. Understanding such transformations from the perspective of the crystalline solid is therefore crucial. A number of previous studies on the separate pressure and temperature dependent behaviour of ZIFs show that they also lie on a figurative triple point of crystalline, solid-amorphous, and liquid states. Transitions between these states tend to occur within a relatively mild pressure- and temperature-regime (roughly up to 10 GPa and 600 °C, as will be seen in the coming chapters) compared to topologically related silicate systems where much higher temperatures and pressures are required. This is an ideal disposition of MOFs as it makes experiments on the general topic of phase transitions easier. These relatively mild conditions also promise accuracy and good resolution in *P*-*T*-space. For these reasons, MOFs are an attractive material system to study the phenomena of solid-liquid, crystalline-amorphous, and crystalline-crystalline transitions. In addition they present interesting test cases, and possibly extend principles that are only established for mono-atomic, closed-packed crystal structures. While thermodynamic and kinetic theories

have been developed to a high degree of complexity, their application to MOFs is often not straight forward due to their low density and their strongly associated building blocks in the form of organic linkers which deviate from the simple stacking of spheres.

This thesis aims to provide a broad perspective on the stability of MOFs, and of what happens beyond these limits. Its primary focus is on the effects of the application of temperature and pressure, and the additional controls of chemical composition and means of observation. In the first instance, this will be phenomenologically addressed by the study of phase constitutions and crystal structures under these various influences. The observations are then discussed in the context of MOFs in general, and other organic as well as inorganic materials. The interplay with compositional controls will be addressed throughout the thesis by direct comparison of the behaviour of two iso-structural MOFs of slightly different chemical composition.

1.7.2 Outline

Chapter 1 provides a wide perspective on the nature of MOFs. It introduces and summarises the potential technological relevance of a class of amorphous MOFs which form by surpassing the stability limits of certain crystalline phases. A brief introduction to established thermodynamic concepts of phase transitions as well as ongoing discussions on related glass science outlines the broader scientific interest of such transformations in MOFs.

Chapter 2 introduces the chemical and structural nature of the two MOF compounds ZIF-4 and ZIF-62. The first part describes both their synthesis and the analytical techniques for their chemical and physical characterisation. The second part describes advanced methods for their study which are then used in the subsequent chapters.

Chapter 3 reports on investigations of the systematics of chemical substitution in ZIF-4, and how the latter relates to ZIF-62 through a solid solution. The effects of the substitution is demonstrated by the high-temperature behaviour and stability of a series of compositions.

Chapter 4 discusses the effect of simultaneous application of pressure and temperature on the stability of ZIF-4 and ZIF-62. The individual *P*-*T*-phase diagrams are constructed from synchrotron powder XRD and optical data, and results are correlated with Raman spectroscopic observations.

Chapter 5 draws on the findings of the previous chapters on the pressure- and temperature stability of ZIF-4 and applies this knowledge to the advancement of a novel processing technique. This technique is based on pressure assisted sintering and allows for the fabrication of monolithic ZIF parts from loose powders.

Chapter 6 covers the previously unreported effect on ZIFs of radiation damage by synchrotron X-rays. Kinetic analysis of the progressive amorphisation via beam damage elucidates possible microscopic mechanisms. Alongside insights to a new pathway for amorphisation, it also discusses how these findings highlight an important factor to consider in any synchrotron-based study of these materials.

Chapter 7 provides a conclusion of this thesis, as well as suggestions to future work that is prompted by the present results.

Chapter 2

Materials and Methodology

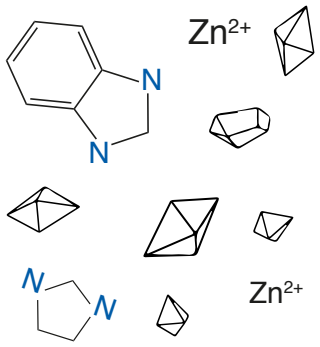

This thesis is based on investigations of two distinct metal-organic framework materials, namely ZIF-4 and ZIF-62. There is only a slight compositional difference between ZIF-4 and ZIF-62, and their underlying crystal structures are in principle very similar, but their physical characteristics, performance, and behaviour at non-ambient conditions differ considerably. An overview and comparison of their reported physical characteristics is given in the first part of this chapter. This is followed by a section on their synthesis and desolvation and the methods employed for their basic structural and chemical characterisation. Finally, the methods used for *in-situ* high-temperature and high-pressure Raman and XRD measurement are presented.

2.1 Materials

2.1.1 ZIF-4

$M^{2+}(Im)_2$ compounds (M= transition metal, Im=imidazolate) are regarded as the archetypical ZIFs given that they are comprised of only unsubstituted and non-functionalised imidazolate linkers and Zn as the most common metal centre (Figure 2.1). Variation of synthesis conditions leads to at least 18 different polymorphs with distinct structures, densities, and topologies (Table 2.1). This polymorphic series presents a large range of relative pore volumes (densities), calculated thermodynamic stabilities[98], experimentally determined enthalpies of formation[99], as well as mechanical properties (Figure 2.2 and 2.3). In addition

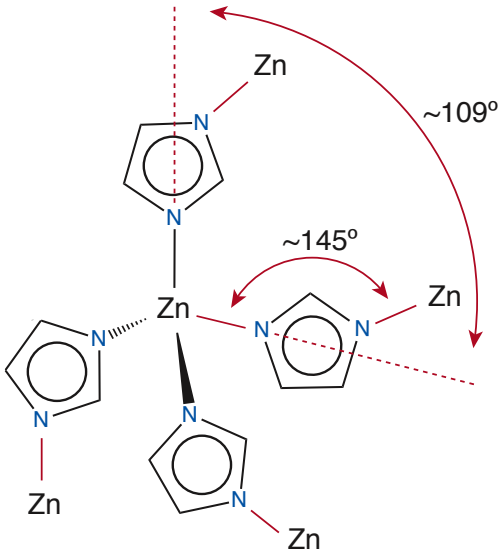

Figure 2.1 Characteristic building unit of ZIFs, illustrated by the example of **ZIF-4** with four crystallographically independent imidazolate linkers coordinating tetrahedral Zn^{2+} cations. Approximate bridging angles are indicated, and are similar to those of SiO_4 networks.

to studying hierarchies of stability, further trends in performance along the polymorphic series of $Zn(Im)_2$ have been established by means of experiments and computer simulations in terms of nitrogen adsorption[34], hydrogen adsorption[100], and mixed gas separation[101].

Among all these micro-porous $Zn(Im)_2$ polymorphs, ZIF-4 has emerged as the most stable at ambient conditions, and thus has been the most studied. First described by Park et al. 2006[34], ZIF-4's scaleable synthesis[102], in combination with its remarkable performance in the separation of olefin/paraffin mixtures[103], its adsorption and retention capacity of radio-active iodine[60], and its shaping abilities[104, 105], demonstrate potential for industrial applications.

Importantly, ZIF-4 is only meta-stable at ambient conditions. Experimentally, this becomes apparent when it is heated or ball-milled. At a certain point, the porous framework of ZIF-4 collapses and a reconstructive phase transition leads to the much denser ZIF-zni of identical chemical composition. ZIF-zni is recoverable to ambient condition and cannot be transformed back to ZIF-4.

The three-dimensional crystal structure of ZIF-4 is based on an orthorhombic unit cell with approximately unit cell parameters of $a = 17\,\text{Å}$, $b = 17.1\,\text{Å}$, $c = 19\,\text{Å}$ and crystallises in the *Pbca* space group. It adopts the **cag** network topology identical to that of the phosphate minerals variscite[114] and strengite[115], and synthetic $CaGa_2O_4$[116]. This topology, i.e.

Table 2.1 Overview of known $Zn(Im)_2$ polymorphs and their structural characteristics.

Name	Net	Space Group	a (Å)	b (Å)	c (Å)	β (°)	Z	V (Å^3)	V/Z	CSD-code	Ref.
ZIF-4-LT	cag	*Pbca*	14.267	14.284	16.413		16	3345	209	IMIDZB12	[106]
β -ZIF-zni	zni	*I41*	22.748	22.748	13.017		32	6736	211	IMIDZB07	[107]
ZIF-zni	zni	*I41cd*	23.481	23.481	12.461		32	6870	215	IMIDZB	[108]
ZIF-4-I	cag	*P21/c*	17.608	14.411	14.703	100.90	16	3664	229	VEJYUF07	[43]
ZIF-coi	coi	*Fdd2*	18.505	23.874	9.315		16	4115	257	KEVLEE	[109]
ZIF-4	cag	*Pbca*	15.395	15.307	18.426		16	4342	271	VEJYUF	[34]
ZIF-1	crb	*P21/n*	9.741	15.266	14.936	98.62	8	2195	274	VEJYEP	[34]
ZIF-64	crb	*P2/n*	21.110	9.906	21.110		16	4414	276	GITTEJ	[110]
	nog	*P21/n*	24.359	9.610	24.804	91.77	20	5803	290	HIFWAV	[111]
	zec	*C2/c*	37.241	19.217	25.547	132.41	40	13499	313	HICGEG	[111]
ZIF-2	crb	*Pbca*	9.679	24.114	24.450		16	5707	357	VEJYIT	[34]
ZIF-3	dft	*P42/mnm*	18.970	18.970	16.740		16	6024	377	VEJYOZ	[34]
SALEM-2	sod	*I-43m*	16.830	16.830	16.830		12	4768	397	HIFVUO01	[112]
	gis	*I41/a*	18.389	18.389	19.129		16	6469	404	HIFVUO	[111]
	afi	*P6/mcc*	26.437	26.437	16.632		24	10067	420	IMIDZB13	[113]
ZIF-6	gis	*I41/amd*	18.515	18.515	20.245		16	6940	434	EQOCOC01	[34]
ZIF-10	mer	*I4/mmm*	27.061	27.061	19.406		32	14210	444	VEJZIU	[34]
	can	*Pnma*	9.626	23.436	41.593		16	9383	596	PAJRUQ	[113]

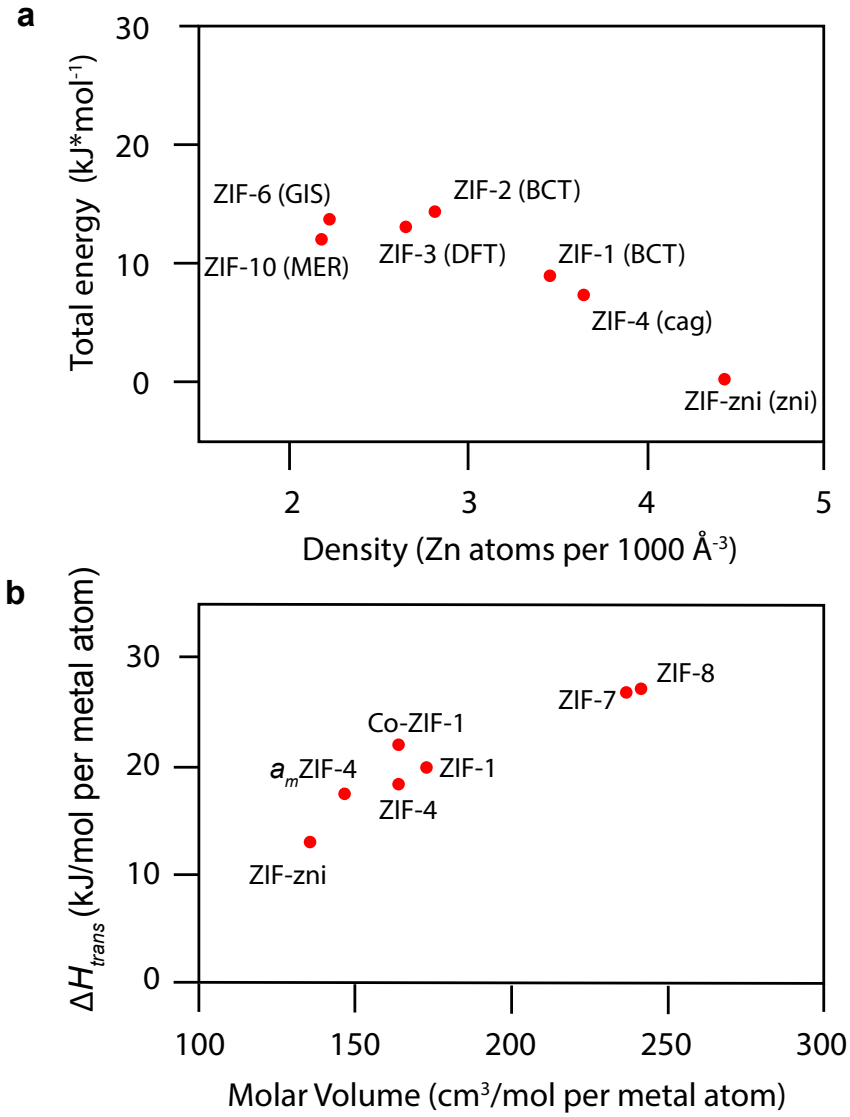

Figure 2.2 **a.** Calculated total energy of known polymorphs of $Zn(Im)_2$ versus density after Lewis et al. 2009[98]. **b.** Enthalpies of formation for a series of ZIFs after Hughes et al. 2013 [99].

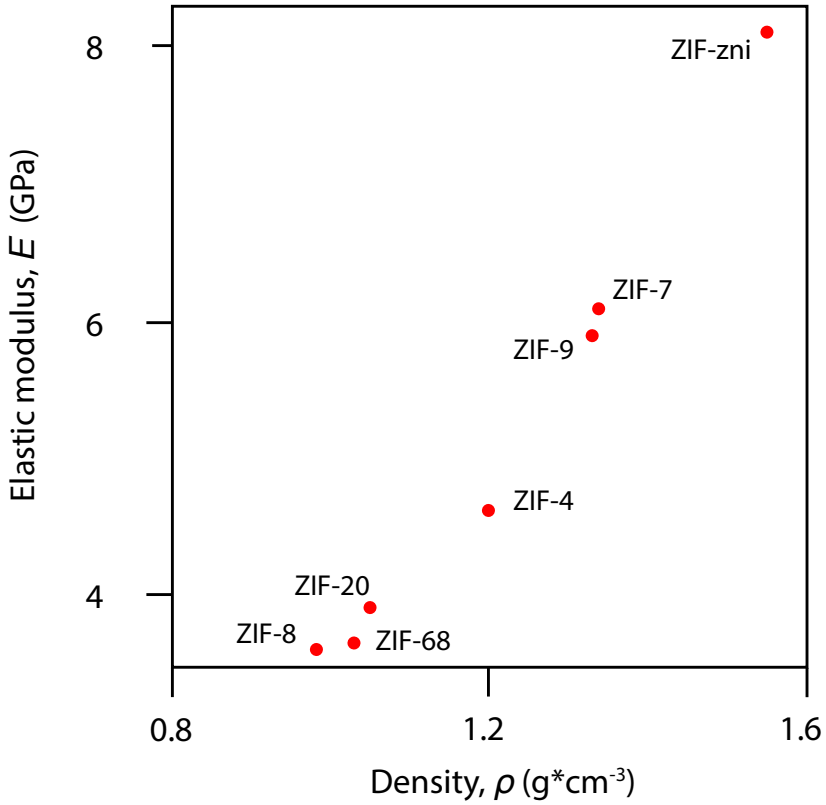

Figure 2.3 Elastic modulus of ZIF single crystals as a function of density after Tan et al. 2010. [35].

the connectivity of the four-fold coordinated metal centres amongst each other, consists of 4-membered, 6-membered, and 8-membered, quasi-planar rings. Figure 2.4 shows two volume slices of the crystal structure of ZIF-4 perpendicular to its *a* and *b* axis, emphasizing the two dimensional networks of these interlocked ring systems.

In addition to the pure $Zn(Im)_2$ ZIF-4, certain isovalent substitutions are known to result in iso-structural compounds, though with altered chemical compositions: the Zn^{2+} metal centre can be replaced by Co^{2+}[117], and the pure imidazolate linker can be substituted by imidazole derivatives such as benzimidazole[110]. The chemical variety that results from substitution of the metal centres significantly broadens if other structure types are taken into account, as reported in Table 2.2.

Table 2.2 Metal-imidazolates of $M^{2+}(Im)_2$ stoichiometry.

Compound	Type/Topology	Reference
$LiB(Im)_4$	zni	[118]
$CuB(Im)_4$	zni	[118]
$Co(Im)_2$	zni	[119]
	dia	[120]
	banalsite	[121]
	CrB_4	[117]
$Ni(Im)_2$	2D	[122]
$Cu(Im)_2$	PtS	[123]
	SOD	[124]
	moganite	[124]
$Cd(Im)_2$	dia	[125]
$Hg(Im)_2$	dia	[125]

Given the large number of polymorphs for a single composition, as detailed in Table 2.1, and the chemical variability for this stoichiometry from Table 2.2, as well as the large number of possible imidazolate derived ligands and transition metals in general, one can presume that a large number of ZIF structures are yet to be discovered.

2.1.2 ZIF-62

ZIF-62 was first described independently from ZIF-4 by Banerjee et al. 2008[110]. However, its chemical composition and crystal structure can be derived from the structure of ZIF-4 by a partial disordered substitution of the imidazolate ligand by benzimidazolate, as will be discussed in Chapter 3.

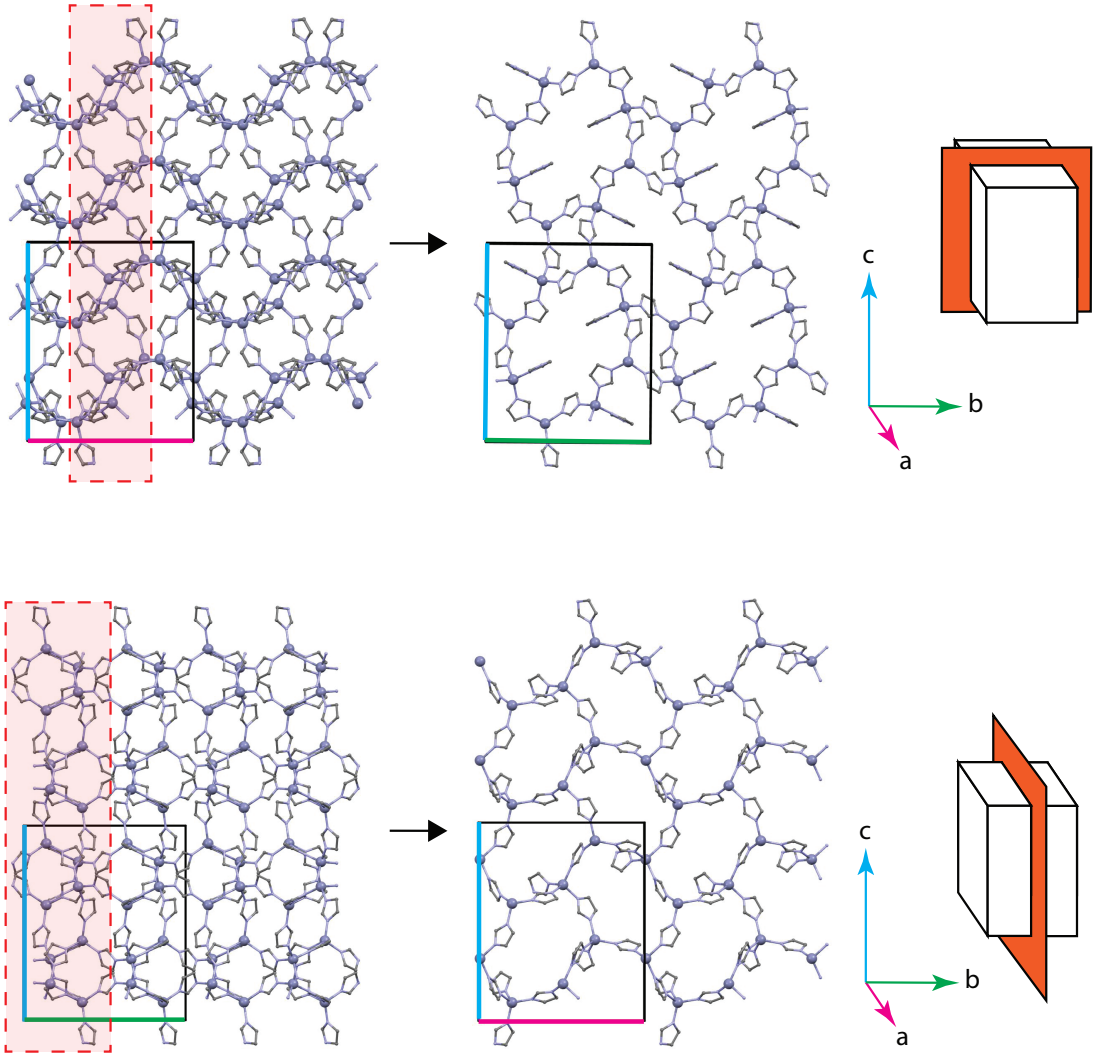

Figure 2.4 The underlying ring-networks of ZIF-4 extending in the crystallographic(010) and (100) plane. For clarity, slices perpendicular to *x* (top) and *y* (bottom), containing the 8- and 4-, and the 6-membered rings, are reduced to ½ and ¼ of the fractional coordinates, respectively, as indicated by the red dashed box. Zn atoms shown in blue, imidazolate rings shown as grey sticks, H atoms omitted.

2.2 Solvothermal synthesis

The synthesis of ZIFs has been achieved via a variety of methods [126]. Importantly, scaled-up procedures for synthesis of bulk quantities of ZIF-4 have also been reported[102, 127]. Solvothermal synthesis is the most commonly employed technique, alongside mechanochemical-, microwave-assisted-, and sono-synthesis, to name but a few. Solvothermal synthesis is a solution-based route carried out in sealed containers. The amount of pressure generated depends on the required temperature for the synthesis and the boiling temperature of the solvent used. Conventionally, high-pressure resistant steel autoclaves (bombs) are used. However, in the present work the combination of relatively low synthesis temperature (140 °C) and the solvent's high boiling point (dimehtylformamide, DMF, 153 °C) safely allowed for the used of Pyrex glass jars with temperature resistant screw lids (Figure 2.5).

Under solvothermal conditions, the generic chemical reactions to form ZIFs requires deprotonation of the imidazole precursor to first form imidazolate. This step is facilitated by thermally induced decarboxylation of DMF[128]. The resulting dimethylamine and its lone ion-pair is capable of deprotonating the imidazole. The negatively charged imidazolate then reacts with the positively charged metal species to form metal-ligand clusters[129]. Extended, porous networks can be formed due to the preferred binding and bridging angles of tetrahedral units, and with the aid of solvent molecules acting as structure-directing agents.

The generic procedures for synthesis of ZIF-4 and ZIF-62 involve the preparation of stock solutions of DMF and $Zn(NO)_3 \cdot 6H_2O$ (0.2 M), $C_3H_4N_2$ (imidazole, 1.5 M), and $C_7H_6N_2$ (benzimidazole, 0.2 M) (purity > 99 %, all purchased from Sigma Aldrich). Appropriate amounts of stock-solutions were measured by weight and mixed together. After thorough stirring, the jars were sealed and placed in a preheated oven. After 96 h, the glass jars were removed from the oven. Fifteen minutes sonication loosens the precipitates from the walls of the glass jar while the solution cools down to ambient temperature. The powder can then be filtered from solution using ash-less Whatman 42 filter-paper, which retains particles larger than 2.5 µm. The recovered material was dried at 80 °C for 30 min. The yield of pure powder from one batch (100 ml) measured as a function of reaction time after 24 h, 48 h, 72 h, and 96 h is shown in Figure 2.6. After 48 h, only a minor increase in total yield is apparent.

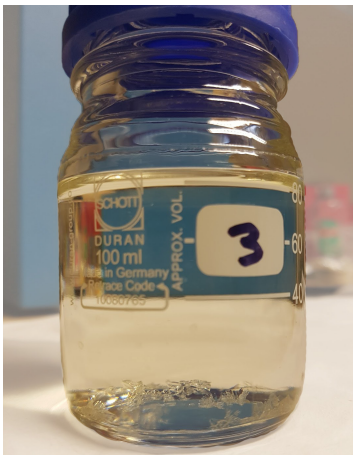

Figure 2.5 Solvothermal synthesis of ZIF-4. A DMF solution with dissolved Zn and Imidazole precursors was heated in a sealed glass jar to 130 °C for 48h. Large single crystals grew on the bottom of the jar.

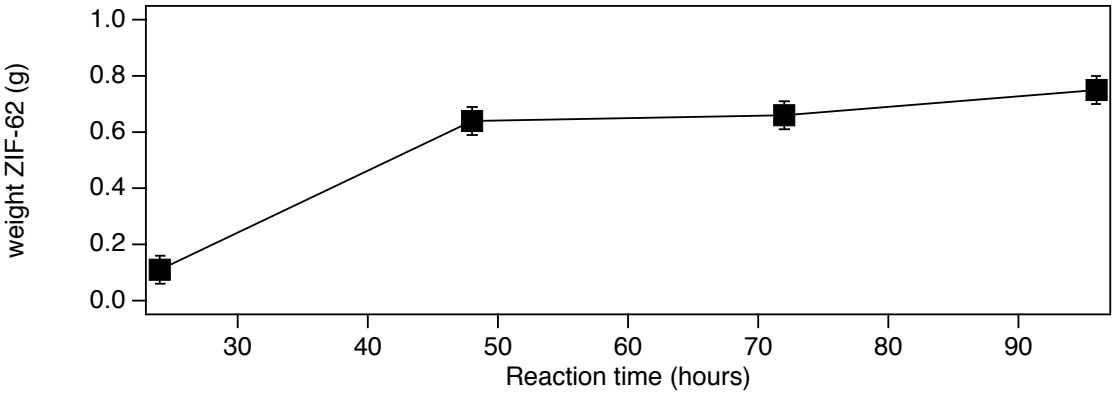

Figure 2.6 The yield of precipitated ZIF-62 powder from 100 ml of solution at 140 °C was measured after filtration using Whatman 42 filter-paper and drying of the products. Error bars are estimated based on filtration efficiency and particle size selection due to the filter-paper.

2.3 Desolvation procedures

ZIFs, as with most porous MOFs, trap solvent molecules in their pores during synthesis and crystal growth. In fact, many MOFs depend on the incorporation of solvent molecules as structure-directing agents[130]. In the case of the synthesis route used here, the ZIF-4 and ZIF-62 structures contained approximately 1 dimethylformaide (DMF) molecule per 2 formula units of ZIF[34]. Also referred to as activation, the process of desolvation typically requires the application of heat and/or vacuum. DMF has a relatively high boiling point of 153 °C. This quality is beneficial in view of its low vapour pressure under solvothermal

conditions in closed containers. However, the high boiling point makes it difficult to desolvate the host frameworks. To facilitate the removal of residual solvent, the as-synthesised products can be solvent-exchanged to replace DMF with dichloromethane (DCM), which has a lower boiling point of 40 °C. The procedure involves the immersion of DMF occupied ZIF in pure DCM for approximately 24 to 48 h. After this, the DCM occupied ZIFs can be desolvated by the application of heat and vacuum.

Raman spectra of the ZIFs provide good indications of thorough solvent exchange or removal by the presence or absence of peaks which correspond to the those solvents. The solvent peaks are mostly well separated from peaks associated with the ZIF framework and are very sensitive, resulting in a low detection limit. The characterization of ZIFs by Raman spectroscopy, including the identification of residual solvent, is discussed in Section 2.5 as part of the general structural and chemical characterisation.

In order to streamline the desolvation process and to ensure reproducibility of pressure, temperature, and time parameters, a custom-built desolvation apparatus was designed (Figure 2.7). Up to three test tubes containing sample material were sealed in cylindric shaped stainless steel containers. These containers were directly attached to a rotary vacuum pump and lowered into a solid block of aluminium. The latter is placed on a generic laboratory hot plate, which provides uniform heat. To monitor the temperature at the sample, one container is furnished with a K-type thermocouple which reaches the bottom of the test tube. Temperature is also monitored at the interface of the aluminium block with the hot plate. Vacuum pressure is monitored with a Pirani gauge. Figure 2.8 shows a typical temperature evolution during the desolvation process.

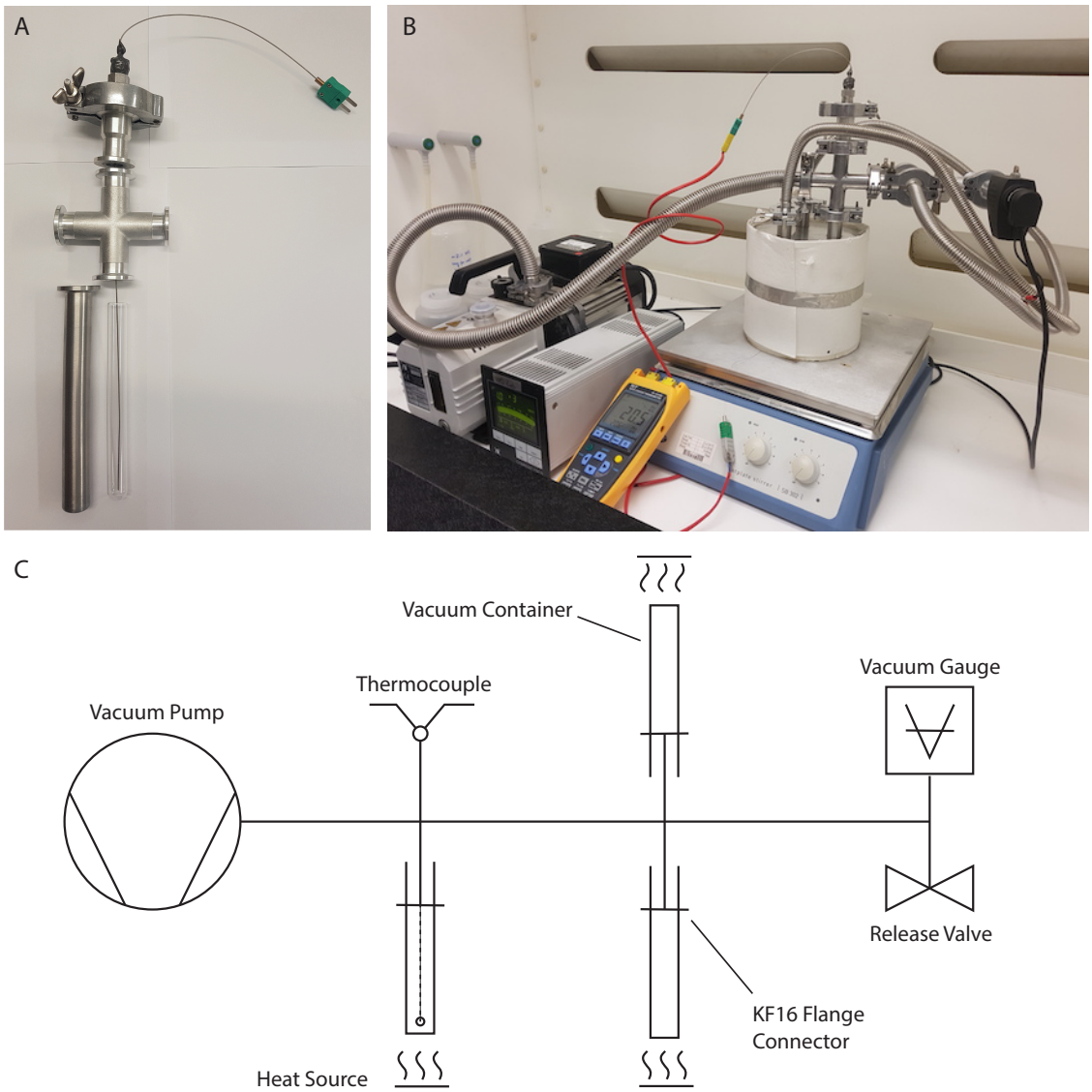

Figure 2.7 Custom-built desolvation equipment consisting of a vacuum pump and a generic laboratory hot plate for simultaneous desolvation of 3 batches. A) isolated view of vacuum container with tightly fitting test tube. The thermocouple for temperature measurement of the contained sample is fed through a flange connector which is sealed with temperature resistand epoxy adhesive. B) Overview of the system under operation with three samples contained in the thermally isolated aluminium block. C) Schematic drawing of the vacuum system, the sample containment, the heat source, and the monitoring ports.

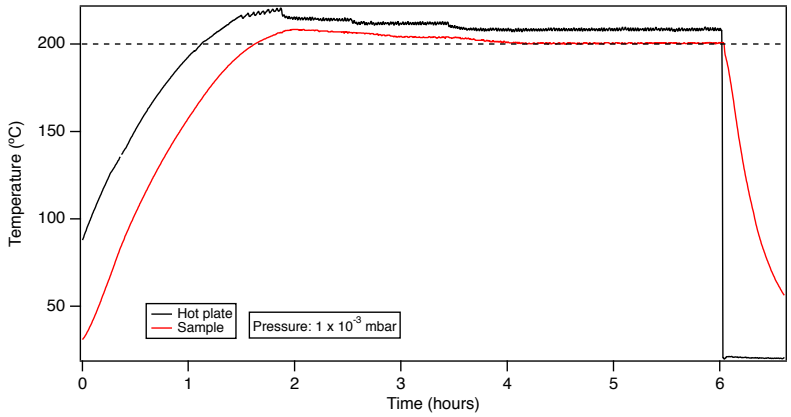

Figure 2.8 Temperature evolution of hot plate and sample during desolvation under vacuum for solvent-bearing ZIF material measured with K-type thermocouples.

2.4 Compositional analysis by HPLC

ZIFs can be synthesised from a multitude of imidazole-derived organic linkers [34, 110]. Importantly, ZIFs can also contain a mixture of linkers. ZIF-62 has a defined formula of $Zn_2(Im)_{1.75}(bIm)_{0.25}$, in reality however, the ratio between the two constituent linkers is variable. Within certain limits, it can be regarded as a continuous solid solution limits according to $Zn(Im)_{2-x}(bIm)_x$, as will be discussed in Chapter 3. Previous studies which addressed the properties of mixed linker ZIFs as a function of composition most commonly used liquid NMR to quantify the ratios of linkers[53]. This thesis establishes an alternative, more accurate, quantification procedure based on high-performance liquid chromatography (HPLC).

HPLC relies on differential retention of dissolved components due to their distinct polarity when a solution of these components is pumped through a column of a solid adsorbent. After this separation process, the concentration of specific solutes is measured sequentially by their characteristic UV absorbance. Having measured a series of standards with know concentrations, a linear function can be used to relate the peak area to actual concentrations. Advantages of HPLC include high sensitivity to low concentrations, high accuracy, and high reproducibility. Additionally, it is relatively quick and takes approximately three minutes measuring time per sample. Conveniently, the measurement may be fully automated for a series of samples. The following procedure for the dissolution of ZIF-62 and subsequent HPLC measurement has proven successful and was used for the chemical characterisation of the synthesised materials throughout all experiments.

2.4.1 HPLC Measurement setup

HPLC analysis of the ZIF samples was performed using a modular Agilent 1100 Series HPLC system composed of a high pressure binary pump, auto-sampler with injector programming capabilities, Peltier type column oven with 6 µL heat exchanger and a Diode Array Detector with a semi-micro flow cell (1.6uL, 6mm path length). The flow-path was connected using 0.12 mm ID stainless steel tubing to minimise peak dispersion. The HPLC column is an Excel C18-PFP with 2 µm particle size (4.6 mm internal diameter × 50 mm length) manufactured by ACE. The C18-PFP stationary phase is prepared by covalently bonding a pentafluorophenyl-octadecylsilane to pure silica. This column is stable to 1000 bars back-pressure and gives good peak shape. The mobile phase consists of solvent A = (water + 0.2% Trifluoroacetic acid (TFA)) and Solvent B = (MeCN + 0.2% TFA). The solvent gradient was set to 3% B isocratic from 0-1 min and 3-60% B 1-3 min. The flow-rate is 1 mL/min with a column temperature of 45 ºC and 1 µL injection. The best wavelength for imidazole is 220 nm (4 nm bandwidth), and for benzimidazole 266 nm (8 nm bandwidth), both have a reference of 550 nm (100 nm bandwidth).

2.4.2 HPLC Standard and sample preparation

Firstly, standards for the quantification of imidazole and benzimidazole were prepared from pure reagents dissolved in H_2O+0.1M formic acid. A linearity and reproducibility test was carried out on a series of ten dilutions, i.e. concentrations, for both compounds. Every sample was prepared and measured in duplicate. In addition, both stock solution and duplicated samples of an intermediate concentration were prepared in duplicate. By doing so, both the resulting linearity and the reproducibility could be evaluated based on two respective R^2 values for the linear fit of peak area *vs.* concentration (Figure 2.9a and 2.9b).

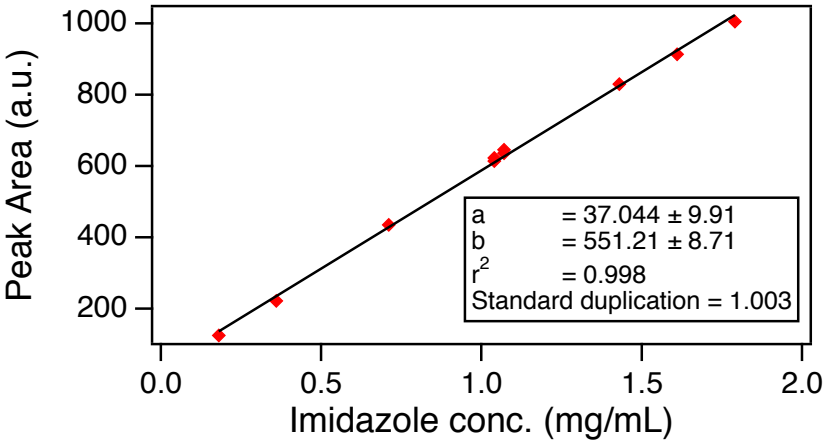

(a) Measured peak area versus imidazole standard concentration. Linear fit parameters are given in textbox.

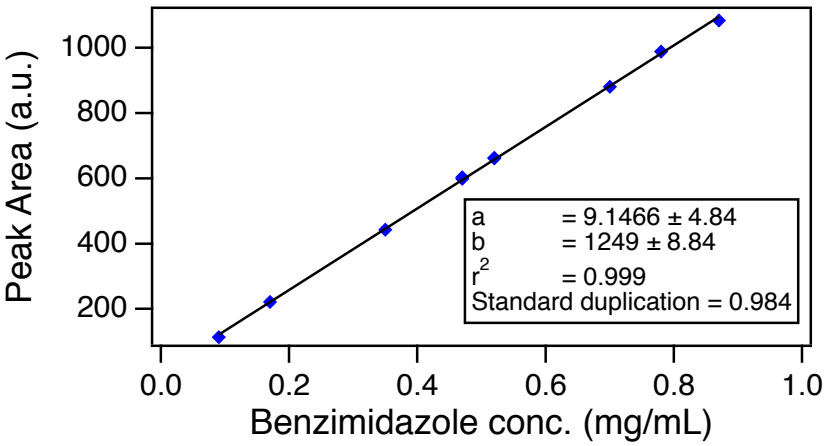

(b) Measured peak area versus benzimidazole standard concentration. Linear fit parameters are given in textbox.

2.5 Raman spectroscopic characterization

The routine characterization of all synthesised ZIF powders involved the measurement of their Raman spectra. These were measured using a confocal LabRam300 Horiba Jobin Yvon spectrometer with a 532 nm laser produced by a diode-pumped solid-state system with incident power of 100 mW. Measurements were collected with a 300 µm confocal hole size and used an Olympus 50x objective with a holographic grating of 1800 mm^{-1}, coupled to a Peltier-cooled front-illuminated CCD detector over the range from 100 to 1600 cm^{-1} with a 2 µm spot size.

Raman spectroscopy provides a relatively simple and quick tool to probe both the structural and the chemical characteristics of the synthesised powders, as well as the homogeneity

of theses characteristics across individual particles. In addition, Raman spectra can be used to confirm the constituent phases by comparison with a reference spectrum, and it is also useful for the detection of residual solvent content (see Section 2.10).

The Raman spectra of desolvated ZIFs show a large number of Raman modes, commonly associated both with vibrations internal to the rings of the organic linkers, Zn-N bonds and lattice phonons. However, a dedicated study on vibrational mode assignments in ZIF-4 and ZIF-62 has not yet been conducted. Consequently, the Raman spectra of the pure imidazole and benzimidazole precursors were used as an approximation for mode assignments in ZIF-4 and ZIF-62. Spectra of pure, crystalline precursors used for synthesis were recorded alongside ZIF-62 and ZIF-4 and observed mode frequencies compared to reported values (Figure 2.11)[131, 132].

Based on these assignments, Raman spectroscopy should in principle also allow for semi-quantitative, to possibly quantitative, analysis of the mixed-linker ratios. Both imidazole and benzimidazole have characteristic peaks, and the ratios of their amplitudes, if they correlate linearly can be used to measure the relative amount of the two types of linkers. This possibility is further explored in Chapter 3, which discusses the chemical variability of ZIF-62 in greater detail.

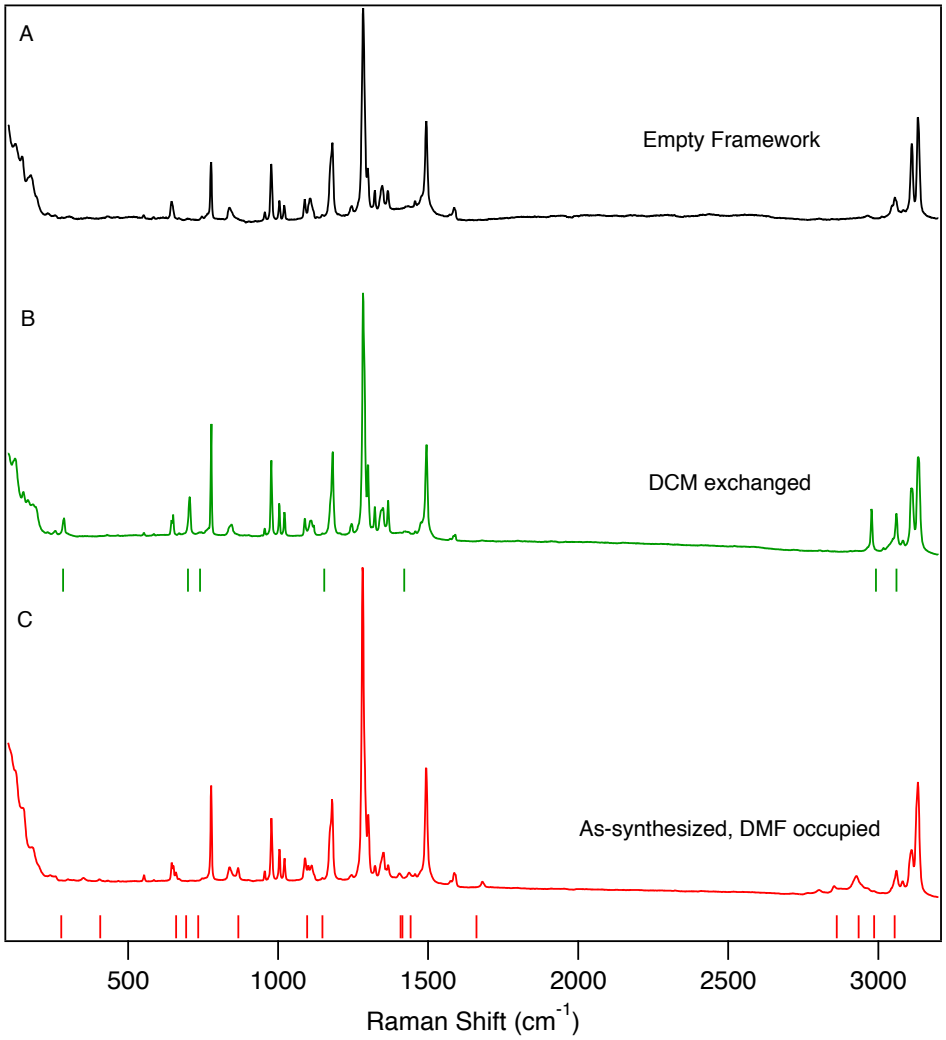

Figure 2.10 Raman spectra of A) as-synthesised, DMF containing ZIF-62, B) solvent-exchanged DCM containing ZIF-62, and C) desolvated empty ZIF-62. Tick marks represent positions of Raman modes of the pure solvents.

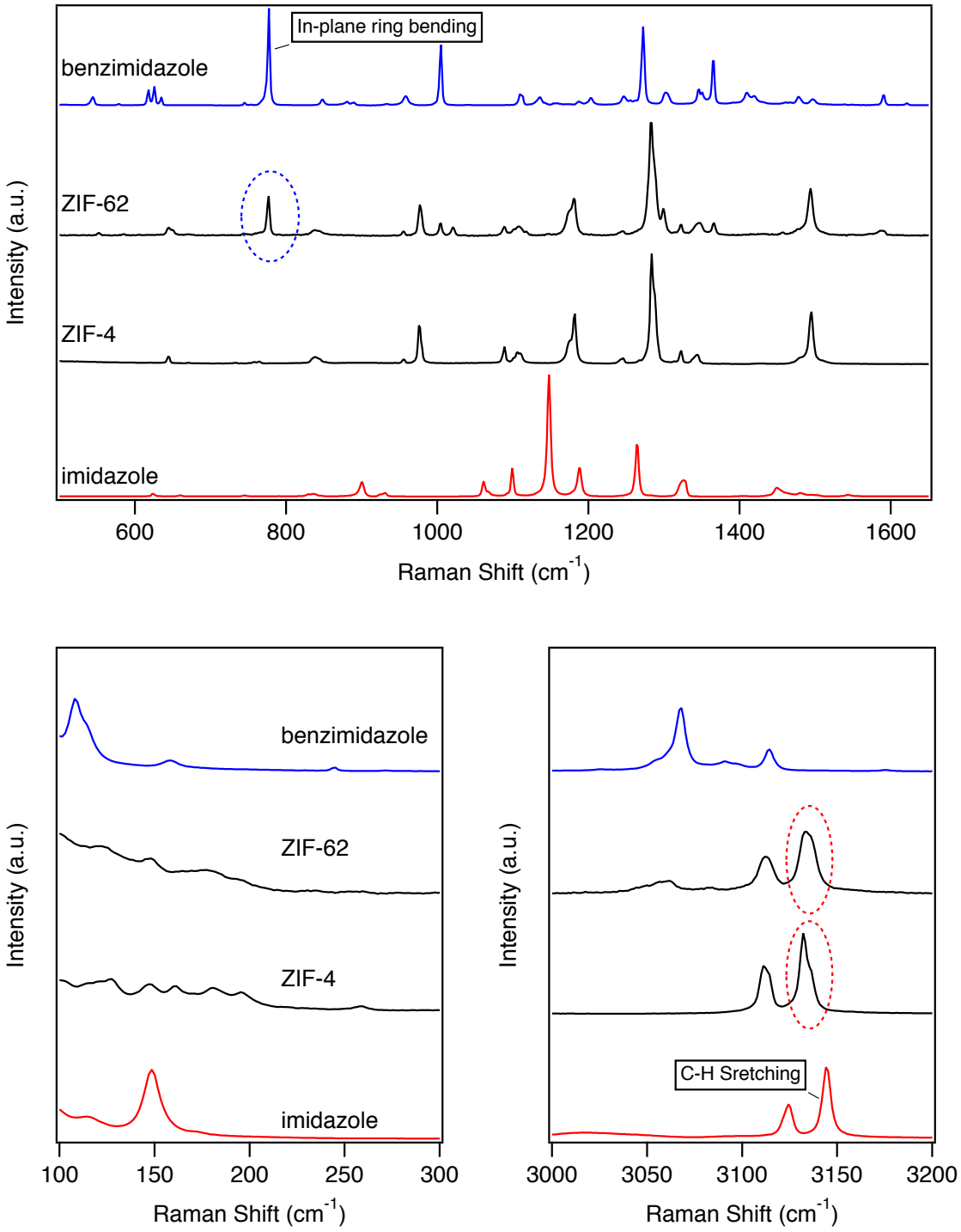

Figure 2.11 Raman spectra of desolvated ZIF-62 and ZIF-4, and crystalline imidazole and benzimidazole in three spectral ranges. Blue and red circles mark benzimidazolate and imidazolate characteristic peaks.

2.6 X-Ray crystallographic characterization

X-ray crystallographic techniques are used for the structural and the crystal-chemical investigation of both polycrystalline bulk powders and individual single-crystals. Powder X-ray diffraction (PXRD) is a widely used technique to determine phase contents, unit cell dimensions, and crystallite sizes. In certain cases, it can even be used to perform structure refinements or structure solutions. Single-crystal X-Ray diffraction (SC-XRD) allows for routine structure refinements and structure solutions, but it does not provide information on bulk powder characteristics in the same way that PXRD does. Both techniques have been used in combination throughout this thesis. The following section gives an overview of the basic single-crystal and powder XRD techniques routinely used for the monitoring and the general characterisation of the synthesised ZIFs.

2.6.1 Powder X-ray diffraction of ZIFs

Powder X-ray diffraction (PXRD) patterns were collected on a Bruker D8 Advance X-ray diffractometer equipped with an incident beam monochromator for Cu$K\alpha_1$ radiation (λ = 1.5406 Å), and a Sol-X detector. The generator was operated at 40 kV and 40 mA. Diffraction data were collected at room temperature in $\theta : 2\theta$ mode and a step-scan of 0.02° 2θ. The samples were carefully ground in an agate mortar and deposited on a flat-plate sample holder. Rietveld and Lebail refinements of the crystal-structural models were performed in TOPAS-Academic V6[133].

In Rietveld refinements [134], a powder pattern is first simulated based on (1) the peak positions, calculated on the basis of the unit cell dimensions and the space group symmetry; (2) the peak intensities, calculated on the basis of the unit cell content (atom types, atom positions, occupancies, etc.); and (3) the peak shapes calculated on the bases of variable contributions such as the line width of the X-rays, geometrical parameters of the diffractometer, as well as sample dependent effects such as crystallite size and micro-strain. In the course of a Rietveld refinement, the software then tries to match the calculated pattern to the experimentally determined pattern *via* a least-square algorithm by varying the parameters of the crystal structure until the best fit is obtained. In order to achieve a physically realistic solution, the mathematically best fitting model has to be scrutinised regarding its chemical soundness, over-parametrisation, and possible correlations. The result is a *refined* crystal structure model.

In contrast, during a Lebail refinement [135], only the peak positions, *i.e.* the unit cell dimensions with a given space group symmetry, are modelled and refined based on

crystallographic information. Peak intensities, on the other hand, are individual matched by freely refinable parameters without physical meaning. The advantage here is that the atomic contents in the unit cell is not needed for a refinement, which simplifies the process in case the structure of the material is not *a priori* known. Unit cell dimensions, and in some cases the symmetry information, can still reliably be refined.

PXRD was the first and most important measure for assessing the successful synthesis of the ZIF powders. The phase purity of the products were monitored by comparing the measured pattern with a reference pattern, calculated from a published crystal-structural model[34]. Phase impurities can be detected in form of additional diffraction peaks down to as little as a few weight-percent. The unit cell dimensions of the materials are directly represented by the peak positions and can be refined against the experimental data. However, in the special cases of ZIF-4 and ZIF-62, the lengths of the a and b repeats are very similar. As a consequence, many positions of the main peaks almost completely overlap. These overlaps caused issues during structureless Lebail refinements, often resulting in the inversion of the x and y axes because peak intensities are not based on a physical model. Therefore, it was necessary to perform Rietveld refinements, where the peak intensities are calculated by the atomic coordinates provided by the structural model.

2.6.2 Single-crystal X-ray diffraction of ZIFs

Single-crystal X-ray diffracion (SC-XRD) was used to validate the published crystal structures of ZIF-4 and ZIF-62, as well as to study the effects of benzimidazole for imidazole substitution, as presented in Chapter 3. Powder X-ray diffraction techniques merge all possible diffraction peaks that fulfil the Bragg-equation at a given angle of 2θ to a two-dimensional profile. In contrast, the advantage of SC-XRD lies in the separate observation of each and every diffraction peak. Thus, single-crystal techniques allow for a much more detailed and unambiguous structure solution and refinement. Typically, atomic positions within the unit cell are refined to much higher accuracy; electron densities that are missing when the simulated data are compared with the observed data can be calculated; atomic displacement parameter can be refined anisotropically; and twinned crystals can be de-convoluted.

Using the synthesis methods described earlier usually yielded materials just at the boundary between poly-crystalline powders and single-crystals. This meant that it was possible to manually pick out individual crystals. However, they proved too small to be measured on the in-house single-crystal diffractometer. As part of these investigations, a sample was therefore sent to the UK National Crystallographic Service[136], which provides superior lab-based

facilities with rapid access. In detail, single-crystal X-ray diffraction data was collected on a four-circle Rigaku FRE+ diffractometer equipped with VHF Varimax confocal mirrors, an AFC12 goniometer, and HyPix 6000 detector. Mo $K\alpha$ radiation was produce by a rotating anode X-ray generator at 45 V and 55 mA.

2.7 High-temperature and high-pressure environments

Both, Raman and powder XRD measurements were used to examine samples *in-situ* at non-ambient conditions, *e.g.* at high-temperature and high-pressure. These two thermodynamic variables both require the sample to be contained during the experiment. This introduced the problem of shielding material in the beam path of the X-rays and laser radiation. This shielding absorbs intensity, and in many cases, contributes a background signal which disturbs the measurements. This is less of a problem in the case of relatively light temperature-shielding as laboratory-sourced radiation provides enough energy to overcome this. On the other hand, the application of high-pressure requires the use of thick diamonds in so-called diamond anvil cells. These diamonds absorb a significant amount of the incoming beam intensity, therefore these experiments required highly brilliant synchrotron radiation. Details of the equipment, and experimental issues and limitations specific to XRD and Raman spectroscopy at high-pressure and high-temperature conditions, are described in more detail in the following sections.

2.7.1 Linkam heating stage for Raman spectroscopy

The Linkam DSC600 system (Figure 2.12) is a versatile and easy-to-operate heating and cooling stage, capable of providing temperatures in the range from $-170\,^{\circ}\mathrm{C}$ to $600\,^{\circ}\mathrm{C}$ (Figure 2.12). Its compact design consisting of a light-weight silver heating block with an embedded temperature sensor which allows for both precise and high heating rates up to $130\,^{\circ}\mathrm{C\,min^{-1}}$, as well as stable isotherms. Low temperatures are achieved by pumping liquid nitrogen through the silver block. Conventional DSC pans (made of Al or Pt) are used to contain the samples. The heater is located in a water-cooled aluminium body with thin glass windows which makes it possible to purge the sample environment with special gases. The entire stage is of a flat design, matching the requirements for its use in optical microscopy systems. Here, the DSC600 system was used in combination with the micro-Raman system described earlier.

Practical issues

Measurements at low temperatures are relatively straight forward. On the other hand, a major issue arose at high-temperatures. It was found that the ZIFs combust when they are illuminated with a laser beam at temperatures above 200 °C. Given that the ZIFs start amorphising at similar temperatures, the effects of thermal amorphisation and laser-induced combustion could not be separated. However, it was found that this problem could be partially resolved by using progressively lowering laser power as the temperature increased. On the downside this resulted in inconsistent acquisition conditions and progressively longer data acquisition times. Flushing the sample environment with N_2 did not resolve the problem. A potential solution was found by flushing a reducing gas mix of Ar + 2 % H_2. Still, a certain amount of laser-induced amorphisation cannot be fully excluded. Another major issue arose from a strong increase in the fluorescence background that amorphous ZIFs produce, which made it impossible to investigate them due to rapid detector saturation.

2.7.2 Heating chamber for PXRD

A radiation-heating stage made by MRI mounted on a Bruker D8 Advance X-ray powder diffractometer was used to perform *in-situ* high-temperature powder X-ray diffraction measurements. This system allows for the fully programmed acquisition of a sequence of powder XRD data at temperatures up to 900 °C, either under vacuum, air, or N_2 atmosphere. Data are typically obtained at a 10 °C to 25 °C interval with a measurement time per temperature step of approximately 20 minutes. Alternatively, the system can also be used for rapid heating experiments of up to 50 °C min^{-1} with a fixed detector position. In this mode, the detector records a relatively small window of 11° 2θ, though at a frame rate that matches the heating rate. The result is the evolution of individual peaks as a function of temperature rather than entire diffraction patterns. Consequently, the options for structural refinements are limited. However, this is an excellent tool for the study of temperature-induced amorphisation and the peak shape evolution under non-equilibrium conditions.

Practical issues

Systematic errors which correlate with the peak positions hamper the accurate determination of unit cell dimensions. Such errors usually stem from the instrumental zero error and the sample displacement in the vertical direction. At variable temperatures, additional sample displacement can be caused by either the compaction or the swelling of powder, as well as the thermal expansion of the alumina sample holder. All these effects interfere with the

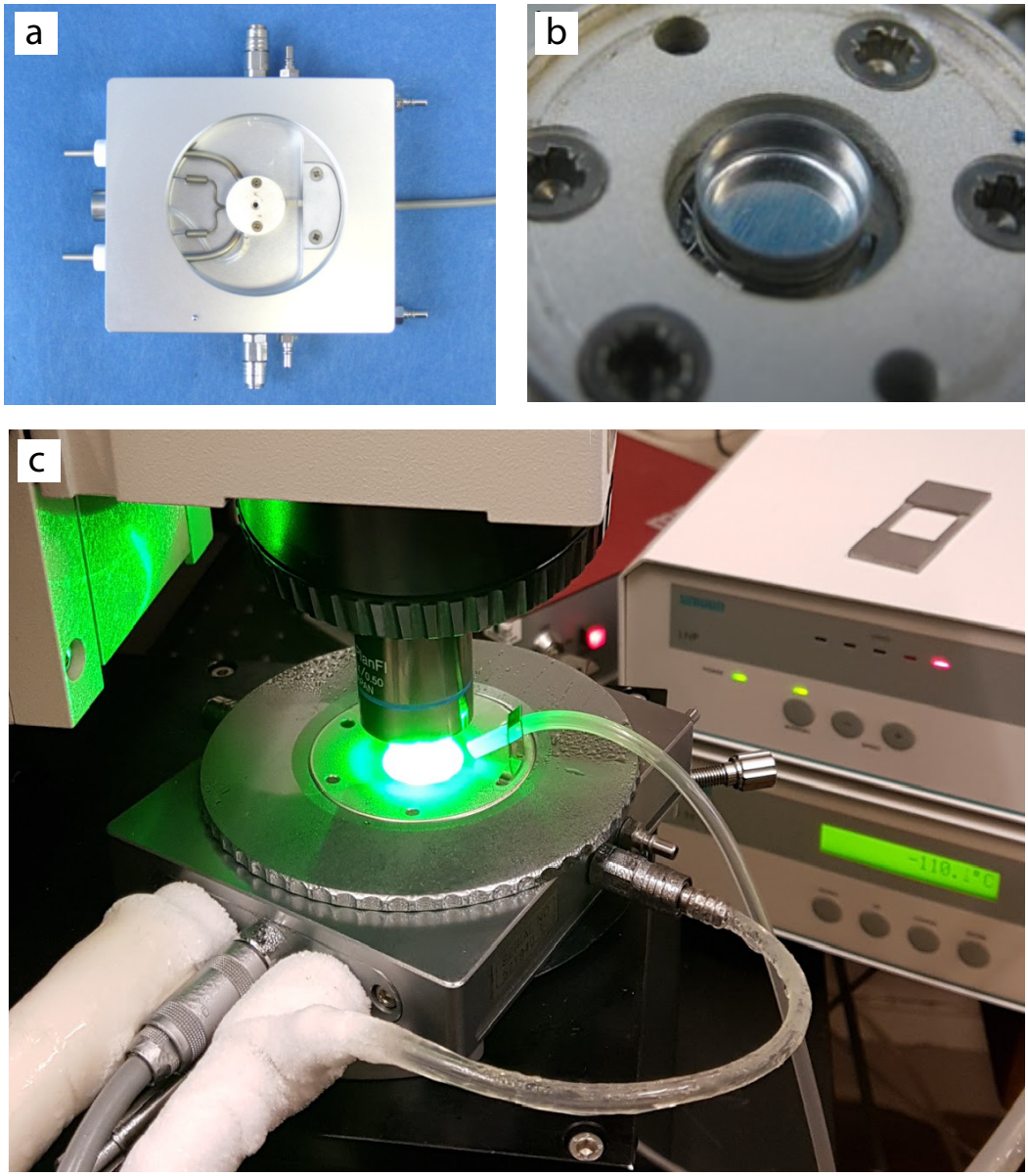

Figure 2.12 a) Linkam DSC600 variable temperature stage (cover removed). Ports include connectors for liquid N_2, cooling water, and flushing gas. b) Close-up view of the heating block (lid removed) containing an Al crucible of 5 mm diameter. c) Fully assembled system at low-temperature including the Raman spectrometer (laser on) and the temperature controller on the right-hand side.

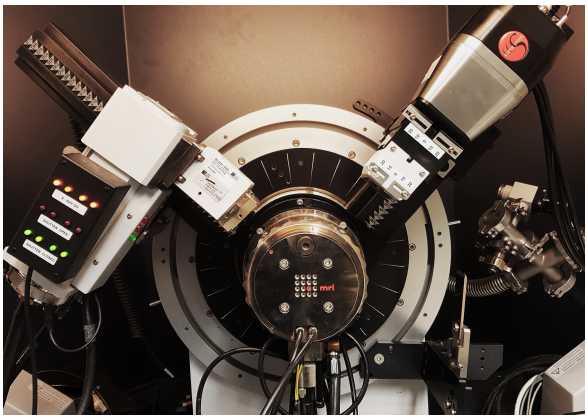

Figure 2.13 MRI high-temperature stage mounted on a Bruker D8 Advance X-ray powder diffractometer.

purely sample-dependent peak shift due to thermal contraction or expansion of the unit cell parameters. An internal, non-reactive standard can be used to de-convolute the contributions of the sample and the systematic errors from geometric aspects. Here, all ZIF powders investigated under variable-temperatures were mixed with a small amount of pure silicon powder that acted as an internal standard. The unit cell parameters of this material was previously calibrated using a certified NIST LaB_6-standard to guarantee accurate absolute values for lattice parameters. Admixing small amounts of Si powder with known and precisely calibrated unit cell parameters also ensured the repeatability of results across different diffractometer setups.

In practice, the Si produces a strong and well defined diffraction peak at approximately 28.6° 2θ. In the first step of a typical Rietveld refinement, the position of the calculated Si peak was held constant by keeping the known lattice parameter of silicon fixed, while only a 2θ-correction was refined. In the case of variable-temperature data, the unit cell parameter of Si was calculated as a function of temperature based on a polynomic function that describes the thermal expansion from the literature[137]. In a second step, the previously refined 2θ-correction was held constant, while the unit cell dimensions of the ZIF were refined. A generic input file for the use with TOPAS academic is provided in the Appendix.

More complex refinement methods, including strategies for structural solution based on rigid body approaches, are described in detail in Chapter 4 as part of the *in-situ* high-temperature and high-pressure experiments.

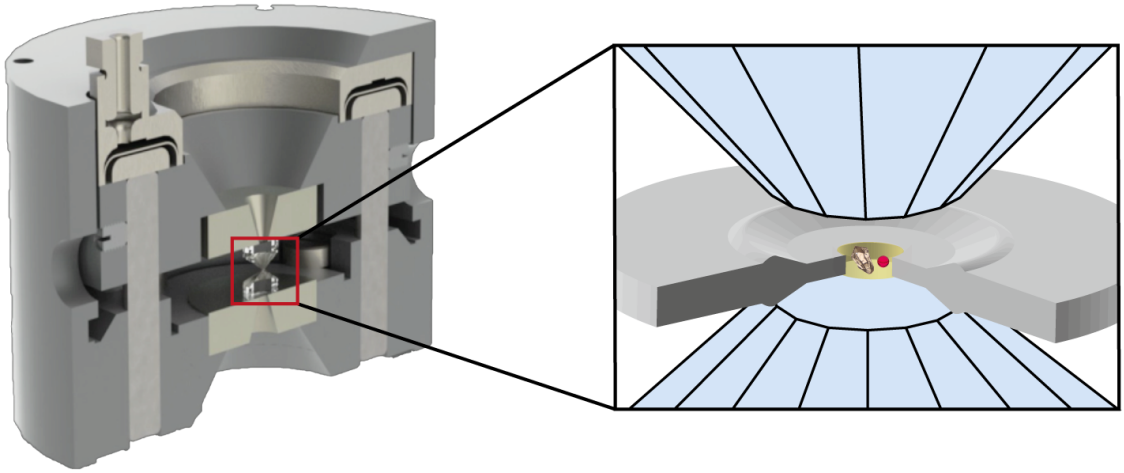

Figure 2.14 Cross-section of a membrane driven diamond anvil cell by Betsa, France. Inlet shows a schematic view of the sample chamber provided by a hole in the gasket material between the two diamond anvils

2.7.3 The diamond anvil cell (DAC)

Diamond anvil cells (DACs) are experimental tools used to investigate materials *in-situ* under high hydrostatic pressure. Two symmetrically opposing diamonds transmit mechanical pressure onto a small area of up to 1 mm^2 on a thin metal foil (gasket) which is placed between the two diamonds (Figure 2.14). A small hole in the gasket provides a compartment to contain the sample, a pressure calibrant, and a pressure transmitting medium which, alongside the plastic deformation of the gasket itself, transforms the external bi-axial pressure into hydrostatic pressure. The compression of the diamonds against each other is achieved by either a lever, tension-screws, or an inflatable membrane. The internal pressure is indirectly measured via the measurement of a calibrated property of the pressure standard. The two most widely used techniques are the pressure-induced shifting of optical fluorescence peaks and the compressibility of a unit-cell volume measured via XRD. The former technique most often uses the fluorescence-line of Cr^{+}-doped ruby, though many other materials have been calibrated[138]. Diffraction standards range from metals and silicates to salts[139, 140]. Due to the high optical purity of the diamonds, they are to a certain degree transparent to electromagnetic radiation such as X-rays or optical lasers, therefore measurements can be performed *in-situ*.

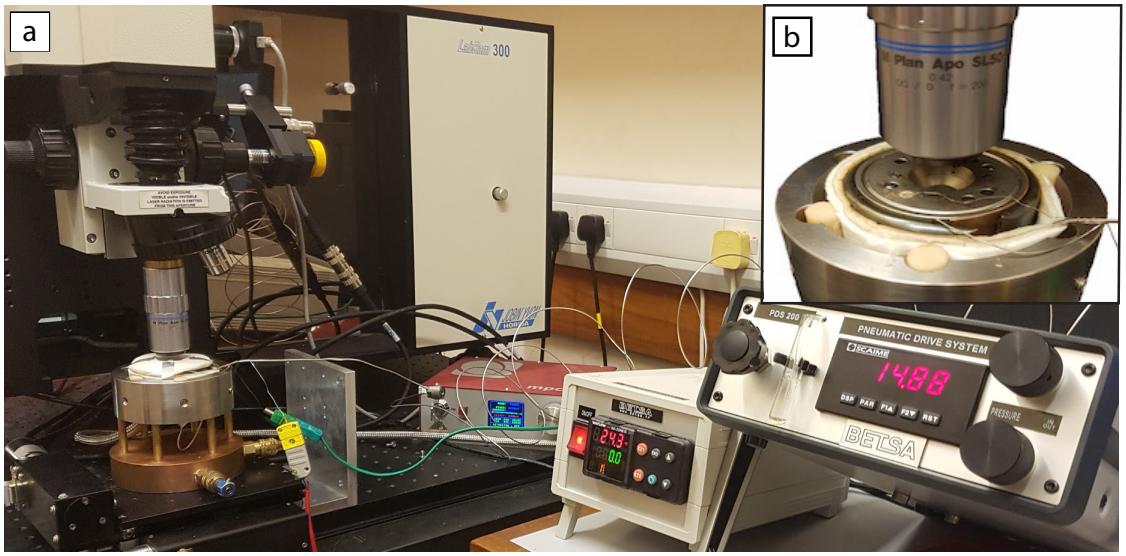

Figure 2.15 High-temperature diamond anvil cell setup for *in-situ* Raman spectroscopy. a) (left to right) Raman spectrometer with confocal optics focused on thermally isolated DAC/heater assembly, 532 nm laser, temperature controller, gas pressure drive for DAC. b) close-up view of uncovered DAC with external resistant heating sleeve.

2.7.4 Heated diamond anvil cell for Raman spectroscopy

Heated DACs allow the experimental study of materials under simultaneous pressure and temperature. The three principal methods of increasing the temperature of the sample in a DAC are (1) electrically external, which heats up the whole body of the DAC[141], (2) electrically internal, which heats up only the diamonds[142], and (3) laser-heating of the sample only[143]. The high-pressure-temperature investigations of ZIF-4 and ZIF-62 employed two similar external whole-cell heating systems, as described in the following section.

The laboratory-based high-pressure-temperature set-up which was used in combination with Raman spectroscopy consisted of a commercially available membrane-driven DAC and an external resistive heater made by BETSA, France. The DAC/heater assembly was held in suspension by a custom-built holder consisting of alumina spacers and a massive, optionally water-cooled, copper base (Figure 2.15). A motorised X-Y-stage allowed for safe and precise alignment of the samples under pressure and temperature.

Practical issues

As with any heated DAC system operating in air, the foremost problem is the danger of the graphitisation of the diamonds upon heating. Given that this is a kinetically controlled reaction, it proved difficult to find an exact number in the literature that stated the temperature limit of pure diamond in air. The maximum temperature achieved during the experiment was 450 °C during a period of approximately 15 minutes, which left the diamonds unimpaired and without any trace of transformation.

The main problems during the high-pressure-temperature experiments concerned the accurate determination of the internal pressure. This is generally difficult because the shift of any pressure-calibrated Raman band of a standard material will also be sensitive to temperature. Ruby has been calibrated in respect to temperature[138, 144], however, the broadening and rapid merging of the two fluorescence peaks upon increasing temperature limits its application to temperatures below 400 °C. Furthermore, it is crucial to have a suitable, i.e. temperature-resistant, pressure-transmitting medium. Since it was mandatory to use a large-molecule medium to prevent the penetration of the medium into the pores of the ZIF frameworks, the choice was reduced to three products: Fluorinert, Daphne Oil, and silicone oil[145]. However, their behaviour at high-temperature is not generally known. It can be assumed that their hydrostatic limits increase with increasing temperature, however, their temperature-stability has not been investigated. The choice of silicone oil was based on recommendations by colleagues and its low price and wide availability. However, the term silicone oil is general and ultimately its composition is unclear. A similar problem exists for the two other media since they are trademark products with undisclosed composition. In conclusion, silicone oil was found to work well.

2.7.5 Heated diamond anvil cell for PXRD

The requirements for DACs to function as viable high-pressure environments for X-ray diffraction studies are more restrictive due to the angular nature of the diffraction signal. The heated DAC system used was custom-built by a research group of the Atomic Weapons Establishment (AWE, Didcot, Figure 2.16). A membrane-driven Boehler-type diamond anvil cell was equipped with an external coiled resistive heater. The DAC-heater-assemblage was contained in a water-cooled vacuum vessel with Kapton windows.

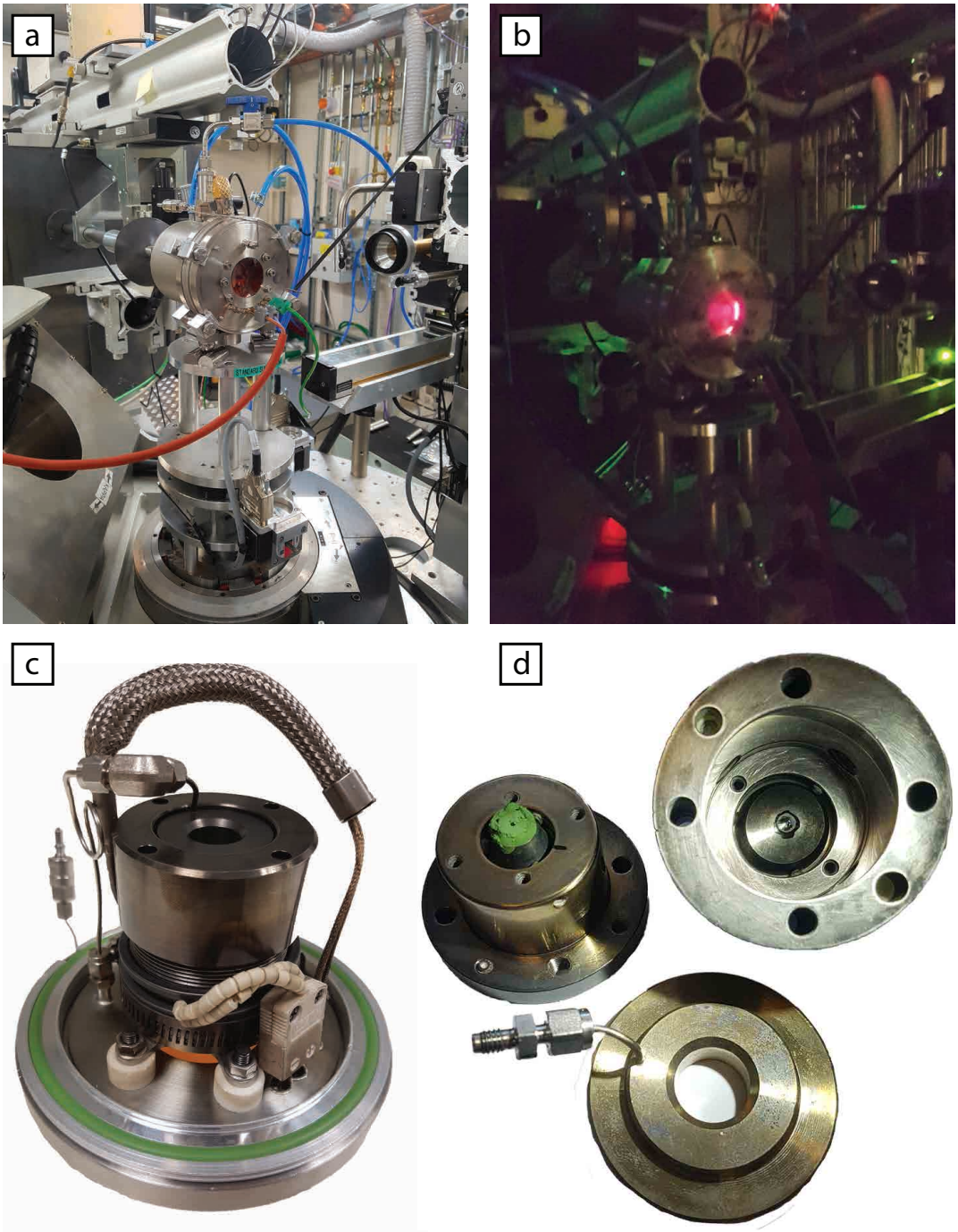

Figure 2.16 a) Water cooled vacuum vessel with Kapton windows an externally resistive-heated, membrane-driven DAC for simultaneous high-P-T powder X-ray diffraction experiments at Diamond synchrotron light source. b) the same system as in a) but operating at 500 °C. c) close-up view of the Boehler type DAC fitted with a resistive heater and membrane pressure drive. d) dismantled DAC.

Practical issues

Due to the weight of Boehler-type DACs and the suboptimal thermal contact in vacuum, the heating rates were considerably lower (0.5 °C min^{-1} to 1 °C min^{-1}) compared to the Betsa system used for the Raman studies. On the other hand, the temperature control was stable, and the slow heating rate in combination with fast data acquisition times on the synchrotron source allowed for measurements during continuous heating without the need for temperature plateaus.

Each diffraction pattern contained a major background signal from the two sequential Kapton windows. Once this background was subtracted from the raw data using a measurement of the empty DAC in the vessel, this was no longer a problem for the data analysis.

Chapter 3

The ZIF-4 – ZIF-62 solid-solution

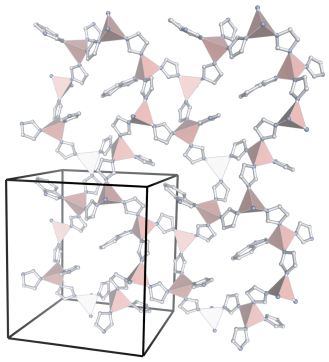

The enormous chemical variability of MOFs is one of the reasons for the rapid progress of their development. Given the large number of possible combinations of metals and organic molecules which can act as network builders, the chemical variability of MOFs is apparently endless. The basic choice of chemical building blocks determines the crystal structures and their general chemical functionalities. Meanwhile, subtle adjustments of a given formulation (*e.g.* doping, substitutions, tagging by functional groups) allow precise control of the properties of a given structure. A well-known example of this are the so-called isoreticular series[146, 147]. These series represent continuously tunable pore sizes within constant network topology and structure, depending on the length of the organic linker in use. However, in contrast to the replacement of all linkers in a given structure, the systematic adjustment of properties can also be achieved by mixing different types of linkers. In the present chapter it will be shown how the isostructural ZIF-4 and ZIF-62 differ from each other only by the small degree of the substitution of benzimidazolate for imidazolate. It demonstrates how this substitution is accommodated in the given crystal structure, and how the presence of different linkers systematically affects their behaviour at high-temperature.

3.1 Variable or fixed composition?

A large number of studies investigate MOFs that are composed of more than one type of organic linker. From a crystal-structural perspective, these mixed-linker MOFs fall into two

main groups. The first group comprises MOFs with multiple types of linkers of contrasting size or geometry. Consequently, each type of linker has a unique structural role (for example $Zn_2(1,4-bdc)_2(dabco)$[148]), hence the proportions of these linkers cannot vary. Changing the stoichiometry would result in different crystal-structures. The second group comprises MOFs with multiple types of linkers of a similar size or geometry. In this case, all linkers have the same structural role (for example MOF-5 [149]), which allows for a variable stoichiometry. The substitution of one type of linker for another would (theoretically) give a continuous compositional range. However, when new mixed-linker MOFs are described, this distinction between the two groups is not always made. As a consequence, the possibility of varying proportions of mixed-linkers is often not considered. For example, in the case of ZIF-62 (originally defined as $Zn(Im)_{1.75}(bIm)_{0.25}$, it has been a long-standing assumption that the ratio between Im and bIm linkers is invariant. However, a more recent study[53] clearly demonstrated the opposite - the chemical composition of ZIF-62 is flexible. Importantly, this variability allows for the tuning of certain properties.

In the fields of metallurgy[150] and mineralogy[151] it is well known and of major significance that a crystalline phase allows for the substitution of some of its components in a continuous compositional range. In mineralogy, this is commonly referred to as a *solid-solution*. This name derives from the fact that the solid-solution behaves like a liquid-solution, allowing the "dissolution" of continuously variable amounts of solutes. The pure compound represents the "solvent", and the incorporated component represents the "solute". Importantly, if isolated, both, the solvent and the solute are crystalline phases, and should be iso-structural or at least structurally very similar. These phases are called "end-members". The assignment, of the phases as solvent or solute is, however, arbitrary.

This conceptual framework of solid solutions was developed in mineralogy because of the ubiquity in nature of the substitution of similarly sized ions. However, this terminology is much less established in chemical sciences, where the purity of substances is usually assumed. In the field of MOFs, many research groups have come up with their own new names for one and the same thing: molecular substitutional alloys[152], MIXMOFs [153], multivariate MOFs (MTV-MOFs) [149], coordination co-polymers [154], defect-engineered MOFs (DEMOFs) [155], or mixed-component MOFs (MC-MOFs) [152].

The earliest experiments on mixed linker MOFs were based on mixtures of chemically identical but structurally isomeric linkers[156]. The result of combining different isomers were iso-compositional MOFs with diverse, and unprecedented, network topologies. The mixing of chemically and structurally diverse linkers in a MOF framework was first achieved by post-synthetic procedures, such as tagging of various functional groups to an existing

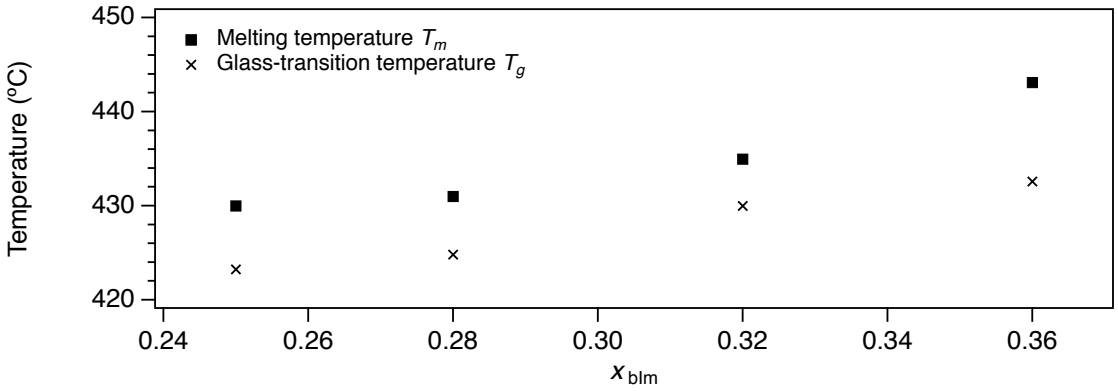

Figure 3.1 The melting- and glass-transition temperatures of compounds from the ZIF-4–ZIF-62 system as a function of bIm linker-substitution, from Qiao et al. (2018)[53].

framework[157]. However, with this approach, it was difficult to control the proportions of the functional groups and the degree to which they were incorporated. The incorporation of a variety of functionalised linkers in a single-step synthesis was realised only shortly afterwards and has subsequently received the most attention[149, 154, 158, 159].

3.2 The ZIF-4 – ZIF-62 system

The content of benzimidazolate (bIm) and imidazolate (Im) in ZIF-62 was originally defined at $Zn(Im)_{1.75}(bIm)_{0.25}$ [110]. This corresponds to a 50 % substitution of bIm for Im on one specific crystallographic site out of four, or a 12.5% substitution over all. In accordance with the generic structural formula $Zn(Im)_{2-x}(bIm)_x$, this composition corresponds to $x_{bIm} = 0.25$, which has been treated as invariant in the majority of research on ZIF-62. However, more recent studies have demonstrated the capability of ZIF-62 to host variable amounts of bIm in the range from $0.25 < x_{bIm} < 0.35$ [53]. Importantly, this has been shown to control the melting temperatures, the glass transition temperatures[53], and the fragilities[45] of the melt-quenched glasses (Figure 3.1).

Theoretically, the single-site substitution mechanism of bIm for Im proposed as the original structure of ZIF-62 can accommodate a maximum of $x_{bIm} = 0.25$. When the crystal-structural is considered it becomes apparent that $x_{bIm} > 0.25$ poses a sterical problem: due to an inversion symmetry centre imposed by the *Pbca* space group, a bIm for Im substitution on the specified site of more than 50 % brings two bIm linkers spatially too close to each other. Therefore, more than one linker-site is required to accommodate the bIm for Im substitution for compositions of $x_{bIm} > 0.25$. Using ^{1}H spin-diffusion NMR,

Qiao et al. detected the presence of two different bIm substitution mechanisms and they schematically suggested a possible second site for substitution. However, this has not been verified by structural refinements or geometric considerations of the three-dimensionally extended structure. Furthermore, there are no accounts of ZIF-62 with a bIm substitution of $x_{bIm} < 0.25$. This is surprising given the overt differences in high-temperature behaviour of ZIF-4 and ZIF-62 (Chapter 2). The research presented in this chapter was motivated by both the lack of knowledge of the precise substitution mechanism as well as the lack of clarity about the effect on the high-temperature behaviour as a function of the degree of substitution.

3.3 Methods

Synthesis and chemical characterisation

A series of progressively higher substituted ZIF-62, as well as pure ZIF-4, was synthesised based on the synthesis protocols described in Section 2.2. Precursor concentrations in the stock solutions, which were used for formulating the individual batches, were calculated such that the total molar sum of solutes remained the same for a given batch volume. Individual batches were prepared by the measurement of adequate amounts of stock solutions by weight. The recipes for all batches produced here can be found in Table A.1 in the Appendix. The reaction time was 72 h for all batches to maximise the yield and chemical homogeneity. The as-synthesised powders were characterised structurally and chemically at ambient conditions by powder X-ray diffraction, Raman spectroscopy, and HPLC, as described in detail in Chapter 2. In order to investigate the substitution mechanism in the sample with the highest bIm content ($x_{bIm} = 0.35$), a single-crystal XRD measurement was performed by the National Crystallographic Service[136]. The structure of this highly substituted ZIF-62 was refined based on this dataset using the SHELX suit[160]. The final Shelx input file is available in the Appendix.

In-situ high-temperature PXRD

The high-temperature behaviour of the ZIF-4–ZIF-62 solid solution was investigated using *in-situ* variable temperature PXRD. The samples were not desolvated prior to the measurements in order to eliminate any influence of inconsistent desolvation procedures or pre-amorphisation of the metastable materials during the desolvation. Laboratory-based variable-temperature PXRD data sets were collected on a Bruker D8 Advance X-ray powder

diffractometer (CuKα) equipped with a MRI radiation-heating stage (Physikalische Geräte GmbH, Germany), as described in Chapter 2.

Amorphisation temperatures of the samples from the solid solution series ZIF-4–ZIF-62 were determined based on the loss of Bragg reflection intensity. The integrated peak intensity of the combined (113) and (221) reflection (from 17° to18° 2θ), after the subtraction of a linear background, was taken to approximate the overall diffraction intensity and thus the progression of amorphisation. In addition, to account for intensity variations due to sample displacement during heating, the Bragg diffraction intensities of the ZIFs were additionally normalised against the intensity of an internal silicon standard to account for sample height displacements due to powder compaction and thermal expansion of the sample holder. The amorphisation temperatures T_a of the ZIFs were equated to the turning point of a sigmoid curve fitted to the diffraction intensity against temperature curves. PXRD patterns were collected for all samples in intervals of 20 °C in the range from 30 °C to 410 °C. The heating rate was 10 °C min^{-1}, with additional two minutes of equilibration time prior to the start of the measurement. Individual scans covered 10° to 30°2θ with a step-size of 0.02° and a collection time of 1 second/step, which resulted in approximately 18 minutes of collection time at a given temperature.

Thermal expansion coefficients were determined from two evacuated samples of pure ZIF-4 and ZIF-62 ($x_{bIm} = 0.25$) composition, respectively. Both samples were additionally annealed in-situ during 6 h at 200 °C under vacuum prior to the collection of PXRD patterns. This was done to ensure full evacuation of the porous crystal structures because it was noted that the unit cell dimension are very sensitive to any change in pore content. Furthermore, as described in Section 2.7.2, the samples were mixed with pure silicon powder to account for sample height displacements due to powder compaction and thermal expansion of the sample holder.

3.4 Results and discussion

3.4.1 Synthesis and chemical composition

Figure 3.2a shows a ternary compositional diagram with the nominal compositions of initial solutions, as well as the compositions of the resulting powders as measured by HPLC. Also included are the nominal compositions and resulting phase assemblages from a previous study[161].gustafsson2013 Figure 3.2b shows the correlation of nominal and measured compositions. The ratios of Im over bIm in crystallised mixed linker ZIF-62 were found to deviate

considerably from the nominal ratios of the Im and bIm precursors in the solutions. Moreover, the trend is not linear, approaching the maximum degree of incorporation asymptotically. From Figure 2.6 in Chapter 2 it is also apparent that, over time, the amount of crystallised material significantly increases by weight. As a consequence the question emerged whether "fractional crystallization" would affect the chemical composition of the products over time. To answer this question, products of a series of nominally identical solutions were bulk chemically analysed after 24 h, 48 h, 72 h, and 96 h reaction time (Figure 3.3). It appears that the bulk chemical composition of as-synthesised ZIF-62 as a function of reaction time is, within the analytical error, constant after 48h. However, the comparatively lower bIm content after just 24 h hints at some time-dependent mechanism. Furthermore it also remains unclear whether the individual grains of the powder are homogeneous or perhaps chemically zoned.

Figure 3.2c shows the virtually linear correlation of the ratios of Im and bIm as measured by HPLC, with the ratios of Im- and bIm-characteristic intensities of Raman peaks at approximately 3150 cm^{-1} and 800 cm^{-1}, respectively (Figure 3.4). This linearity promises a new way to quantify the ratios of linkers in mixed-linker MOFs in general.

3.4.2 Substitution mechanism

Figure 3.5 displays the PXRD patterns of intermediate compounds, as well as the end-members, of the ZIF-4–ZIF-62 solid-solution. The intensities were normalised by the first diffraction peak at ca. 9° 2θ. While a qualitative change of the relative peak intensities is apparent, the accurate evolution of the intensities remains elusive due to unclear effects of sample preparation on flat sample holders such as preferred orientation. Attempts to refine occupancies of bIm were not successful, i.e. they did not result in sensible, consistent numbers. On the other hand, the unit cell volume, when plotted against the measured composition (Figure 3.6), linearly increases up to $x_{bIm} = 0.25$. At $x_{bIm} > 0.25$, the unit cell volume does not increase any further. This behaviour hints at a saturation effect when bIm occupies all the possible substitution sites to a certain degree.

As shown in Figure 3.7, the substitution of bIm for Im is possible on all four of the individual Im sites if they are regarded in isolation. However, restrictions on site occupancies (occ.) apply due to sterical hindrance of bIm molecules which are spatially brought too close together due to the symmetrically equivalent sites they occupy in the extended crystal structure. The substitution sites are here named after the N-sites labels of the original crystal structure: N1N8, N2N6, N3N7, and N4N5, respectively. Based on simple geometric assessments of a reasonable minimum distance between two opposing bIm linkers, it follows

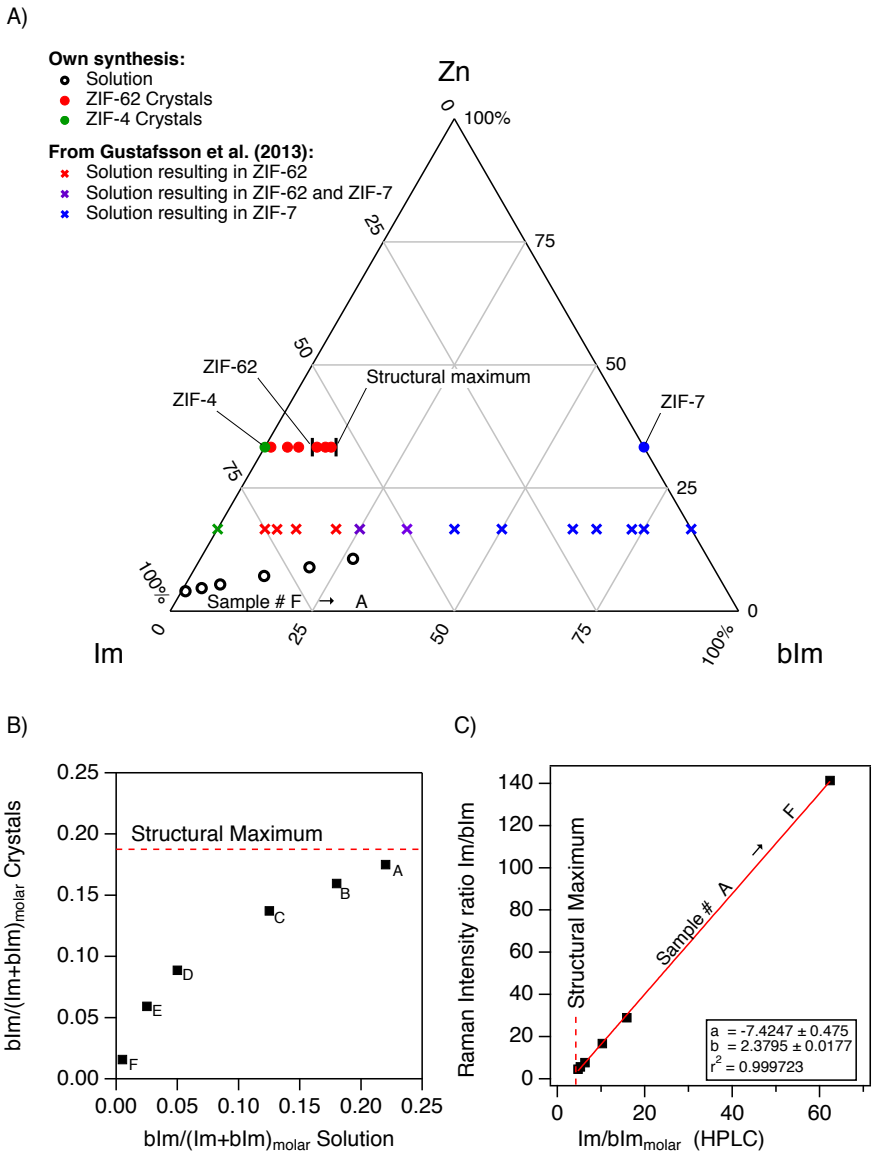

Figure 3.2 Chemical compositions of Solutions and ZIF-62 crystals. **A)** Ternary diagram in mol-percent. Crosses represent compositions of solutions from [161]. Crystallised products were only assessed based on phase identification by powder XRD; no chemical composition of products is provided in the reference. **B)** the composition of ZIF-62 crystals as a function of composition of the solution, measured in molar fraction of bIm linkers per total amount of linkers. A structural limit is approached asymptotically. **C)** The ratio of intensities of Im and bIm characteristic Raman modes at around 800 cm^{-1} and 3150 cm^{-1}, respectively, as a function of the composition of ZIF-62 crystals as measured by HPLC, fitted by a straight line.

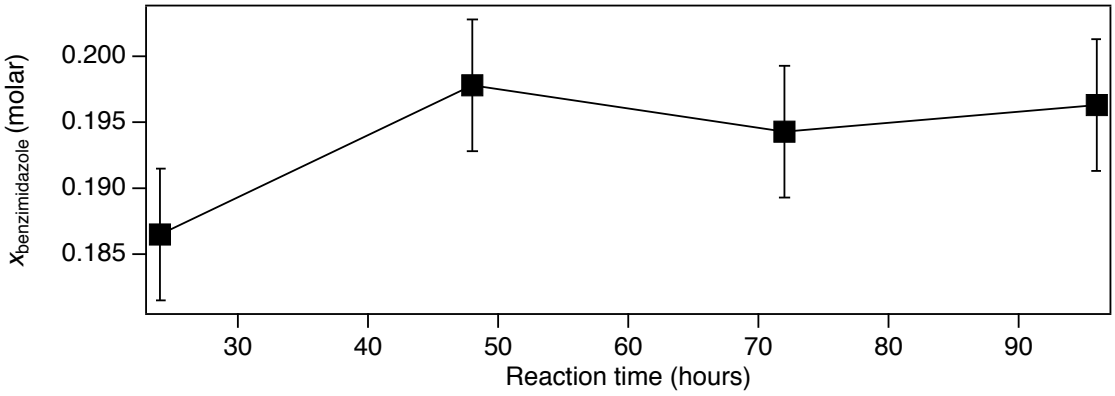

Figure 3.3 The composition of precipitated ZIF-62 powder from 100 ml at 130 °C as a function of time was measured after filtration and drying of the products. $x_{benzimidazole}$ corresponds to the molar amount of bIm per formula unit. Error bar correspond to a standard deviation of 3σ.

that occ.$_{(N1N8+N2N6)} \leq 0.25$ and occ.$_{(N3N7+N4N5)} \leq 0.5$, which results in a total possible substitution of $Zn(Im)_{1.625}(bIm)_{0.375}$. To elucidate the additional crystallographic site, which is necessary to accommodate this maximum substitution level, a single-crystal XRD measurement on ZIF-62 with the composition $Zn(Im)_{1.65}(bIm)_{0.35}$ was collected at the National Crystallographic Service. The structural refinement based on this measurement (Table 3.1 and Appendix) revealed that the additional position to accommodate bIm substitution is the N4N5 site. This became clear from residual electron densities, which were located by subtracting the calculated from the observed structure factors, *i.e.* from difference Fourier maps. Certain peaks in these residuals could be assigned to missing atoms in the crystal-structural model which, given the resemblance of their arrangement with that of the atoms in a bIm molecule, corresponded to the presence of additional bIm ligands. Rigid bodies, of both the substituting bIm ligand and the basic Im ligand were used to refine their respective positions as well as fractional occupancies on the specific site. It was found that the refined site occupancies correspond well to the theoretical maxima of the individual substitution sites established earlier.

3.4.3 High-temperature stability

Firstly, all samples undergo a crystalline–amorphous transition upon heating. This is conflicting with several literature reports[53, 162], which report that crystalline ZIF-62 is stable up to its melting point at 430 °C. However, by carefully scrutinising the sources on which those conclusions are based, it appears that the amorphisation of those samples prior to

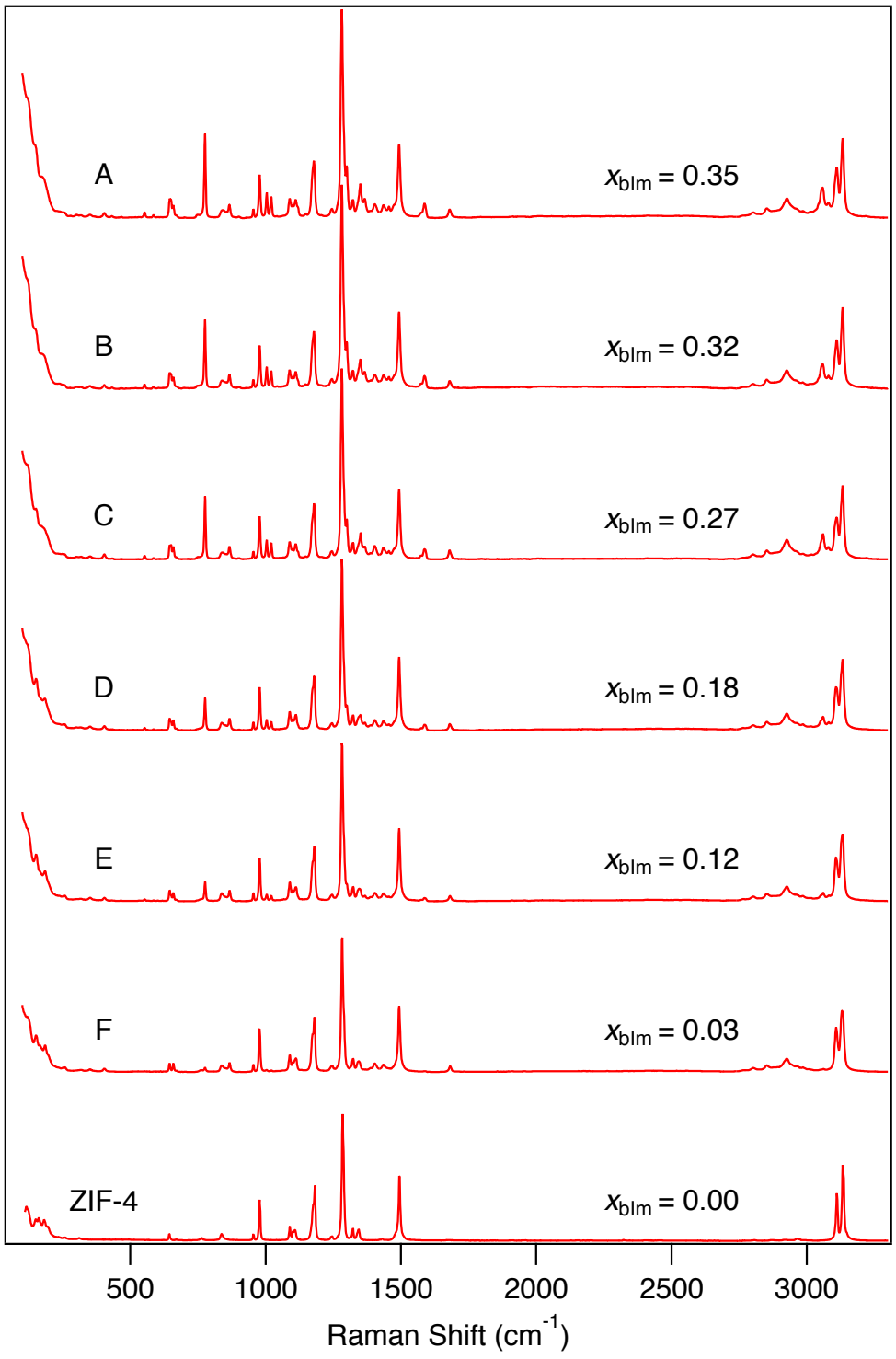

Figure 3.4 Raman spectra ($\lambda = 532$ nm) of progressively higher substituted ZIF-62. Pure imidazole ZIF-4 is given as a reference at the bottom. x_{bIm} refers to the molar amount of benzimidazole in $Zn(Im)_{2-x}(bIm)_x$. Intensities were normalised to Raman peak at 1500 cm^{-1}. Note the presence of DMF in this series. The bIm-characteristic peak used for the quantification of the linker-substitution is located at approximately 750 cm^{-1}.

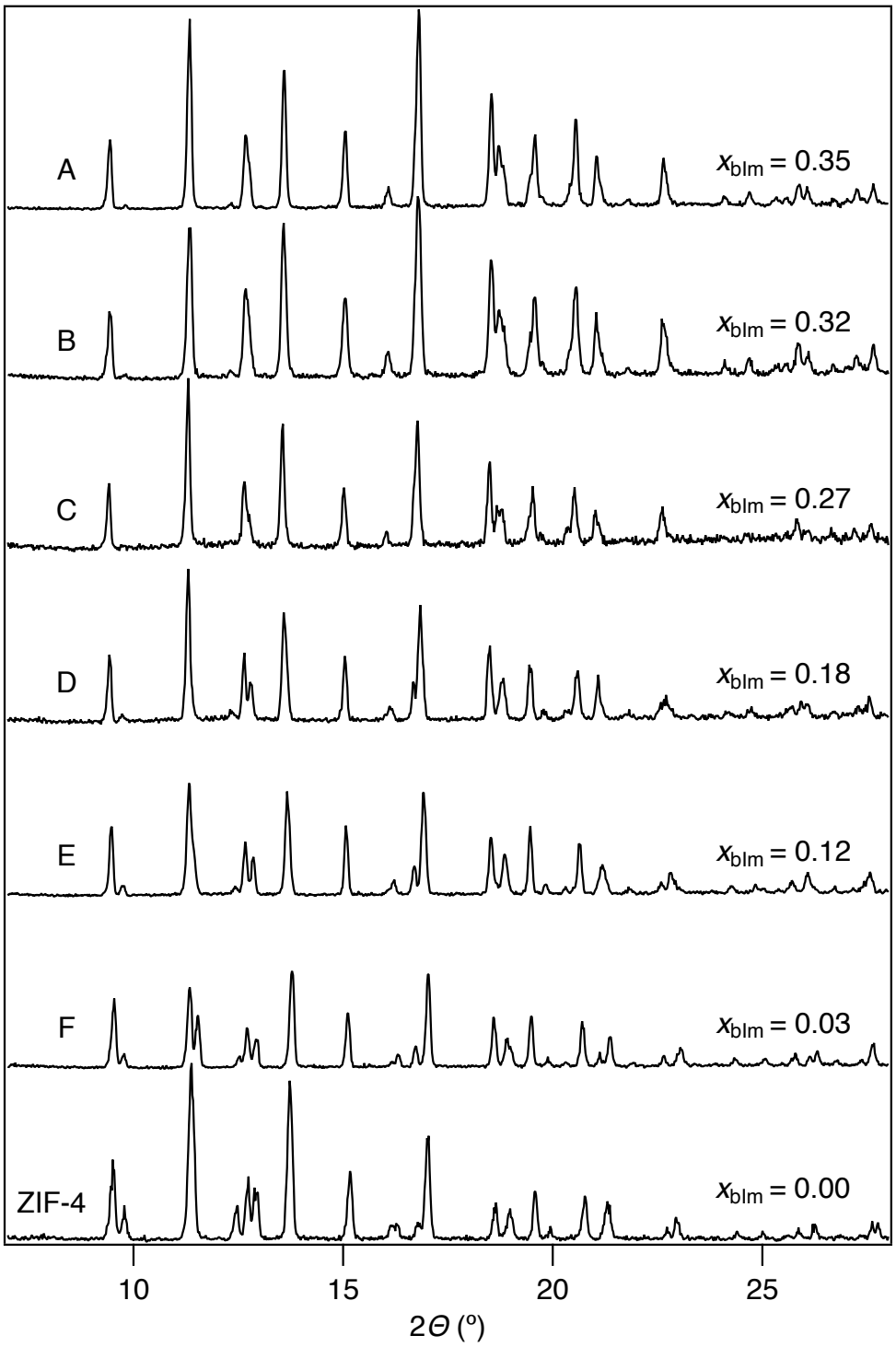

Figure 3.5 Powder XRD patterns ($\lambda = 1.54\,\text{Å}$) of progressively higher substituted ZIF-62. Pure imidazole ZIF-4 is given as a reference at the bottom. x_{bIm} refers to the molar amount of benzimidazole in $Zn(Im)_{2-x}(bIm)_x$. Intensities were normalised to the first diffraction peak. However, relative intensities are somewhat unreliable due to possible artefacts of preferred orientation.

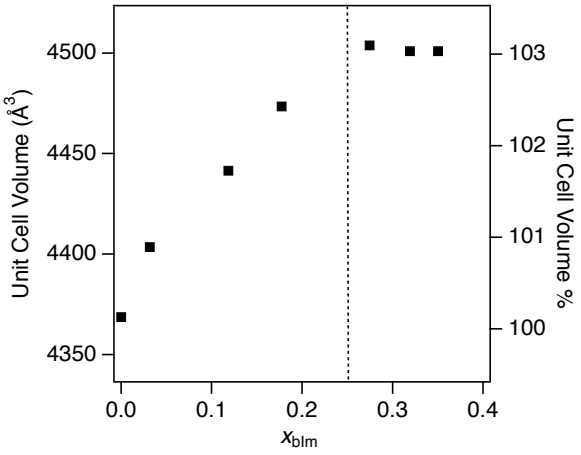

Figure 3.6 The unit cell volume of progressively higher substituted ZIF-62. The chemical composition on the x-axis was measured by HPLC, while the volume on the y-axis was determined from structural refinements based on powder XRD patterns. Error bars are smaller than symbols.

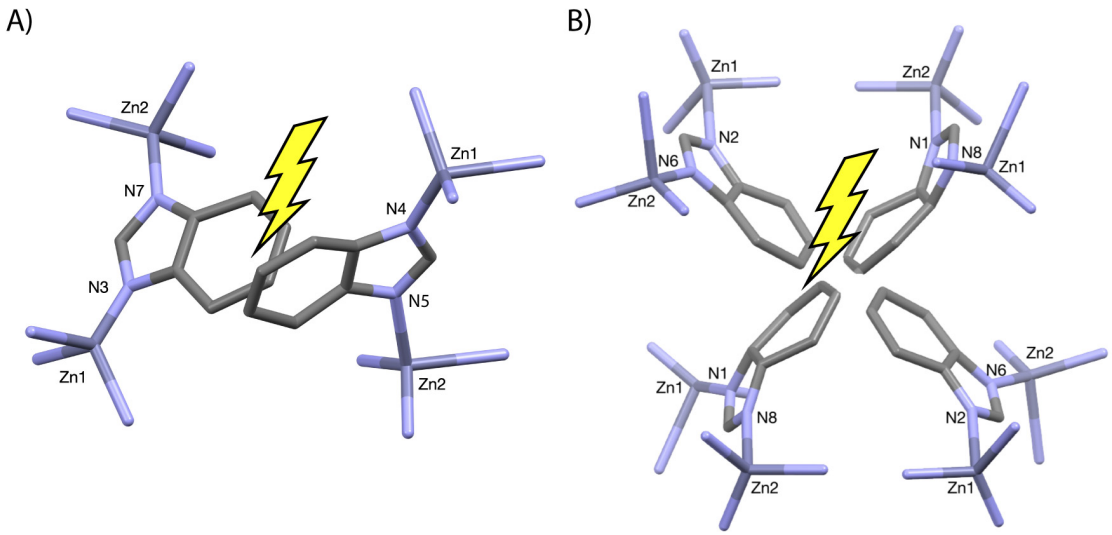

Figure 3.7 Local crystal structures of benzimidazole for imidazole substituted sites in ZIF-62. Hydrogen atoms are omitted for clarity. A) The two sterically opposed benzimidazole linkers occupy crystallographically independent sites. N4N5 and N3N7 linkers can host a maximum occupancy factor of 0.5 bIm in sum. B) N2N6 and N1N8 not only clash as independent linkers, but also get spatially too close to their symmetry related equivalent sites. A maximum site occupation factor of 0.25 in sum for the two sites is possible.

Table 3.1 Data collection and refinement parameters for maximal benzimidazole-substituted ZIF-62.

λ /Å	0.71073
T /K	100
Sum formula	$Zn_2N_8C_{12}H_{12}$
Crystal size /mm	0.01*0.03*0.04
Crystal system	Orthorhombic
Space group	Pbca
Z	8
a /Å	15.4123(9)
b /Å	15.6109(15)
c /Å	18.0575(17)
α /°	90.0
β /°	90.0
γ /°	90.0
V /Å	4344.6(4)
Reflection used in unit cell refinement	3904
Θ range for unit cell /°	2.1 - 22.6
All data	43362
Θ range for all data /°	1.7 - 26.4
R_{int}	0.066
R_{sigma}	0.048
wR_2	0.232
R_1 (all data)	0.099
R_1 ($I > 4\sigma(I)$)	0.079
GooF	1.033
Largest Residual /$e * \text{Å}^{-3}$	0.86

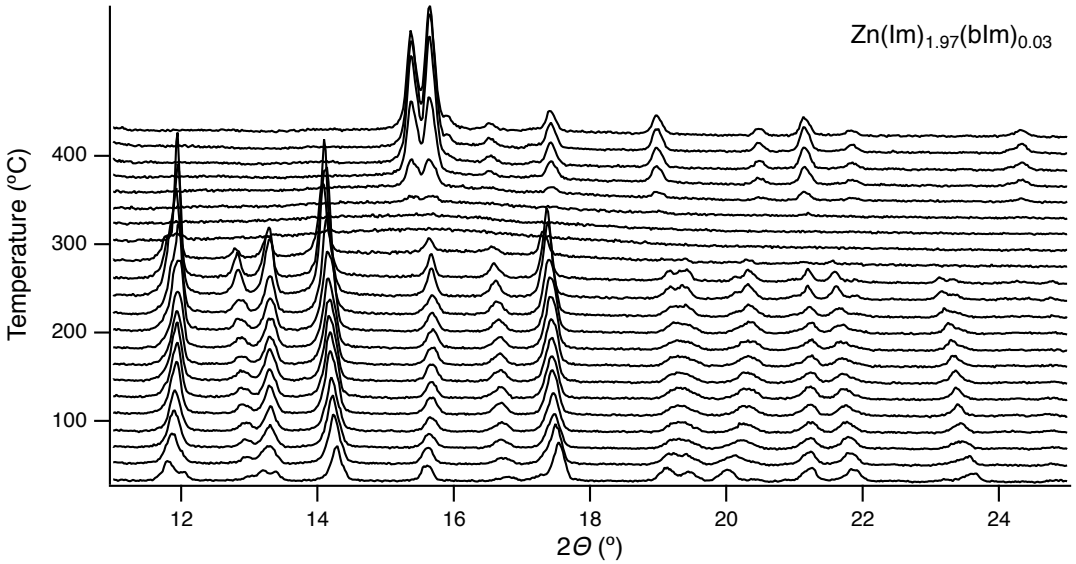

Figure 3.8 Stacked PXRD patterns at variable temperature of a sample from the ZIF-4–ZIF-62 solid solution with x_{bIm}=0.03. The initially crystalline material amorphises and recrystallises to ZIF-zni upon heating.

melting was simply overlooked. The contrary, that ZIF-62 does amorphise below it's melting point, finds support in several independent studies[45, 163]. However, the temperature of amorphisation also depends on the applied heating rate. Therefore, at a high enough heating rate it should theoretically be possible to extend the apparent thermal stability limit towards higher temperatures.

One of the major differences between pure ZIF-4 and bIm substituted ZIF-62 lies in the fact that ZIF-4 recrystallises to the dense ZIF-zni polymorph just below 400 °C, whereas ZIF-62 stays amorphous up to its melting point. Here, recrystallisation of the initial phase to ZIF-zni was, in addition to pure ZIF-4, also observed for the composition of x_{bIm}=0.03 at 370 °C (Figure 3.8) – any higher degree of substitution prevented the recrystallisation. However, whether the recrystallised material in fact homogeneously incorporates the bIm linkers remains unclear, a phase separation process cannot theoretically be excluded at this point. Yet, already a degree of substitution as small as x_{bIm}=0.1, corresponding to only 5%, completely obstructs this recrystallisation.

Furthermore, the degree of bIm substitution substantially affected the thermal stability of the crystalline starting material. The thermal amorphisation, as tracked by the integrated Bragg peak intensity of the (113) and (221) reflections, is shown in Figure 3.9a. Figure 3.9b shows the temperatures of amorphisation (T_a), defined by the turning points of the sigmoidal curve fits. It is apparent that T_a increases by approximately 50 °C from the unsubstituted

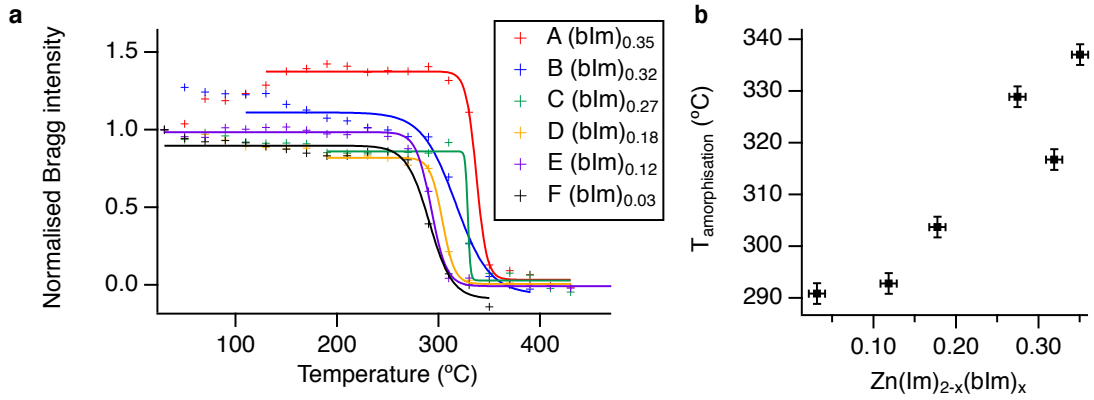

Figure 3.9 a) Thermal amorphisation of samples from the ZIF-4–ZIF-62 solid solution. The intensity was integrated over the (113) and (221) reflections and normalised to the initial intensity at 30 °C. The data were fitted with a sigmoidal curve. b) The turning points of the sigmoidal curves were taken to represent the temperature of amorphisation T_a.

to the maximally substituted sample. This increase in thermal stability can qualitatively be understood in terms of the increased rigidity of the substituted framework due to the bulkier bIm ligands.

Table 3.2 Linear thermal expansion coefficients of ZIF-4 and ZIF-62.

	ZIF-62 30 °C to 300 °C ($\times 10^{-5}$)	ZIF-4 30 °C to 220 °C ($\times 10^{-5}$)
a	-0.9 ± 0.1	-0.2 ± 0.1
b	4.7 ± 0.1	-4.3 ± 0.3
c	0.0 ± 0.9	5.6 ± 0.2
volume	4.0 ± 1.0	-0.4 ± 0.1

3.4.4 Thermal expansion

The thermal expansion was investigated for the two fully evacuated endmember compounds ZIF-4 and ZIF-62($x_{bIm} = 0.25$). Figure 3.10 shows a comparison of the behaviour of the two materials, alongside the corresponding sections of their crystal structural models. Table 3.2 lists the linear and volume thermal expansion coefficients extracted from linear fits to the experimentally determined unit cell dimensions at variable temperatures.

For ZIF-62, the thermal expansion is net-zero along the *c*-axis, slightly negative along the *a*-axis, and strongly positive along the *b*-axis. This extreme anisotropic behaviour can be understood from the topology of the rings formed by interconnected Zn sites. A network of 8-membered rings extends perpendicular to *a* with bIm linkers protruding along the major-axes of their elliptical shape. This direction is dominantly parallel to *b*. Shearing of the rings perpendicular to the bIm linkers by expansion along *c* is therefore sterically blocked. A network of 6-membered rings extending predominantly perpendicular to *b* is of a more isotropic and rigid geometry, resulting in a subtler response along *a* and *c* compared to *b*. In comparison, the structurally identical but unsubstituted ZIF-4 shows no hindrance by bulky benzimidazole linkers and indeed strongly contracts along *c*, while also expanding along *b*.

As a result, ZIF-4 and ZIF-62 also have a strikingly different volume expansion, as shown in Figure 3.11. For ZIF-62, the thermal volume-expansion is positive and quasi-linear from ambient-temperature up to 250 °C, consistent with previous computational work indicating positive thermal expansion for ZIFs of cag topology[164]. In contrast, ZIF-4 shows a net zero volume-expansion, which is a somewhat rare occurrence [165, 166].

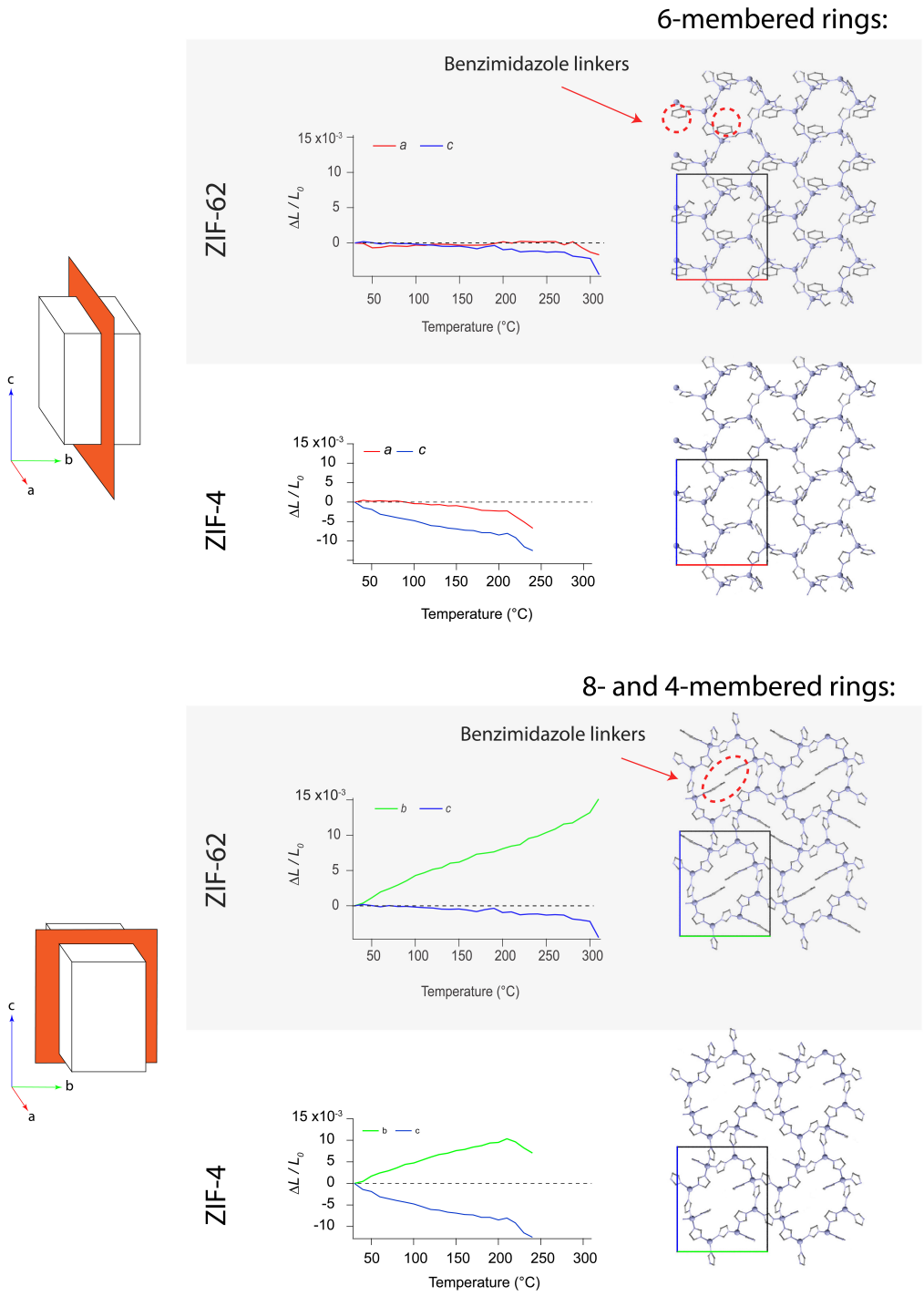

Figure 3.10 The anisotropic thermal expansion of ZIF-62 ($x_{bIm} = 0.25$) and ZIF-4 is compared with the structures that extend in the crystallographic *a*-*c*- and *b*-*c*-plane. For clarity, these planes are shown as slices that only encompass ½ and ¼ of the fractional coordinates on the perpendicular axes, as indicated by the orange dashed box to the right. H atoms are omitted. Along *c*, ZIF-4 shows a negative thermal expansion, whereas ZIF-62 shows an almost negligible change in length. From the crystal-structure models it appears that this direction corresponds to the direction along which the benzimidazole substituted linkers protrude the 8-membered rings (marked by dashed red ellipse).

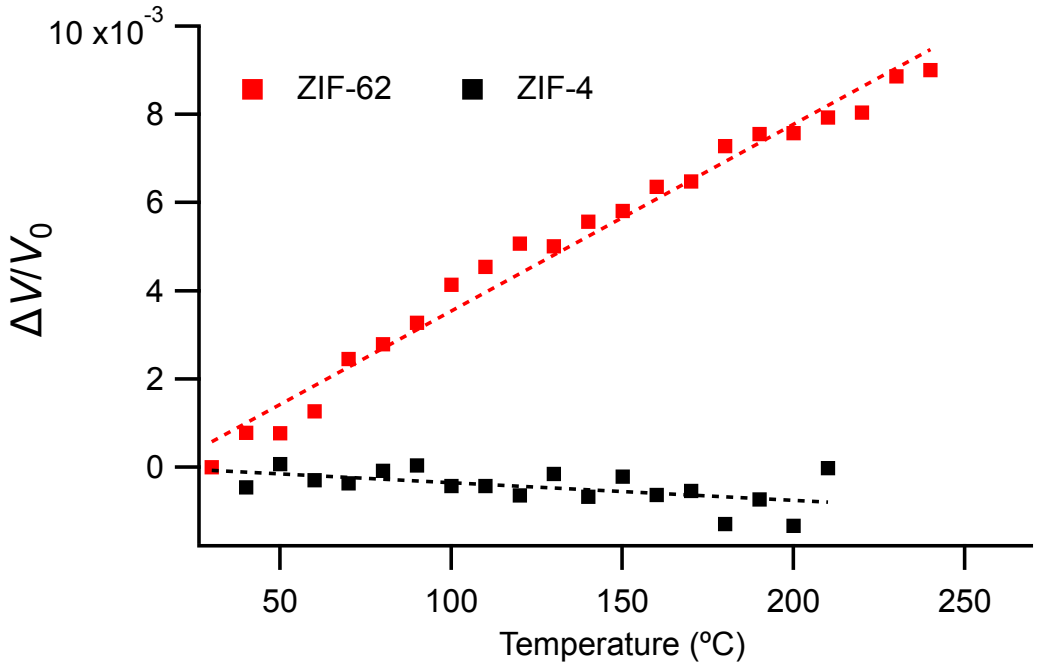

Figure 3.11 Thermal volume-expansion of ZIF-4 and ZIF-62.

3.5 Conclusion

The acknowledgement of the phenomenon that two or more chemical components can continuously substitute for each other in a single crystalline phase appears to be relatively new to the research field of MOF chemistry. This is reflected by the inconsistent nomenclature used where this possibility is recognised. It is presumably for this reason that the majority of mixed-linker MOFs are investigated with the assumption of a fixed chemical compositions. The possibility of linker-compositional variations are thus often overlooked. In their seminal work on ZIF synthesis, Banerjee et al. (2008) report 10, out of a total of 25 novel ZIF structures, which comprise mixed linkers. Many of these compositions are arguably not fixed. The unexplored variations in linker-ratios thus leave open a large parameter space for the improvement of the physical and chemical performance of these MOFs. Here, it was established how the chemical composition of a mixed-linker MOF ZIF-62 can be varied during synthesis and how the products can be chemically analysed using a HPLC and Raman spectroscopic methods. Furthermore, by utilizing powder and single-crystal X-ray diffraction techniques, it was shown how the crystal structure accommodates this variation, and how the high-temperature characteristics of these materials systematically vary with changing composition. In detail, it was found that there is a structurally controlled limitation to the degree of benzimidazolate substitution. Thermal stabilities, as well as the thermal expansion

coefficients increase with increasing benzimidazolate substitution levels. These findings not only emphasises the importance of accurate determination of the structural formula of individual mixed-linker samples, but they also provides an easy to control synthesis parameter which allows for the tuning of physical and chemical properties of the important ZIF-4–ZIF-62 family.

Chapter 4

P-T Phase Diagrams of ZIF-4 and ZIF-62

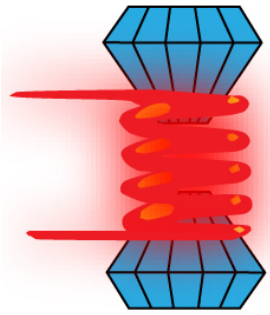

Synthesis and performance assessments of crystalline metal-organic frameworks for storage and host-guest interactions is wide spread. However, in-depth investigations into individual compounds are often left ignored in a relentless hunt for the highest gas uptake or largest surface area. Sparse knowledge of structural behaviour and phase stability in pressure (P) and temperature (T) space is a shortcoming typical for the usual approaches in the field of MOF research. Yet, structural variations and phase transitions along P and T trajectories are not only of fundamental physical interest but are also critical in understanding many structure-property relations[167]. For instance, some reported mechanisms of high-pressure gas uptake in ZIFs require reversible gate-opening[39, 168]. On the other hand, the thermal stability of a MOF structure can be crucial for potential applications in industrial settings such as temperature-swing absorption[169].

Phase transitions of crystalline MOFs at either high-pressure or high-temperature have been reported a number of times. However, there are no reports to date on their behaviour at combined high-pressure and high-temperature conditions. Meanwhile, amorphisation, *i.e.* the loss of structural long-range order, and melting of MOFs at such conditions has only recently been recognised. In this chapter, the first two pressure-temperature phase diagrams ever reported in the family of MOFs are explored using *in-situ* powder X-ray diffraction, Raman spectroscopy and optical microscopy. It is shown that the application of simultaneous pressure and temperature on the isostructural MOFs ZIF-62 and ZIF-4 results in an intriguing interplay of crystalline polymorphs, high- and low-density amorphous phases, and liquid

phases. Furthermore, the slight chemical difference between these two ZIFs results in a remarkable divergence of their behaviour at such extreme conditions.

4.1 ZIFs at high-temperature and high-pressure

A number of studies on non-ambient behaviour of ZIF-4 and its related ZIF-62 have emerged over the last decade. The main motivation for these studies was the discovery and subsequent investigation of MOF glasses and MOF liquids. These materials are of special interest due to their nature as a new class of melt-quenched glass material formed of amorphous SiO_2-like continuous random networks[89], as described in Chapter 1. The formation of MOF glasses via solid state conversion or melt-quenching is of great importance due to their inherent MOF-like chemical connectivity and composition[45, 89]. The glass formed from ZIF-62 has been demonstrated to exhibit significant resistance against crystallization[53], whilst that formed from ZIF-76, a chemically closely related compound, has recently been demonstrated to show permanent, accessible porosity[170]. Alongside their unique internal structures, MOF glasses and liquids are also of great interest since they provide a route to manufacturing complex, monolithic glassy MOF objects from MOF powders by melt-casting or hot-pressing[105, 171]. An overview of previously reported non-ambient behaviour of ZIF-4 and ZIF-62 is given in the following section

ZIF-4

The *high-temperature* behaviour of ZIF-4 was first described by Bennett et al. (2010)[65]. Crystalline ZIF-4 was reported to undergo a crystalline-to-amorphous transition at approximately 300 °C. This amorphisation event is characterized upon further heating by a transition from a low-density to a high-density glass[89]. The low-density state of ZIF-4 is particularly interesting because it may represent an amorphous state with a potential energy equivalent to the corresponding crystalline state. Such states have been termed 'perfect' glasses due to their relatively low entropy[84]. The recoverable amorphous phase (α-ZIF) was described as a continuous random network analogous to amorphous SiO_2. Above 400 °C, amorphous α-ZIF recrystallises to the densest known ZIF phase ZIF-zni. This phase has been known since 1980[108]. Subsequently, ZIF-zni melts at 590 °C. At approximately 600 °C, this melt thermally decomposes. Both (α-ZIF), ZIF-zni, and the ZIF-melt retain the characteristic local environment and connectivity of tetrahedral ZnN_4 nodes. Amorphisation to α-ZIF and recrystallization to ZIF-zni are universal for all polymorphic starting phases of $Zn(Im)_2$[42].

At low temperatures, Wharmby et al. reported a porous-to-dense phase transition at −130 °C. The crystal structure of this low-temperature phase involves a cooperative rotation of imidazolate linkers resulting in a 23 % smaller unit cell volume compared to ZIF-4 at room temperature[106].

The first *high-pressure* study on ZIF-4 was presented in 2011[43]. Bennett et al. discovered pressure-induced amorphisation of the empty ZIF-4 framework. Using a non-penetrating pressure transmitting medium, amorphisation occurred at approximately 1 GPa. Using a small molecule, penetrating medium, the ZIF-4 framework was stabilised up to pressures of approximately 4 GPa. DMF solvent occupation of the ZIF-4 frameworks increased the amorphisation threshold to approximately 5 GPa for both penetrating and non-penetrating pressure media. In addition, DMF containing ZIF-4 also showed an intermediate high-pressure phase just below 0.3 GPa. In all cases, the amorphisation occurred over a certain pressure range and was reversible upon depressurization to ambient conditions. A second high pressure study on ZIF-4 followed in 2018[71]. These authors resolved the pressure range up to 2 GPa in minute increments and found a phase transition for empty ZIF-4 using a non-penetrating medium just below 0.1 GPa. This is contradictory to the previous study and was explained by uncertainties about the extent of desolvation and possible absorption of environmental humidity in the earlier study. They showed that subsequent amorphisation at higher pressures is not reversible when the maximal pressure exceeds 1 GPa. Both, the high-pressure and high-temperature behaviour of ZIF-4, including their variations depending on pore-occupancy, is summarised schematically in Figure 4.1

ZIF-62

The *high-temperature* behaviour of ZIF-62 was first described by Gustafsson et al. (2013) [161]. *In-situ* variable-temperature powder XRD measurements revealed structural amorphisation in the range from 350 °C to 400 °C. Bennett et al. (2016)[45] report a lower amorphisation temperature of ZIF-62 based on DSC scans of approximately 330 °C. In a later study by Qiao et al.[53], it was reported that ZIF-62 does not amorphise but retains crystallinity up to its melting temperature. Yet another study by Longley et al. again report amorphisation before melting[162]. This discrepancy remains unresolved and possible reasons behind the diverging observations, such as slightly differing chemical composition or differing desolvation procedures, are only speculative at this point. Yet, a good agreement exists for the melting temperature of ZIF-62 under inert atmosphere, which is reported at 430 °C, preceding the thermal decomposition at approximately 500 °C[45]. A schematic

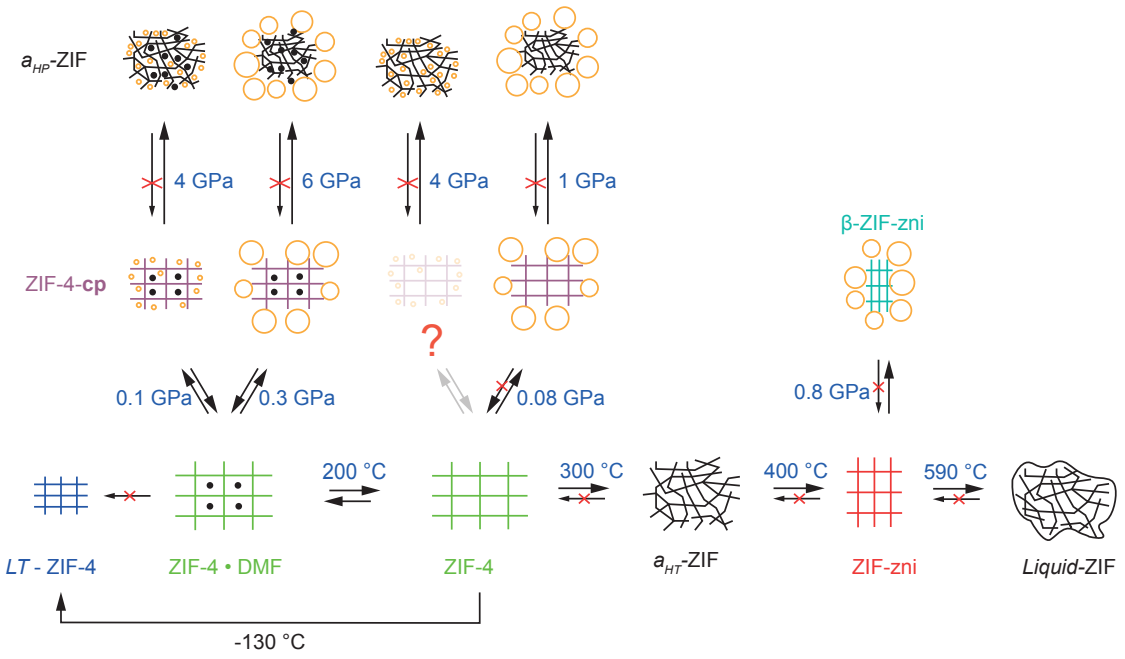

Figure 4.1 Schematic overview of known transformations of ZIF-4 at high-temperature and high-pressure. Large and small orange spheres represent non-penetrating and penetrating pressure transmitting media, respectively. Black dots indicate the presence of DMF solvent molecules from synthesis.

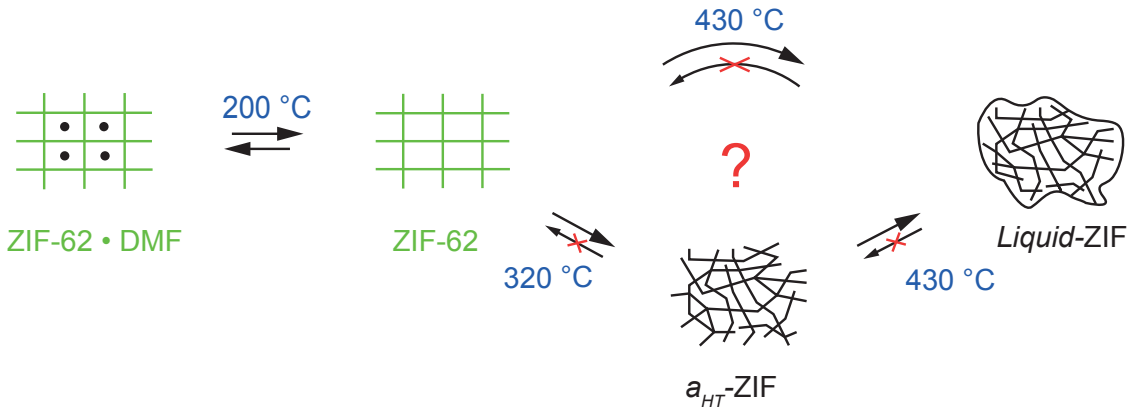

Figure 4.2 Schematic overview of known transformations of ZIF-62 at high-temperature and high-pressure. Large orange spheres represent non-penetrating pressure transmitting media. Black dots indicate the presence of DMF solvent molecules from synthesis.

overview of this observations is given in Figure 4.2. Results of *high-pressure* experiments have not yet been reported for ZIF-62.

4.2 Methods

Data acquisition

Ambient-P high-T PXRD data were collected for both ZIF-4 and ZIF-62, with the respective compositions of $Zn(Im)_2$ and $Zn(Im)_{1.75}(bIm)_{0.25}$, under vacuum on a Bruker D8 Advance equipped with a MRI radiation-heating stage (see Chapter 2). High-P ambient-T PXRD data was collected for ZIF-4 on the MS beamline ($\lambda = 0.6200$ Å) at the Swiss Light Source, Switzerland, using a membrane-driven diamond anvil cell (MDAC) with Daphne Oil 7474 as a non-penetrating pressure transmitting medium. Simultaneous high-P and high-T powder diffraction data from ZIF-62 and ZIF-4 were obtained at beamline I15, Diamond Light Source, Didcot (UK). A membrane-driven diamond anvil cell (DAC) was equipped with a custom-built external heater (See Chapter 2). High-purity silicon oil (AP100, Sigma-Aldrich) was used as pressure-transmitting medium. Internal pressures were calculated from the unit cell volume of NaCl using equation-of-state parameters from literature[140]. A thermocouple glued on to one of the diamonds provided temperature measurements. The DAC-internal P was raised with an initial membrane pressure. This membrane pressure was kept constant throughout the individual runs. Temperature was raised continuously at an average rate of

0.5 K/min for run 1 and 1 K/min for run 2, resulting in simultaneous increase of T and P. Diffraction patterns were collected roughly every 10 K.

Melting points of ZIF-62 at high-P were determined visually from lab-based, externally-heated DAC experiments in silicon oil as pressure transmitting medium (see Chapter 2). The temperature was measured using a K-type thermocouple glued to one of the diamonds. Pressure was determined from the shift of the fluorescence peaks of ruby[172] corrected for the T-induced shift[144]. Temperature was increased continuously at approximately 5 K/min, while the initial membrane pressure was kept constant. The lowest possible pressure at a certain temperature is dictated by the isochoric path followed through T increase. Therefore it was not possible to access pressures below 2 GPa between 300 °C and 350 °C. After reaching maximum T and P conditions, the external heater was switched off resulting in an approximate cooling rate of 2.5 K/min. Pressure was released after reaching room-T. The gaskets containing ZIF-62 were transferred to SEM stubs, kept under vacuum for 48h to evaporate silicon oil residuals, and carbon coated for subsequent SEM imaging. Back-scattered electron images were acquired on a FEI Qemscan Quanta650F operated at 10 kV at a working distance of 10 mm.

PXRD data analysis

Rietveld fitting of experimental PXRD data was performed using TOPAS-Academic[133]. Synchrotron-based PXRD data collected as a function of pressure and temperature were fitted sequentially using experimental peak shapes from LaB_6 reference measurements. A fixed background profile was measured on an fully assembled, but empty, DAC in the vacuum vessel. This background was scaled together with sixth order Chebychev polynomial. Eight order spherical harmonics were applied to correct intensities for preferred-orientation artefacts. More specific strategies for these refinements are individually discussed in Section 4.3.2.

4.3 Results and discussion

4.3.1 ZIF-62

The raw data of all high-P-T XRD experiments are compiled in Figures 4.3–4.5. Figures 4.6 and 4.7 show the Raman spectra of ZIF-62 recorded at increasing temperature until amorphisation, as well as selected peak fitting results. Figure 4.8 combines all phase observations made by DSC measurements, PXRD, and optical microscopy at variable P-

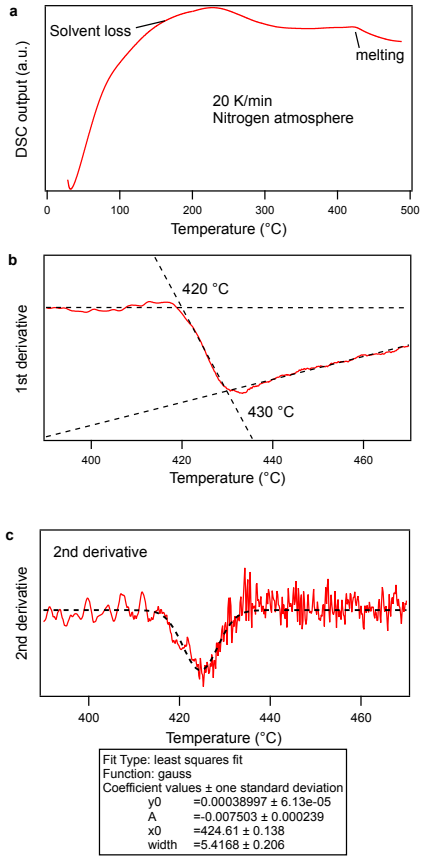

Figure 4.3 DSC scan of as-synthesised, solvated ZIF-62. **a**, Heat flow as a function of temperature featuring a broad peak due to solvent loss. **b**, 1st derivative of DSC signal in the Temperature range of melting. Intersections of linear fits indicate on- and off-sets of melting event. **c**, 2nd derivative of DSC signal, pinning down peak melting at 425 °C.

and T-conditions for ZIF-62, including the derived stability fields, and corresponding SEM images of recovered material with representative morphology.

Solid-state amorphisation

At ambient P, the ZIF-62 structure underwent T-induced amorphisation at ca. 320 °C which is in good agreement with a previous study[45]. At high-P and ambient-T, the framework underwent amorphisation at ca. 5 GPa. Importantly, T- and P-induced amorphisation in ZIF-62 were found to be distinct in nature. The high-pressure ambient-temperature PXRD experiment demonstrated amorphization to occur at 5 GPa. This amorphous phase reverted to the starting crystalline phase upon decompression, and the amorphization is thus ascribed to a displacive transition (Figure 4.9). Further evidence for this was found by

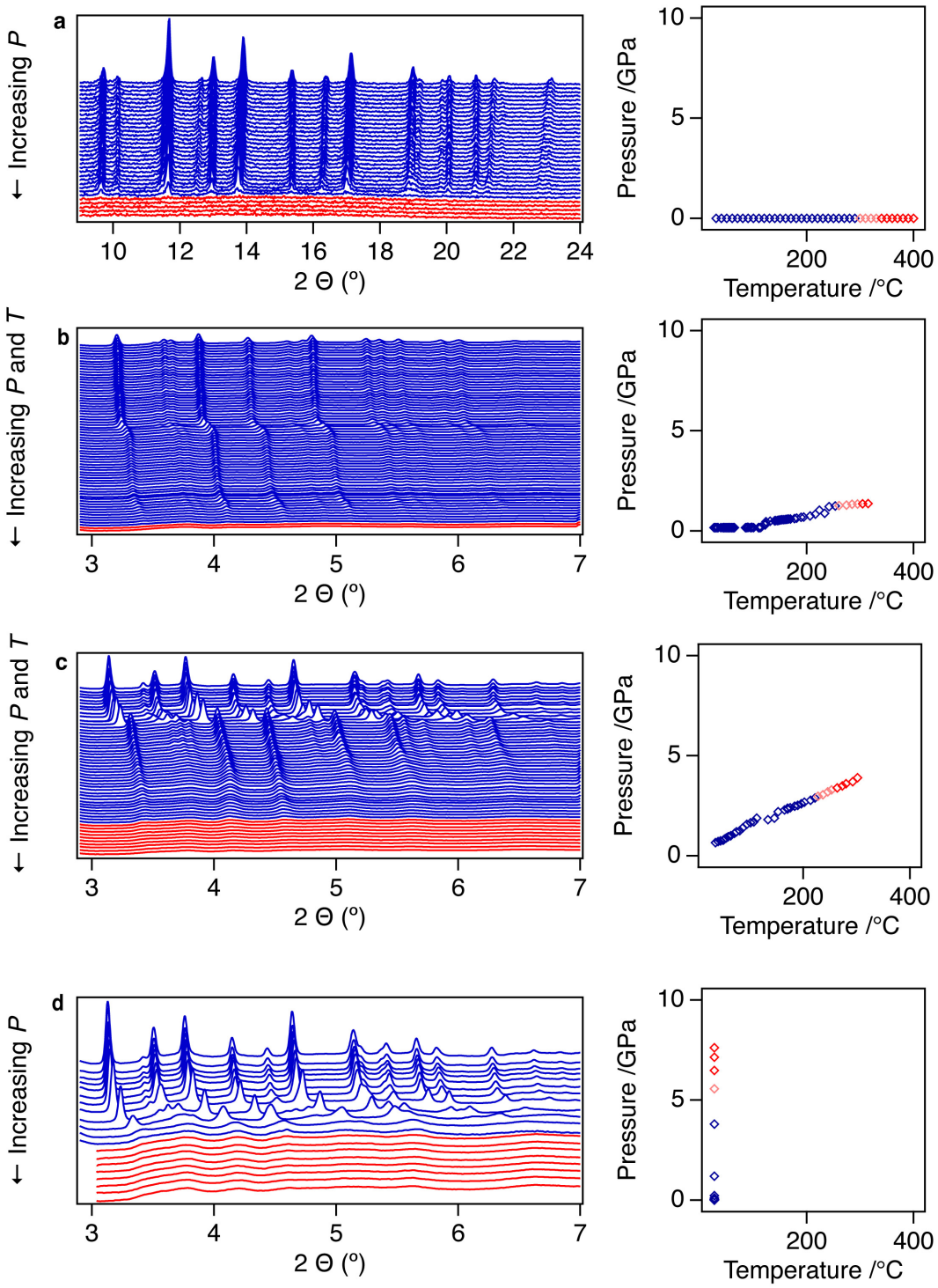

Figure 4.4 PXRD raw data – linear y-scale. All data is plotted with the first measurement at the back, increasing P and/or T towards the front. Panels on the right show *P-T*-condition of the individual runs.

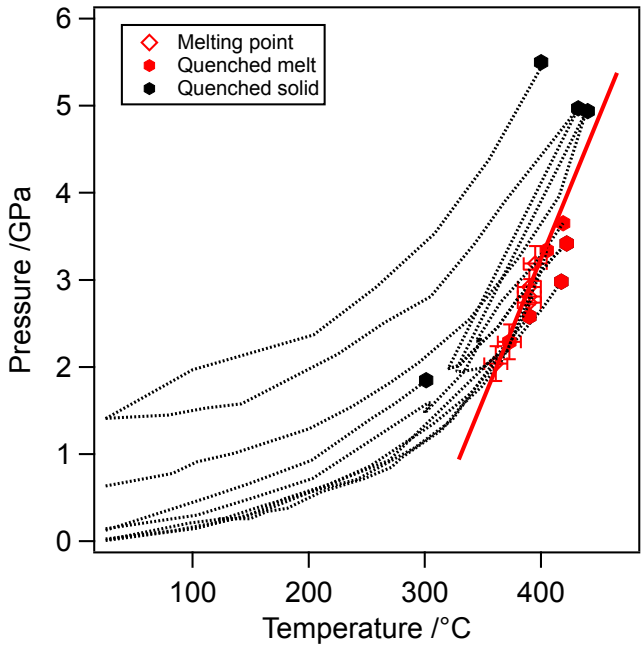

Figure 4.5 *P*-*T*-trajectories of melting point determination. *P*-*T*-conditions are constrained to follow isochores in dotted lines.

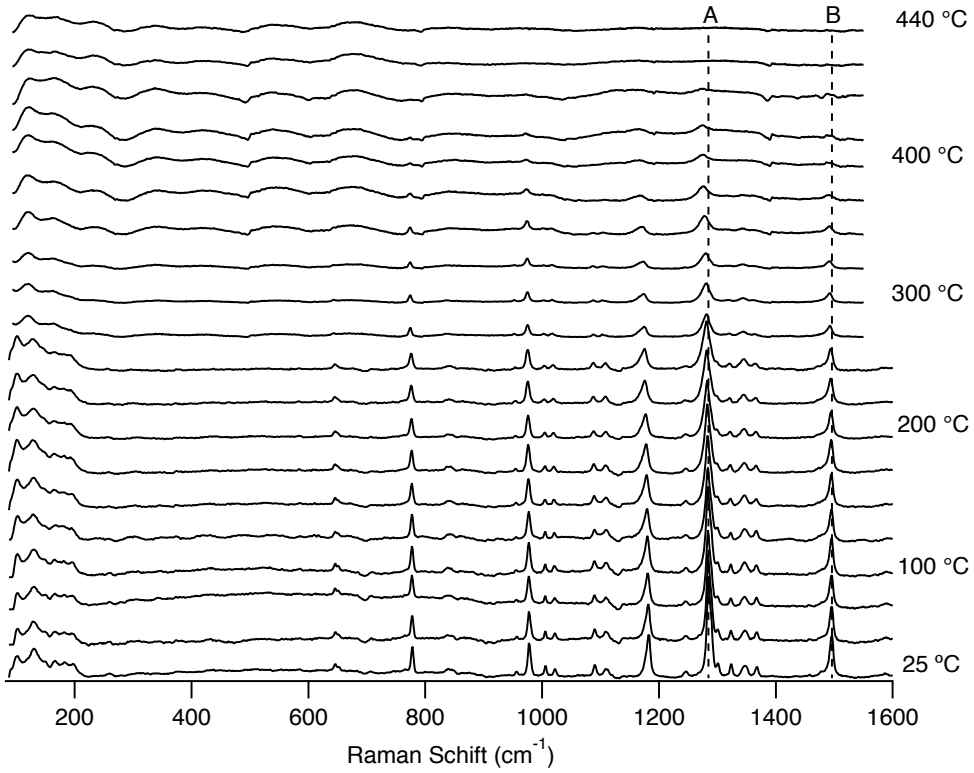

Figure 4.6 Raman spectra of ZIF-62 from ambient temperature to 440 °C. Peak fitting results from modes denoted by A and B are shown in Figure S4.7.

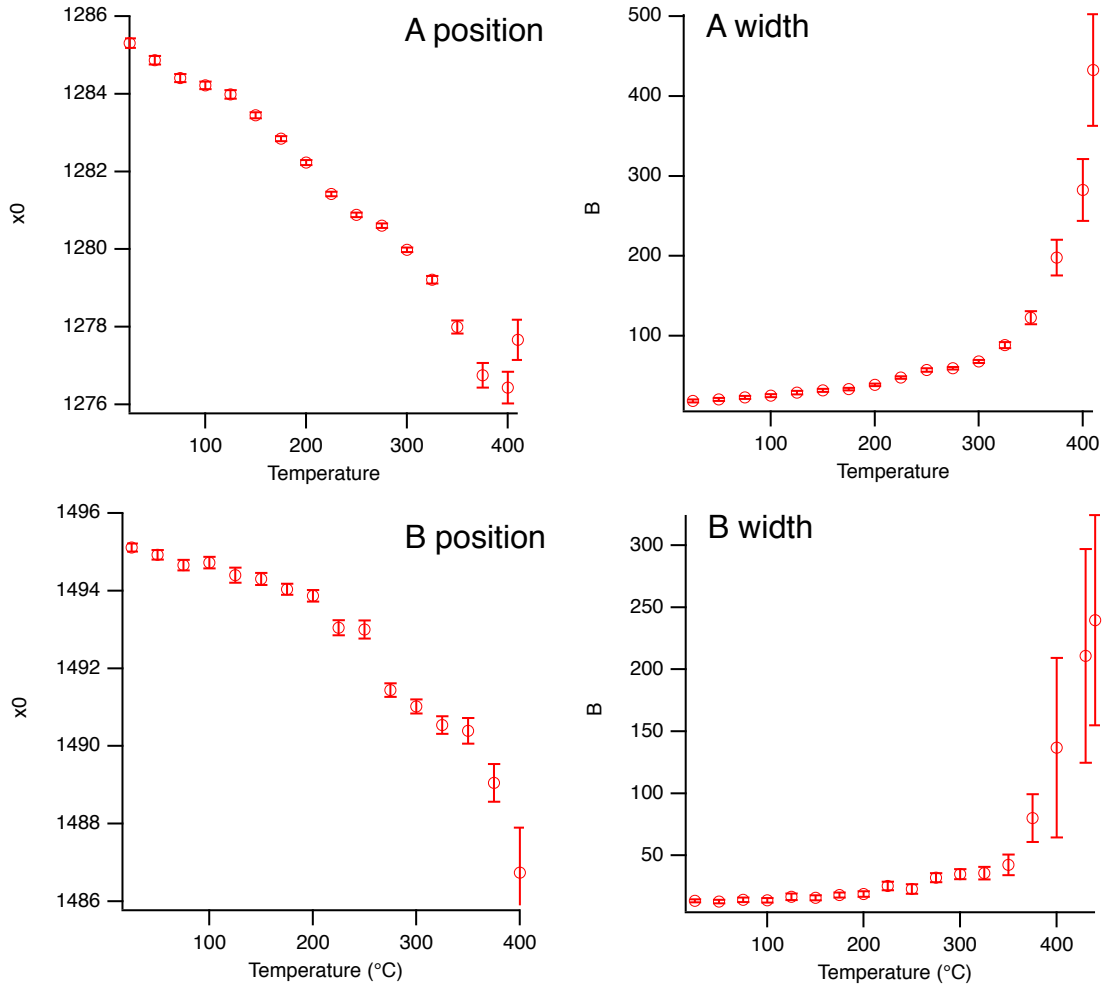

Figure 4.7 Position and width from peak fitting the Raman modes denoted by A and B in Figure S4.6.

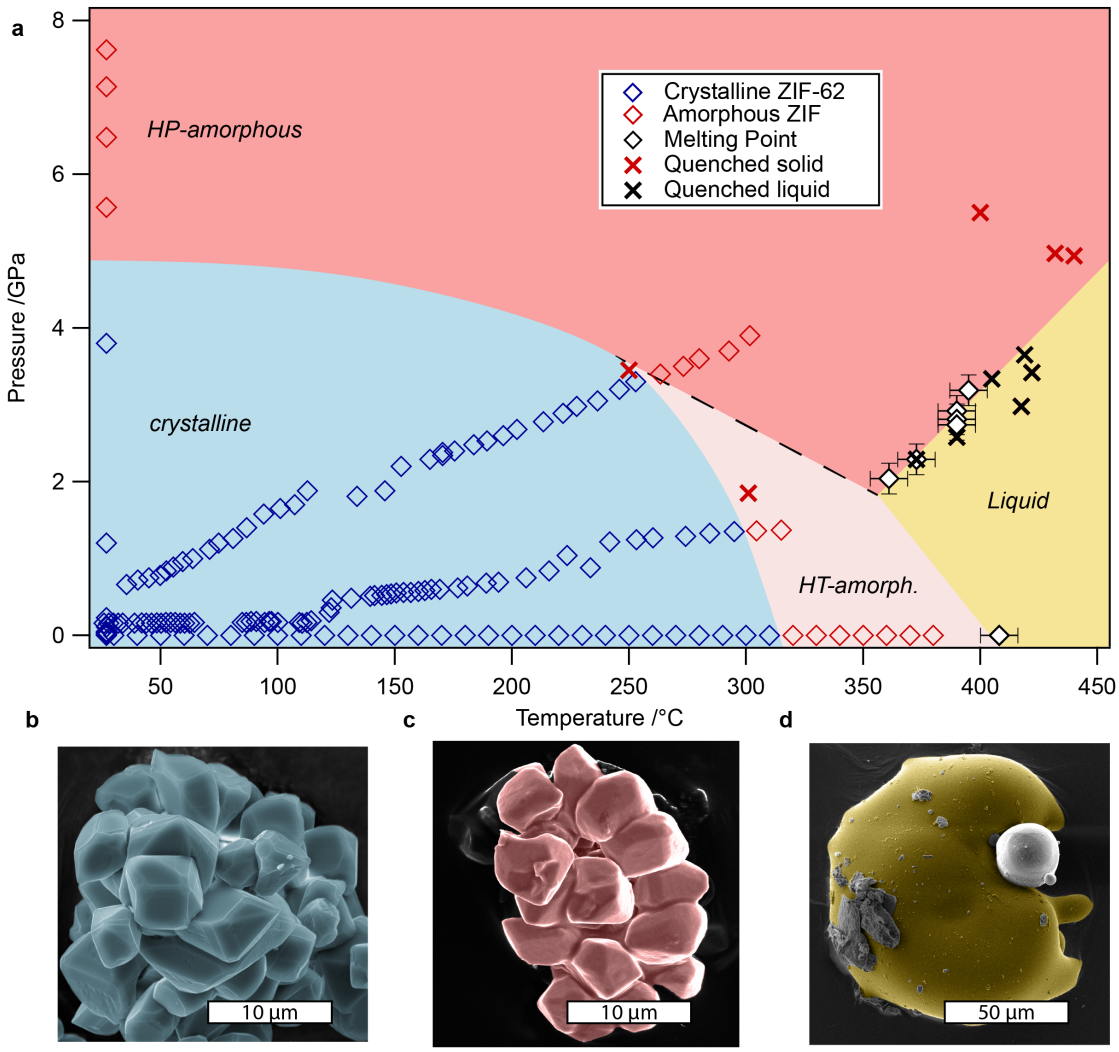

Figure 4.8 Experimentally derived *P*-*T*-phase diagram for ZIF-62 **a** The stability field of crystalline ZIF-62 is shown in blue, tracing phase analysis from PXRD (blue diamonds). Two distinct amorphous phases with higher and lower densities relative to each other are shown in dark and light red, respectively. This distinction is based on changing slopes of both crystalline-amorphous, and solid-liquid phase-boundaries. Liquid ZIF-62 is shown in yellow, tracing melting points (black diamonds) observed optically at high-*P* and using DSC at ambient *P*. Crosses indicate quenching conditions of samples for which morphological analysis was carried out. **b**, **c**, and **d**, Representative scanning-electron microscopic images of three of the four main phases of ZIF-62, in false colours corresponding to the stability fields. Crystalline, as-synthesised ZIF-62 (blue), high-*P* amorphous (red), quenched from 400 °C, 5.5 GPa. High-*P* molten (yellow), quenched from 420 °C, 3.4 GPa. Bright sphere embedded in melt-quenched sample is a ruby single crystal used as a pressure gauge in the high-*P* experiments.

in-situ Raman spectroscopy: the loss of all modes upon compression was fully reversed upon decompression (Figure 4.10). Similarly, the related ZIF-4 also undergoes reversible pressure-induced amorphization[43]. In contrast, thermal amorphization of ZIF-62 is irreversible, and thus ascribed to a reconstructive phase transition. Amorphisation at simultaneous high-P and -T is therefore expected to bear signature of both effects. Moreover, the changing slope of the crystalline to solid-amorphous transition (4.8) found across P-T-space is indicative of high-P and high-T amorphous phases with different densities. This can be derived from the $\Delta S/\Delta V$ term of the Clausius-Clapeyron relation (4.1) for a boundary with a changing slope.

$$\delta P/\delta T = \Delta S/\Delta V \tag{4.1}$$

The high-P and high-T amorphous phases are denoted a_{HP} and a_{HT}, and the corresponding crystalline-amorphous transitions c-a_{HP} and c-a_{HT}, respectively. The relative slopes of the transitions dominated by either c-a_{HP} or c-a_{HT} in P-T-space can be written as

$$\left|\frac{\delta P}{\delta T}\right|_{(c-a_{HP})} < \left|\frac{\delta P}{\delta T}\right|_{(c-a_{HT})} \tag{4.2}$$

It follows from the Clausius-Clapeyron relation, if the degree of disorder in each of the amorphous phases is similar, that

$$\Delta V_{(c-a_{HT})} < \Delta V_{(c-a_{HP})} \tag{4.3}$$

and consequently, a_{HP} is found to be of higher density than a_{HT}, as would be anticipated under the influence of pressure. An approximate boundary between a_{HT} and a_{HP} may be defined by extrapolating the $c-a_{HP}$ boundary to higher pressures (dashed line in Figure 4.8). The resulting negative slope of the this a_{HT}-a_{HP} boundary is in agreement with equation 4.1.

Melting

The melting point of ZIF-62 at ambient-P was identified by DSC scans at ca. 425 °C (Figure 4.3). Melting points at high-P ranging from approximately 2 GPa to 3.5 GPa were determined visually and are shown in Figure 4.5. Six independent melting points at variable P were fitted linearly with a slope of $\delta P/\delta T = 0.031(4)$. Achievable P-T-conditions in DAC experiments are constrained to lie on isochores dictated by the properties of the pressure-transmitting medium. For this reason, it was not technically feasible to target P-T-conditions for low-P

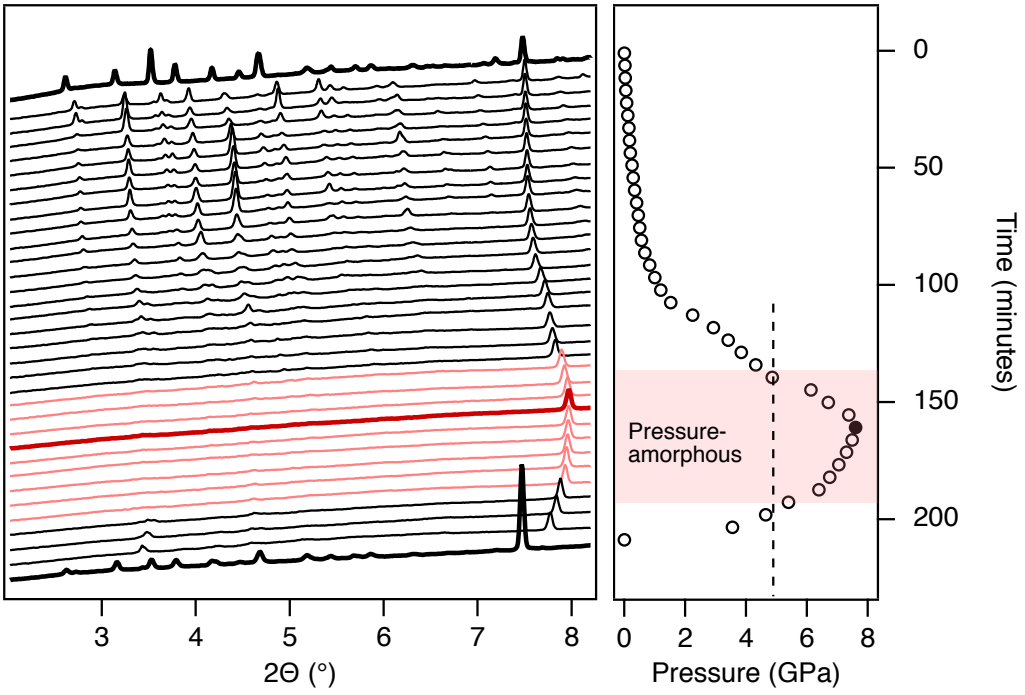

Figure 4.9 Stacked plot of *in-situ* high-*P* PXRD patterns of ZIF-62. Pressures, as determined from admixed NaCl (peak between 7° and 8° 2θ), and timing of the experiment in minutes are indicated for each pattern on the right. Patterns without any diffraction peaks are shown in red and are assigned to the pressure-amorphous state of ZIF-62. Thick black lines at top and bottom represent measurements taken at initial ambient pressure and final ambient pressure, respectively. The threshold pressure for amorphisation and subsequent recrystallization is approximately 5 GPa and shaded in light red.

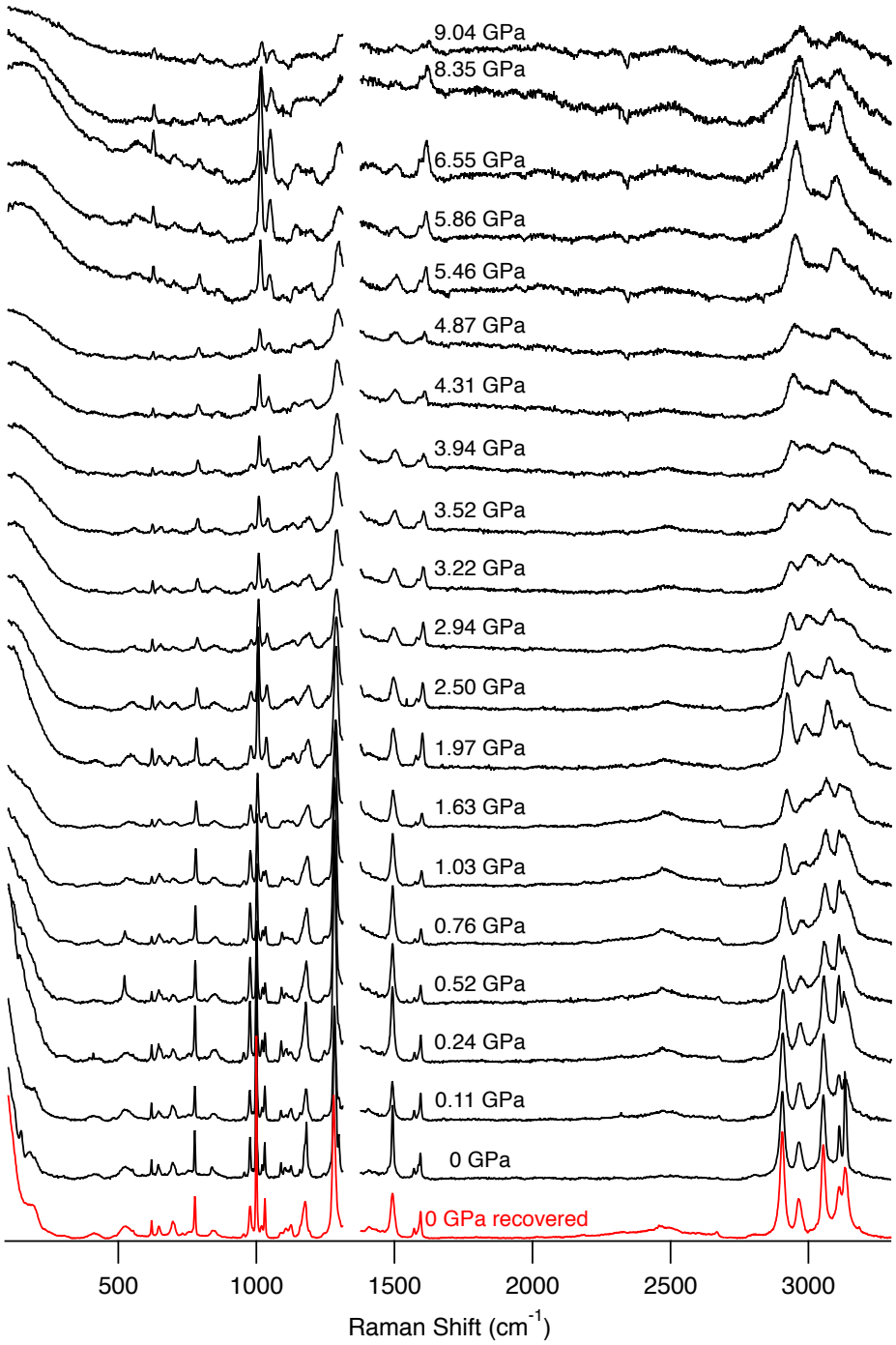

Figure 4.10 Stacked plot of *in-situ* high-*P* Raman spectra. Pressures, determined from the fluorescence band of ruby, are indicated for each spectrum. The recovered spectrum measured at ambient *P* is shown in red.

and high-T. However, it is possible to constrain the upper limit of the melting curve up to approximately 5 GPa by tracking the lowest-P isochore that does not result in melting, indicated in Figure 4.8 by red crosses.

The negative slope of the melting curve interpolated from ambient pressure to < 2 GPa implies the existence of a solid phase with lower density than the liquid phase. At pressures > 2 GPa, the slope of the melting curve has a positive gradient, implying the opposite: a solid phase with a higher density than the liquid phase. Both conditions are in accordance with, and support, the model of two distinct amorphous phases a_{HT} and a_{HP} as discussed in the previous paragraph. The intersection of the low- and high-P melting curve with the assumed boundary between a_{HT} and a_{HP} (dashed line in Figure 4.8) theoretically defines a triple point. However, due to the limitation in achievable low-P-high-T conditions, the exact location of this triple point remains uncertain.

4.3.2 ZIF-4

ZIF-4 generally shows much richer polymorphism than ZIF-62, both upon heating and compression. In addition, there has been a number of previous accounts to which these results may be compared, specifically of the isolated high-P behaviour. For clarity, the pure high-P behaviour and the combined high-P-T behaviour are therefore discussed separately. Powder XRD patterns of all high-P-T experiments are shown in Figures 4.11-4.16. Representative whole-pattern fitting results for the experimental PXRD data are given in Figures 4.17–4.19.

Transformations at high-pressure–ambient-temperature

The high-P behaviour (at ambient-T) of ZIF-4 has previously been studied under a variety of conditions. A compilation of the findings of Bennett et al. (2011)[43], Henke et al. (2018)[71], and the results from the present investigation are shown in Figure 4.20, alongside indications of the respective experimental conditions. A summary of crystal structural parameters of all high-P-ambient-T phases of ZIF-4 is given in Table 4.1.

Two previous studies reported two distinct, monoclinic, high-P phases of ZIF-4: ZIF-4-I in the presence of solvent, and ZIF-4-cp for the evacuated framework. Here, it was found that at pressure below 0.1 GPa ZIF-4 rapidly transforms to a previously unreported orthorhombic phase. This phase will be termed ZIF-4-cp-II (closed pore), in accordance with the established nomenclature. ZIF-4 and ZIF-4-cp-II coexist over a range of approximately 0.5 GPa. In contrast to the previously reported high-P phases which amorphise above 1 GPa, the new ZIF-4-cp-II phase underwent a further transition at *ca.* 1 GPa to a new, even

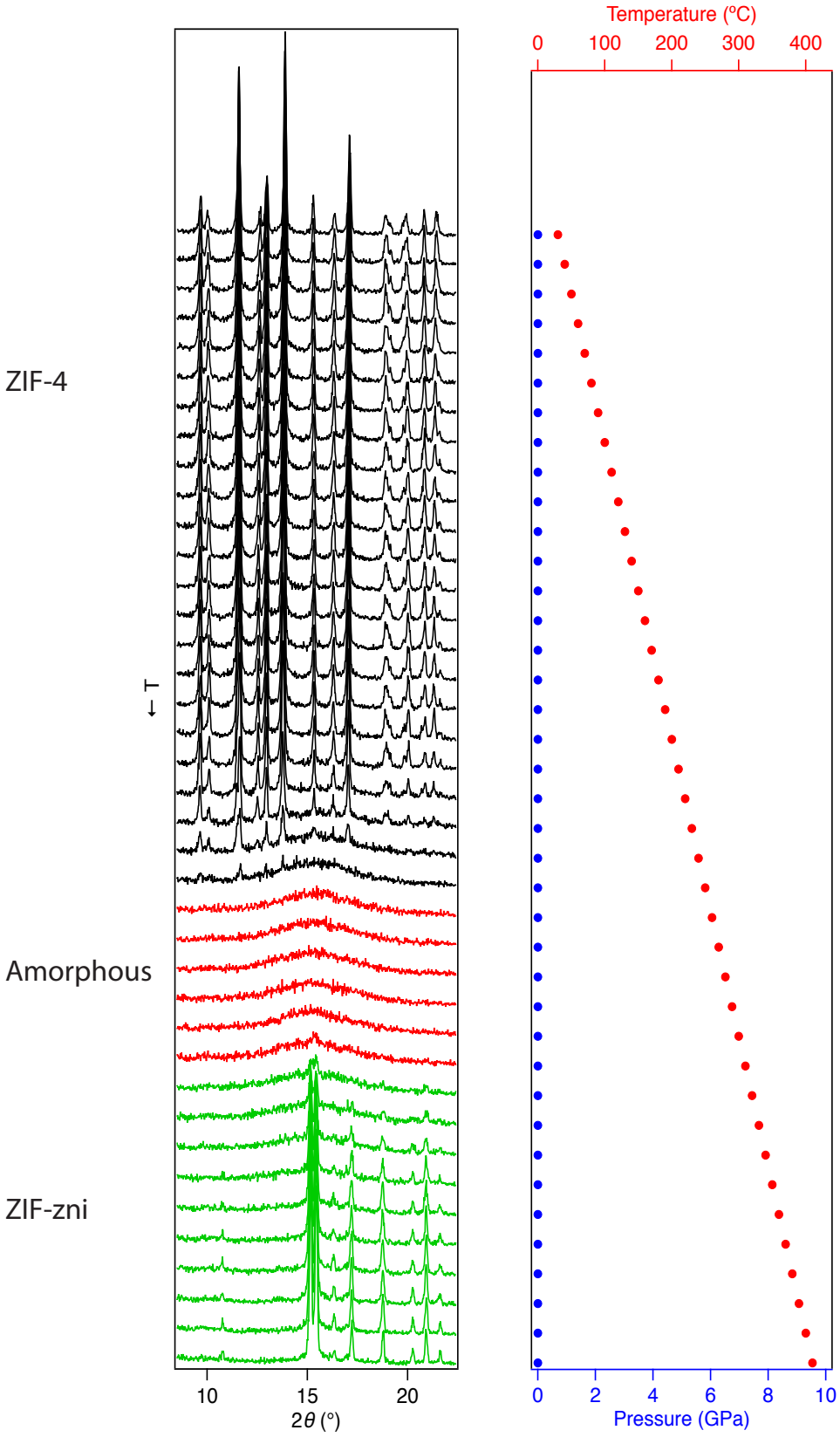

Figure 4.11 PXRD raw data – linear y-scale. All data is plotted with the first measurement at the top, increasing T towards the bottom. Panel on the right shows P-T-condition of the experimental run. High-temperature–vacuum-conditions, Bruker D8, Cu$K_\alpha \lambda = 1.54$ Å.

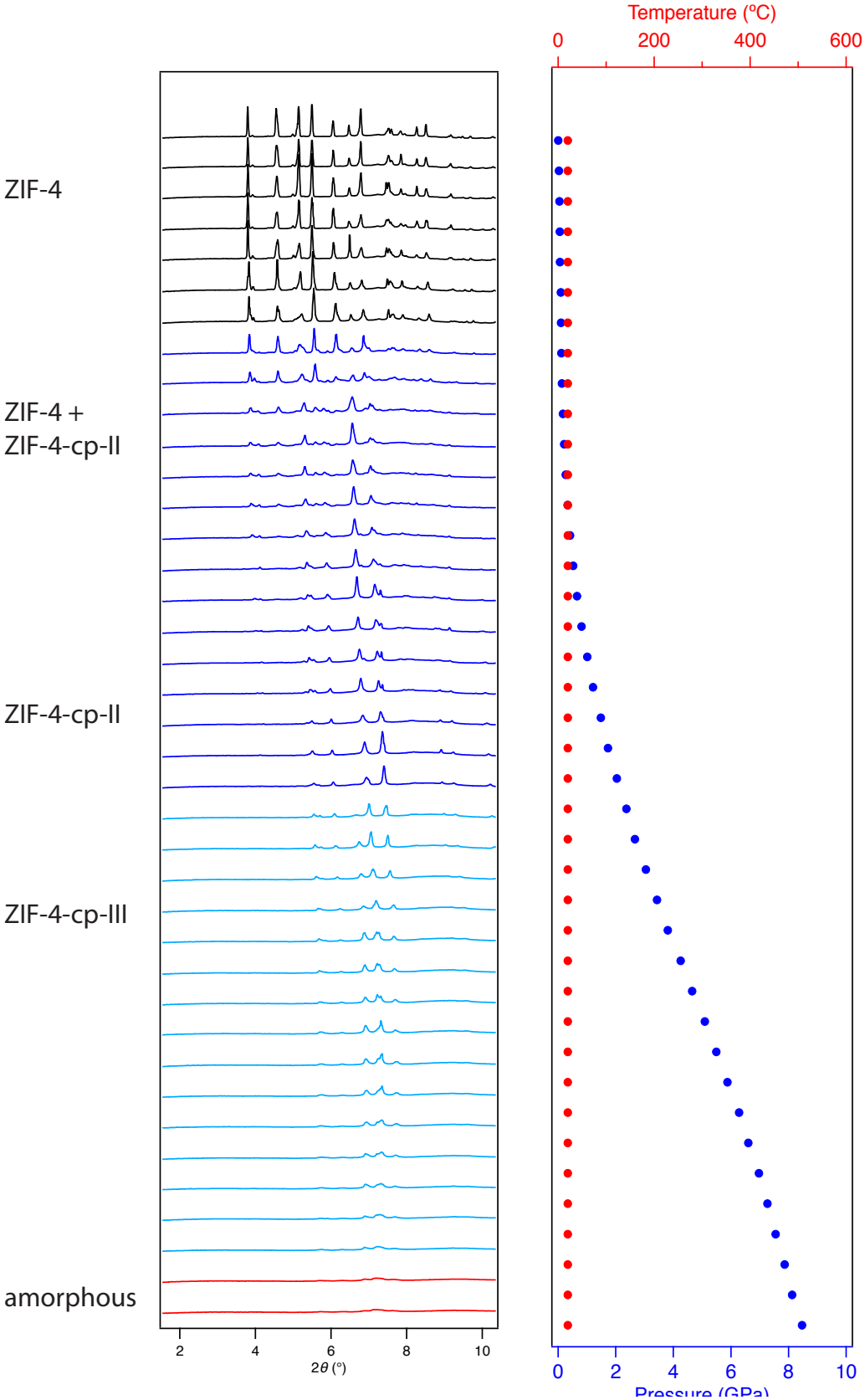

Figure 4.12 PXRD raw data – linear y-scale. All data is plotted with the first measurement at the top, increasing P towards the bottom. Panel on the right shows P-T-condition of the experimental run. High-pressure–ambient-temperature conditions, MS beamline, λ = 0.6200 Å, Swiss Light Source.

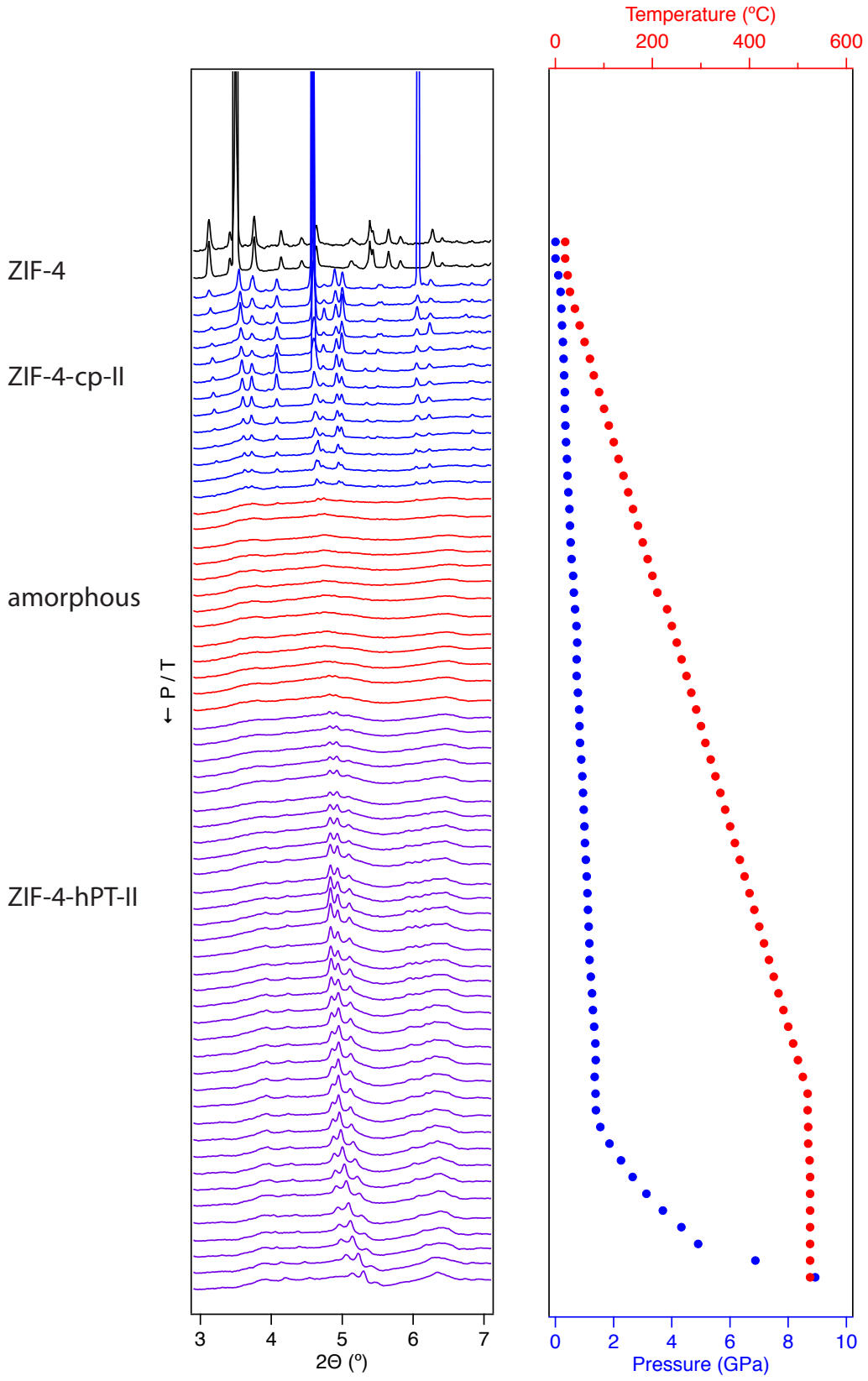

Figure 4.13 PXRD raw data – linear y-scale. All data is plotted with the first measurement at the top, increasing P and T towards the bottom. Panel on the right shows P-T-condition of the experimental run. I15 beamline, $\lambda = 0.4246$ Å, Diamond Light Source.

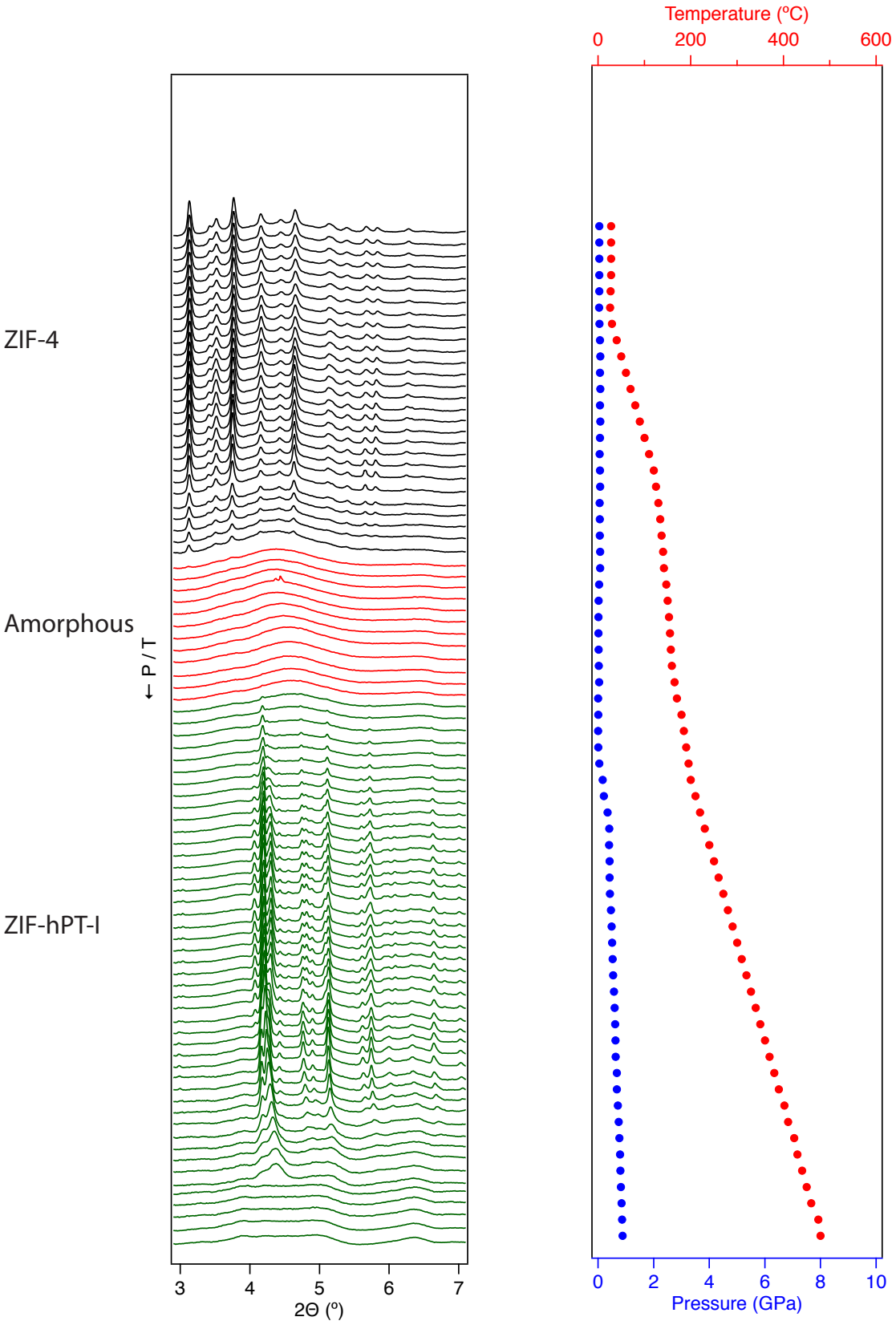

Figure 4.14 PXRD raw data – linear y-scale. All data is plotted with the first measurement at the top, increasing P and T towards the bottom. Panel on the right shows P-T-condition of the experimental run. I15 beamline, $\lambda = 0.4246$ Å, Diamond Light Source.

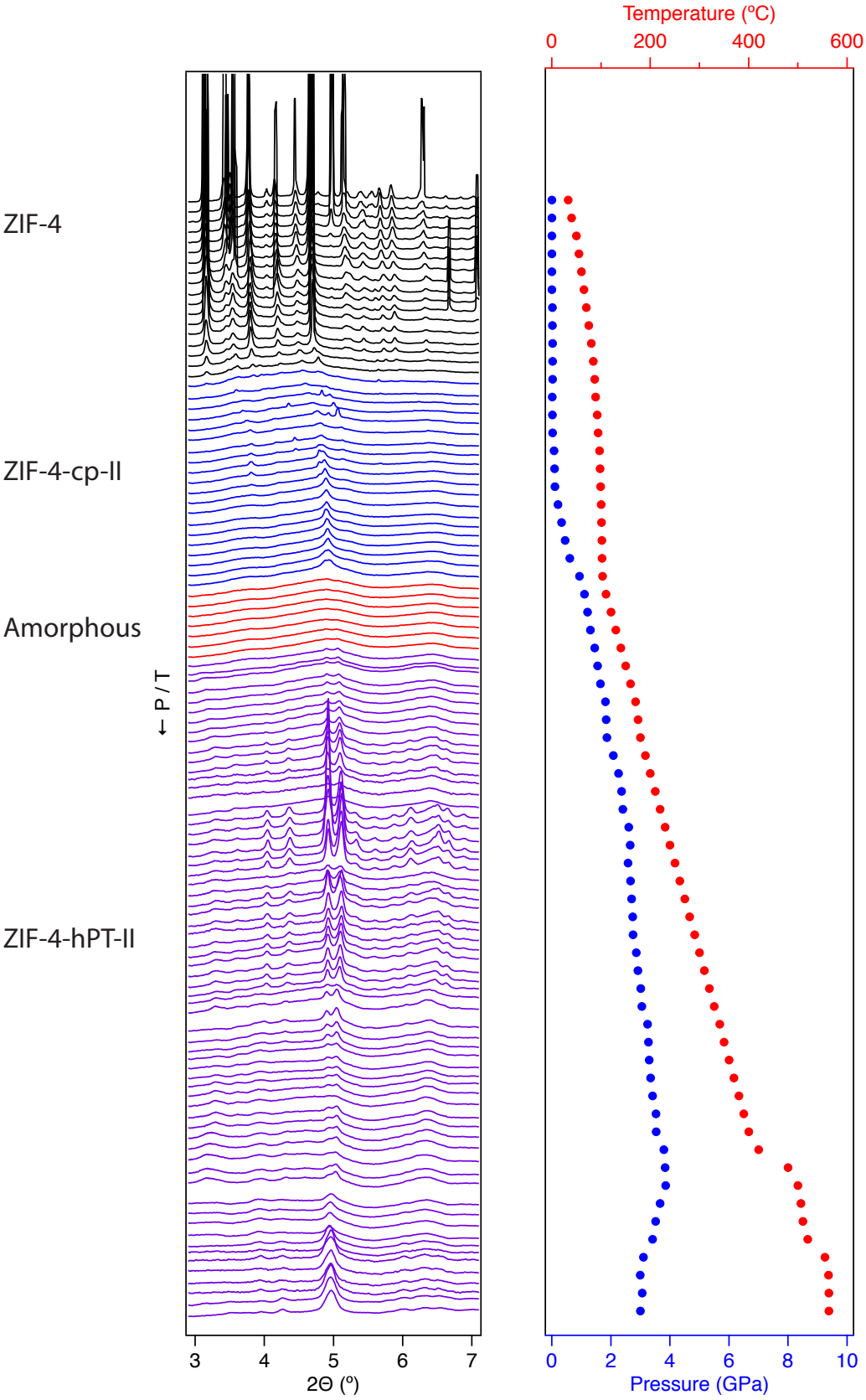

Figure 4.15 PXRD raw data – linear y-scale. All data is plotted with the first measurement at the top, increasing P and T towards the bottom. Panels on the right show P-T-condition of the experimental run. I15 beamline, $\lambda = 0.4246$ Å, Diamond Light Source.

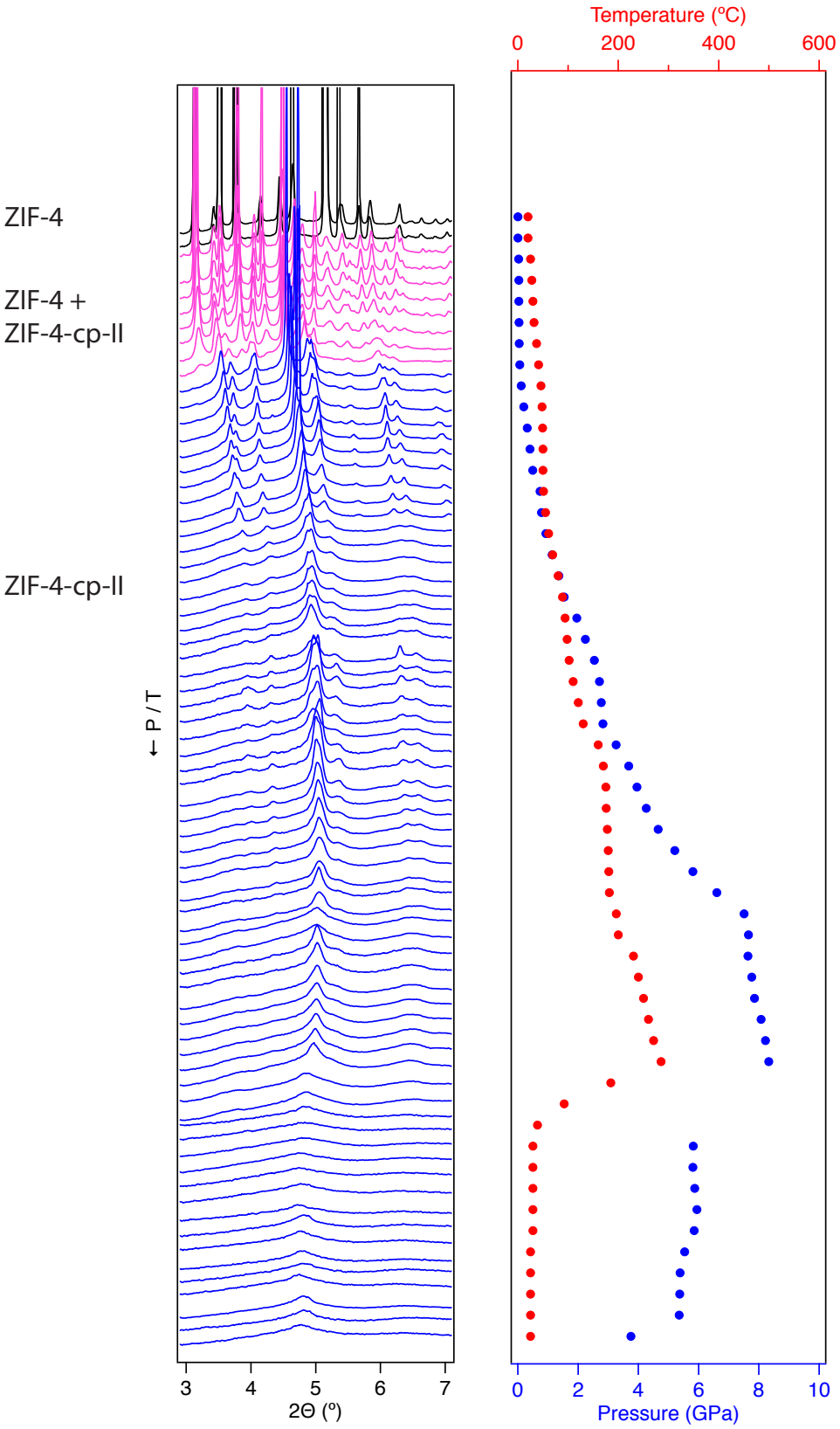

Figure 4.16 PXRD raw data – linear y-scale. All data is plotted with the first measurement at the top, increasing P and T towards the bottom. Panel on the right shows P-T-condition of the individual runs. I15 beamline, $\lambda = 0.4246$ Å, Diamond Light Source.

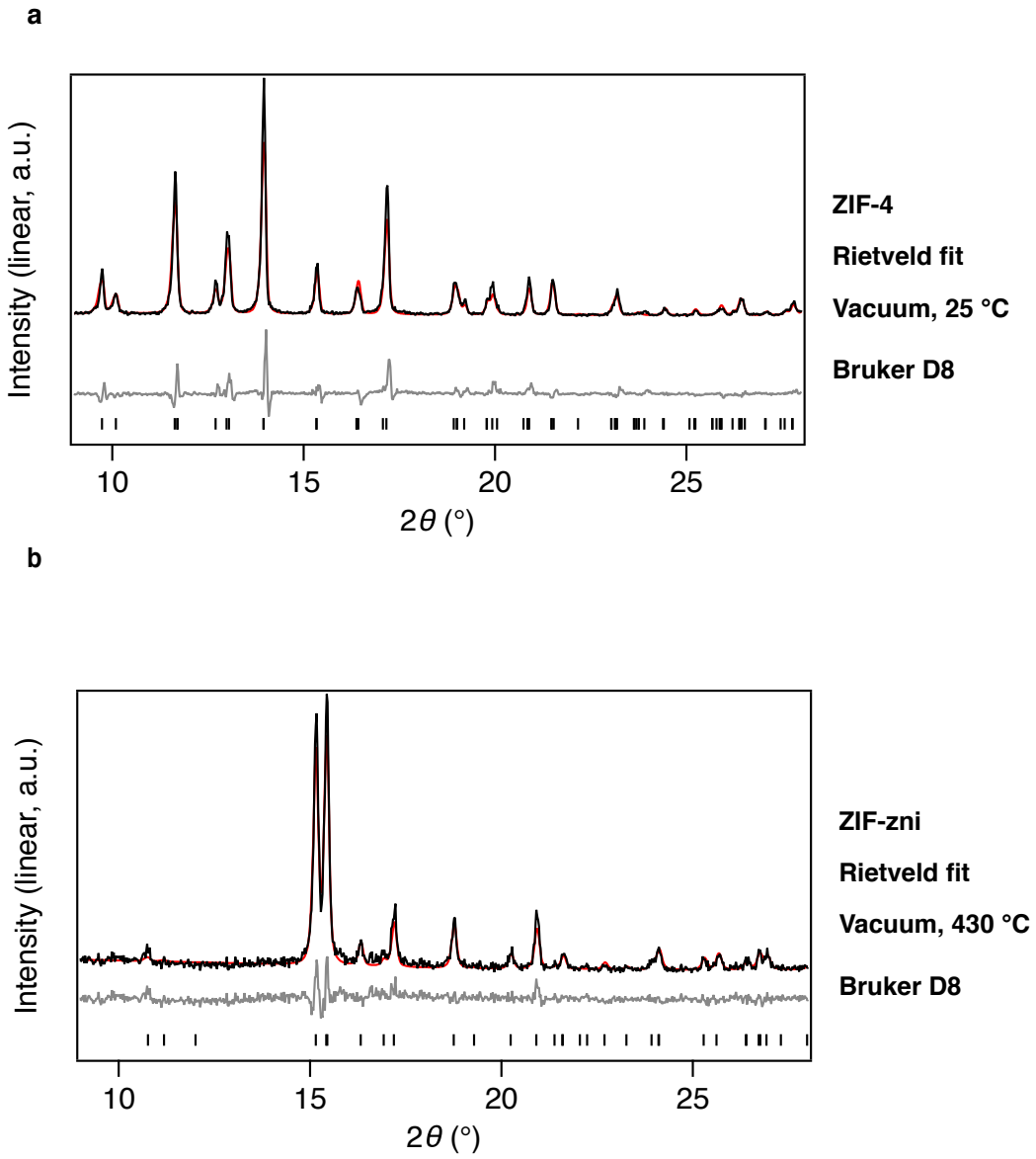

Figure 4.17 Representative Rietveld fitting results from the high-temperature–vacuum experiments on the Bruker D8 diffractometer (Cu$K_\alpha, \lambda = 1.54$ Å). a) Rietveld fit of ZIF-4 b) Rietveld fit of ZIF-zni

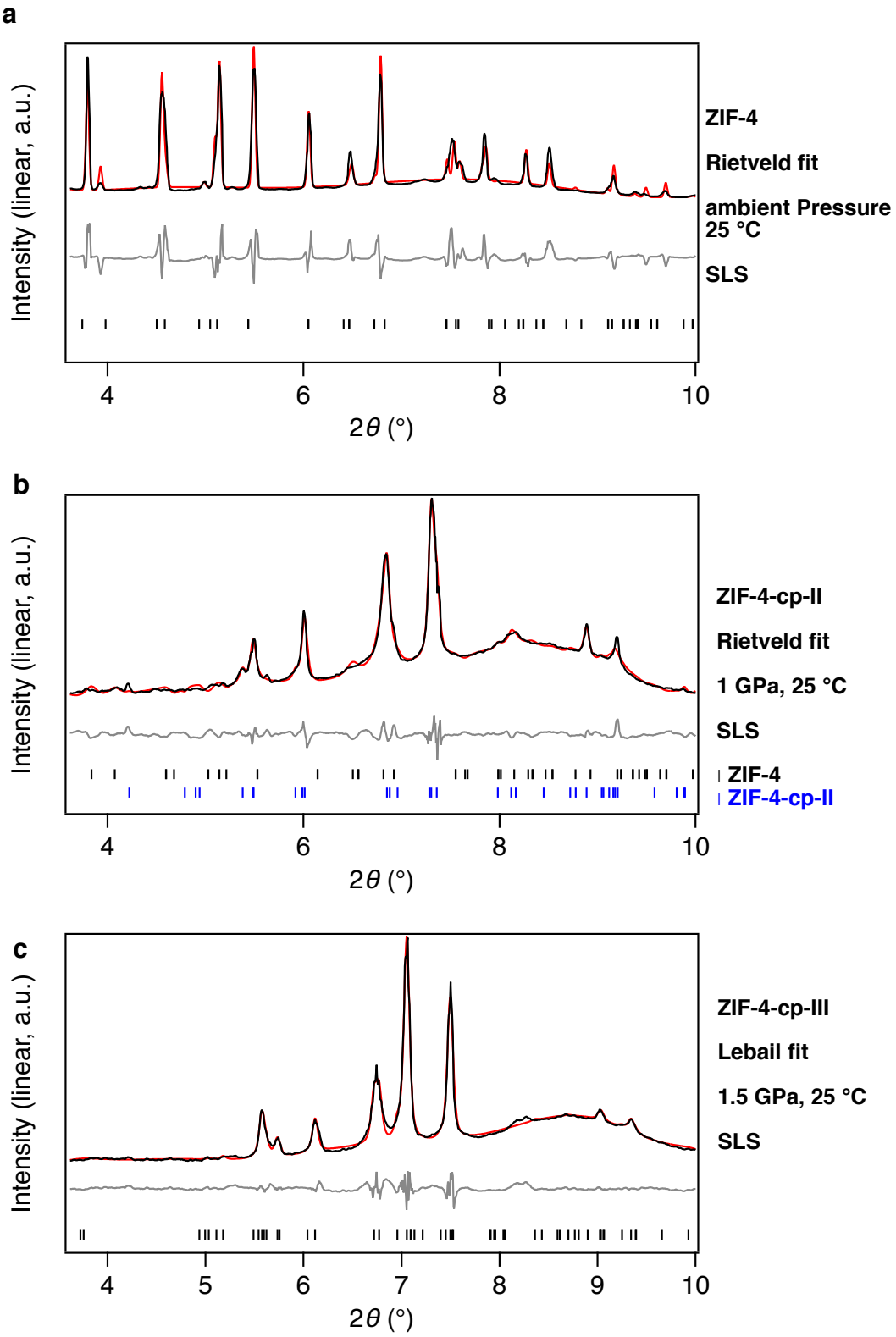

Figure 4.18 Representative Lebail and Rietveld fitting results from the ambient-temperature-high-pressure experiments performed at the MS beamline (λ = 0.6200 Å), Swiss Light Source. a) Rietveld fit of ZIF-4 b) Rietveld fit of a mixture of ZIF-4-cp-II and ZIF-4 c) Lebail fit of ZIF-4-cp-III.

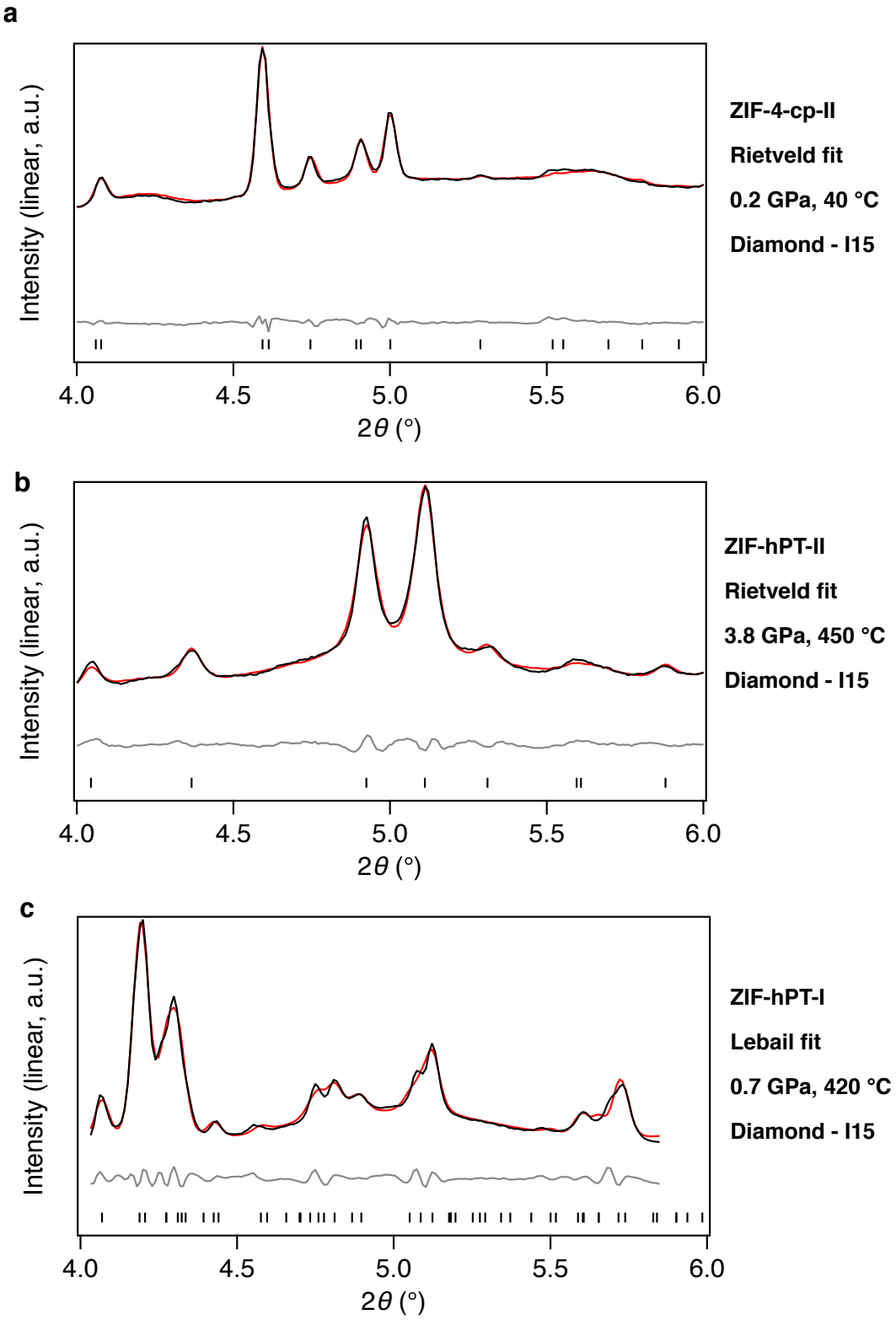

Figure 4.19 Representative Lebail and Rietveld fitting results from the high-temperature-high-pressure experiments performed at the I15 beamline (λ = 0.4246 Å), Diamond Light Source. a) Rietveld fit of ZIF-4-cp-II b) Lebail fit of ZIF-hPT-I, c) Rietveld fit of ZIF-hPT-II.

denser phase, which will be termed ZIF-4-cp-III. This transition is characterised by symmetry lowering to a monoclinic system which results in the appearance of new diffraction peaks. ZIF-4-cp-III amorphises only above 7 GPa.

These results appear to be conflicting with the findings of both previous studies. The experimental difference which is most likely responsible for this discrepancy is the difference in pressurisation rates. During the present experiment, pressure was deliberately increased at a high rate of approximately 2.5 GPa/minute up to 8 GPa, which is an estimated 100 times faster than achievable in conventional experiments as reported in earlier experiments[43, 71]. This faster rate facilitated a richer range of polymorphic behaviour than witnessed in other studies. It becomes apparent that the kinetic control of the pressurisation rate plays a very important role, and this is rarely taken into consideration[173].

Table 4.1 High-pressure ambient-temperature polymorphs of ZIF-4

	ZIF-4	ZIF-4-I	ZIF-4-cp	ZIF-4-cp-II	ZIF-4-cp-III
a	15.395(1)	17.608(1)	14.235(1)	14.506(1)	15.828(1)
b	15.307(1)	14.411(1)	14.874(1)	14.313(1)	14.211(1)
c	18.426(1)	14.703(1)	16.330(1)	14.714(1)	14.266(1)
β	90	100.90(1)	91.55(1)	90	116.13(1)
Vol (Å)	4342	3664	3457	3055	2882
S.G.	*Pbca*	$P2_1/c$	$P2_1/c$	*Pbca*	$P2_1/c$
P (GPa)	0	0.001	0.08	0.65	1.48
T (°C)	25	25	25	25	25
CSD-code	VEJYUF	VEJYUF07	n.a.	n.a	n.a.
Ref.	[34]	[43]	[71]	This study	This study

Transformations at high-pressure–high-temperature

The *P*-*T*-diagram shown in Figure 4.21 contains the traces of four individual runs with simultaneous *P* and *T* increase, and one trace each of the high-*P*-ambient-*T*, and the ambient-*P*-high-*T* runs. The phases observed at each point are represented by the colour of the markers, and schematic phase boundaries are indicated by coloured fields, strictly as a guide to the eye only. Reconstructive, and thus irreversible phase boundaries are indicated by dashed lines. Table 4.2 details the crystal structural parameters of the high-*P*-*T* phases.

The first transition at simultaneous high-*P*-*T* is that of ZIF-4 – ZIF-4-cp-II, which occurs at 40 °C and 0.1 GPa. This transition is the same as that at high-*P*-ambient-*T*, which was

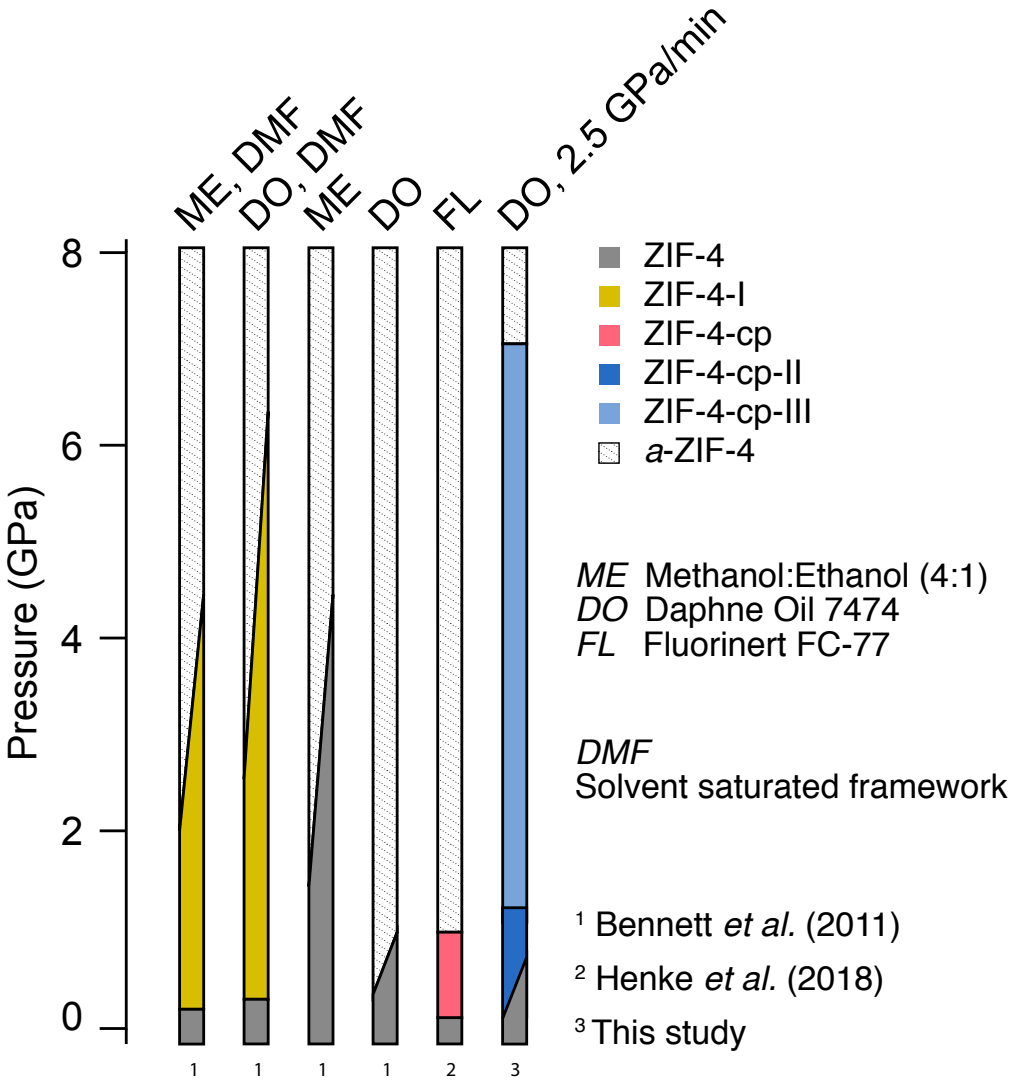

Figure 4.20 Comparison of high-pressure behaviours of ZIF-4 at ambient temperature.

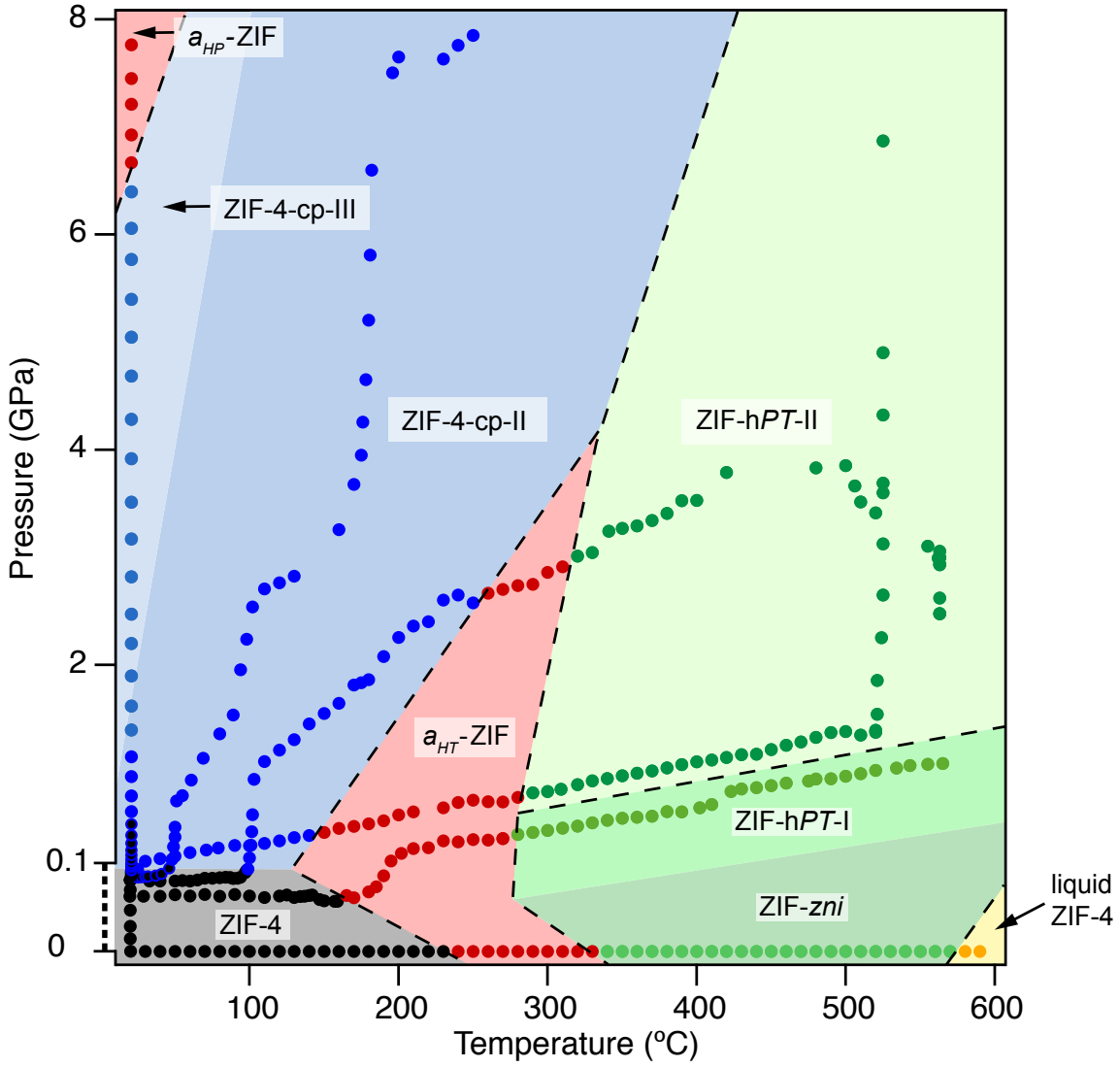

Figure 4.21 Pressure-temperature phase diagram of ZIF-4. The pressure-range from 0 GPa to 0.1 GPa has been magnified for better visibility and is thus not to scale. Solid symbols represent the experimental points and they are coloured according to the phases observed in-situ. Coloured outlines of phase boundaries are drawn as guides to the eye. Dashed lines indicate irreversible, reconstructive transitions.

Table 4.2 High-pressure-high-temperature polymorphs of ZIF-4.

	ZIF-cp-II	ZIF-zni[a]	β-ZIF-zni[b]	ZIF-hPT-I[a]	ZIF-hPT-II[a]
a	15.567(1)	23.481(1)	22.748(1)	22.863(1)	13.496(1)
b	14.445(1)	23.481(1)	22.748(1)	23.839(1)	9.884(1)
c	15.451(1)	12.461(1)	13.017(1)	11.636(1)	9.165(1)
Vol (Å)	3251	6871	6736	6342	1223
S.G.	*Pbca*	$I4_1cd$	$I4_1$	*n.a.*[c]	*Pbca*
P (GPa)	0.15	0	0	0.46	0.81
T (°C)	30	25	25	300	290
CSD-code	1903482	IMIDZB	IMIDZB12	n.a.	1903495
Ref.	This work	[108]	[107]	This work	This work

[a] Recrystallised from amorphous a-ZIF-4
[b] High-pressure form of ZIF-zni, not observed during our experiments
[c] The space group has not unequivocally been determined; a space group with no systematic absences (*Pmmm*) was used for the Pawley refinement.

discussed in the previous section. In contrast to the ambient-*T* experiment, the simultaneous application of heat here stabilises the ZIF-4-cp-II phase up to at least 8 GPa and 250 °C without further transition to ZIF-4-cp-III. However, at comparatively lower pressures but higher temperatures (140 °C–0.4GPa, and 250 °C–2.6 GPa), ZIF-4-cp-II amorphises to *a*-ZIF-4. This is analogous to the known amorphisation of ZIF-4 to *a*-ZIF-4 at 250 °C–ambient-*P*[42]. Importantly, the Clapeyron slope of the ZIF-4 – *a*-ZIF-4 transformation is negative, while that of the ZIF-4-cp-II – *a*-ZIF-4 transformation is positive. This implies increasing relative densities in the order ZIF-4 < *a*-ZIF-4 < ZIF-4-cp-II. An equivalent change of the slope from negative to positive with increasing *P* was shown for the melting curve of ZIF-62.

Upon further heating and pressurisation of *a*-ZIF-4, two new transformations are associated with the recrystallisation of two distinct high-*P*-*T* phases: ZIF-hPT-I at 0.4 GPa–270 °C, and ZIF-hPT-II at 0.8 GPa–290 °C and 3 GPa–320 °C. Both new phases remain stable until the maximal achieved conditions of these experiments. Importantly, the melting of these phases within the given temperature limits was not observed. The melting curve of ZIF-zni at elevated *P* is thus tentatively indicated with a positive Clapeyron slope. This behaviour can be justified by the formation of the high-density crystalline phases ZIF-hPT-I and ZIF-hPT-II prior to the (hypothetical) melting. In contrast, the previously reported melting behavior of ZIF-62 follows a negative Clapeyron slope due to the higher density of the liquid compared to the solid-amorphous precursor.

High-*P*-*T* polymorphs of ZIF-4

ZIF-4-cp-II The unit cell and space group for ZIF-4-cp-II were found to be identical to those of the ZIF-4-LT structure[106], which occurs when ZIF-4 is cooled below $-130\,^{\circ}\mathrm{C}$. Yet, the calculated intensities of the powder pattern of ZIF-4-LT did not match the here observed pattern. However, based on the ZIF-4-LT starting model, a new structural model for ZIF-cp-II could successfully be solved and refined. To this end, the geometry of the Im and bIm linkers were restrained by rigid bodies. The corner–centroid distances were refined isotropically (to account for thermal expansion or compression), while the interatomic angles were held fixed. The positions of these rigid bodies were refined both in translation and rotation with respect to the crystal axes. Further geometrical constraints were introduced to keep tetrahedral angles in the ZnN_4 units within reasonable values of approximately $109° \pm 5°$, as well as Zn–N distances within approximately $2\,\text{Å} \pm 0.05\,\text{Å}$. Furthermore, the geometry of the Zn–Im–Zn units was pushed to be quasi-planar with bridging angles of approximately $145° \pm 5°$ (Figure 4.22). With these constraints in place, least-square refinements finally lead to the proposed model.

The difference between ZIF-4 and the new high-*P* ZIF-4-cp-II phase, both orthorhombic with space group *Pbca*, is a density increase by a factor of approximately 1.35, which is marked by an abrupt volume contraction (Figure 4.23). While the topology is preserved upon this densification, the 6- and 8-membered rings of the cag topology are visibly squeezed (Figure 4.24). The densification is accomplished by a displacive transition involving the rotation of the imidazolate linkers around the N–N hinge, and the increase of Zn–Im–Zn angles by (on average) 10°. A similar mechanism was described for the ZIF-4 – ZIF-4-LT transformation[106]; an overlay of the asymmetric units of ZIF-cp-II and ZIF-4-LT is shown in Figure 4.25.

ZIF-4-cp-III The structure of ZIF-4-cp-III could not be reliably determined due to poor data quality. However, a new unit cell based on a orthorhombic to monoclinic symmetry lowering of the unit cell of ZIF-4-cp-II is suggested, which results in a good structure-less Lebail fit (Figure 4.18c). This unit cell was found using the built-in indexing algorithm of TOPAS academic. Since the transition from ZIF-4-cp-II to ZIF-4-cp-III is instantaneous, it can further be suggested that this orthorhombic to monoclinic transition can be classified as a displacive transition, and that the structure thus retains the cag topology. The unit cell volume continuously decreases across the ZIF-4-cp-II – ZIF-4-cp-III transition (Figure 4.23).

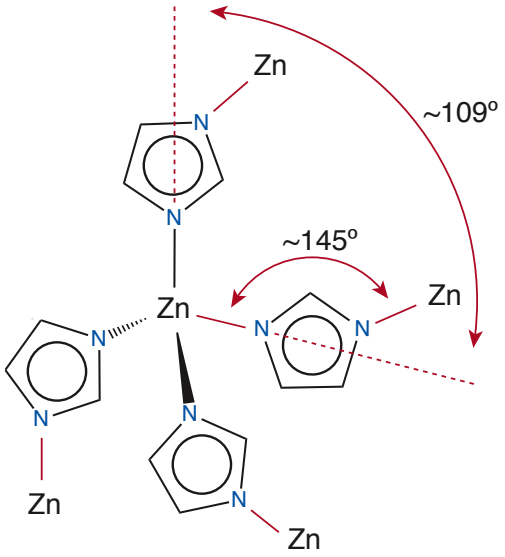

Figure 4.22 Characteristic building unit of ZIF-4 with four crystallographic independent linkers which tetrahedrally coordinate Zn centres. Approximate bridging- and interatomic angles are indicated as used to restrain the structures during structure refinements.

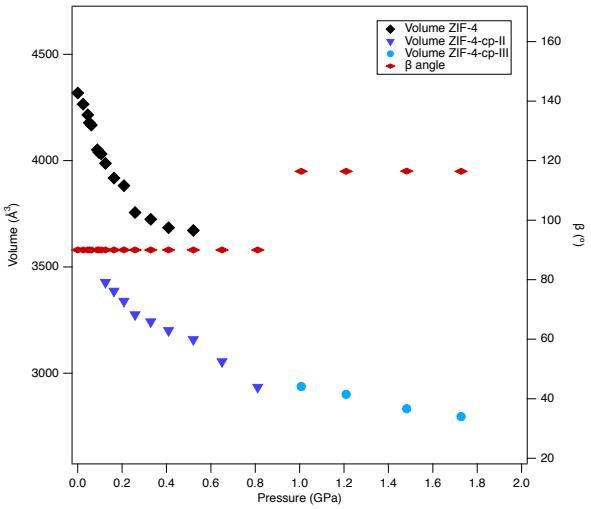

Figure 4.23 Evolution of the unit cell volume and β-angle as a function of pressure at ambient temperature across the transition ZIF-4 – ZIF-4-cp-II – ZIF-4-cp-III. ZIF-4 and ZIF-4-cp-II co-exist over approximately 0.5 GPa

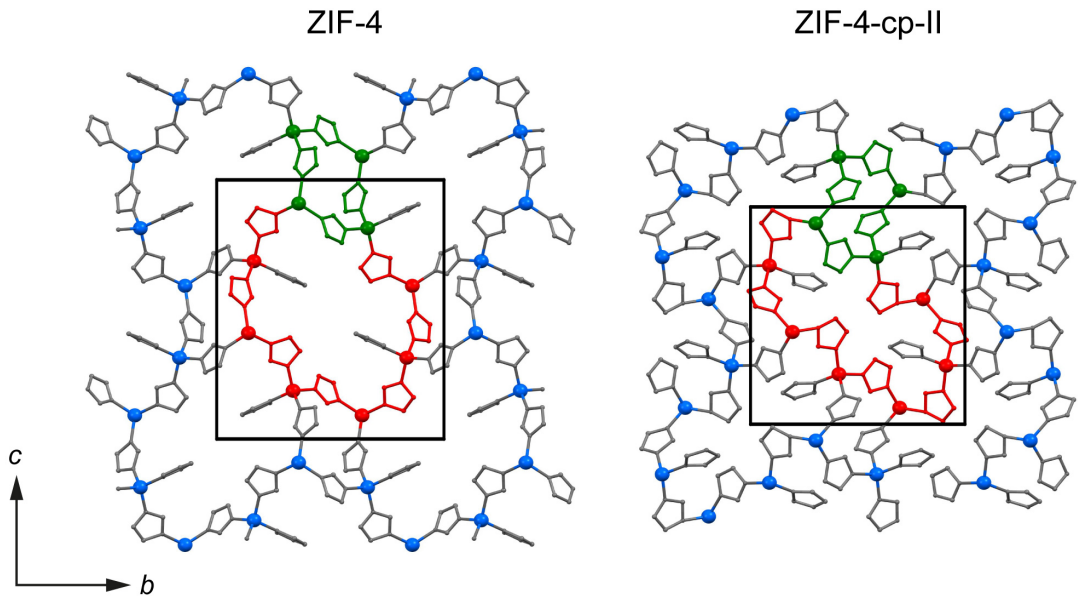

Figure 4.24 Comparison of the structures of ZIF-4 (left) and ZIF-4-cp-II at 0.2 GPa (right). Zn = blue, imidazolate = grey, H is omitted. The 4-, and 8-membered rings of the cag topology are indicated in green and red, respectively.

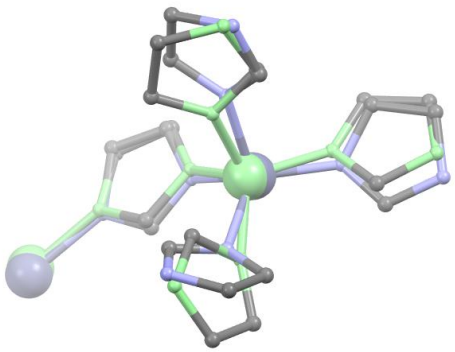

Figure 4.25 Overlay of the asymmetric units of ZIF-4-LT (blue N and Zn) and ZIF-4-cp-III (green N and Zn). The two structures share approximately the same unit cell dimensions and the same space group, leaving the main difference between the two in the orientation of the Imidazolate linkers.

ZIF-hPT-I The structure of ZIF-hPT-I could not be solved based on the present data. However, a new orthorombic unit cell (found using the built-in indexing algorithm of TOPAS academic) is proposed, which is supported by successful structure-less Lebail refinements (Figure 4.19c). Consequently, it is unclear to what extent ZIF-hPT-I structurally differs from ZIF-*zni*, and its high-*P* polymorph β-ZIF-*zni*, given the very similar unit cell dimensions of all three phases (Table 4.2). Furthermore, interconversion of the two phases ZIF-hPT-I and ZIF-hPT-II, is kinetically hindered, as demonstrated by their widely overlapping apparent stabilities (Figure 4.26). The most likely explanation for these meta-stable extensions is a distinct topology of the two structures. This would imply that any transition between them is reconstructive, *i.e.* requires the breakage and reformation of Zn–N bonds for interconversion. Further evidence for a distinct topology stems from the observation that around 550 °C ZIF-hPT-I amorphised at 6 GPa, while ZIF-hPT-II proofed stable at least up to 8 GPa (Figure 4.26).

ZIF-hPT-II The structure of ZIF-hPT-II (Figure 4.27) was found to be analogous to previously reported $Cd(Im)_2$ and $Hg(Im)_2$ phases[125] and is based on a double-interpenetrated diamondoid network. This interpenetration is surprising given the relative short Zn–N bonds compared to Cd–N and Hg–N bonds, and previously it had therefore been deemed impossible for a $Zn(Im)_2$ compound[125]. Two-fold interpenetrated diamondoid $Zn(Im)_2$ networks were also simulated in a number of space groups, none of which was found to be energetically favourable at ambient conditions[174]. Whether ZIF-hPT-II is stable at ambient conditions remains experimentally unknown, though it is unlikely to undergo a reconstructive bond breaking process upon decompression. A second-order Birch-Murnaghan equation of state was fitted from 1.4 to 4.9 GPa to the refined unit cell volumes of ZIF-hPT-II, obtained from isothermal compression at 520 °C. The resulting bulk modulus (K_0) is 21.6(1) GPa (Figure 4.28). In comparison, the dense ZIF-zni has a bulk modulus of 14 GPa at ambient temperature.

4.4 Comparison of ZIF-4 and ZIF-62

It is well known how ZIF-4 and its partially linker substituted relative ZIF-62 significantly differ in their high-*T* behaviour[45]. For example, the recrystallisation mechanism leading to the transformation of ZIF-4 to ZIF-*zni* upon heating is inhibited in ZIF-62 due to the presence of bulky benzimidazolate ligands. The presence of benzimidazolate also lowers the melting temperature of ZIF-62 relative to ZIF-4 and extends the stability range of that

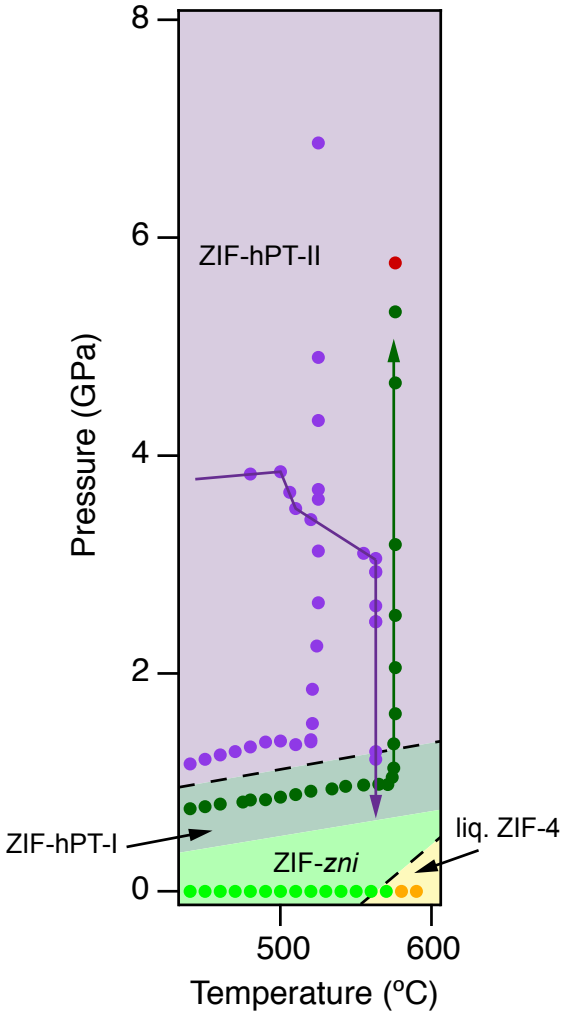

Figure 4.26 Close-up view on the high-T section of the ZIF-4 phase diagram. The two traces emphasised by arrows were omitted in the main article for clarity. The meta-stable extension of the both phases into the other phase fields is indicative of two distinct topologies of the underlying structures that kinetically hinders the conversion.

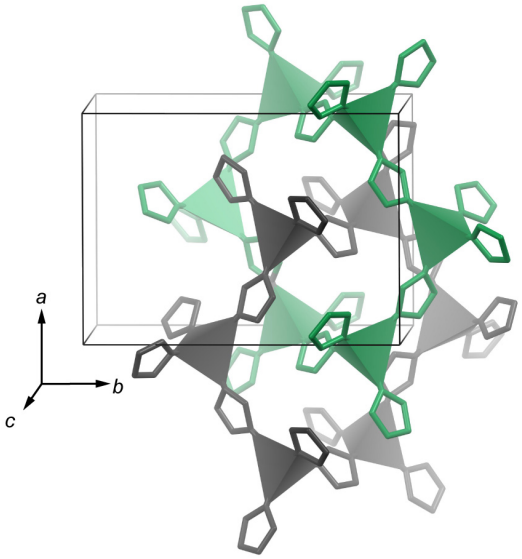

Figure 4.27 Structural model of ZIF-hPT-II represented by ZnN_4 tetrahedra and imidazolate linkers without H atoms (unit cell content is reduced for clarity). Two interpenetrated, unconnected diamondoid networks in grey and green emerge based on the interconnected Zn(Im)4 units.

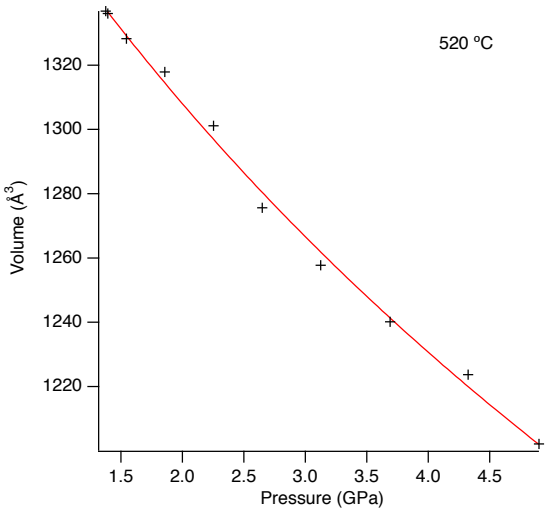

Figure 4.28 Second-order Burch Murnaghan equation of state(red line) was fitted from 1.4 to 4.9 GPa to the refined unit cell volumes of ZIF-hPT-II (black crosses) obtained from isothermal compression at 520 °C. The resulting bulk modulus (K_0) is 21.6(1) GPa.

melt. Comparison of the high-*P*-*T* behaviour of ZIF-4 with that of ZIF-62 reveals an even wider-ranging control of the presence of the benzimidazolate linker. In fact, none of the displacive or reconstructive transformations at high-*P*-*T* conditions observed in ZIF-4 occur in ZIF-62. Furthermore, ZIF-62 amorphises above 5 GPa, while ZIF-4 has been shown to undergo *P*-induced amorphisation at comparable pressurisation rates at a much lower *P* of around 1 GPa[43]. The significant difference in high-*P* stability at ambient-*T* between these two ZIFs may be explained by the more sterically hindered benzimidazolate linkers protruding into the pore cavities and offering additional stabilization against collapse (see also Chapte 3). The structural stabilisation of ZIF-62 through linker substitution has been confirmed by computational studies: force-field based molecular dynamics simulations of the elastic properties of ZIF-62 and ZIF-4 demonstrated higher bulk (4.7 GPa), Young's (8.7 GPa) and shear (3.6 GPa) moduli in ZIF-62, compared to ZIF-4 (2.7 GPa, 5.6 GPa and 2.4 GPa, respectively)[175].

Furthermore, in the case of ZIF-62, it was inferred that two distinct, though adjacent, high-*T* and high-*P* amorphous phases exist. Here, in the case of ZIF-4, the two equivalent high-*T* and high-*P* amorphous phases are separated by other crystalline phases. This is further support that the high-*T* and high-*P* induced amorphous phases of this ZIF system, as previously reported, indeed are structurally distinct.

4.5 Critical Considerations

The compilation of all the high-*T*, high-*P* and high-*P*-*T* data reported in previous literature as well as the present study into a single thermodynamically valid *P*-*T* phase-diagram requires critical consideration of several experimental and theoretical issues: (1) the rates of pressure- and temperature increase, (2) the influence of the pressure transmitting media, (3) sample dependent effects (4) the definition of a phase transition, and (5) whether the overall energy landscape of the system with $Zn(Im)_2$composition, or the local energy landscape of the ZIF-4 network with cag topology is in question. Meanwhile, these points not only concern the question of internal consistency for a single phase, but also whether it is appropriate to cross-compare multiple phases and studies.

(1) Experimentally determined phase boundaries will always depend on the transformation kinetics between the two adjacent phases. In particular, reconstructive transformations can be very sluggish and may allow a phase to persist in a metastable state outside its thermodynamic *P*-*T* stability field[75]. Furthermore, kinetic effects can allow two distinct phases to coexist over a certain range of conditions. The most important factor which controls this is

the pressurisation and/or heating rate. In addition to shifting of apparent phase boundaries, there is also a possibility that altogether different polymorphs form depending on these rates[173]. Therefore, under ideal circumstances, multiple data sets should be recorded at identical rates if they are to be compared. Technically, this can be difficult to achieve, in particular when working with high pressure.

(2) Different types of non-penetrating pressure transmitting media have been used in past and present studies. Fluorinert, silicone oil, and Daphne Oil have distinct hydrostatic limits, at ambient temperature, of approximately 2 GPa, 2.5 GPa, and 4 GPa, respectively[145]. This limit will affect the onset pressures of amorphisation[176, 177], and may therefore also preclude the transformation to higher-pressure polymorphs. Furthermore, it appears that the type of pressure-transmitting medium also affects the structure of high-*P* polymorphs. Upon compressing ZIF-4 at ambient-*T*, the use of Fluorinert results in the formation of the monoclinic ZIF-4-cp phase, while both the use of Daphne Oil and silicone oil result in the orthorhombic ZIF-4-cp-II phase. This can only be explained by an unknown and unexpected interaction of the medium with ZIF-4. While this is less of a problem with dense and inert materials, the porous and soft MOFs are prone to react differently depending on the pressure transmitting medium used.

(3) There are several sample dependent factors which have been shown to influence the experimental outcome of non-ambient studies. For example, residual solvent molecules in microporous materials has been shown to inhibit[106] as well as promote[43] phase transitions. It is therefore important to either carefully evacuation, or deliberately solvate starting materials. Furthermore, it is widely accepted that crystallite size can play a major role and affect the thermodynamic landscape of phase transitions[178, 179]. However, such effects only become significant when the crystal size is decreased to the nm scales[180].

(4) Additional difficulties for determining accurate phase boundaries arise from the softness[181] of porous structures. Depending on the available data, there is not always a clear-cut distinction whether the response to variable pressure or temperature is that of a phase transition *sensu stricto*, or that of a highly flexible structure accommodating a large degree of continuous geometric relaxation. For instance, the low-temperature transition in ZIF-4 was structurally described as a symmetry preserving continuous volume contraction[106]. Yet it may be classified as a discontinuous phase transition given the fact that it is accompanied by an exothermic signal found in DSC measurements. A combination of techniques may therefore be necessary to clearly detect and identify phase boundaries.

(5) Finally, the interpretation of experimentally derived *P-T*-phase diagrams of MOFs requires a clear definition of the scope of phase-stability. High kinetic barriers can extend

the apparent stability of some phases indefinitely, or prevent the formation of certain phases altogether, as discussed in point (1). This is exemplified very well indeed by the behaviour of ZIF-4, which is, for a start, only metastable at ambient conditions. The intricate network of ZIF-4 is difficult to recrystallise, i.e. transform reconstructively, due to the bulky and rigid organic molecules present in its structure. As a result, ZIF-4 is metastable up to approximately 250 °C[99]. Above this temperature, instead of transforming to the most stable crystalline conformation, the system adopts an energetically intermediate amorphous state[42, 176]. At higher temperature still, when a reconstructive transition is kinetically possible, ZIF-4 recrystallises to ZIF-zni. However, ZIF-zni only represents the thermodynamically stable phase above 360 °C, despite the fact that it is recoverable to ambient conditions[109]. The thermodynamically most stable phase between ambient-T and the formation of ZIF-zni, ZIF-coi[109], is never observed. As a consequence of these kinetic controls, the outcome of a P-T phase diagram study in strongly associated systems like MOFs will depend heavily on the P-T paths taken during the experiment.

With regard to the P-T diagrams of ZIF-4 here, it is, for example, unclear whether the transformation of ZIF-4 to the iso-topological ZIF-4-cp-III reflects a global energy minimisation. The known competing phase, β-ZIF-zni, has an almost identical density, and a potential high-P polymorph of ZIF-coi is also likely to exist, but has not yet been described. Furthermore, the onsets of crystallisations of the ZIF-hPT-I and ZIF-hPT-II phases are unlikely to reflect a transition dictated only by a favourable change in free energy. It is more likely that these transitions mark the overcoming of thermal activation barriers for recrystallisation. On the other hand, any of the crystalline-amorphous boundaries, for both ZIF-4 and ZIF-62, depend on the rates of heating and pressurisation. In conclusion, the phase diagrams presented in here are technically not thermodynamic phase diagrams *sensu stricto*, but indications of phase behaviour under a certain set of conditions.

4.6 Conclusion

The effect of simultaneous compression and heating ZIF-62 and ZIF-4 has been investigated *in-situ* using optical microscopy, Raman spectroscopy, and powder X-ray diffraction. These extreme conditions results in a broad range of phase transitions: Crystalline–crystalline, crystalline–solid-amorphous, crystalline–liquid, solid-amorphous–solid-amorphous, and solid-amorphous–liquid. Phase boundaries for these transitions have been approximated, based both on direct observation, as well as by inferring behaviour from thermodynamic

considerations. The two resulting *P-T* phase diagrams are the first of their kind for any materials in the family of metal-organic frameworks.

The main findings for **ZIF-62** include the determination of its melting curve, and the definition of stability fields of crystalline, pressure-amorphised, and temperature-amorphised phases in pressure-temperature-space. The melting at simultaneous high-pressure and high-temperature follows a negative Clapeyron slope, with decreasing melting temperature upon increasing pressure. This is characteristic for a low-density solid phase which melts to a liquid of higher density. Aside from the fundamental interest in negative Clapeyron slope melting behaviour displayed here, reducing the melting temperature is an important engineering objective in developing new MOF glasses. The lowering of the melting temperature at high-pressure opens a route to previously unattainable synthesis of a wide range of amorphous, liquid, and melt-quenched MOF states, by avoiding decomposition upon heating at ambient pressure.

The pressure-temperature study of **ZIF-4** reveals four previously unknown $Zn(Im)_2$ polymorphs. The crystal structures of two extremely pressure-, and temperature-, resistant phases with a cag- and double-interpenetrated diamondoid-topology, respectively, were solved from powder XRD data. The overall pressure-temperature behaviour of ZIF-4 is strikingly different from the closely related ZIF-62, which demonstrates an impressive influence of slight chemical tuning on structural stability and kinetic controls on phase transition in MOFs.

Finally, the study of MOFs under simultaneous high-*P* and -*T* ultimately links polymer chemistry with mineralogy. Tools which are typically used for non-ambient studies in mineral sciences have been adapted in the MOF field, which provides a compelling new perspective on MOFs, and draws parallels between their rich phase transition behaviour and those of classical inorganic solids such as SiO_2.

Chapter 5

Sintering monolithic structures of ZIF-4

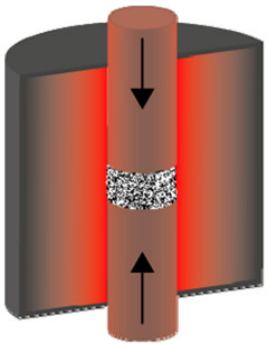

The consolidation of loose MOF powders into mechanically robust bulk parts is an important step towards the large-scale employment of MOF materials in applications. The main challenge with any such process is to avoid the destruction of the fragile crystalline framework upon consolidation. This chapter reports the first use of a pressure-assisted sintering technique on metal-organic framework powders, which allows for the fast production of monoliths based on fully crystalline ZIF-4, alongside other polymorphic phases. Moreover, it is shown how these sintered materials comprises a large, interconnected macroporosity which theoretically provides, compared to the initial powder, an almost unimpaired interface for gas–solid or liquid–solid interaction. These results provide a proof-of-concept for a novel route to manufacture a diverse range of monolithic MOF objects.

5.1 Background

5.1.1 Powder versus Monoliths

MOF synthesis most commonly yields material in form of poly-crystalline powders. Whilst providing high surface area, fine powders are difficult to handle in industrial settings, such as pressure-, temperature-, or vacuum-swing adsorption systems. Powders can clog reactors and pipes, and cause pressure drops in columns due to compaction. Furthermore, high gravimetric and volumetric gas uptake capacities for storage applications are only achievable with densely

packed systems[68]. Ideally, manufactured objects made of MOFs should have hierarchical pore structures that allow efficient through-flow and sufficient crystal surface exposure. Suitable processes for converting functional MOF powders into usable monolithic forms are thus crucial for the practical deployment of MOF-based gas handling technology[182]. Table 5.1 lists the most prevalent techniques reported in literature for processing loose powder into monolithic structures. The use of a binder adds mechanical integrity to the intermediate or final product but is usually associated with the reduction of accessible surface area and pore blockage. Binder-free mechanical densification on the other hand suffers from rather poor mechanical stability of the products.

In contrast, recent advances in the field of amorphous MOFs extend the range of potential applications of these materials to non-porous materials. For example, amorphisation of MOFs has been shown to improve the retention of previously adsorbed harmful substances[58, 60], as well as to significantly increase proton conductivity[171]. Furthermore, quenching of molten MOFs has been reported to result in optically transparent materials with unique mechanical properties[53]. Melt-quenched bulk parts can be manufactured by heat treatment of previously sintered, fully densified and homogeneous compacts[183]. Given the high viscosity of MOF melts, the retention of the shape upon melting of an initially monolithic structure can be envisaged.

5.1.2 Sintering

Sintering, i.e. the fusion of initially loose particles by heating below the material's melting temperature, is a consolidation process that has not yet been explored in the field of MOF engineering. During sintering, loose particles are fused together at elevated temperatures by atomic diffusion across particle boundaries. This process is driven by the tendency to minimise the surface and interface energies of adjacent grains. The required temperatures are usually around two thirds of a materials melting temperature. Sintering is a well established method in the ceramic and metallurgic industries. The advantages of sintering in conventional applications include net-shaped products and controllable porosity. Two steps are required in its simplest form: (1) formation of a "green body" by pressing powder into a mould and (2) heat treatment to fuse the particles together. As a further development, pressure-assisted sintering combines these two steps in one. Pressure assistance has been shown to lower the required sintering temperatures of certain ceramics and metals [184].

Here, pressure-assisted sintering of MOFs is explored by the field-assisted sintering technique (FAST). In FAST sintering, also referred to as Spark Plasma Sintering (SPS), the

sample is uniaxially compressed by punches and a die which are both made of high-strength graphite (Figure 5.1). These graphite pressing tools simultaneously act as electrodes for a pulsed direct current which generates resistive heat. Depending on the electrical conductivity of the material to be sintered, heat is also generated internally in the contained powder compact. This sintering technique is well-established and commercially available, and allows for industrial scale-up of the process[185].

The SPS technique has already proven useful for the fabrication of monoliths from zeolites. For example, silicalite-1 and ZSM-5 zeolite powders have been compacted to macroporous bulk parts with unimpaired crystallinity[186]. Gas adsorption measurements revealed that the microporosity of the zeolite material was almost entirely preserved. Meanwhile, the zeolite material ZSM-5 was also shown to form a fully densified, transparent glass, using the same technique, but at higher temperatures[187].

ZIF-4 is an ideal model MOF compound to test the usefulness of SPS sintering for manufacture of solid MOF objects due to its relatively high temperature and pressure stability (see Chapter 4). This prototypical ZIF compound has also demonstrated selectivity of paraffin over olefin[103] as an example of its applicability, and it can be produced economically in relatively large quantities[102]. At ambient pressure, ZIF-4 transforms into the X-ray amorphous *a*-ZIF at approximately 270 °C and recrystallises into the dense ZIF-*zni* upon further heating to 350 °C[65]. These transitions are kinetically controlled and therefore take effect over a range of temperatures, depending on the heating rates.

Table 5.1 Summary of previously investigated consolidation processes for MOFs.

Technique	MOF name	Binder	Reference
Mechanical densification	MOF-177	-	[68]
Paste extrusion and heating	MIL-101 (Cr)	Bentonite/Water	[188]
Gel formation	HKUST-1	Acetonitrile	[189]
Dispersion-evaporation	ZIF-8	-	[104]
3D-printing	MOF-74(Ni)	Bentonite/Polyvinyl	[190]
Centrifugal granulation	UiO-66	Sucrose	[191]
Crystallisation on substrate/template	MOF-74(Ni)	-	[192]

5.2 Methods

ZIF-4 powder was synthesised via a solvothermal route as described in Chapter 2. For one batch, 160 ml of dimethylformamide (DMF), 2.4 g zinc nitrate hexahydrate ($Zn(NO_3)_2\,6\,H_2O$),

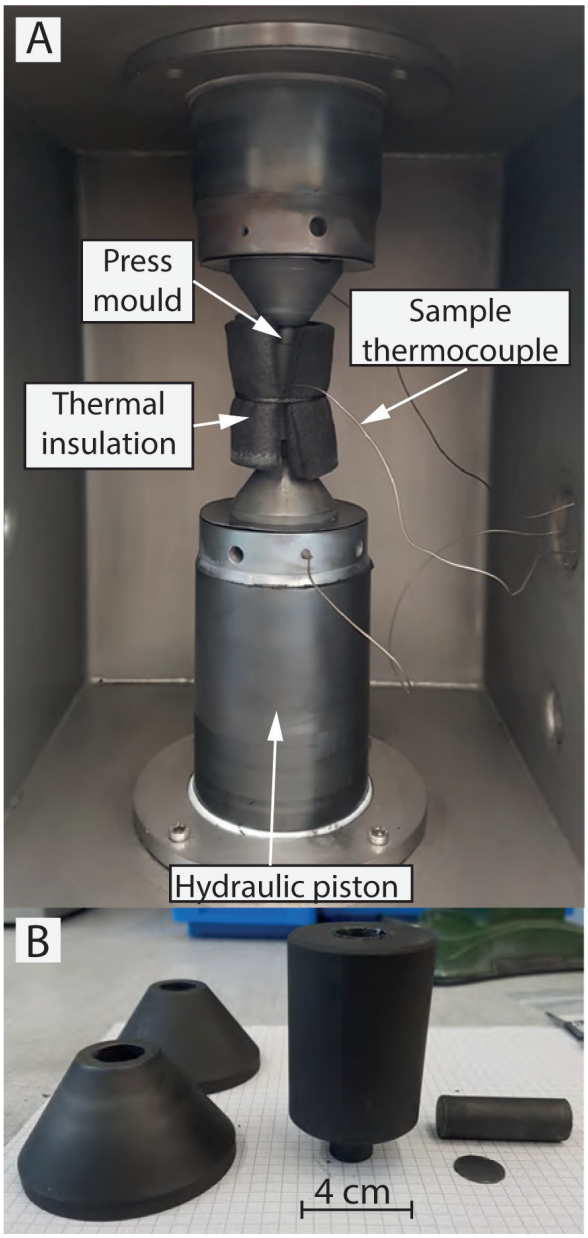

Figure 5.1 (A) Processing chamber of the FAST sintering facility. (B) Graphite pressing tools.

and 1.8 g of imidazole (Im) were mixed and filled in a glass jar with temperature resistant screw lid. The solution was held at 140 °C for 96 h. Precipitate ZIF-4 crystals were filtered from the liquid. For solvent exchange, fresh, DMF-containing ZIF-4 was immersed in dichloromethane (DCM) for 48 h, while being stirred gently. The DCM was replaced after 24 h with fresh DCM. Solvent exchanged DCM-containing ZIF-4 was desolvated at 140 °C for 48 h under vacuum (approximately 0.1 mbar). Complete desolvation was confirmed by Raman spectroscopy. The particle size distribution of the obtained pure ZIF-4 powder was measured using a Beckman Coulter LS-13-320 laser diffraction particle size analyser in suspension mode.

The sintering process was performed under vacuum on a HP-D 10 SPS facility, FCT System GmbH, Germany. Powder samples were weighed (*ca.* 2 g) and filled into the graphite dies. A type-K thermocouple was inserted centrally in a hole in the wall of the die. The process chamber was evacuated. The temperature was raised at a rate of $50\,^{\circ}\mathrm{C\,min^{-1}}$ by resistive heat generated from passing a pulsed direct current (max. 0.35 kA, 4.65 V) through the graphite parts. After 2 minutes dwell time, the samples were cooled at approximately $-50\,^{\circ}\mathrm{C\,min^{-1}}$.

Fragments of the bulk samples were embedded in epoxy resin. The surfaces were polished with 0.25 µm water-based diamond suspensions and carbon coated. Back-scattered electron images were acquired on a FEI Qemscan Quanta650F operated at 10 kV, at a working distance of 13 mm.

Room-temperature powder X-ray diffraction (PXRD) data were collected using a Bruker-AXS D8 diffractometer using CuKα radiation and a LynxEye position-sensitive detector in Bragg-Brentano geometry on a crushed portion of the sintered material. Temperature-dependent powder diffraction data was collected on the same machine equipped with a MRI radiation-heating stage in air. Pure silicon powder was mixed with ZIF-4 and used as an internal standard for sample height displacement corrections. Rietveld fitting of diffraction patterns based on a ZIF-4 structure model from literature was performed using TOPAS (V6). Variable-temperature powder XRD data sets were fitted parametrically. First, only the silicon peaks were fitted, refining individual sample displacements with fixed T-dependent standard lattice parameters. Subsequently, ZIF-4 and ZIF-*zni* were fitted with fixed specimen displacements based on published structural models[34, 108]

Skeletal densities were measured by He-pycnometry using a Micromeritics Accupyc 1340. The typical mass used was 0.3 g. The values listed in Table 5.2 are the mean and standard deviation from a cycle of 10 measurements. The bulk density of the macro-porous sample C was determined from its bulk volume and weight. Thermo-mechanical analysis

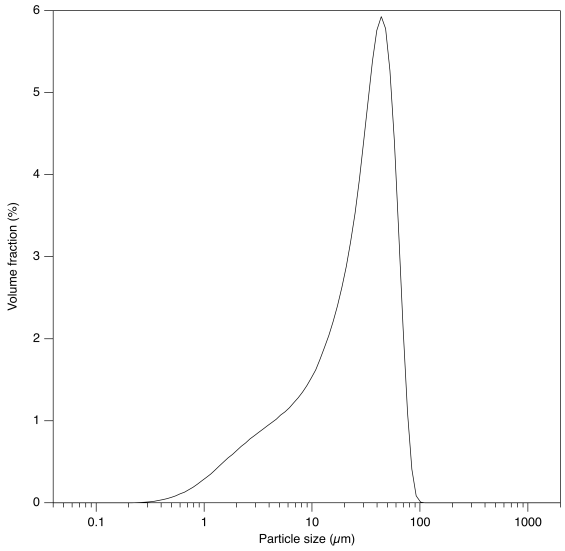

Figure 5.2 Particle size distribution of starting powder measured by Laser diffraction.

was performed using TMA Q400 system (TA instruments) at a heating rate of 5 °C min^{-1} under 0.05 N static force in the temperature range from 20 °C to 550 °C. Nano-indentation experiments were performed using a MTS Nano-indenter with a Berkovich diamond tip of 100 nm radius. Compression tests were carried out on a Tinius Olsen H5KS Benchtop Tester. X-ray micro-tomography images were acquired on a Bruker Skyscan 1272 Micro-CT system. The resulting projections were processed into 3D data sets using a full cone beam Feldkamp reconstruction algorithm with NRecon software (Bruker).

5.3 Results and discussion

The starting powder was confirmed to be pure, desolvated, crystalline ZIF-4, with a particle-size distribution shown in Figure 5.2. Monoliths of all three polymorphic phases have been manufactured (Figure 5.3) by controlling the sintering conditions as set out in Table 5.2 and . Powder XRD patterns are shown in Figure 5.4.

Sample A consists of pure, crystalline ZIF-4. The interconnected macroporosity amounts to 40-45% of the total volume, as calculated from micro-computed tomography (micro-CT) data (Figure 5.5, and is confirmed by a comparison of the helium pycnometric skeletal density with the bulk density. This porosity is the result of a grain-supported microstructure and is thus controlled by the particle size of the starting powder. Consequently, milling, fractionation, or controlled crystal growth of the initial powder materials are all mechanisms which may act to result in the specific pore characteristics. Furthermore, this microstructural

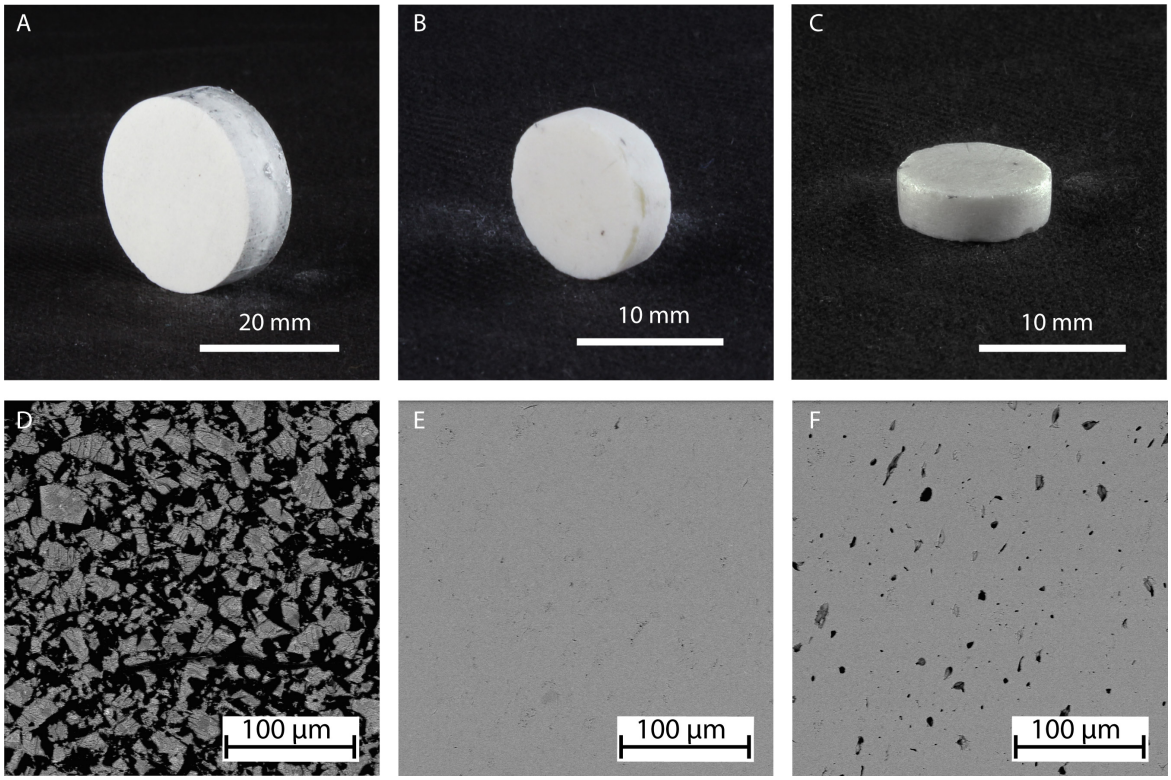

Figure 5.3 Photographs and SEM backscattered electron images of sintered ZIF-4 monoliths. (A & D) Crystalline ZIF-4 (B & E) amorphous ZIF (C & F) recrystallised ZIF-zni. Sample B: Collapse of the crystallinity and softening of the grains supporting the originally highly porous microstructure lead to an almost fully densified microstructure. Sample C: recrystallization to ZIF-*zni*from amorphous a-ZIF entails a density increase, i.e. volume decrease, that could be responsible for the formation of isolated porosity (black spots).

Table 5.2 Sintering Conditions and Bulk Material Properties of Sintered ZIF-4 Powders

	Phase	T (°C)	P (MPa)	α ($10 \times 10^{-6}\,K^{-1}$)	skeletal density ($g\,cm^{-3}$)	envelope density ($g\,cm^{-3}$)
A	ZIF-4	250	10	14.2(1)[a]	1.52(1)	0.84(1)
B	a-ZIF	300	50	30.3(1)[b]		1.58(1)
C	ZIF-*zni*	430	50	8.5(1)[c], 4.3(1)[d]		1.55(1)

[a]30–250 °C, [b]30–200 °C, [c]30–350 °C, [d]350–480 °C

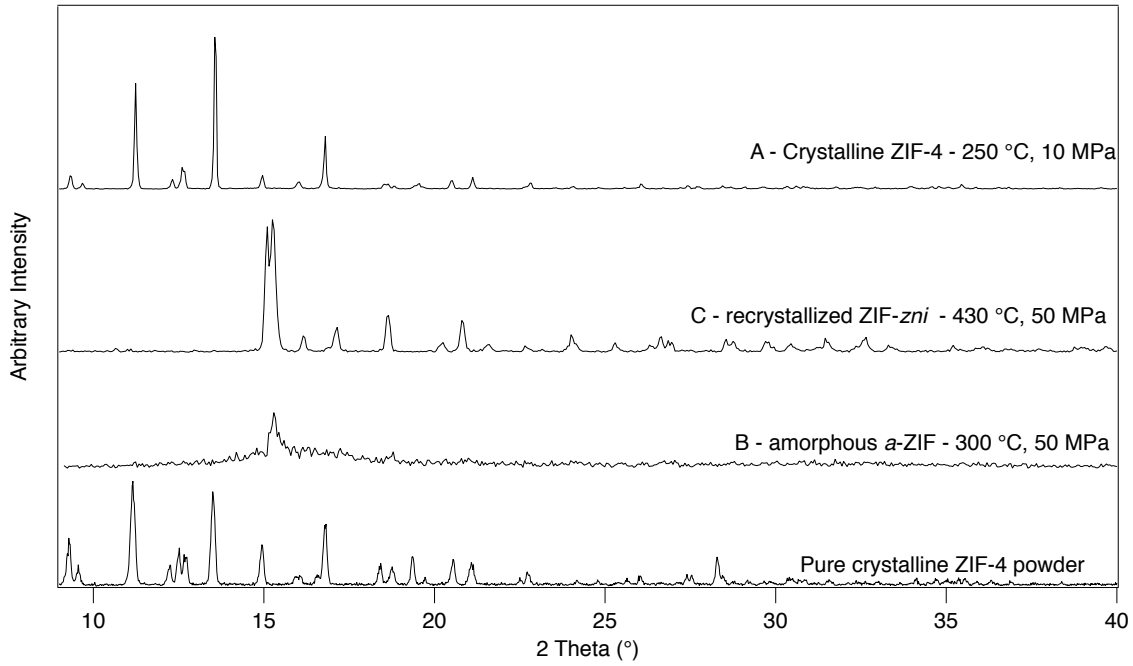

Figure 5.4 Powder X-ray diffraction patterns from crushed portions of sintered monoliths for phase identification and pure ZIF-4 powder.

control, given by the characteristics of the starting material, also allows for the adjustment of bulk mechanical properties.

Sample B and **Sample C** consist of *a*-ZIF and fully recrystallised ZIF-*zni*, respectively. The microstructure of these glass-ceramic-like materials is relatively dense, with only a small fraction of isolated porosity of the recrystallised ZIF-*zni*. This is probably due to the higher density of ZIF-*zni* compared to *a*-ZIF.

Figure 5.6a shows a linear thermal expansion of the manufactured monoliths from thermo-mechanical analysis (TMA). Bulk coefficients of thermal expansion (CTEs) across the appropriate temperature ranges are listed in Table 5.2. These bulk CTEs are linear and isotropic and represent the sum of randomly oriented anisotropic domains. By using TMA, it was also possible to determine the CTE of amorphous *a*-ZIF, for which XRD methods fail. CTEs based on unit cell dimensions measured by variable-temperature powder XRD of crystalline ZIF-4 and ZIF-*zni* are given in Figure 5.7 for comparison. Interestingly, the thermal expansion of the crystalline lattice is strongly anisotropic. Both ZIF-4 and ZIF-*zni* show negative thermal expansion in at least one crystallographic direction. Despite this, however, the resulting overall volume thermal expansion, as measured by XRD, is still positive.

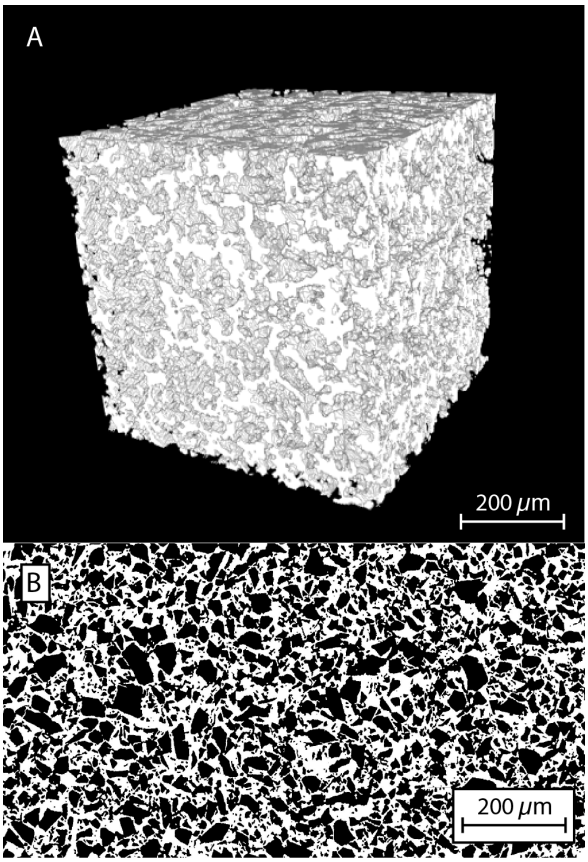

Figure 5.5 Two- and three-dimensional imaging of a highly porous monolith (sample A, 250 °C, 10 MPa) consisting of pure, crystalline ZIF-4. Top: X-ray micro-CT. Bottom: Threshold scanning electron microscopy–backscattered electron (SEM–BSE) image of polished surfaces. White represents pore space. The scale bar is the same for both images.

Figure 5.6b shows mechanical test curves from compressive strength as well as the results from nano-indentation measurements for all three samples. Elastic moduli and hardness values are systematically lower compared to reported nano-indentation values[42]. This can be interpreted as the response of a softer grain support: the individually probed crystals are embedded in a weaker medium compared to the more ideal setting of epoxy-embedded single crystals. This effect is most pronounced in the porous structure of sample A. Additionally, uniaxial compression during sintering may have affected the mechanical integrity of the crystallites.

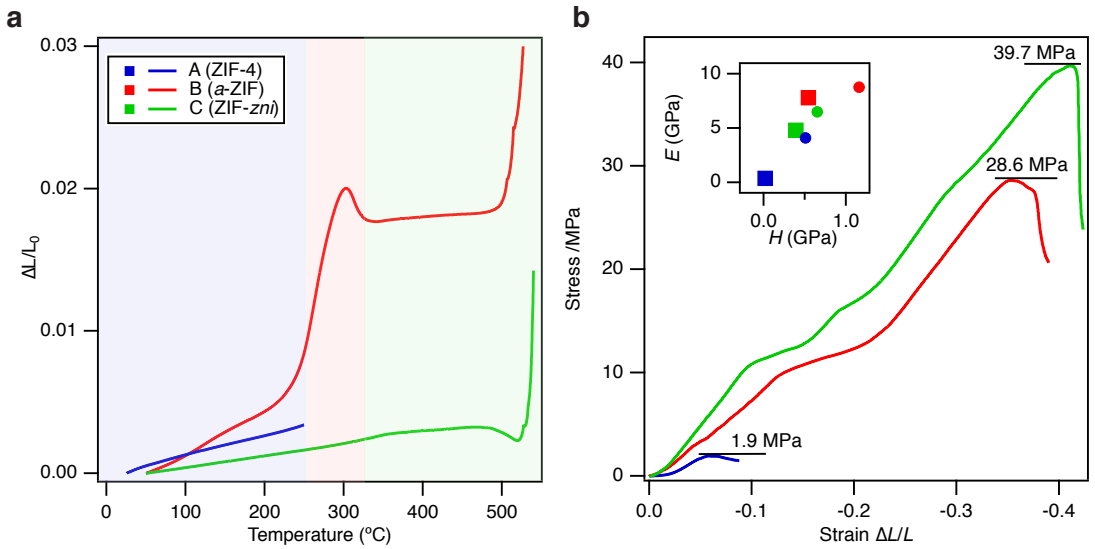

Figure 5.6 Thermo-mechanical characteristics of sintered monoliths of ZIF-4, *a*-ZIF, and ZIF-*zni*. a) Linear thermal bulk expansion from TMA measurements. ZIF-4 is only shown in its stability region. Recrystallization of *a*-ZIF to ZIF-*zni* results in strong expansion and non-monotonic behaviour. b) Stress versus strain plot of the data from compressive testing of monoliths of all three phases. Inset: Elastic moduli versus hardness values from nano-indentation measurements (squares, our data; circles, from literature[42]; error bars are smaller than the symbols).

Conventionally, micro-porosity data from BET adsorption measurements serves as a measure of adsorption performance of a MOF in the context of potential applications [193]. However, both the ZIF-4 starting powder and the sintered monoliths showed negligible porosity from such measurements. This is in contrast to a literature report [72]. A likely reason for this discrepancy may be due to the fact that ZIF-4 undergoes a porous- to dense phase transition upon cooling to 120 K [106]. Since N_2 adsorption is measured at 77 K, it is no surprise that ZIF-4 shows low microporosity at the low temperature of measurement. The fact that data reported in literature show the opposite trend can be explained by the presence

of residual DMF molecules, which was demonstrated (in the same study) to hinder pore closure.

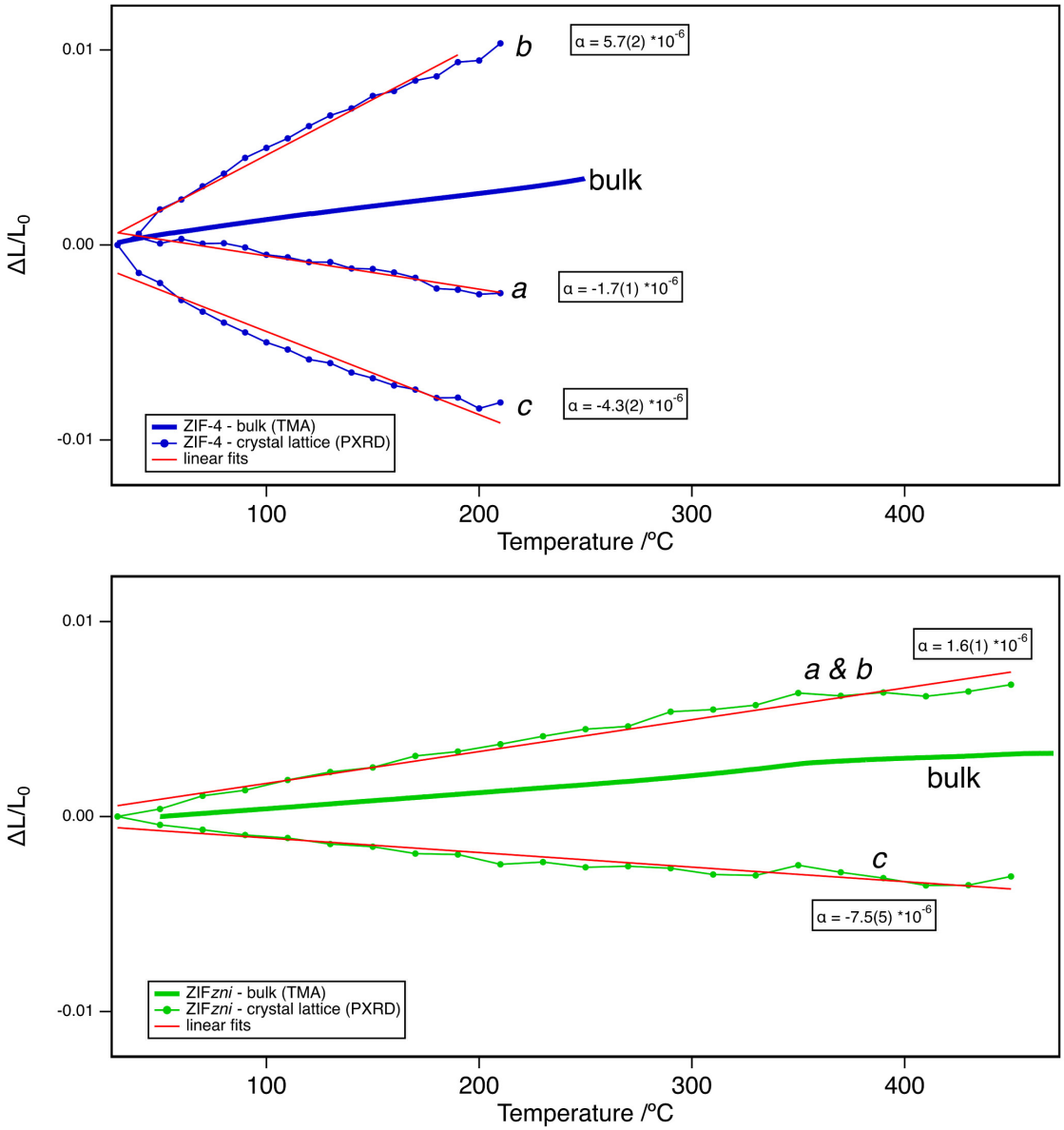

Figure 5.7 Temperature dependent unit cell dimensions (XRD)and isotropic bulk expansion (TMA) of ZIF-4 (top) and ZIF-*zni* (bottom). Thermal expansion coefficients α are derived from the slope of the linear fits in red lines.

5.4 Conclusion

Surprisingly, the use of thermal sintering, a long-established technique in most other material classes, has not been considered for the fabrication of MOF bulk parts. In this Chapter, it is shown for the first time that sintering is indeed suitable for manufacturing MOF objects. More specifically, Spark Plasma Sintering, a pressure-assisted sintering process based on resistively-heated pressing tools, was used to transform initially loose, crystalline ZIF-4 powder into mechanically robust bulk parts. The constituent phase of these parts, i.e. the specific polymorphic form of ZIF-4, could be targeted by adjustment of the pressure and the temperature applied during the sintering process. The three materials thus produced as bulk parts include crystalline ZIF-4, amorphous *a*-ZIF, and recrystallised ZIF-*zni*. Alongside this control over the basic crystal structure of the material, the processing parameters have also been shown to control the three-dimensional micro-structure of the monoliths, and consequently their mechanical properties. Importantly, the monolith composed of crystalline ZIF-4 shows a large, interconnected macroporosity of almost 50 volume-%. This macroporosity, together with the unimpaired microporosity of the ZIF, results in a material with hierarchical porosity that provides a useful interface for gas–solid or liquid–solid interaction.

Furthermore, fully densified monoliths have also been obtained based on amorphous *a*-ZIF and recrystallised ZIF-zni. Both materials show a much higher mechanical strength compared to the macro-porous ZIF-4 monolith. These materials could prove extremely useful as intermediate steps in the production of melt-quenched ZIF glasses: the SPS processing serves as a quick net-shape to near-net-shape production method, while reheating of such parts above their melting temperature can transform them into optically transparent glasses.

Chapter 6

X-ray radiation induced amorphisation of ZIFs

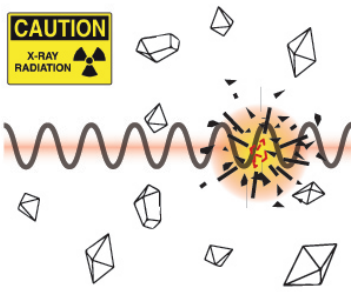

X-ray radiation is known to be capable of inducing structural changes and disorder in a wide variety of materials. With one reported exception[194], MOFs do not generally appear to be prone to such X-ray radiation damage. Whether this reflects the true characteristics of this class of materials or simply reflects a lack of reporting or investigation is unclear. In this chapter it is shown how synchrotron X-ray radiation is capable, under certain conditions, of amorphising the three metal-organic frameworks ZIF-4, ZIF-62, and ZIF-*zni*. This study also includes a kinetic analysis of the transformation processes that result from X-ray irradiation, as well as a description of the structural evolution of the individual ZIF phases, with progressive amorphisation.

6.1 Amorphisation induced by X-rays

Laboratory-based X-ray diffraction (XRD) is a fundamental characterisation technique for crystalline materials, routinely employed by a broad scientific community for structure solution, phase identification, or phase composition analysis. Synchrotron-generated X-rays are often employed when a larger degree of structural detail is required, or a materials response to special, non-ambient environments is of interest. The most important difference between laboratory- and synchrotron-generated X-rays is that the latter is more than a more than a billion times more brilliant in terms of photon flux. Additionally, synchrotron X-rays

may be tuned across a range of energies or wavelength. Compared to a laboratory-based experiments, both factors exponentially increase the dose of ionizing radiation a sample is exposed to at a given time during a measurement at a synchrotron source. This dose of X-rays interacts with the sample material in various ways. Firstly, inelastic Compton scattering transfers some of a photon's energy to a recoiling electron of an atom, resulting in the emittance of a photon of lower energy. Secondly, the photoelectric effect results in all of a photon's energy being absorbed by an atom. As a consequence, due to recombination of the atom's electrons, an inner shell electron and excess energy in form of an Auger electron or X-rays are emitted. Finally, elastic Rayleigh scattering involves no energy exchange between the incident and scattered photons. An overview of X-ray radiation induced amorphisation processes for a variety of materials is presented in the following section in form of a brief literature review.

6.1.1 Biological materials

Amorphisation of biological materials due to irradiation with X-rays is a well known phenomenon in the field of macro-molecular crystallography[195]. The reported symptoms of radiation damage in such crystals include a decrease of diffraction intensity and resolution; decrease in density or increase in unit cell volume and an increase in atomic displacement parameters; reduction of metal centres; and site-specific structural damage[196]. These effects are usually described in terms of primary and secondary processes. Primary processes include the interaction of X-rays with the crystal through the Compton, the photoelectric, and the Auger effect. This results in bond breaking due to photo-oxidation[197]. Emerging free radicals can then cause secondary radiation damage through subsequent chemical reactions. While primary processes depend solely on the absorbed X-ray dose, secondary processes are thermally-activated and thus temperature dependent. This explains why radiation damage in biological material is reduced at cryogenic temperatures[198].

6.1.2 Other materials

Radiation damage has also extensively been observed in small-molecule organic, mineral and inorganic systems. Diffraction intensity reduction over time has previously also been reported for a metal-organic framework[194] with the composition $Ca(H_2O)_6[CaGd(oxydiacetate)_3]_2 \cdot 4\,H_2O$. However, this phenomenon was mentioned only as a side note and no further details or discussion were provided. Silicon semiconductors exposed to synchrotron X-rays have also been observed to suffer diminishing diffraction

intensities as a function of X-ray exposure[199]. This effect was observed for Si on a SiO_2 substrate and is believed to be associated with Frenkel defects forming at the interface when SiO_2 is reduced to Si and free oxygen. Anthracene crystals were shown to develop unspecified crystal defects during exposure to lab-source Cu$K\alpha$ radiation, which adversely affected photo-luminescence properties[200]. The temperature-dependent modulation of the incommensurate structure of $[N(CH_3)_4]_2ZnCl_4$ was shown to build up significant hysteresis due to radiation-damage-induced pinning which arose from exposure to lab-source Mo$K\alpha$ radiation[201]. $Br(2,4,6-trimethyl-pyridine)_2ClO_4$, also a modulated structure, was reported to lose all satellite reflections and diffuse scattering within a few minutes of synchrotron X-ray irradiation[202]. 4,5,10,11 – tetraoxa – 1,2,7,8 – tetraazatricyclo[6.4.1.12,7]tetradecane was observed to significantly lose diffraction intensity and showed increased unit cell volume over four weeks of constant irradiation with lab-source Mo$K\alpha$ radiation[203]. Lastly, a survey of nine materials including an inorganic mixed oxide, three aromatic molecules, four metal-organic complexes, and an antibiotic provided evidence of X-ray radiation induced diffraction intensity decay of up to 40 % on lab-source diffractometers[204].

6.1.3 Other ionising radiation

More recently, in an attempt to engineer top-down patterned amorphous MOFs, scanning electron beams have been used to amorphise ZIF-L. This demonstrated the susceptibility of ZIFs to electron beam damage and the potential of this method to manufacture small scale amorphous device material[205]. While on the one hand radiation-induced amorphisation may be a useful way to synthesise amorphous MOFs, the phenomenon of radiation damage may also be deleterious or problematic. For example, gamma irradiation has been shown to destroy the porous framework of ZIF-8, and others, which is primarily a concern for radio active waste capture applications[206]. Furthermore, radiation self-damage has been widely discussed in inorganic crystalline materials and minerals containing fissile elements, and is frequently seen in uranium or thorium-bearing zircon (zirconium silicate) as well as a number of other minerals[207]. This localised self-damage due to fission decay is termed metamictisation.

6.2 Materials and methods

ZIF-4 and ZIF-62 were synthesised under solvothermal conditions according to the procedure detailed in Chapter 2. ZIF-62 was transferred in a vacuum container to an Ar-atmosphere

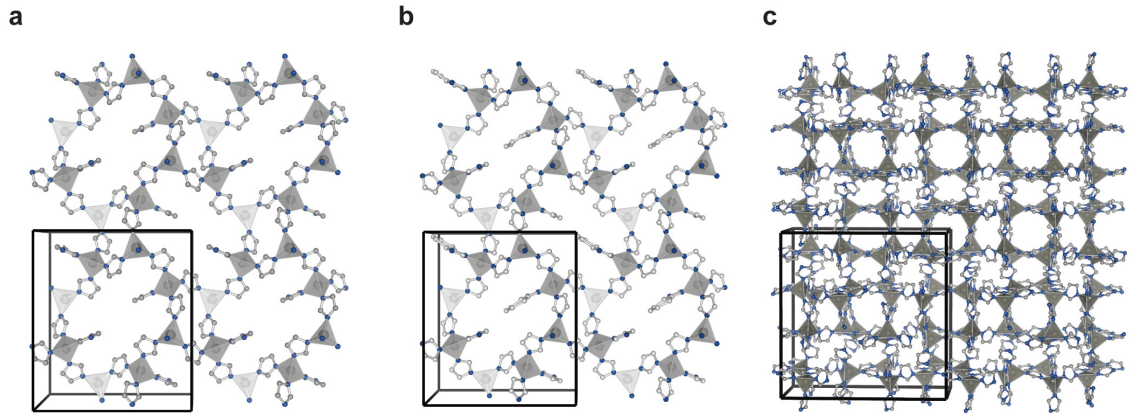

Figure 6.1 Crystal structures of a) ZIF-4 (VEJYUF) viewed perpendicular to the x-axis b) ZIF-62 (GIZJOP) viewed perpendicular the *x*-axis, and c) ZIF-*zni* (IMIDZB) viewed perpendicular to the *z*-axis. Note additional benzimidazole ligands protruding into the cavities of the 8-membered rings in ZIF-62. For clarity, hydrogen atoms are omitted and only the range of fractional coordinates from 0.2 to 0.8 along the projection of view are shown. Unit cells are not to scale.

glovebox (<0.1 ppm O_2 and H_2O) and loaded into 0.3 mm-diameter glass capillaries. The capillaries were sealed with silicone grease and subsequently flame-sealed in air. ZIF-4 was loaded into capillaries in air. ZIF-*zni* was recrystallised from ZIF-4 in air at 400 °C for 1 hour. The crystal structures of the three phases are shown for comparison in Figure 6.1.

X-ray powder diffraction measurements were performed on the Material Science beamline[208], Swiss Light Source, equipped with a Mythen microstrip detector[209]. The wavelength was calibrated using a Si standard from NIST to 0.620 28 Å, corresponding to 19.988 keV and a photon flux of 2×10^{13} photons/second[208]. Given a beam cross-section of 0.84 mm^2 and the approximately illuminated area of the capillary of 0.42 mm^2, the incident photon flux at the sample is estimated to be 2×10^{13} photons/second. The ZIF samples were repeatedly exposed to the unattenuated beam for successive periods of 30 seconds until the diffraction signal was completely, or almost completely, lost. This procedure was repeated for ZIF-4 and ZIF-62 at temperatures of 25 °C, 100 °C, and 200 °C, with temperature controlled using a calibrated hot air blower. The diffraction patterns were sequentially fitted using TOPAS academic[133] to extract unit cell dimensions. Sequential Rietveld refinements were performed using TOPAS-Academic Version 6. The instrumental contribution to peak shapes was separately determined using a NAC ($Na_2Al_2Ca_3F_{14}$) standard. Structural models of ZIF-4, ZIF-62 and ZIF-*zni* were taken from corresponding literature[34, 108]. An initial

refinement against the first measurement of each sequence was performed to refine an aberration correction stemming from the MYTHEN detector. In addition, to match observed peak intensities as close as possible, a spherical harmonic preferred-orientation correction was introduced. These parameters were held fixed from then on, and only a 5th order Chebychev polynomial, the unit cell dimensions, and a Lorentzian contribution to strain-related peak broadening were refined over the 2θ-range from 3° to 9° for ZIF-4 and ZIF-62, and from 2° to 8° for ZIF-*zni*. The fraction of remaining crystallinity over time was extracted by integrating the number of counts over a 2θ-range of 0.7°, covering the well-separated (111) and (002) peaks, after subtracting a linear baseline. The same procedure was used for ZIF-*zni* over a 2θ-range of 0.5°, covering the partly overlapping (400), (112), and (321) peaks. Here it was assumed that the degree of amorphisation can be expressed as the fraction of remaining Bragg diffracting intensity with respect to the initial Bragg intensity.

6.3 Results and discussion

6.3.1 X-ray exposure at ambient temperature

A photograph of a capillary containing pristine (white) and X-ray amorphised (dark section) ZIF-4 is shown in Figure 6.2. The same darkening was observed for ZIF-62 and ZIF-*zni* after beam exposure until complete amorphisation. Diffraction intensities over time for ZIF-4, ZIF-62, and ZIF-*zni* at ambient temperature are shown in Figure 6.3. Given the narrow width of the initial XRD peaks, all three samples appear to be well-crystalline materials. When exposed to the X-ray beam, however, all three samples show complete loss of diffraction intensity from the Bragg peaks, accompanied by significant peak broadening and, in the case of ZIF-4, peak splitting. For the three individual ZIF samples, the volume fraction of amorphous material as a function of time, $x(t)$, measured by the integrated and normalised diffraction intensity, evolved similarly in a sigmoidal fashion, though over significantly different time scales (Figure 6.4). The cumulative exposure times after which only 50 % of the initial diffraction intensity remained were 6 minutes, 14 minutes, and 81 minutes, for ZIF-4, ZIF-62, and ZIF-*zni*, respectively. The same stability trend for this set of ZIFs is reported for their response to high-temperature[45, 105] and mechanical pressure[43, 210]. In agreement with their relative resilience under heat or pressure, the resistance to X-ray induced amorphisation is probably controlled by the mechanical rigidity of the ZIF structure. The accumulation of local defects and the subsequent growth of amorphous domains of higher density than the crystalline matrix provoked structural collapse. The more robust the

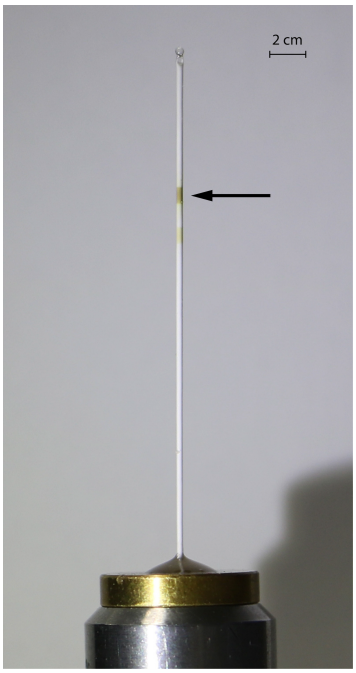

Figure 6.2 Image of the capillary used for synchrotron experiments at the SLS MS-beamline. White material is pristine ZIF-4, while darkened section is where the beam hit the capillary and the X-ray induced amorphisation occurred.

remaining crystalline structure, the greater the amount of local structural damage that has to be accumulated to cause pervasive long-range disorder and loss of coherently diffracting domains.

It is clear that there can be a range of fundamental effects that give rise to radiation damage and subsequent amorphisation (see introduction). Interestingly, the organic linkers remain intact upon amorphisation. This is apparent from the fact that radiation-amorphised ZIF-4 can be recrystallised to ZIF-*zni* upon heating to 400 °C (Figure 6.6). This observation is an indication that the observed amorphisation is likely primarily caused by the effect of photo-oxidation of the Zn centres. This leads to the breakage of Zn–N bonds and subsequently to the collapse of the crystalline framework. More evidence for photo-oxidation can be found in the fact that the susceptibility of the ZIFs to beam-damage appears to depend on the energy of the X-ray beam. This is evident from comparing the present results with those of Chapter 4. The two sets of experiments made use of synchrotron X-rays of 29 keV and 20 keV, respectively, on the same materials. No significant amorphisation was observed as a result of beam exposure at 29 keV. In contrast in this experiment, complete amorphisation was observed within a short time when irradiating with 20 keV X-rays. This can be understood from tabulated[211] X-ray mass energy-absorption coefficients (μ_{en}/ρ) of

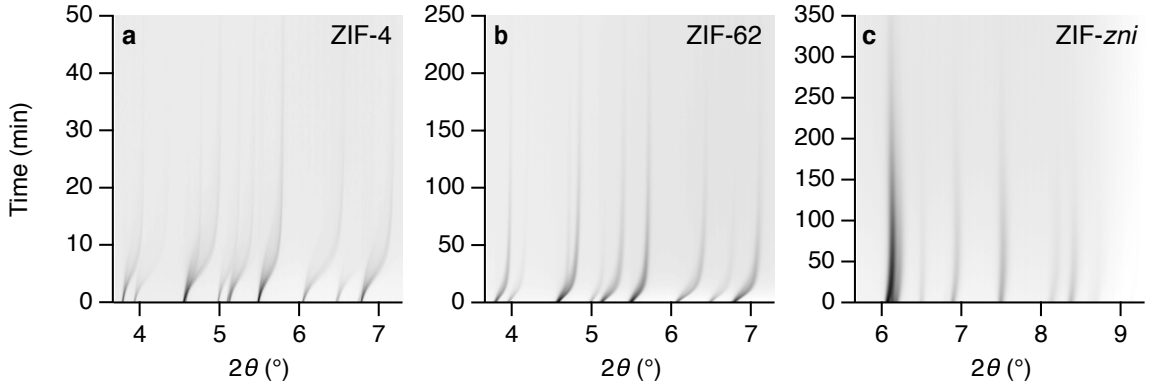

Figure 6.3 X-ray powder diffraction intensities as a function of exposure time measured at ambient temperature. a) ZIF-4, b) ZIF-62, c) ZIF-*zni*, in order of increasing stability of the crystalline structure to the X-ray beam.

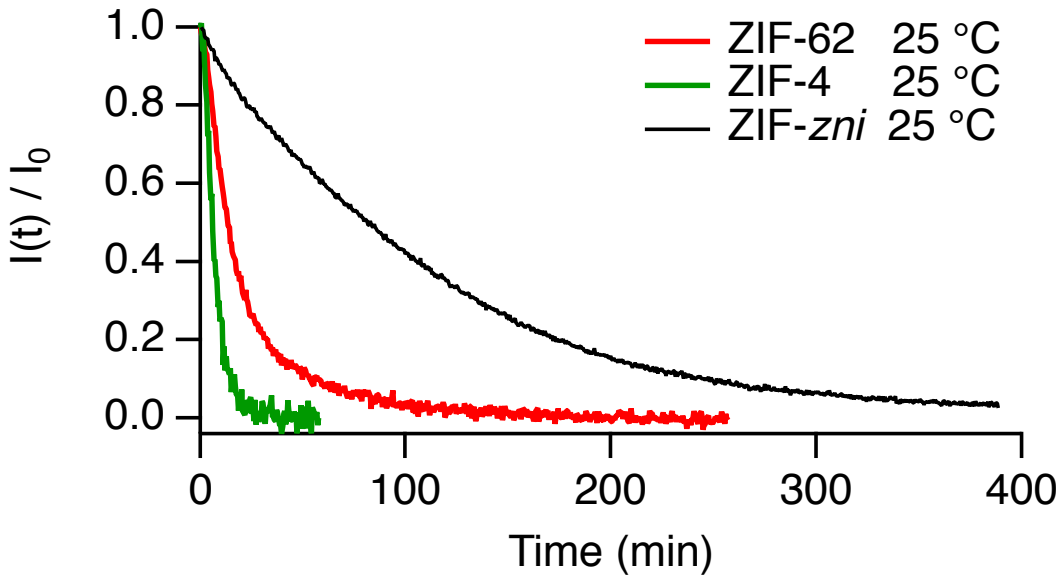

Figure 6.4 Decay of diffraction intensities of ZIFs versus exposure time at 25 °C. Intensities are all normalised to the intensity at t_0.

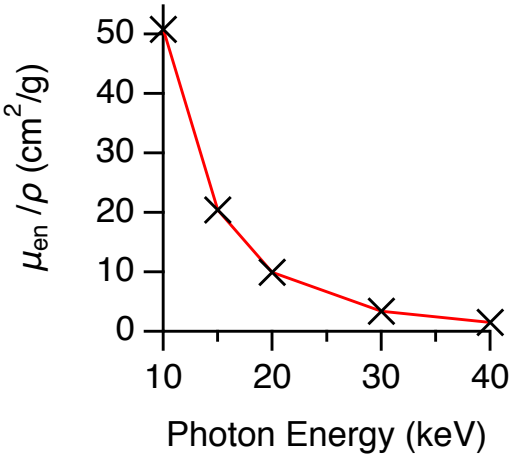

Figure 6.5 Atomic scattering factors for $Zn(Im)_2$ as a function of X-ray energy[211].

the mixtures of the elements in the ZIF samples as a function of beam energy (Figure 6.5). This simple consideration demonstrates an increase of absorbed energy by a factor of three in the experiment at 20 keV compared to the previous experiment at 29 keV.

6.3.2 Kinetic Analysis at variable temperature

An Avrami plot of the fraction of transformed material over time theoretically results in a straight line[212] if (1) the transformation of the bulk material from an initial phase to the product phase corresponds to a random and homogeneous nucleation, and (2) the growth rate of the new phase is constant over time and isotropic in space. In such an ideal case, the Avrami exponent n is defined as the gradient of the Avrami plot. Theoretically, knowledge of the value of n allows for an interpretation of the rate-limiting mechanism of transformation. However, Avrami plots of the time dependence of the amorphous fraction of ZIF-4, ZIF-62, and ZIF-*zni* at ambient temperature do not plot as straight lines (Figure 6.7), as would be expected for an ideal iso-kinetic transformation with constant nucleation and growth rates. Similarly, Avrami plots of the amorphous fraction of ZIF-4 and ZIF-62 at constant elevated temperatures of 100 °C and 200 °C (based on the data in Figure 6.8) also do not plot as straight lines. Instead, in order to evaluate the evolution of the local Avrami exponents over the course of the amorphisation reaction, the Avrami plots of the three ZIFs, at both ambient-, and high-temperatures, were divided into segments of constant intervals on the logarithmic time-axis. These segments were subsequently fitted by straight lines (Figures 6.9–6.11). The Avrami exponents n, which resulted from these segmented linear fits, are shown as a function of the amorphous fraction x in Figure 6.12.

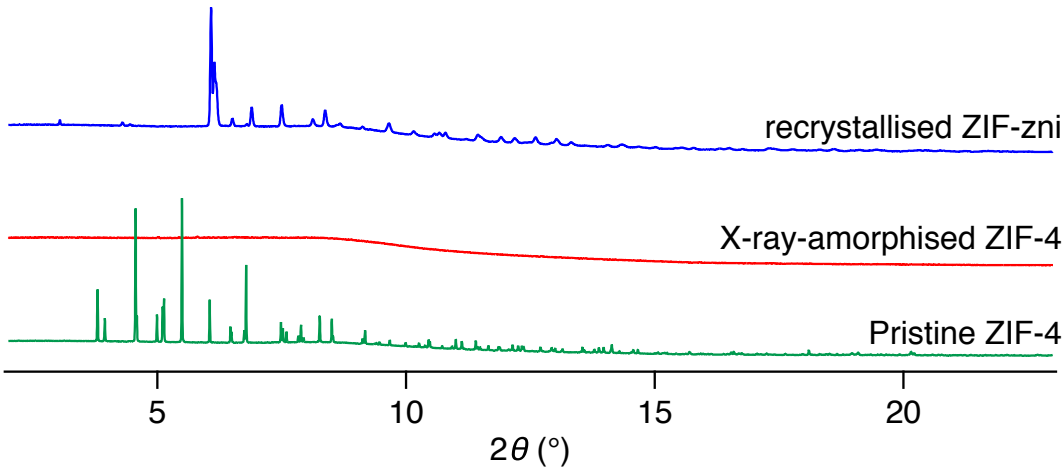

Figure 6.6 Green: Starting material, pristine ZIF-4. Red: Fullly amorphous ZIF-4 after exposure to X-ray beam during 1 h. Blue: Fully recrystallised ZIF-xni from X-ray beam-amorphised material (red) after heating during 1 h at 400 °C.

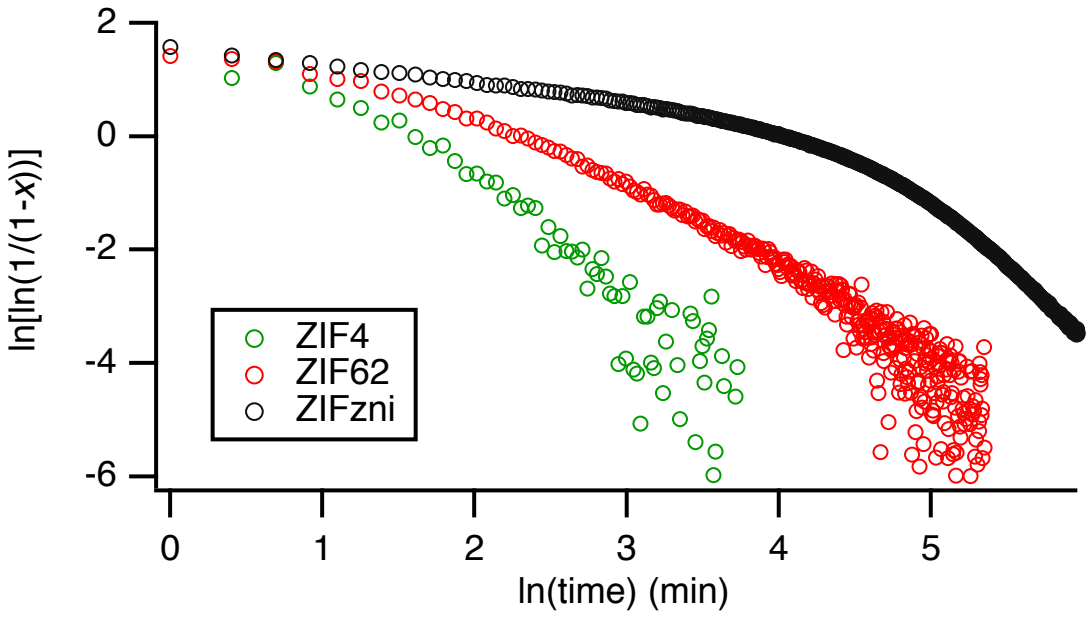

Figure 6.7 Avrami plot of the crystalline–amorphous transition of ZIF-4, ZIF-62, and ZIF-*zni*.

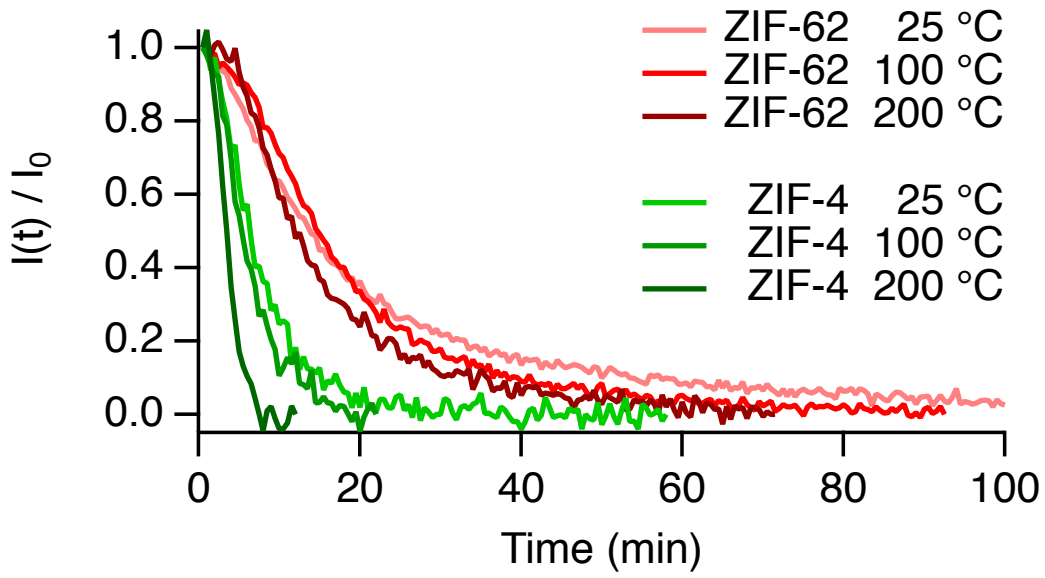

Figure 6.8 Decay of diffraction intensities of ZIF-4 and ZIF-62 versus exposure time at 100 °C and 200 °C. Intensities are all normalised to the intensity at t_0.

Ambient temperature

At ambient temperature (Figure 6.12a), all three ZIFs show continuously increasing Avrami exponents n as a function of x. While ZIF-4 and ZIF-*zni* show an approximately linear increase of n with x, the behaviour of n in ZIF-62 is non-linear. Furthermore, the absolute values of n obtained for the individual ZIF phases also significantly from amongst each other.

Deviations of a transformation from the ideal behaviour assumed by the Avrami equation can arise from several conditions summarised under the three following categories[213]: (1) inhomogeneous nucleation, (2) anisotropic growth , and (3) time-dependent nucleation and size-dependent growth. All these effects can cause variation of the Avrami exponent with time or reaction progression. However, they generally result in a reduction of n with progressing transformation. In contrast, an increases of n with progressing transformation, as observed here, has been reported to be a result of transient nucleation[214]. In this model, which was developed to explain a nucleation and growth transformation, nuclei are initially only formed on grain boundaries. The subsequent growth of these nuclei is confined to two-dimensions. As the grain boundaries saturate, the nucleation spreads to the bulk of the grains, where unobstructed growth in three dimensions becomes possible. As a result, n will increase with time. Meanwhile, in the case of such a transition from nucleation at grain

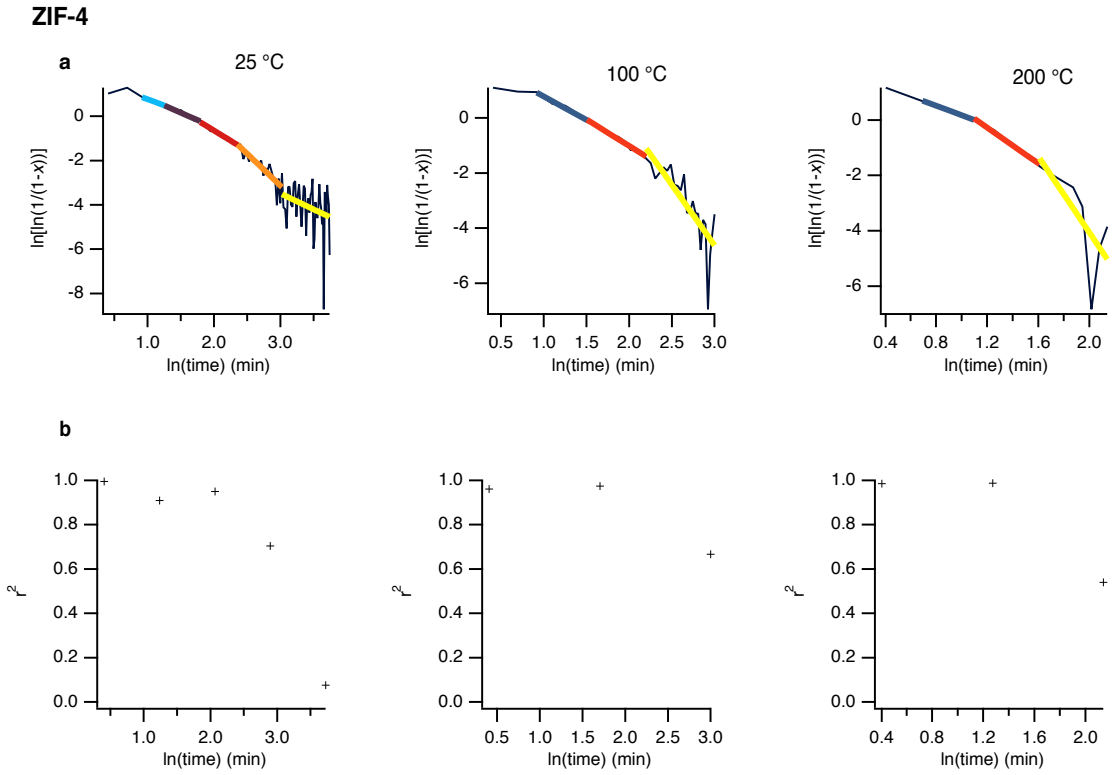

Figure 6.9 a) Avrami plots of the amorphisation process of ZIF-4 at variable temperatures and linear fits to segments of equal length on the logarithmic time-axis in colour b) r^2 values of linear fits.

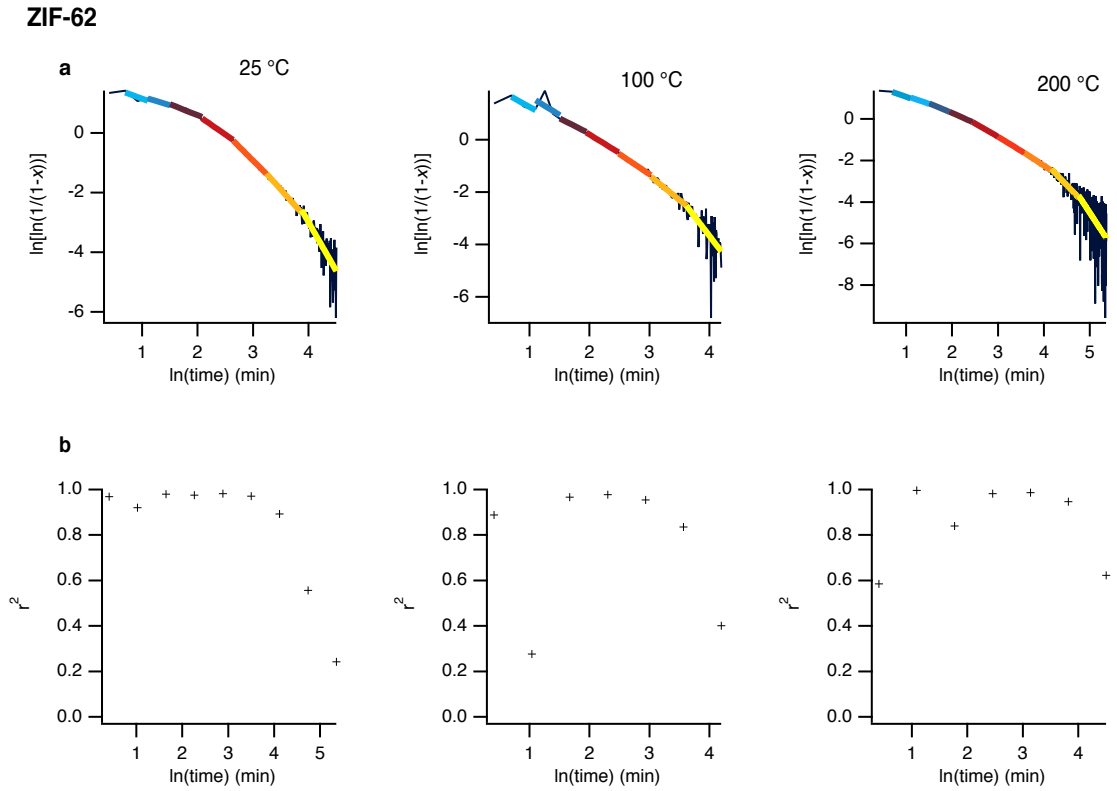

Figure 6.10 a) Avrami plots of the amorphisation process of ZIF-62 at variable temperatures and linear fits to segments of equal length on the logarithmic time-axis in colour b) r^2 values of linear fits.

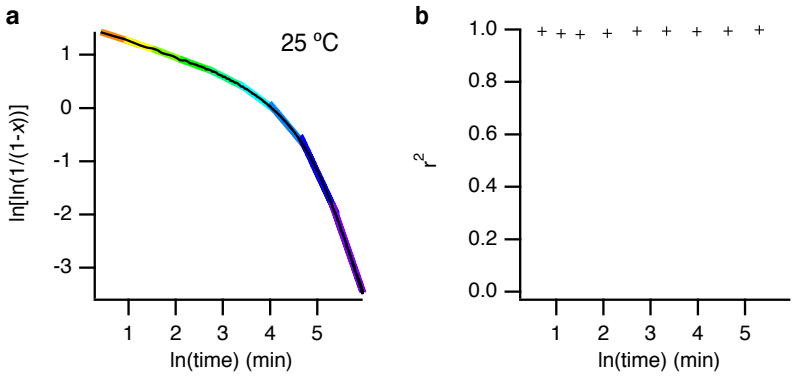

Figure 6.11 a) Avrami plots of the amorphisation process of ZIF-*zni* at 25 °C and linear fits to segments of equal length on the logarithmic time-axis in colour b) r^2 values of linear fits.

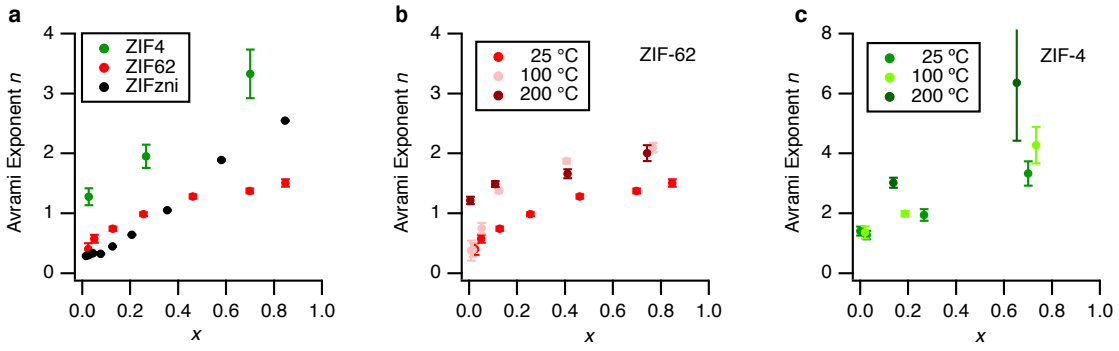

Figure 6.12 The evolution of Avrami exponents with progressive amorphisation x. a) comparison of three different ZIFs at room temperature. b) comparison of ZIF-62 at three different temperature. c) comparison of ZIF-4 at three different temperatures

boundaries to nucleation in the bulk, it is expected that the transformation behaviour would also depend on the initial grain size and grain shape[215].

In summary, all three ZIFs show an overall increasing n with time, which can be explained by a significant inhomogeneity of nucleation and/or anisotropy of growth of the amorphous domains. The effect of this rate limitation changes at a constant rate with time for ZIF-4 and ZIF-*zni*, which results in a linearly increasing n for both ZIF phases. For ZIF-62, this primary effect seems to overlap with a secondary effect, which causes the dampening of the primary effect. It can only be speculated that the disordered, partial imidazolate for benzimidazolate substitution of ZIF-62 is a possible reason for this.

High-temperature

With increasing temperature (25 °C, 100 °C, and 200 °C) the X-ray radiation-induced amorphisation of ZIF-62 and ZIF-4 generally results in a faster amorphisation and an overall increase of the Avrami exponent n with time (Figure 6.8, Figure 6.12b & 6.12c). For **ZIF-4**, n linearly increases with x for all investigated temperatures. Meanwhile, the gradient of n/x also increases linearly with temperature (Figure 6.13). In contrast, for **ZIF-62**, increasing the temperature to 200 °C results in constant increase of n over time. At the intermediate temperature of 100 °C, this accelerating effect is less pronounced and is possibly still kinetically hindered.

At present, the influence of temperature on radiation-induced amorphisation is only qualitatively known. Underlying mechanisms cannot be clearly identified based on the present results. This is partly due to the non-linearity of the Avrami plots, which otherwise

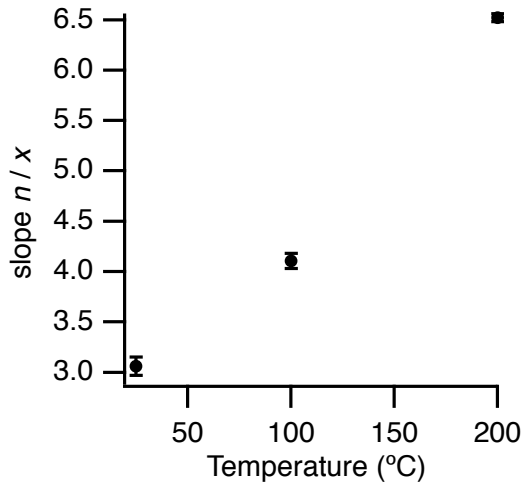

Figure 6.13 The gradient of the Avrami plots of the amorphisation of ZIF-4 (Figure 6.12c) as a function of temperature.

could be used to determine empirical activation energies[75]. Furthermore, the trends with increasing temperatures are different for the two ZIF phases under investigation.

6.3.3 Evolution of unit cell dimensions

The evolution of the unit cell dimension with X-ray exposure time is shown in Figure 6.14. All structures become denser and show a significant decrease in unit cell volume with increasing amorphisation. The volume of ZIF-*zni*, however, recovers and expands again after approximately 100 minutes. The *a* and *b* unit cell parameters of ZIF-4 and ZIF-62 behave in a very similar manner, while the *c* unit cell repeat contracts to a different extent for the two structures. ZIF-*zni* shows very different behaviour with the *a* repeat shrinking in the first 100 minutes and subsequently expanding, and an expanding *c* repeat.

The evolution of the unit cell volume reflects the averaged long-range characteristics of the progressively amorphising bulk material. The monotonous decrease of unit cell volumes in ZIF-4 and ZIF-62, by almost 20 % and 15 % respectively, suggests a well-dispersed nucleation of defects an the growth of amorphous domains of higher density than the initial crystalline structure. This would result in a homogeneous volume collapse of the unit cells hosting these defects, accompanied by increasing micro-strain which is observed as peak broadening. The densification of ZIFs on radiation-induced amorphisation is in contrast to the behaviour of most other crystalline material, for example metamict minerals, which are always of lower density than their crystalline counterparts.

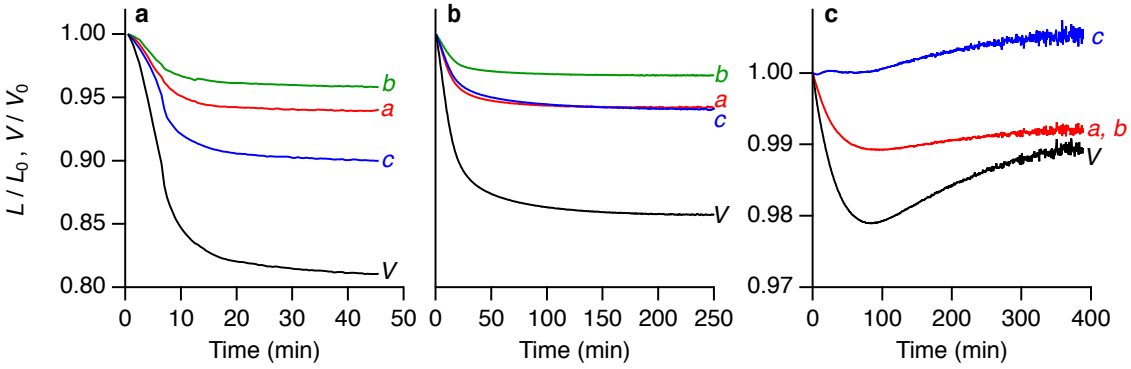

Figure 6.14 Evolution of unit cell dimensions from Rietveld refinements at ambient temperature versus exposure time. Cell lengths and volumes are normalised to the values at t_0. Estimated standard deviation is smaller than symbols. a) ZIF-4 b) ZIF-62 (y-axis same scale as ZIF-4) c) tetragonal ZIF-*zni* (differently scaled *y*-axis).

The difference in unit cell contraction between ZIF-4 and ZIF-62 is mainly controlled by the contraction along the crystallographic *z*-axis. This can be attributed to the presence of bulkier benzimidazolate ligands in ZIF-62 protruding into the main cavities along this direction. A comparable structural stabilisation for ZIF-62 over ZIF-4 has been observed in both thermal- and pressure-induced amorphisation[175].

In contrast, ZIF-*zni* only shows a small degree of volume collapse (of approximately 2 %) followed by an expansion of approximately 1 %. Beam heating can be excluded as the origin of this secondary expansion because, based on measured thermal expansion coefficients[105, 216], in order to expand the volume by 1 %, an unreasonably large temperature increase of approximately 300 °C would be necessary. It can be speculated that this increase might be due to a 'negative-pressure' exerted on the remaining isolated crystalline domains embedded in a pervasive higher density amorphous matrix, similar to anti-glass formation in radiation self-damaged minerals[217]. An analogous effect is not be observed for the porous ZIF-4 and ZIF-62 materials, since it is likely precluded by the speed of complete amorphisation.

6.3.4 Evolution of peak shapes

The peak shape evolution of selected Bragg peaks of ZIF-4, ZIF-62, and ZIF-*zni* is shown in Figure 6.15. The selected peaks for ZIF-4 and ZIF-62 correspond to the (111) and (002) reflections, and they do not overlap with any other peaks. For ZIF-,*zni* the peaks corresponding to (400), (112), and (321) were chosen as they are the relatively strongest peaks. They all should reflect a relatively low influence of micro-strain due to their position

at low 2θ. Yet it is evident that the decrease in intensity is accompanied by significant broadening, which in the case of ZIF-4 results in clear peak splitting. This observation indicates the development of two structural domains with distinct volume contraction over time. The effect is less pronounced in ZIF-62, but nonetheless visible, particularly for the (002) peak. It is for this reason that whole-pattern refinement methods were not deemed adequate to represent the decay of diffraction intensity. Instead, the counts were integrated over the range of these two peaks. The reason for the strong broadening and eventual splitting can be attributed to severe micro-strain due to the collapsing of the low-density crystalline structure to a dense amorphous structure.

[218]

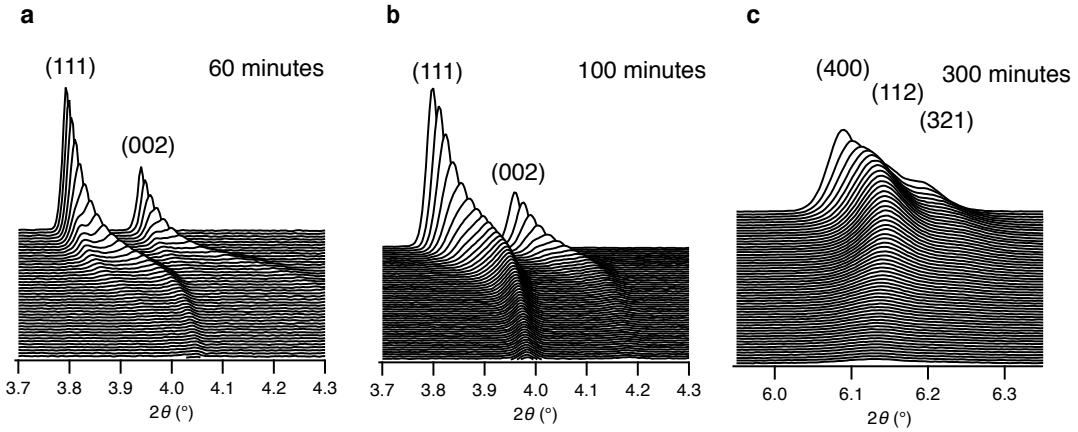

Figure 6.15 Peak shape evolution of a) ZIF-4, b) ZIF-62, and c) ZIF-*zni* during 60 minutes, 100 minutes, and 300 minutes, respectively. Strong anisotropic broadening, and in case of ZIF-4 splitting is visible.

6.4 Conclusions

Synchrotron X-rays were shown to trigger a mechanism that led to the breakdown of both porous and dense crystalline MOFs to amorphous phases. Importantly, amorphisation occurred irrespective of the sample atmosphere (N_2 and air). Meanwhile, the organic linkers were unaffected by the amorphisation, which is consistent with the fact that it is possible to recrystallise radiation-amorphised ZIF-4 to ZIF-*zni* by re-heating. These observations hint at photo-oxidation of Zn and subsequent breakage of Zn–N bonds as the primary process of X-ray beam damage. Furthermore, elevated temperature promoted radiation-induced amorphisation at temperatures below the normal limits of metastability. This points to the presence of a thermally activated, secondary process in the course of amorphisation. It is

also apparent that the choice of beam energy drastically influences the stability of the three ZIF phases under investigation, which can be explained by X-ray mass energy-absorption as a function of beam energy.

Kinetic analysis of the progressive amorphisation by means of Avrami plots revealed that the rate limiting mechanism depends on the fraction of amorphised material. Such non-isokinetic behaviour indicates the possibility of preferred nucleation sites, anisotropic growth of amorphous domains, or time-dependent nucleation and size-dependent growth.

While the underlying mechanism of amorphisation and the kinetic analysis of this process are not conclusive, these results nonetheless have important general implications for X-ray synchrotron studies on metal-organic frameworks. It is necessary to assess the X-ray radiation stability of MOFs prior to the actual experiment in order to rule out the potential for beam damage. This is of particular importance for studies on the stability of a materials when the effect of radiation damage, as shown here, has the same effect as the reaction to an external variable such as temperature or pressure. Furthermore, the findings of this study might also shed light on diverging literature reports on, for example, stability limits at high-temperature – X-ray radiation damage might here be the key to reconciling conflicting experimental results.

Chapter 7

Concluding Remarks

The zeolitic imidazolate frameworks ZIF-4 and ZIF-62 have played a special role in the recent development of metal-organic framework materials. Although it has been shown that they cannot compete with the best-performing MOFs in terms of, for example, gas adsorption capacity, they nevertheless initiated the exploration of novel amorphous, molten, and melt-quenched states in the family of MOFs. Importantly, the chemical compositions of such MOF glasses are identical to their crystalline precursors and they also retain their chemical connectivity. Consequently, these materials are not only of fundamental interest due to their unique glass structures, but they also have promising properties for a range of applications, as discussed in Chapter 1. Understanding the mechanisms which lead to the formation of MOF glasses is integral to understanding their structures, and facilitates their synthesis. This thesis explored a range of external factors that can affect crystalline-to-amorphous transitions, including chemical substitution, the application of pressure and temperature, and exposure to ionising radiation. This chapter summarises and reflects on these findings, as well as making recommendations for how this work could be advanced in future.

7.1 Chemical tuning in the ZIF-4 – ZIF-62 system

Chapter 2 established how high-performance liquid chromatography (HPLC), Raman spectroscopy, and X-ray diffraction techniques can be used for the chemical and structural characterisation of materials from the ZIF-4 – ZIF-62 solid-solution. The HPLC analysis proved to be a particularly suitable technique providing chemical analysis with higher accuracy than the traditionally used NMR measurements. Both Raman spectroscopy and powder X-ray diffraction were shown to be useful for semi-quantitative to quantitative chemical analysis of ZIFs based on a calibration of Raman intensities or unit cell volumes. These three

tools have not routinely been used in MOF research so far, but the ease of their procedure makes them viable options.

Using these techniques, Chapter 3 showed how the continuous chemical variation of the ZIF-4 – ZIF-62 system is accommodated in the crystal structure. This knowledge facilitates the understanding of structure-property relationships which vary as a function of composition. Furthermore, it was explored how the high-temperature behaviour of materials from this solid solution varies as a function of their changing chemical composition. In detail it was found that the thermal stability of the crystalline phases increases systematically by as much as 50 °C with increasing degree of linker substitution. Furthermore, the thermal expansion of the respective endmember compositions also show a substantial variation, ranging from a net zero volume-expansion for ZIF-4 to a positive volume-expansion for ZIF-62. This findings point out the wide-ranging implications of tunable mixed-linker compositions in MOFs.

7.2 ZIFs at high pressure and temperature

Chapter 4 explored how ZIF-4 and ZIF-62 respond to the application of pressure and temperature, as well as simultaneous pressure and temperature. These results, alongside theoretical considerations, were used to construct pressure-temperature phase diagrams of each compound. The main findings were (1) their melting behaviour at high-pressure, (2) the characterization of polymorphic structures, and (3) the definition (or approximation) of phase stability fields:

(1) When ZIF-62 melts at simultaneous high-pressure and high-temperature, the melting curve follows a negative Clapeyron slope – the melting temperature reduces with increasing pressure. Thermal melting at high-pressure, compared to melting at ambient-pressure, thus affords a novel route to the synthesis of MOF liquids and glasses at lower temperatures. This relationship may open a route to previously unattainable synthesis of a wide range of amorphous, liquid, and melt-quenched MOF states, by avoiding their decomposition upon heating at ambient pressure.

(2) Polymorphic phases of the initial ZIFs at high-pressure-temperature conditions include crystalline, pressure-amorphised, temperature-amorphised and liquid states. Importantly, four new crystalline polymorphs of ZIF-4 were discovered. Two of the crystal structures were successfully solved based on powder X-ray diffraction data, while the other two phases could be assigned with plausible unit cells and space groups. Two distinct solid-amorphous phases – one of relatively higher-density formed at

high-pressure, and one of relatively lower-density formed at high-temperature – were delineated by theoretical considerations based on the gradients of the respective phase boundaries. This overall high degree of structural flexibility under the effect of pressure and temperature demonstrates that it is possible to synthesise novel MOF phases under extreme conditions.

(3) Phase boundaries in pressure-temperature-space were drawn according to, both, direct observation of the transformations, and thermodynamic considerations. The general validity of these phase boundaries were discussed in view of the large influence of kinetic controls on phase transitions of such highly polymerised MOF structures. Knowledge of phase boundaries, i.e. phase stability limits, at high-pressure and high-temperature conditions are essential for applications of any material at non-ambient conditions.

Finally, tools which are mainly used for non-ambient studies in mineral sciences were adapted for the MOF field. This provides a compelling new perspective on MOFs and allows parallels to be drawn between their rich phase transition behaviour, and that of classical inorganic solids such as SiO_2. Thus the innovative use of these techniques plays an important role in diversifying the field of MOF research.

7.3 Pressure-assisted sintering of ZIF-4

Chapter 5 showed that Spark Plasma Sintering, a pressure-assisted sintering technique, is an effective method for the fabrication of monolithic structures from loose ZIF powders. The constituent phase of such bulk parts could be targeted by adjusting the pressure and temperature conditions at which the powders were sintered. The resulting monoliths were tested for their mechanical properties including density, compressive strength, hardness, and elasticity. These results are interesting for several potential applications:

(1) The macroporous monoliths consisting of crystalline ZIF-4 show a hierarchical, interconnected porosity. The large accessible surface area is promising for gas- or liquid-adsorption. While ZIF-4 might not be the ideal MOF for such applications due to its limited microporosity, these experiments nevertheless provide a proof-of-concept.

(2) The process of simultaneous densification and amorphisation at high temperature and pressure could be exploited as a technique to irreversibly trap previously adsorbed, harmful guest species.

(3) The fully densified monoliths which consist of amorphous *a*-ZIF and recrystallised ZIF-*zni* are ceramic-like materials with distinct thermo-mechanical properties. Given the high viscosity of ZIF melts, such sintered parts would retain their shapes when they are reheated to above their melting temperatures. Theoretically, such a process could thus serve to produce melt-quenched bulk parts.

7.4 X-ray radiation induced amorphisation

Chapter 6 demonstrated that exposure to synchrotron X-ray radiation, under certain conditions, can result in the amorphisation of ZIF-4, ZIF-62, and ZIF-*zni*. During the experiments at Swiss Light Source synchrotron, complete amorphisation was observed on timescales ranging from minutes to hours. Given a varying transformation rate as the transformation proceeds, the process could be classified as non-isokinetic in all three cases. The underlying mechanism bears the signature of inhomogeneous nucleation and anisotropic growth, which is reflected by increasing Avrami exponents with time. Furthermore, the amorphisation rate accelerates with increasing temperature, even below the usual thermal stability limit of each crystalline phase.

While the exact mechanisms of the interaction with X-rays and the subsequent amorphisation remain subject to speculation, these observations have nevertheless important implications for any experiment on MOFs that is carried out at synchrotron sources. The presumed stability of a MOF in an intense X-ray beam needs to be tested before the actual experiments. This is of particular importance if the investigations are addressing the stability of a MOF with respect to an external variable. If radiation damage is active, the two effects can no longer be deconvoluted. Nevertheless, X-ray radiation induced amorphisation not only posed experimental problems for the structural study of crystalline phases, but it also presents a new mechanism capable of forming new amorphous MOFs.

7.5 Future work

The thesis explored several new approaches to studying structural stability, as well as to processing of MOFs. All of these studies were conducted with either ZIF-4 or ZIF-62, which served as excellent model compounds. Applying these techniques to the exploration of the behaviour of other MOFs, both inside and outside the ZIF family, would be a step forward from here. Are negative Clapeyron gradients a general feature of melting curves of MOFs? Can pressure-assisted sintering be used to fabricate monoliths of highly microporous

MOFs such as MOF-5 or UiO-66? Are other MOFs also susceptible to X-ray induced amorphisation? While such questions about the generality of a phenomenon are part of any scientific discussion, it is particularly worthwhile to ask them in the research field of MOFs, given the highly diverse chemical and structural range of MOF compounds.

More specific points which remain unanswered by the present findings stem from the difficulty to encompass and resolve the large parameter space considered here. This includes the main variables of interest - *pressure*, *temperature*, and *composition* - but also other experimental conditions which were kept constant. These partly, or completely, unexplored variables are areas of investigation for future work:

Chemical composition That the behaviour at high-pressure and high-temperature depends on chemical composition has only been addressed through the endmember compositions. However, given that ZIF-4 and ZIF-62 can exist in continuous solid solution, it can be expected that many properties will systematically vary with composition. Furthermore, some phenomena are only observed for one of the two endmembers (e.g. recrystallisation of amorphous phases). The critical points of transitions in terms of compositional variation also remain unknown.

Time Almost all transformations described in this thesis are thermally activated. The time necessary to complete a transformation at isothermal conditions will thus be highly variable. For example, given enough time and elevated temperatures, melt quenched MOF glasses might still recrystallise. Similarly, crystalline ZIF-4 might amorphise at temperatures below the temperature limits defined here. The time-dependence is therefore an important additional variable to fully predict the behaviour of these materials at non-ambient conditions.

Rate Another poorly understood variable controlling transformations is the increase rate of change of pressure and temperature. Changing rates are known to be capable of shifting the critical conditions for transition, or of provoking altogether different transitions. These influences have only tangentially been addressed here. Concerted studies on the control of time and rate would be beneficial not only for the furthering our understanding of the behaviour of MOFs, but would probably also reconcile conflicting experimental results in the literature.

Pressure-transmitting medium The role of the pressure-transmitting medium, which transforms uniaxial pressure in diamond anvil cell experiments to a hydrostatic regime,

is still largely unexplored. For example, it is not systematically known how hydrostatic limits, molecule size, high-T stability, or chemical inertness can influence the behaviour of MOFs.

Atmosphere Another potential question would be what the type of atmosphere – reducing, inert, oxidising, or humid – have on the high-temperature stability of ZIFs. Depending on the atmosphere, the effect of graphitisation, thermal decomposition, or hydrolysis of the metal–linker bonds cannot be entirely excluded when assessing the transformation from crystalline to amorphous phases.

***P–T* paths** Investigations at quasi-static, simultaneous high-pressure and high-temperature conditions always follow a specific pressure-temperature-path. These P–T paths cannot arbitrarily be controlled during an experiment due to technical limitations. Whether the observations depend on the P–T paths is largely dictated by the reversibility and speed of transitions. It thus remains unclear if the present findings would be the same if, for example, pressure was increased at constant temperature, as opposed to temperature increase at constant pressure.

Apart from these unexplored variables, there is also ample scope for more detailed understanding of the present results:

- The high-pressure-temperature studies on both, ZIF-4 and ZIF-62, pointed out the existence of two distinct amorphous phases. While a density contrast could be delineated, it remains unclear how the structures of these two phases are different from each other. The most obvious tool to study this difference would be total scattering analysis of material recovered to ambient conditions.

- The structures of the X-ray radiation amorphised ZIFs also remain unclear, and whether the polymorphic form of the initial phase influences the structure of the resulting amorphous phase is uncertain.

- The crystal structures of two crystalline high-pressure-temperature polymorphs remain unsolved. Again, the most straight forward way to solve this problem would be to perform *ex-situ* XRD measurements. Large enough quantities for such experiments could also be produced using a large volume press or a Paris-Edinburgh press. In addition to structural studies, the production of such high-pressure-temperature phases in larger quantities might also lead to the development of new, monolithic bulk materials with unique mechanical properties for the given chemical composition.

References

1. Batten, S. R. *et al.* Terminology of metal–organic frameworks and coordination polymers (IUPAC Recommendations 2013). *Pure and Applied Chemistry* **85,** 1715–1724 (2013).
2. Rouquerol, J. *et al.* Recommendations for the characterization of porous solids (Technical Report). *Pure and Applied Chemistry* **66,** 1739–1758 (1994).
3. Friedel, G. New experiments on zeolites. *Bull. Soc. Fr. Minéral. Cristallogr* **19,** 363–390 (1896).
4. Feng, P., Bu, X. & Stucky, G. D. Hydrothermal syntheses and structural characterization of zeolite analogue compounds based on cobalt phosphate. *Nature* **388,** 735–741 (1997).
5. Moghadam, P. Z. *et al.* Development of a Cambridge Structural Database Subset: A Collection of Metal-Organic Frameworks for Past, Present, and Future. *Chemistry of Materials* **29,** 2618–2625 (2017).
6. Yaghi, O. M. & Li, H. Hydrothermal Synthesis of a Metal-Organic Framework Containing Large Rectangular Channels. *Journal of the American Chemical Society* **117,** 10401–10402 (1995).
7. Morris, R. E. & Wheatley, P. S. Gas Storage in Nanoporous Materials. *Angewandte Chemie International Edition* **47,** 4966–4981 (2008).
8. Murray, L. J., Dinca, M. & Long, J. R. Hydrogen storage in metal-organic frameworks. *Chemical Society Reviews* **38,** 1294–1314 (2009).
9. Sumida, K. *et al.* Carbon Dioxide Capture in Metal–Organic Frameworks. *Chemical Reviews* **112,** 724–781 (2012).
10. Li, J.-R., Kuppler, R. J. & Zhou, H.-C. Selective gas adsorption and separation in metal-organic frameworks. *Chemical Society Reviews* **38,** 1477–1504 (2009).
11. Lee, J. *et al.* Metal-organic framework materials as catalysts. *Chemical Society Reviews* **38,** 1450–1459 (2009).
12. Farrusseng, D., Aguado, S. & Pinel, C. Metal–Organic Frameworks: Opportunities for Catalysis. *Angewandte Chemie International Edition* **48,** 7502–7513 (2009).
13. Ma, L., Abney, C. & Lin, W. Enantioselective catalysis with homochiral metal-organic frameworks. *Chemical Society Reviews* **38,** 1248–1256 (2009).
14. Gascon, J., Corma, A., Kapteijn, F. & Llabrés i Xamena, F. X. Metal Organic Framework Catalysis: Quo vadis? *ACS Catalysis* **4,** 361–378 (2014).
15. Horcajada, P. *et al.* Porous metal–organic-framework nanoscale carriers as a potential platform for drug delivery and imaging. *Nature Materials* **9,** 172–178 (2010).

16. Huxford, R. C., Della Rocca, J. & Lin, W. Metal–organic frameworks as potential drug carriers. *Current Opinion in Chemical Biology* **14,** 262–268 (2010).

17. McKinlay, A. C. *et al.* BioMOFs: Metal–Organic Frameworks for Biological and Medical Applications. *Angewandte Chemie International Edition* **49,** 6260–6266 (2010).

18. Kim, H. *et al.* Water harvesting from air with metal-organic frameworks powered by natural sunlight. *Science* **356,** 430–434 (2017).

19. Kreno, L. E. *et al.* Metal–Organic Framework Materials as Chemical Sensors. *Chemical Reviews* **112,** 1105–1125 (2012).

20. Campbell, M. G., Sheberla, D., Liu, S. F., Swager, T. M. & Dincă, M. An Electrically Conductive 2D Metal–Organic Framework for Chemiresistive Sensing. *Angewandte Chemie International Edition* **54,** 4349–4352 (2015).

21. Choi, K. M. *et al.* Supercapacitors of Nanocrystalline Metal–Organic Frameworks. *ACS Nano* **8,** 7451–7457 (2014).

22. Sheberla, D. *et al.* Conductive MOF electrodes for stable supercapacitors with high areal capacitance. *Nature Materials* **16,** 220–224 (2016).

23. Hendon, C. H., Tiana, D. & Walsh, A. Conductive metal-organic frameworks and networks: fact or fantasy? *Physical Chemistry Chemical Physics* **14,** 13120–13132 (2012).

24. Lu, G. *et al.* Imparting functionality to a metal–organic framework material by controlled nanoparticle encapsulation. *Nature Chemistry* **4,** 310–316 (2012).

25. Mercedes, A., Esther, C., Belén, F., i Xamena Francesc X., L. & Hermenegildo, G. Semiconductor Behavior of a Metal-Organic Framework (MOF). *Chemistry – A European Journal* **13,** 5106–5112 (2007).

26. Ryder, M. R. *et al.* Dielectric Properties of Zeolitic Imidazolate Frameworks in the Broad-Band Infrared Regime. *The Journal of Physical Chemistry Letters* **9,** 2678–2684 (2018).

27. Coudert, F.-X. Responsive Metal–Organic Frameworks and Framework Materials: Under Pressure, Taking the Heat, in the Spotlight, with Friends. *Chemistry of Materials* **27,** 1905–1916 (2015).

28. Schneemann, A. *et al.* Flexible metal-organic frameworks. *Chemical Society Reviews* **43,** 6062–6096 (2014).

29. Carrington, E. J. *et al.* Solvent-switchable continuous-breathing behaviour in a diamondoid metal–organic framework and its influence on CO_2 versus CH_4 selectivity. *Nature Chemistry* **9,** 882–889 (2017).

30. Krause, S. *et al.* A pressure-amplifying framework material with negative gas adsorption transitions. *Nature* **532,** 348–352 (2016).

31. Longley, L., Li, N., Wei, F. & Bennett, T. D. Uncovering a reconstructive solid–solid phase transition in a metal–organic framework. *Royal Society Open Science* **4,** 171355–171359 (2017).

32. Lapidus, S. H., Halder, G. J., Chupas, P. J. & Chapman, K. W. Exploiting High Pressures to Generate Porosity, Polymorphism, And Lattice Expansion in the Nonporous Molecular Framework $Zn(CN)_2$. *Journal of the American Chemical Society* **135,** 7621–7628 (2013).
33. Chen, B., Yang, Z., Zhu, Y. & Xia, Y. Zeolitic imidazolate framework materials: recent progress in synthesis and applications. *Journal of Materials Chemistry A* **2,** 16811–16831 (2014).
34. Park, K. S. *et al.* Exceptional chemical and thermal stability of zeolitic imidazolate frameworks. *Proceedings of the National Academy of Sciences* **103,** 10186–10191 (2006).
35. Tan, J. C., Bennett, T. D. & Cheetham, A. K. Chemical structure, network topology, and porosity effects on the mechanical properties of Zeolitic Imidazolate Frameworks. *Proceedings of the National Academy of Sciences* **107,** 9938–9943 (2010).
36. Zhao, P. *et al.* Pressure-induced oversaturation and phase transition in zeolitic imidazolate frameworks with remarkable mechanical stability. *Dalton Transactions* **44,** 4498–4503 (2015).
37. Moggach, S. A., Bennett, T. D. & Cheetham, A. K. The Effect of Pressure on ZIF-8: Increasing Pore Size with Pressure and the Formation of a High-Pressure Phase at 1.47 GPa. *Angewandte Chemie International Edition* **48,** 7087–7089 (2009).
38. Fairen-Jimenez, D. *et al.* Opening the Gate: Framework Flexibility in ZIF-8 Explored by Experiments and Simulations. *Journal of the American Chemical Society* **133,** 8900–8902 (2011).
39. Aguado, S. *et al.* Guest-induced gate-opening of a zeolite imidazolate framework. *New Journal of Chemistry* **35,** 546–550 (2011).
40. Zhao, P. *et al.* Phase Transitions in Zeolitic Imidazolate Framework 7: The Importance of Framework Flexibility and Guest-Induced Instability. *Chemistry of Materials* **26,** 1767–1769 (2014).
41. Zhang, Z., Yao, Z.-Z., Xiang, S. & Chen, B. Perspective of microporous metal-organic frameworks for CO_2 capture and separation. *Energy & Environmental Science* **7,** 2868–2899 (2014).
42. Bennett, T. D. *et al.* Thermal Amorphization of Zeolitic Imidazolate Frameworks. *Angewandte Chemie International Edition* **50,** 3067–3071 (2011).
43. Bennett, T. D. *et al.* Reversible pressure-induced amorphization of a zeolitic imidazolate framework (ZIF-4). *Chemical Communications* **47,** 7983–7985 (2011).
44. Bennett, T. D. & Cheetham, A. K. Amorphous Metal–Organic Frameworks. *Accounts of Chemical Research* **47,** 1555–1562 (2014).
45. Bennett, T. D. *et al.* Melt-Quenched Glasses of Metal–Organic Frameworks. *Journal of the American Chemical Society* **138,** 3484–3492 (2016).
46. Phan, A. *et al.* Synthesis, Structure, and Carbon Dioxide Capture Properties of Zeolitic Imidazolate Frameworks. *Accounts of Chemical Research* **43,** 58–67 (2010).
47. Bennett, T. D., Cheetham, A. K., Fuchs, A. H. & Coudert, F.-X. Interplay between defects, disorder and flexibility in metal-organic frameworks. *Nature Chemistry* **9,** 11–16 (2017).

48. Kitagawa, S. Future Porous Materials. *Accounts of Chemical Research* **50,** 514–516 (2017).

49. Bennett, T. D. & Horike, S. Liquid, glass and amorphous solid states of coordination polymers and metal–organic frameworks. *Nature Reviews Materials* (2018).

50. Angell, C. A. Formation of Glasses from Liquids and Biopolymers. *Science* **267,** 1924–1935 (2003).

51. Rivera, V. & Manzani, D. *Technological Advances in Tellurite Glasses* (Springer, 2017).

52. Gloriant, T. Microhardness and abrasive wear resistance of metallic glasses and nanostructured composite materials. *Journal of Non-Crystalline Solids* **316,** 96–103 (2003).

53. Qiao, A. *et al.* A metal-organic framework with ultrahigh glass-forming ability. *Science Advances* **4** (2018).

54. Gaillac, R. *et al.* Liquid metal-organic frameworks. *Nature Materials* **16,** 1149–1154 (2017).

55. Haizheng, T., Bennett, D. T. & Yuanzheng, Y. Melt-Quenched Hybrid Glasses from Metal–Organic Frameworks. *Advanced Materials* **29,** 1601705–1601711 (2017).

56. Zhou, C. *et al.* Polymorph formation for a zeolitic imidazolate framework composition - $Zn(Im)_2$. *Microporous and Mesoporous Materials* **265,** 57–62 (2018).

57. Shimizu, G. K. H., Taylor, J. M. & Kim, S. Proton Conduction with Metal-Organic Frameworks. *Science* **341,** 354–355 (2013).

58. Sava, D. F. *et al.* Capture of Volatile Iodine, a Gaseous Fission Product, by Zeolitic Imidazolate Framework-8. *Journal of the American Chemical Society* **133,** 12398–12401 (2011).

59. Chapman, K. W., Sava, D. F., Halder, G. J., Chupas, P. J. & Nenoff, T. M. Trapping guests within a nanoporous metal-organic framework through pressure-induced amorphization. *Journal of the American Chemical Society* **133,** 18583–18585 (2011).

60. Bennett, T. D., Saines, P. J., Keen, D. A., Tan, J.-C. & Cheetham, A. K. Ball-Milling-Induced Amorphization of Zeolitic Imidazolate Frameworks (ZIFs) for the Irreversible Trapping of Iodine. *Chemistry – A European Journal* **19,** 7049–7055 (2013).

61. Orellana-Tavra, C. *et al.* Amorphous metal–organic frameworks for drug delivery. *Chemical Communications* **51,** 13878–13881 (2015).

62. Su, Z., Miao, Y.-R., Zhang, G., Miller, J. T. & Suslick, K. S. Bond breakage under pressure in a metal organic framework. *Chemical Science* **8,** 8004–8011 (2017).

63. Schwarz, R. B. & Johnson, W. L. Remarks on solid state amorphizing transformations. *Journal of the Less Common Metals* **140,** 1–6 (1988).

64. Mishima, O., Calvert, L. D. & Whalley, E. 'Melting ice' I at 77 K and 10 kbar: a new method of making amorphous solids. *Nature* **310,** 393–395 (1984).

65. Bennett, T. D. *et al.* Structure and Properties of an Amorphous Metal-Organic Framework. *Physical Review Letters* **104,** 115503–115507 (2010).

66. Keen, D. A. & Bennett, T. D. Structural investigations of amorphous metal-organic frameworks formed via different routes. *Physical Chemistry Chemical Physics* **20,** 7857–7861 (2018).

67. Keen, D. A. & Dove, M. T. Local structures of amorphous and crystalline phases of silica, SiO_2 , by neutron total scattering. *Journal of Physics: Condensed Matter* **11,** 9263–9273 (1999).

68. Zacharia, R., Cossement, D., Lafi, L. & Chahine, R. Volumetric hydrogen sorption capacity of monoliths prepared by mechanical densification of MOF-177. *Journal of Materials Chemistry* **20,** 2145–2151 (2010).

69. Ortiz, A. U., Boutin, A., Fuchs, A. H. & Coudert, F.-X. Investigating the Pressure-Induced Amorphization of Zeolitic Imidazolate Framework ZIF-8: Mechanical Instability Due to Shear Mode Softening. *The Journal of Physical Chemistry Letters* **4,** 1861–1865 (2013).

70. Chapman, K. W., Halder, G. J. & Chupas, P. J. Pressure-Induced Amorphization and Porosity Modification in a Metal-Organic Framework. *Journal of the American Chemical Society* **131,** 17546–17547 (2009).

71. Henke, S. *et al.* Pore closure in zeolitic imidazolate frameworks under mechanical pressure. *Chemical Science* **9,** 1654–1660 (2018).

72. Bennett, T. D. *et al.* Facile Mechanosynthesis of Amorphous Zeolitic Imidazolate Frameworks. *Journal of the American Chemical Society* **133,** 14546–14549 (2011).

73. Baxter, E. F. *et al.* A comparison of the amorphization of zeolitic imidazolate frameworks (ZIFs) and aluminosilicate zeolites by ball-milling. *Dalton Transactions* **45,** 4258–4268 (2016).

74. Cao, S., Bennett, T. D., Keen, D. A., Goodwin, A. L. & Cheetham, A. K. Amorphization of the prototypical zeolitic imidazolate framework ZIF-8 by ball-milling. *Chemical Communications* **48,** 7805–7807 (2012).

75. Putnis, A. *An Introduction to Mineral Sciences* (Cambridge University Press, 1992).

76. Lindemann, F. A. The calculation of molecular vibration frequencies. *Physikalische Zeitschrift* **11,** 609–613 (1910).

77. Born, M. Thermodynamics of Crystals and Melting. *The Journal of Chemical Physics* **7,** 591–603 (1939).

78. Wolf, G. H. & Jeanloz, R. Lindemann Melting Law: Anharmonic correction and test of its validity for minerals. *Journal of Geophysical Research: Solid Earth* **89,** 7821–7835 (1984).

79. Oxtoby, D. W. New perspectives on freezing and melting. *Nature* **347,** 725–730 (1990).

80. Stillinger, F. H. & Weber, T. A. Point defects in bcc crystals: Structures, transition kinetics, and melting implications. *The Journal of Chemical Physics* **81,** 5095–5103 (1984).

81. Granato, A. V. Interstitialcy model for condensed matter states of face-centered-cubic metals. *Physical Review Letters* **68,** 974–977 (1992).

82. Golde, S., Palberg, T. & Schöpe, H. J. Correlation between dynamical and structural heterogeneities in colloidal hard-sphere suspensions. *Nature Physics* **12,** 712–717 (2016).

83. Angell, C. A. Formation of Glasses from Liquids and Biopolymers. *Science* **267,** 1924–1935 (1995).

84. Angell, C., Moynihan, C. & Hemmati, M. 'Strong' and 'superstrong' liquids, and an approach to the perfect glass state via phase transition. *Journal of Non-Crystalline Solids* **274,** 319–331 (2000).

85. Dyre, J. Colloquium: The glass transition and elastic models of glass-forming liquids. *Reviews of Modern Physics* **78,** 953–972 (2006).

86. Kauzmann, W. The nature of the glassy state and the behavior of liquids at low temperatures. *Chemical reviews* **43,** 219–256 (1948).

87. Endo, H., Tamura, K. & Yao, M. Liquid metals and semiconductors under pressure. *Canadian Journal of Physics* **65,** 266–285 (1987).

88. Ponyatovsky, E. & Barkalov, O. Pressure–induced amorphous phases. *Materials Science Reports* **8,** 147–191 (1992).

89. Bennett, T. D. *et al.* Hybrid glasses from strong and fragile metal-organic framework liquids. *Nature Communications* **6,** 8079–8086 (2015).

90. Angell, C. A., Ngai, K. L., McKenna, G. B., McMillan, P. F. & Martin, S. W. Relaxation in glassforming liquids and amorphous solids. *Journal of Applied Physics* **88,** 3113–3157 (2000).

91. Richet, P. & Gillet, P. Pressure-induced amorphization of minerals; a review. *European Journal of Mineralogy* **9,** 907–933 (1997).

92. Sharma, S. M. & Sikka, S. Pressure induced amorphization of materials. *Progress in Materials Science* **40,** 1–77 (1996).

93. Whalley, E., Klug, D. D. & Handa, Y. P. Entropy of amorphous ice as determined by a new thermodynamic method. *High Pressure Research* **4,** 381–383 (1990).

94. Sokolov, A. P. The glass transition: New ideas in an age-old field. *Endeavour* **21,** 109–113 (1997).

95. Stillinger, F. H. & Debenedetti, P. G. Glass Transition Thermodynamics and Kinetics. *Annual Review of Condensed Matter Physics* **4,** 263–285 (2013).

96. Schmelzer, J. W., Abyzov, A. S., Fokin, V. M. & Schick, C. Kauzmann paradox and the crystallization of glass-forming melts. *Journal of Non-Crystalline Solids* **501,** 21–35 (2018).

97. Farha, O. K. & Hupp, J. T. Rational Design, Synthesis, Purification, and Activation of Metal-Organic Framework Materials. *Accounts of Chemical Research* **43,** 1166–1175 (2010).

98. Lewis, D. W. *et al.* Zeolitic imidazole frameworks: structural and energetics trends compared with their zeolite analogues. *CrystEngComm* **11,** 2272–2276 (2009).

99. Hughes, J. T., Bennett, T. D., Cheetham, A. K. & Navrotsky, A. Thermochemistry of zeolitic imidazolate frameworks of varying porosity. *Journal of the American Chemical Society* **135,** 598–601 (2013).

100. Chen, E.-Y., Liu, Y.-C., Zhou, M., Zhang, L. & Wang, Q. Effects of structure on hydrogen adsorption in zeolitic imidazolate frameworks. *Chemical Engineering Science* **71,** 178–184 (2012).

101. Battisti, A., Taioli, S. & Garberoglio, G. Zeolitic imidazolate frameworks for separation of binary mixtures of CO_2, CH_4, N_2 and H_2: A computer simulation investigation. *Microporous and Mesoporous Materials* **143,** 46–53 (2011).

102. Hovestadt, M. *et al.* Scale-up of the Synthesis of Zeolitic Imidazolate Framework ZIF-4. *Chemie Ingenieur Technik* **89,** 1374–1378 (2017).

103. Hartmann, M., Böhme, U., Hovestadt, M. & Paula, C. Adsorptive Separation of Olefin/Paraffin Mixtures with ZIF-4. *Langmuir* **31,** 12382–12389 (2015).

104. Tian, T., Velazquez-Garcia, J., Bennett, T. D. & Fairen-Jimenez, D. Mechanically and chemically robust ZIF-8 monoliths with high volumetric adsorption capacity. *Journal of Materials Chemistry A* **3,** 2999–3005 (2015).

105. Widmer, R. N. *et al.* Manufacturing Macroporous Monoliths of Microporous Metal–Organic Frameworks. *ACS Applied Nano Materials* **1,** 497–500 (2018).

106. Wharmby, M. T. *et al.* Extreme Flexibility in a Zeolitic Imidazolate Framework: Porous to Dense Phase Transition in Desolvated ZIF-4. *Angewandte Chemie International Edition* **54,** 6447–6451 (2015).

107. Spencer, E. C., Angel, R. J., Ross, N. L., Hanson, B. E. & Howard, J. A. K. Pressure-Induced Cooperative Bond Rearrangement in a Zinc Imidazolate Framework: A High-Pressure Single-Crystal X-Ray Diffraction Study. *Journal of the American Chemical Society* **131,** 4022–4026 (2009).

108. Lehnert, R. & Seel, F. Darstellung und Kristallstruktur des Mangan(II)- und Zink(II)-Derivates des Imidazols. *Zeitschrift für anorganische und allgemeine Chemie* **464,** 187–194 (1980).

109. Schröder, C. A., Baburin, I. A., van Wüllen, L., Wiebcke, M. & Leoni, S. Subtle polymorphism of zinc imidazolate frameworks: temperature-dependent ground states in the energy landscape revealed by experiment and theory. *CrystEngComm* **15,** 4036–4040 (2013).

110. Banerjee, R. *et al.* High-throughput synthesis of zeolitic imidazolate frameworks and application to CO_2 capture. *Science* **319,** 939–43 (2008).

111. Tian, Y.-Q. *et al.* Design and Generation of Extended Zeolitic Metal–Organic Frameworks (ZMOFs): Synthesis and Crystal Structures of Zinc(II) Imidazolate Polymers with Zeolitic Topologies. *Chemistry – A European Journal* **13,** 4146–4154 (2007).

112. Karagiaridi, O. *et al.* Opening ZIF-8: A Catalytically Active Zeolitic Imidazolate Framework of Sodalite Topology with Unsubstituted Linkers. *Journal of the American Chemical Society* **134,** 18790–18796 (2012).

113. Shi, Q. *et al.* Zeolite CAN and AFI-Type Zeolitic Imidazolate Frameworks with Large 12-Membered Ring Pore Openings Synthesized Using Bulky Amides as Structure-Directing Agents. *Journal of the American Chemical Society* **138,** 16232–16235 (2016).

114. Kniep, R., Mootz, D. & Vegas, A. Variscite. *Acta Crystallographica Section B* **33,** 263–265 (1977).

115. Song, Y., Zavalij, P. Y., Suzuki, M. & Whittingham, M. S. New Iron(III) Phosphate Phases: Crystal Structure and Electrochemical and Magnetic Properties. *Inorganic Chemistry* **41,** 5778–5786 (2002).

116. Deiseroth, H. J. & Müller -Buschbaum, H. Über Erdalkalimetalloxogallate. III. Untersuchung des Aufbaus von $CaGa_2O_4$. *Zeitschrift für anorganische und allgemeine Chemie* **396,** 157–164 (1973).

117. Tian, Y.-Q. *et al.* Two Polymorphs of Cobalt(II) Imidazolate Polymers Synthesized Solvothermally by Using One Organic Template N,N-Dimethylacetamide. *Inorganic Chemistry* **43,** 4631–4635 (2004).

118. Zhang, J. *et al.* Zeolitic Boron Imidazolate Frameworks. *Angewandte Chemie International Edition* **48,** 2542–2545 (2009).

119. Sturm, M., Brandl, F., Engel, D. & Hoppe, W. Die Kristallstruktur von Diimidazolylkobalt. *Acta Crystallographica Section B* **31,** 2369–2378 (1975).

120. Tian, Y.-Q. *et al.* $[Co_5(im)_{10}]$: A Metal-Organic Open-Framework with Zeolite-Like Topology. *Angewandte Chemie* **114,** 1442–1444 (2002).

121. Tian, Y.-Q. *et al.* The Silica-Like Extended Polymorphism of Cobalt(II) Imidazolate Three-Dimensional Frameworks: X-ray Single-Crystal Structures and Magnetic Properties. *Chemistry – A European Journal* **9,** 5673–5685 (2003).

122. Masciocchi, N., Castelli, F., Forster, P. M., Tafoya, M. M. & Cheetham, A. K. Synthesis and Characterization of Two Polymorphic Crystalline Phases and an Amorphous Powder of Nickel(II) Bisimidazolate. *Inorganic Chemistry* **42,** 6147–6152 (2003).

123. Jarvis, J. & Wells, A. The structural chemistry of cupric compounds. *Acta Crystallographica* **13,** 1027–1028 (1960).

124. Masciocchi, N. *et al.* Extended Polymorphism in Copper(II) Imidazolate Polymers: A Spectroscopic and XRPD Structural Study. *Inorganic Chemistry* **40,** 5897–5905 (2001).

125. Masciocchi, N. *et al.* Synthesis and ab-initio XRPD structure of group 12 imidazolato polymers. *Chemical Communications* **16,** 2018–2019 (2003).

126. Stock, N. & Biswas, S. Synthesis of Metal-Organic Frameworks (MOFs): Routes to Various MOF Topologies, Morphologies, and Composites. *Chemical Reviews* **112,** 933–969 (2012).

127. Hovestadt, M., Schwegler, J., Schulz, P. S. & Hartmann, M. Synthesis of the zeolitic imidazolate framework ZIF-4 from the ionic liquid 1-butyl-3-methylimidazolium imidazolate. *The Journal of Chemical Physics* **148,** 193837–193842 (2018).

128. Muzart, J. N, N-Dimethylformamide: much more than a solvent. *Tetrahedron* **65,** 8313–8323 (2009).

129. Burrows, A. D. *et al.* Solvent hydrolysis and templating effects in the synthesis of metal–organic frameworks. *CrystEngComm* **7,** 548–550 (2005).

130. Yaghi, O. M. *et al.* Reticular synthesis and the design of new materials. *Nature* **423,** 705–714 (2003).

131. Morsy, M. A., Al-Khaldi, M. A. & Suwaiyan, A. Normal Vibrational Mode Analysis and Assignment of Benzimidazole by ab Initio and Density Functional Calculations and Polarized Infrared and Raman Spectroscopy. *The Journal of Physical Chemistry A* **106,** 9196–9203 (2002).

132. Markham, L. M., Mayne, L. C., Hudson, B. S. & Zgierski, M. Z. Resonance Raman studies of imidazole, imidazolium, and their derivatives: the effect of deuterium substitution. *The Journal of Physical Chemistry* **97,** 10319–10325 (1993).

133. Coelho, A. A. TOPAS and TOPAS-Academic: an optimization program integrating computer algebra and crystallographic objects written in C plus. *Journal of Applied Crystallography* **51,** 210–218 (2018).

134. Rietveld, H. M. A profile refinement method for nuclear and magnetic structures. *Journal of Applied Crystallography* **2,** 65–71 (1969).

135. Bail, A. L., Duroy, H. & Fourquet, J. Ab-initio structure determination of $LiSbWO_6$ by X-ray powder diffraction. *Materials Research Bulletin* **23,** 447–452 (1988).

136. Coles, S. J. & Gale, P. A. Changing and challenging times for service crystallography. *Chemical Science* **3,** 683–689 (2012).

137. Stinton, G. W. & Evans, J. S. O. Parametric Rietveld refinement. *Journal of Applied Crystallography* **40,** 87–95 (2007).

138. Datchi, F. *et al.* Optical pressure sensors for high-pressure-high-temperature studies in a diamond anvil cell. *High Pressure Research* **27,** 447–463 (2007).

139. Angel, R. J., Allan, D. R., Miletich, R. & Finger, L. W. The Use of Quartz as an Internal Pressure Standard in High-Pressure Crystallography. *Journal of Applied Crystallography* **30,** 461–466 (1997).

140. Dorogokupets, P. I. & Dewaele, A. Equations of state of MgO, Au, Pt, NaCl-B1, and NaCl-B2: Internally consistent high-temperature pressure scales. *High Pressure Research* **27,** 431–446 (2007).

141. Dubrovinskaia, N. & Dubrovinsky, L. Whole-cell heater for the diamond anvil cell. *Review of Scientific Instruments* **74,** 3433–3437 (2003).

142. Bassett, W. A., Shen, A. H., Bucknum, M. & Chou, I. A new diamond anvil cell for hydrothermal studies to 2.5 GPa and from -190 to 1200 °C1200 °C. *Review of Scientific Instruments* **64,** 2340–2345 (1993).

143. Andrault, D., Fiquet, G., Charpin, T. & le Bihan, T. Structure analysis and stability field of β-iron at high P and T. *American Mineralogist* **85,** 364–371 (2000).

144. Rekhi, S., Dubrovinsky, L. S. & Saxena, S. K. Temperature-induced ruby fluorescence shifts up to a pressure of 15 GPa in an externally heated diamond anvil cell. *High Temperatures-High Pressures* **31,** 299–305 (1999).

145. Klotz, S., Chervin, J. C., Munsch, P. & Marchand, G. L. Hydrostatic limits of 11 pressure transmitting media. *Journal of Physics D: Applied Physics* **42,** 075413–075420 (2009).

146. Eddaoudi, M. *et al.* Systematic Design of Pore Size and Functionality in Isoreticular MOFs and Their Application in Methane Storage. *Science* **295,** 469–472 (2002).

147. Banerjee, R. *et al.* Control of Pore Size and Functionality in Isoreticular Zeolitic Imidazolate Frameworks and their Carbon Dioxide Selective Capture Properties. *Journal of the American Chemical Society* **131,** 3875–3877 (2009).

148. Dybtsev, D. N., Chun, H. & Kim, K. Rigid and Flexible: A Highly Porous Metal–Organic Framework with Unusual Guest-Dependent Dynamic Behavior. *Angewandte Chemie International Edition* **43,** 5033–5036 (2004).

149. Deng, H. *et al.* Multiple Functional Groups of Varying Ratios in Metal-Organic Frameworks. *Science* **327,** 846 (2010).

150. Reed-Hill, R. E., Abbaschian, R. & Abbaschian, R. *Physical metallurgy principles* (Brooks/Cole Engineering Division Monterey, Calif, USA, 1973).

151. Geiger, C. A. *Solid solutions in silicate and oxide systems* (The Mineralogical Society of Great Britain and Ireland, 2001).

152. Burrows, A. D. Mixed-component metal-organic frameworks (MC-MOFs): enhancing functionality through solid solution formation and surface modifications. *CrystEngComm* **13,** 3623–3642 (11 2011).

153. Kleist, W., Jutz, F., Maciejewski, M. & Baiker, A. Mixed-Linker Metal-Organic Frameworks as Catalysts for the Synthesis of Propylene Carbonate from Propylene Oxide and CO_2. *European Journal of Inorganic Chemistry* **2009,** 3552–3561 (2009).

154. Koh, K., Wong-Foy, A. G. & Matzger, A. J. MOF@MOF: microporous core-shell architectures. *Chemical Communications,* 6162–6164 (2009).

155. Fang, Z. *et al.* Structural Complexity in Metal–Organic Frameworks: Simultaneous Modification of Open Metal Sites and Hierarchical Porosity by Systematic Doping with Defective Linkers. *Journal of the American Chemical Society* **136,** 9627–9636 (2014).

156. Du, M., Jiang, X.-J. & Zhao, X.-J. Molecular Tectonics of Mixed-Ligand Metal-Organic Frameworks: Positional Isomeric Effect, Metal-Directed Assembly, and Structural Diversification. *Inorganic Chemistry* **46,** 3984–3995 (2007).

157. Burrows Andrew, D., Frost Christopher, G., Mahon Mary, F. & Richardson, C. Post-Synthetic Modification of Tagged Metal–Organic Frameworks. *Angewandte Chemie International Edition* **47,** 8482–8486 (2008).

158. Koh, K., Wong-Foy, A. G. & Matzger, A. J. A Porous Coordination Copolymer with over 5000 m^2/g BET Surface Area. *Journal of the American Chemical Society* **131,** 4184–4185 (2009).

159. Marx, S., Kleist, W., Huang, J., Maciejewski, M. & Baiker, A. Tuning functional sites and thermal stability of mixed-linker MOFs based on MIL-53(Al). *Dalton Transactions* **39,** 3795–3798 (2010).

160. Sheldrick, G. M. A short history of *SHELX*. *Acta Crystallographica Section A* **64,** 112–122 (2008).

161. Gustafsson, M. & Zou, X. Crystal formation and size control of zeolitic imidazolate frameworks with mixed imidazolate linkers. *Journal of Porous Materials* **20,** 55–63 (2013).

162. Longley, L. *et al.* Liquid phase blending of metal-organic frameworks. *Nature Communications* **9,** 2135–2145 (2018).

163. Frentzel-Beyme, L. *et al.* Porous purple glass – a cobalt imidazolate glass with accessible porosity from a meltable cobalt imidazolate framework. *Journal of Materials Chemistry A* **7,** 985–990 (2019).

164. Du Bourg, L. B., Ortiz, A. U., Boutin, A. & Coudert, F. X. Thermal and mechanical stability of zeolitic imidazolate frameworks polymorphs. *APL Materials* **2,** 124110–124119 (2014).

165. Queen, W. L. *et al.* Site-Specific CO_2 Adsorption and Zero Thermal Expansion in an Anisotropic Pore Network. *The Journal of Physical Chemistry C* **115,** 24915–24919 (2011).

166. Gao, Q. *et al.* Tunable Thermal Expansion from Negative, Zero, to Positive in Cubic Prussian Blue Analogues of $GaFe(CN)_6$. *Inorganic Chemistry* **57,** 14027–14030 (2018).

167. Ryder, M. R. *et al.* Identifying the Role of Terahertz Vibrations in Metal-Organic Frameworks: From Gate-Opening Phenomenon to Shear-Driven Structural Destabilization. *Physical Review Letters* **113,** 215502–215508 (2014).

168. Coudert, F.-X., Mellot-Draznieks, C., Fuchs, A. H. & Boutin, A. Prediction of Breathing and Gate-Opening Transitions Upon Binary Mixture Adsorption in Metal-Organic Frameworks. *Journal of the American Chemical Society* **131,** 11329–11331 (2009).

169. McDonald, T. M. *et al.* Cooperative insertion of CO_2 in diamine-appended metal-organic frameworks. *Nature* **519,** 303–308 (2015).

170. Zhou, C. *et al.* Metal-organic framework glasses with permanent accessible porosity. *Nature Communications* **9,** 5042–5051 (2018).

171. Chen, W. *et al.* Glass Formation of a Coordination Polymer Crystal for Enhanced Proton Conductivity and Material Flexibility. *Angewandte Chemie International Edition* **55,** 5195–5200 (2016).

172. Dewaele, A., Torrent, M., Loubeyre, P. & Mezouar, M. Compression curves of transition metals in the Mbar range: Experiments and projector augmented-wave calculations. *Physical Review B* **78,** 104102–104115 (2008).

173. Fisch, M., Lanza, A., Boldyreva, E., Macchi, P. & Casati, N. Kinetic Control of High-Pressure Solid-State Phase Transitions: A Case Study on l-Serine. *The Journal of Physical Chemistry C* **119,** 18611–18617 (2015).

174. Baburin, I. A. & Leoni, S. Modelling polymorphs of metal–organic frameworks: a systematic study of diamondoid zinc imidazolates. *CrystEngComm* **12,** 2809–2816 (2010).

175. Widmer, R. N. *et al.* Pressure promoted low-temperature melting of metal–organic frameworks. *Nature Materials* **18,** 370–376 (2019).

176. Greaves, G. N. & Sen, S. Inorganic glasses, glass-forming liquids and amorphizing solids. *Advances in Physics* **56,** 1–166 (2007).

177. Machon, D. *et al.* Pseudoamorphization of Cs_2HgBr_4. *Phys. Rev. B* **68,** 144104–144111 (2003).

178. Navrotsky, A. Nanoscale Effects on Thermodynamics and Phase Equilibria in Oxide Systems. *ChemPhysChem* **12,** 2207–2215 (2011).

179. Zhang, C., Gee, J. A., Sholl, D. S. & Lively, R. P. Crystal-Size-Dependent Structural Transitions in Nanoporous Crystals: Adsorption-Induced Transitions in ZIF-8. *The Journal of Physical Chemistry C* **118,** 20727–20733 (2014).

180. Belenguer, A. M., Lampronti, G. I., Cruz-Cabeza, A. J., Hunter, C. A. & Sanders, J. K. M. Solvation and surface effects on polymorph stabilities at the nanoscale. *Chemical Science* **7,** 6617–6627 (2016).

181. Horike, S., Shimomura, S. & Kitagawa, S. Soft porous crystals. *Nature Chemistry* **1,** 695–704 (2009).

182. Ren, J. & North, B. Shaping Porous Materials for Hydrogen Storage Applications: A Review. *Journal of Technology Innovations in Renewable Energy* **3,** 12–20 (2014).

183. Li, S. *et al.* Mechanical Properties and Processing Techniques of Bulk Metal–Organic Framework Glasses. *Journal of the American Chemical Society* **141,** 1027–1034 (2019).

184. Guillon, O. *et al.* Field-Assisted Sintering Technology/Spark Plasma Sintering: Mechanisms, Materials, and Technology Developments. *Advanced Engineering Materials* **16,** 830–849 (2014).

185. Tokita, M. in *Handbook of Advanced Ceramics (Second Edition)* (ed Somiya, S.) 1149–1177 (Academic Press, Oxford, 2013).

186. Vasiliev, P. *et al.* Strong Hierarchically Porous Monoliths by Pulsed Current Processing of Zeolite Powder Assemblies. *ACS Applied Materials & Interfaces* **2,** 732–737 (2010).

187. Wang, L., Jiang, W., Chen, L. & Shen, Z. Formation of a unique glass by spark plasma sintering of a zeolite. *Journal of Materials Research* **24,** 3241–3245 (2009).

188. Hong, W. Y., Perera, S. P. & Burrows, A. D. Manufacturing of metal-organic framework monoliths and their application in CO_2 adsorption. *Microporous and Mesoporous Materials* **214,** 149–155 (2015).

189. Chen, Y. *et al.* Shaping of Metal–Organic Frameworks: From Fluid to Shaped Bodies and Robust Foams. *Journal of the American Chemical Society* **138,** 10810–10813 (2016).

190. Thakkar, H., Eastman, S., Al-Naddaf, Q., Rownaghi, A. A. & Rezaei, F. 3D-Printed Metal–Organic Framework Monoliths for Gas Adsorption Processes. *ACS Applied Materials & Interfaces* **9,** 35908–35916 (2017).

191. Ren, J. *et al.* A more efficient way to shape metal-organic framework (MOF) powder materials for hydrogen storage applications. *International Journal of Hydrogen Energy* **40,** 4617–4622 (2015).

192. Rezaei, F. *et al.* MOF-74 and UTSA-16 film growth on monolithic structures and their CO_2 adsorption performance. *Chemical Engineering Journal* **313,** 1346–1353 (2017).

193. Walton, K. S. & Snurr, R. Q. Applicability of the BET Method for Determining Surface Areas of Microporous Metal-Organic Frameworks. *Journal of the American Chemical Society* **129,** 8552–8556 (2007).

194. Suescun, L. *et al.* The structure of cubic MOF $Ca(H_2O)_6(CaGd(oxydiacetate)_3)_2$: A comparison between structural models obtained from Rietveld refinement of conventional and synchrotron X-ray powder diffraction data and standard refinement of single-crystal X-ray diffraction data. *Powder Diffraction* **27,** 232–242 (2012).

195. Ravelli, R. B. & Garman, E. F. Radiation damage in macromolecular cryocrystallography. *Current Opinion in Structural Biology* **16,** 624–629 (2006).

196. Garman, E. F. Radiation damage in macromolecular crystallography: what is it and why should we care? *Acta Crystallographica Section D* **66,** 339–351 (2010).

197. Teng, T.-y. & Moffat, K. Primary radiation damage of protein crystals by an intense synchrotron X-ray beam. *Journal of Synchrotron Radiation* **7,** 313–317 (2000).

198. Müller, R., Weckert, E., Zellner, J. & Drakopoulos, M. Investigation of radiation-dose-induced changes in organic light-atom crystals by accurate *d*-spacing measurements. *Journal of Synchrotron Radiation* **9,** 368–374 (2002).

199. Polvino, S. M. *et al.* Synchrotron microbeam x-ray radiation damage in semiconductor layers. *Applied Physics Letters* **92,** 224105–224108 (2008).

200. Yokoi, K. & Ohba, Y. Recovery of X-ray radiation damage in anthracene single crystals. *Chemical Physics Letters* **56,** 560–562 (1978).

201. Bziouet, M., Almairac, R. & Saint-Gregoire, P. The influence of X-ray radiation damage on the incommensurate phase in $N(CH_3)_4)_2ZnCl_4$. *Journal of Physics C: Solid State Physics* **20,** 2635 (1987).

202. Morgan, L. C. F. *et al.* Unexpected behaviour in derivatives of Barluenga's reagent. *Chemical Communications* **54,** 9849–9852 (2018).

203. Seiler, P. & D Dunitz, J. Detection of Radiation Damage in Organic Crystals. *Australian Journal of Physics* **38,** 405–412 (1985).

204. Abrahams, S. C. International Union of Crystallography Commission on Crystallographic Apparatus single-crystal radiation damage survey. *Acta Crystallographica Section A* **29,** 111–116 (1973).

205. Conrad, S. *et al.* Controlling Dissolution and Transformation of Zeolitic Imidazolate Frameworks by using Electron-Beam-Induced Amorphization. *Angewandte Chemie International Edition* **57,** 13592–13597 (2018).

206. Volkringer, C. *et al.* Stability of metal–organic frameworks under gamma irradiation. *Chemical Communications* **52,** 12502–12505 (2016).

207. Woodhead, J. A., Rossman, G. R. & Silver, L. T. The metamictization of zircon: Radiation dose-dependent structural characteristics. **76,** 74–82 (1991).

208. Willmott, P. R. *et al.* The Materials Science beamline upgrade at the Swiss Light Source. *Journal of Synchrotron Radiation* **20,** 667–682 (2013).

209. Bergamaschi, A. *et al.* The MYTHEN detector for X-ray powder diffraction experiments at the Swiss Light Source. *Journal of Synchrotron Radiation* **17,** 653–668 (2010).

210. Bennett, T. D. *et al.* Mechanical Properties of Dense Zeolitic Imidazolate Frameworks (ZIFs): A High-Pressure X-ray Diffraction, Nanoindentation and Computational Study of the Zinc Framework $Zn(Im)_2$, and its Lithium-Boron Analogue, $LiB(Im)_4$. *Chemistry – A European Journal* **16,** 10684–10690 (2010).

211. Hubbell, J. H. & Seltzer, S. M. *Tables of x-ray mass attenuation coefficients and mass energy-absorption coefficients 1 keV to 20 meV for elements z = 1 to 92 and 48 additional substances of dosimetric interest* tech. rep. (United States, 1995).

212. Avrami, M. Kinetics of Phase Change. I General Theory. *The Journal of Chemical Physics* **7,** 1103–1112 (1939).

213. Weinberg, M. C., Birnie, D. P. & Shneidman, V. A. Crystallization kinetics and the JMAK equation. *Journal of Non-Crystalline Solids* **219,** 89–99 (1997).

214. Goetz, R. L. Particle stimulated nucleation during dynamic recrystallization using a cellular automata model. *Scripta Materialia* **52,** 851–856 (2005).

215. Semiatin, S. *et al.* Deformation and recrystallization behavior during hot working of a coarse-grain, nickel-base superalloy ingot material. *Metallurgical and Materials Transactions A* **35,** 679–693 (2004).

216. Snell, E. H., Bellamy, H. D., Rosenbaum, G. & van der Woerd, M. J. Non-invasive measurement of X-ray beam heating on a surrogate crystal sample. *Journal of Synchrotron Radiation* **14,** 109–115 (2007).

217. Redfern, S. A. T. Length scale dependence of high-pressure amorphization: the static amorphization of anorthite. *Mineralogical Magazine* **60,** 493–498 (1996).

218. Wu, H., Simmons, J. M., Srinivas, G., Zhou, W. & Yildirim, T. Adsorption Sites and Binding Nature of CO_2 in Prototypical Metal-Organic Frameworks: A Combined Neutron Diffraction and First-Principles Study. *The Journal of Physical Chemistry Letters* **1,** 1946–1951 (2010).

Appendix A

A

Solution	Molality (mol/L)	Volume Solution	mol of solute	Zn:Im:bIm:DMF	Mass solution (g)
Zn	0.2	19.400	0.004	1.00	19.468
Im	1.5	15.186	0.023	5.87	15.887
bIm	0.2	48.814	0.010	2.52	47.233
DMF		16.600	1.292	332.88	15.670
	sum	100.00			

B

Solution	Molality (mol/L)	Volume Solution	mol of solute	Zn:Im:bIm:DMF	Mass solution (g)
Zn	0.2	19.400	0.004	1.00	19.468
Im	1.5	20.543	0.031	7.94	21.491
bIm	0.2	43.457	0.009	2.24	42.050
DMF		16.600	1.292	332.88	15.670
	sum	100.00			

C

Solution	Molality (mol/L)	Volume Solution	mol of solute	Zn:Im:bIm:DMF	Mass solution (g)
Zn	0.2	19.400	0.004	1.00	19.468
Im	1.5	28.912	0.043	11.18	30.245
bIm	0.2	35.088	0.007	1.81	33.952
DMF		16.600	1.292	332.88	15.670
	sum	100.00			

D

Solution	Molality (mol/L)	Volume Solution	mol of solute	Zn:Im:bIm:DMF	Mass solution (g)
Zn	0.2	19.400	0.004	1.00	19.468
Im	1.5	42.216	0.063	16.32	44.162
bIm	0.2	21.784	0.004	1.12	21.079
DMF		16.600	1.292	332.88	15.670
	sum	100.00			

E

Solution	Molality (mol/L)	Volume Solution	mol of solute	Zn:Im:bIm:DMF	Mass solution (g)
Zn	0.2	19.400	0.004	1.00	19.468
Im	1.5	50.753	0.076	19.62	53.093
bIm	0.2	13.247	0.003	0.68	12.818
DMF		16.600	1.292	332.88	15.670
	sum	100.00			

F

Solution	Molality (mol/L)	Volume Solution	mol of solute	Zn:Im:bIm:DMF	Mass solution (g)
Zn	0.2	19.400	0.004	1.00	19.468
Im	1.5	60.805	0.091	23.51	63.609
bIm	0.2	3.195	0.001	0.16	3.092
DMF		16.600	1.292	332.88	15.670
	sum	100.00			7.439

Figure A.1 Detailed recipes for the synthesis of the ZIF-62 solid-solution series.

Input file for structural refinement of ZIF-62 for Shelxl

```
TITL 2018ncs0407_r1_100k_a.res in Pbca
shelx.res
created by SHELXL−2016/6 at 13:46:27 on 08−Jan−2019
CELL 1.54178 15.4415 15.6208 18.1256 90 90 90
ZERR 4.00 0.0009 0.0015 0.0017 0.000 0.000 0.000
LATT 1
SYMM 1/2 − X, − Y, 1/2 + Z
SYMM − X, 1/2 + Y, 1/2 − Z
SYMM 1/2 + X, 1/2 − Y, − Z
SFAC ZN N C O H
UNIT 136 144 72 34 4
L.S. 20
DFIX −2.5 0.02 ZN1 O1SB
SUMP 0.8 0.2 1.0 5 1.0 6 1.0 7
ACTA
EADP C1SA C1SB C1SC C2SA C2SB C2SC C3SA C3SB C3SC O1SA O1SB O1SC N1SA N1SB N1SC

WGHT 0.138400 7.595900
FVAR 0.16723 0.50062 0.26474 0.13036 0.34701 0.15466 0.29830
ZN2 1 0.505680 0.664054 0.187125 11.00000 0.05319 0.06623 =
0.05759 0.00003 −0.00890 −0.00051
ZN1 1 0.200753 0.864016 0.093365 11.00000 0.05377 0.05644 =
0.06830 0.00504 −0.00101 0.00110
PART 1
N8 2 0.441255 0.763444 0.146506 11.00000 0.04819 0.06014 =
0.06670 0.00375 −0.00503 −0.00816
C17 3 0.355414 0.766896 0.139061 11.00000 0.05099 0.06102 =
0.05988 0.00360 −0.00074 −0.00407
AFIX 43
H17 5 0.319528 0.721695 0.152495 11.00000 −1.20000
AFIX 0
N1 2 0.324864 0.839173 0.111206 11.00000 0.05361 0.05609 =
0.07973 0.01101 0.00321 −0.00116
C1 3 0.397104 0.886302 0.095620 11.00000 0.05955 0.05989 =
0.12077 0.02058 −0.00392 −0.01077
C6 3 0.470033 0.840797 0.117761 11.00000 0.06506 0.06339 =
0.08959 0.01612 −0.01154 −0.01606
CC1 3 0.552122 0.866917 0.102352 31.00000 0.02574 0.03298 =
0.03039 −0.00901 −0.00533 −0.00530
AFIX 43
HC1 5 0.599976 0.834595 0.116305 21.00000 −1.20000
AFIX 0
CC2 3 0.561613 0.946032 0.063866 21.00000 0.08733 0.06781 =
0.10072 −0.01374 0.01054 −0.02160
AFIX 43
HC2 5 0.616574 0.968950 0.056780 21.00000 −1.20000
AFIX 0
CC3 3 0.490952 0.988400 0.037360 21.00000 0.10337 0.05735 =
0.07612 −0.00929 0.01684 −0.01037
CC4 3 0.408191 0.959375 0.050011 21.00000 0.06937 0.05591 =
0.08247 −0.00598 0.00765 0.00338
AFIX 43
HC4 5 0.360697 0.986913 0.029220 21.00000 −1.20000

PART 2
AFIX 6
N5 2 0.599776 0.639095 0.118600 −31.00000 0.05542
C10 3 0.600806 0.648162 0.046767 −31.00000 0.04791
AFIX 43
H10 5 0.553744 0.669497 0.020555 −31.00000 −1.20000
AFIX 5
N4 2 0.674296 0.624546 0.014028 −31.00000 0.05814
CB2 3 0.680131 0.606426 0.134814 −31.00000 0.08543 0.24471 =
0.06485 0.03870 0.00506 0.09451
AFIX 43
HB2 5 0.699968 0.592703 0.181794 −31.00000 −1.20000
AFIX 5
CB3 3 0.726864 0.597170 0.070241 −31.00000 0.08949 0.25362 =
```

```
0.06685 0.02551 −0.00015 0.10025
AFIX 43
HB3 5 0.783065 0.576399 0.065796 −31.00000 −1.20000

PART 3
AFIX 5
N11 2 0.668923 0.602863 0.002457 31.00000 0.07117
C22 3 0.617284 0.649556 0.043089 31.00000 41.00000
AFIX 43
H22 5 0.601380 0.704944 0.030032 31.00000 −1.20000
AFIX 5
C21 3 0.675444 0.527311 0.040767 31.00000 41.00000
N10 2 0.589099 0.611935 0.104617 31.00000 0.06390
C23 3 0.626107 0.532326 0.104274 31.00000 41.00000
C24 3 0.703526 0.441714 0.014012 31.00000 41.00000
AFIX 43
H24 5 0.726599 0.434496 −0.032972 31.00000 −1.20000
AFIX 5
C25 3 0.607257 0.462207 0.149443 31.00000 41.00000
AFIX 43
H25 5 0.571461 0.466620 0.190531 31.00000 −1.20000
AFIX 5
C26 3 0.694141 0.374256 0.061006 31.00000 41.00000
AFIX 43
H26 5 0.719493 0.322424 0.047938 31.00000 −1.20000
AFIX 5
C27 3 0.649389 0.378120 0.126710 31.00000 41.00000
AFIX 43
H27 5 0.644987 0.330042 0.156739 31.00000 −1.20000
AFIX 0

PART 0
N6 2 0.558754 0.692206 0.283713 11.00000 0.06421 0.05973 =
0.06066 0.00427 −0.00895 −0.00312
C12 3 0.595595 0.765357 0.301272 11.00000 0.05939 0.06433 =
0.05983 0.00896 −0.00706 −0.00490
AFIX 43
H12 5 0.595726 0.812655 0.270110 11.00000 −1.20000
AFIX 0
N2 2 0.632418 0.765707 0.367125 11.00000 0.05939 0.05415 =
0.06144 0.00206 −0.00982 0.00638
C7 3 0.618695 0.686120 0.392599 11.00000 0.13686 0.06744 =
0.07216 0.01899 −0.04556 −0.02483
AFIX 43
H7 5 0.636845 0.665427 0.438156 11.00000 −1.20000
AFIX 0
C13. 3 0.574515 0.641079 0.341734 11.00000 0.14749 0.06422 =
0.08643 0.02033 −0.05548 −0.03351
AFIX 43
H13 5 0.557721 0.584123 0.346038 11.00000 −1.20000
AFIX 0
N7 2 0.419943 0.569677 0.194109 11.00000 0.06179 0.06053 =
0.05767 0.00110 0.00257 0.00109
C15 3 0.400627 0.516800 0.138754 11.00000 0.06518 0.06124 =
0.06246 −0.00166 0.00387 −0.00893
AFIX 43
H15 5 0.430148 0.516842 0.094031 11.00000 −1.20000
AFIX 0
N3 2 0.335483 0.464160 0.153309 11.00000 0.06244 0.05669 =
0.07449 0.00104 0.00589 −0.00173
C8 3 0.314124 0.484212 0.224258 11.00000 0.11292 0.08142 =
0.10536 −0.01866 0.06353 −0.03060
AFIX 43
H8 5 0.270706 0.457771 0.251556 11.00000 −1.20000
AFIX 0
C14 3 0.365237 0.548000 0.248950 11.00000 0.11805 0.07433 =
0.07712 −0.01649 0.03318 −0.02196
AFIX 43
H14 5 0.363132 0.572702 0.295599 11.00000 −1.20000

PART 5
AFIX 6
```

```
N1SA 2 0.668813 0.336228 0.099291 51.00000 0.21356 0.12450 =
0.09753 0.01445 0.01955 0.02466
O1SA 4 0.807123 0.369793 0.064965 51.00000 0.21356 0.12450 =
0.09753 0.01445 0.01955 0.02466
C1SA 3 0.761575 0.311913 0.095605 51.00000 0.21356 0.12450 =
0.09753 0.01445 0.01955 0.02466
AFIX 43
H7SA 5 0.783764 0.260610 0.113505 51.00000 −1.20000
AFIX 5
C2SA 3 0.635978 0.253678 0.069983 51.00000 0.21356 0.12450 =
0.09753 0.01445 0.01955 0.02466
AFIX 37
H1SA 5 0.679140 0.228231 0.038804 51.00000 −1.20000
H2SA 5 0.584213 0.263631 0.041932 51.00000 −1.20000
H3SA 5 0.623338 0.215766 0.110254 51.00000 −1.20000
AFIX 5

C3SA 3 0.663034 0.303954 0.178754 51.00000 0.21356 0.12450 =
0.09753 0.01445 0.01955 0.02466
AFIX 37
H4SA 5 0.624199 0.256033 0.180986 51.00000 −1.20000
H5SA 5 0.641828 0.348976 0.209953 51.00000 −1.20000
H6SA 5 0.719447 0.286585 0.195229 51.00000 −1.20000
AFIX 6

PART 6
N1SB 2 0.657794 0.345991 0.103180 61.00000 0.21356 0.12450 =
0.09753 0.01445 0.01955 0.02466
O1SB 4 0.563598 0.434324 0.042551 61.00000 0.21356 0.12450 =
0.09753 0.01445 0.01955 0.02466
C1SB 3 0.602643 0.362715 0.037660 61.00000 0.21356 0.12450 =
0.09753 0.01445 0.01955 0.02466
AFIX 43
H7SB 5 0.597258 0.325463 −0.002100 61.00000 −1.20000
AFIX 5
C2SB 3 0.625873 0.257321 0.114981 61.00000 0.21356 0.12450 =
0.09753 0.01445 0.01955 0.02466
AFIX 37
H1SB 5 0.668210 0.225346 0.142274 61.00000 −1.20000
H2SB 5 0.616225 0.230343 0.068108 61.00000 −1.20000
H3SB 5 0.572558 0.258979 0.142186 61.00000 −1.20000
AFIX 5
C3SB 3 0.731173 0.314243 0.053939 61.00000 0.21356 0.12450 =
0.09753 0.01445 0.01955 0.02466
AFIX 37
H4SB 5 0.726537 0.253358 0.047911 61.00000 −1.20000
H5SB 5 0.785803 0.327872 0.076327 61.00000 −1.20000
H6SB 5 0.727363 0.341517 0.006588 61.00000 −1.20000

AFIX 6

PART 7
N1SC 2 0.699752 0.253590 0.147874 61.00000 0.21356 0.12450 =
0.09753 0.01445 0.01955 0.02466
O1SC 4 0.653547 0.308463 0.037758 61.00000 0.21356 0.12450 =
0.09753 0.01445 0.01955 0.02466
C1SC 3 0.651220 0.320704 0.107212 61.00000 0.21356 0.12450 =
0.09753 0.01445 0.01955 0.02466
AFIX 43
H7SC 5 0.622613 0.366135 0.129699 61.00000 −1.20000
AFIX 5
C2SC 3 0.748476 0.314581 0.195118 61.00000 0.21356 0.12450 =
0.09753 0.01445 0.01955 0.02466
AFIX 37
H1SC 5 0.722158 0.317075 0.243054 61.00000 −1.20000
H2SC 5 0.747388 0.370422 0.173020 61.00000 −1.20000
H3SC 5 0.807369 0.295657 0.199810 61.00000 −1.20000
AFIX 5
C3SC 3 0.627281 0.246659 0.204738 61.00000 0.21356 0.12450 =
0.09753 0.01445 0.01955 0.02466
AFIX 37
H4SC 5 0.631491 0.192726 0.229875 61.00000 −1.20000
```

```
H5SC 5 0.572253 0.250476 0.180311 61.00000 −1.20000
H6SC 5 0.632484 0.292413 0.239819 61.00000 −1.20000

AFIX 0
HKLF 4



REM 2018ncs0407_r1_100k_a.res in Pbca
REM R1 = 0.0799 for 2934 Fo > 4sig(Fo) and 0.0990 for all 3946 data
REM 249 parameters refined using 1 restraints

END
```

Input file for structural refinement of ZIF-4-cp-II for TOPAS academic (V6)

```
xdd 265403.xy
do_errors
r_wp rwp 0.61880604 r_exp 5.47951087 r_p 0.466483844 r_wp_dash 0.567124023 r_p_dash 0.428100515 r_exp_dash 5.02186799 weighted_Durbin_Watson 0.529642731 gof
    ↪ 0.11293089
x_calculation_step 0.01
start_X 2
finish_X 6.65
iters 0
chi2_convergence_criteria 0.000005
LP_Factor(90)
lam
ymin_on_ymax 0.0001
la 1 lo 0.4246 lh 0.000001


 macro File { 265764_empty−120s.xy }
 user_y bkgr { #include File }
 prm !s 0.41389‘ min 1e−9
 fit_obj = s∗bkgr;
 bkg −28.4051009‘ 16.804978‘ −1.28460164‘ −2.00815929‘ 3.25677138‘ −1.10200282‘ −0.987475545‘

 str
                TCHZ_Peak_Type( , 0.09613_0.01929, ,−0.03810_0.00208, , 0.00313_0.00762, ,−0.00025_0.00753, , 0.04033_0.00995, , 0.00705_0.00091)
                scale @ 4.72896519e−009‘
                r_bragg 0.0627525222
                a !lpa 14.566590‘
                b !lpb 14.444780‘
                c !lpc 15.451019‘
                al 90
                be 90
                ga 90
                volume 3251.067‘
                space_group "Pbca"
                site Zn1 x =xZn1;: 0.27133 y =yZn1;:0.31110 z =zZn1;:0.06790 occ Zn 1 beq 3
                site Zn2 x =xZn2;: −0.02246 y =yZn2;:0.09192 z =zZn2;:0.21685 occ Zn 1 beq 3
                site A x 0.07751 y 0.26097 z 0.13525 occ B 0     beq 3
                site N1A x 0.14116 y 0.27967 z 0.09483 occ N 1     beq 3
                site N2A x 0.03359 y 0.20043 z 0.16018 occ N 1     beq 3
                site C1A x 0.10943 y 0.19326 z 0.11020 occ C 1     beq 3
                site C2A x 0.08493 y 0.34023 z 0.13533 occ C 1     beq 3
                site C3A x 0.01845 y 0.29126 z 0.17571 occ C 1     beq 3
                site B x 0.37425 y 0.43999 z 0.19488 occ B 0     beq 3
                site N1B x 0.33577 y 0.40073 z 0.14125 occ N 1     beq 3
                site N2B x !xN2B 0.43371 y !yN2B 0.49036 z !zN2B 0.20830 occ N 1 beq 3
                site C1B x 0.40819 y 0.45797 z 0.12982 occ C 1     beq 3
                site C2B x 0.31653 y 0.39775 z 0.22680 occ C 1     beq 3
                site C3B x 0.37706 y 0.45314 z 0.26824 occ C 1     beq 3
```

```
        site C x 0.38960 y 0.13921 z 0.10697 occ B 0      beq 3
        site N1C x 0.33562 y 0.19152 z 0.08334 occ N 1      beq 3
        site N2C x !xN2C 0.42699 y !yN2C 0.11156 z !zN2C 0.16721 occ N 1 beq 3
        site C1C x 0.36277 y 0.17911 z 0.16620 occ C 1      beq 3
        site C2C x 0.38307 y 0.13164 z 0.03313 occ C 1      beq 3
        site C3C x 0.43954 y 0.08222 z 0.08497 occ C 1      beq 3
        site D x 0.30966 y 0.41401 z −0.09854 occ B 0      beq 3
        site N1D x 0.28245 y 0.36743 z −0.04391 occ N 1      beq 3
        site N2D x !xN2D 0.37460 y !yN2D 0.43557 z !zN2D −0.13575 occ N 1 beq 3
        site C1D x 0.37071 y 0.37352 z −0.07036 occ C 1      beq 3
        site C2D x 0.23179 y 0.42571 z −0.09296 occ C 1      beq 3
        site C3D x 0.28875 y 0.46783 z −0.14972 occ C 1      beq 3
'symmetry−equivalent dummies for geometric constraints:
        site N2B_1 x =−xN2B+0.5;:0.06629 y =yN2B+0.5−1;:−0.00964 z =zN2B;:0.20830 occ N 0
        site N2C_1 x =xN2C+0.5−1;:−0.07301 y =yN2C;:0.11156   z =−zN2C+0.5;:0.33279 occ N 0
        site N2D_1 x =xN2D+0.5−1;:−0.12540 y =−yN2D+0.5;:0.06443 z =−zN2D;:0.13575 occ N 0

        site Zn2_1 x =xZn2+0.5;: 0.47754 y =yZn2;:0.09192    z =−zZn2+0.5;:0.28315 occ Zn 0
        site Zn2_2 x =−xZn2+0.5;: 0.52246 y =yZn2+0.5;:0.59192 z =zZn2;:0.21685 occ Zn 0
        site Zn2_3 x =xZn2+0.5;: 0.47754 y =−yZn2+0.5;:0.40808 z =−zZn2;:−0.21685 occ Zn 0

'xyz of Zn positions
        prm !xZn1 0.27133
        prm !xZn2 −0.02246
        prm !yZn1 0.31110
        prm !yZn2 0.09192
        prm !zZn1 0.06790
        prm !zZn2 0.21685

'Rigid body movements
        prm !prm_xrotA −112.30075 min −132  max −40
        prm !prm_xrotB 173.01496 min 138  max 200
        prm !prm_xrotC −8.95945  min −50  max 42
        prm !prm_xrotD −119.84111 min −120  max −52
        prm !prm_yrotA −27.48915  min −50  max −10
        prm !prm_yrotB −28.27214  min −44  max −4
        prm !prm_yrotC −36.32675  min −58  max −18
        prm !prm_yrotD 139.55189 min 105 max 145
        prm !prm_zrotA −143.85537 min −158  max −118
        prm !prm_zrotB 42.22263  min 17  max 57
        prm !prm_zrotC −40.95247  min −59  max −19
        prm !prm_zrotD −143.74952 min −179  max −100
        prm !prm_xtransA 0.07751
        prm !prm_xtransB 0.37425
        prm !prm_xtransC 0.38960
        prm !prm_xtransD 0.30966
        prm !prm_ytransA 0.26097
        prm !prm_ytransB 0.43999
        prm !prm_ytransC 0.13921
        prm !prm_ytransD 0.41401
        prm !prm_ztransA 0.13525
        prm !prm_ztransB 0.19488
        prm !prm_ztransC 0.10697
        prm !prm_ztransD −0.09854

 PO_Spherical_Harmonics(sh, 8 load sh_Cij_prm {
        y00 !sh_c00 1.00000
        y20  !sh_c20 −0.09467‘
        y22p  !sh_c22p −0.11442‘
        y40  !sh_c40 −0.44731‘
        y42p  !sh_c42p 0.83979‘
        y44p  !sh_c44p −1.02449‘
        y60  !sh_c60 −0.26669‘
        y62p  !sh_c62p 0.85583‘
        y64p  !sh_c64p 0.62435‘
        y66p  !sh_c66p 0.09222‘
        y80  !sh_c80 1.38252‘
        y82p  !sh_c82p −0.21523‘
        y84p  !sh_c84p 0.20565‘
        y86p  !sh_c86p 0.58753‘
        y88p  !sh_c88p 1.60796‘
 })
```

```
'==========================================
rigid_A
Rotate_about_axies(xrotA =prm_xrotA;,yrotA =prm_yrotA;,zrotA =prm_zrotA;)
Translate(xtransA =prm_xtransA;,ytransA =prm_ytransA;,ztransA =prm_ztransA;)
rigid_B
Rotate_about_axies(xrotB =prm_xrotB;,yrotB =prm_yrotB;,zrotB =prm_zrotB;)
Translate(xtransB =prm_xtransB;,ytransB =prm_ytransB;,ztransB =prm_ztransB;)
rigid_C
Rotate_about_axies(xrotC =prm_xrotC;,yrotC =prm_yrotC;,zrotC =prm_zrotC;)
Translate(xtransC =prm_xtransC;,ytransC =prm_ytransC;,ztransC =prm_ztransC;)
rigid_D
Rotate_about_axies(xrotD =prm_xrotD;,yrotD =prm_yrotD;,zrotD =prm_zrotD;)
Translate(xtransD =prm_xtransD;,ytransD =prm_ytransD;,ztransD =prm_ztransD;)

macro rigid_A {

        rigid
                load z_matrix {
                        A
                        C1A A =dist_Cntr;
                        N1A A =dist_Cntr; C1A 72
                        C2A A =dist_Cntr; N1A 72 C1A 180
                        C3A A =dist_Cntr; C2A 72 N1A 180
                        N2A A =dist_Cntr; C3A 72 C2A 180}}

macro rigid_B {
    rigid
                load z_matrix {
                        B
                        C1B B =dist_Cntr;
                        N1B B =dist_Cntr; C1B 72
                        C2B B =dist_Cntr; N1B 72 C1B 180
                        C3B B =dist_Cntr; C2B 72 N1B 180
                        N2B B =dist_Cntr; C3B 72 C2B 180}}

macro rigid_C {
        rigid
                load z_matrix {
                        C
                        C1C C =dist_Cntr;
                        N1C C =dist_Cntr; C1C 72
                        C2C C =dist_Cntr; N1C 72 C1C 180
                        C3C C =dist_Cntr; C2C 72 N1C 180
                        N2C C =dist_Cntr; C3C 72 C2C 180}}

macro rigid_D {
        rigid
                load z_matrix {
                        D
                        C1D D =dist_Cntr;
                        N1D D =dist_Cntr; C1D 72
                        C2D D =dist_Cntr; N1D 72 C1D 180
                        C3D D =dist_Cntr; C2D 72 N1D 180
                        N2D D =dist_Cntr; C3D 72 C2D 180}}

'==========================================
    penalties_weighting_K1 100

    'imidazolate size
    prm !dist_Cntr 1.15000 min 1.1 max 1.15

    'Tetrahedral N − N
    prm !angle_width2 5
    prm !angle_weight2 1

    'distance Zn − N
    prm !bond_width 0.02
    prm !bond_weight 10000

    'planarity of Zn−Im−Zn
    prm !Flat_width 0
```

```
prm !Flat_weight 50

    Distance_Restrain(Zn1  N1A ,1.94, 1.99363 ,bond_width, bond_weight)
    Distance_Restrain(Zn1  N1B ,1.94, 1.96004 ,bond_width, bond_weight)
    Distance_Restrain(Zn1  N1C ,1.94, 1.97927 ,bond_width, bond_weight)
    Distance_Restrain(Zn1  N1D ,1.94, 1.91646 ,bond_width, bond_weight)

    Distance_Restrain(Zn2  N2A ,1.94, 1.97232 ,bond_width, bond_weight)
    Distance_Restrain(Zn2  N2B_1 ,1.94, 1.95981 ,bond_width, bond_weight)
    Distance_Restrain(Zn2 N2C_1 ,1.94, 1.95749 ,bond_width, bond_weight)
    Distance_Restrain(Zn2 N2D_1 ,1.94, 1.99408 ,bond_width, bond_weight)

    Angle_Restrain(N1A Zn1 N1B ,109.5, 119.02708 ,angle_width2, angle_weight2)
    Angle_Restrain(N1A Zn1 N1C ,109.5, 103.06853 ,angle_width2, angle_weight2)
    Angle_Restrain(N1A Zn1 N1D ,109.5, 111.42077 ,angle_width2, angle_weight2)
    Angle_Restrain(N1D Zn1 N1B ,109.5, 101.55490 ,angle_width2, angle_weight2)
    Angle_Restrain(N1B Zn1 N1C ,109.5, 106.27020 ,angle_width2, angle_weight2)
    Angle_Restrain(N1C Zn1 N1D ,109.5, 116.05181 ,angle_width2, angle_weight2)

    Angle_Restrain(N2A Zn2 N2B_1 ,109.5, 106.97046 ,angle_width2, angle_weight2)
    Angle_Restrain(N2A Zn2 N2C_1 ,109.5, 116.53991 ,angle_width2, angle_weight2)
    Angle_Restrain(N2A Zn2 N2D_1 ,109.5, 100.98533 ,angle_width2, angle_weight2)
    Angle_Restrain(N2D_1 Zn2 N2B_1 ,109.5, 107.73501 ,angle_width2, angle_weight2)
    Angle_Restrain(N2B_1 Zn2 N2C_1 ,109.5, 114.72795 ,angle_width2, angle_weight2)
    Angle_Restrain(N2C_1 Zn2 N2D_1 ,109.5, 108.72785 ,angle_width2, angle_weight2)

    Flatten( Zn1 N1A C3A C2A N2A C1A Zn2 , 1.95600204, Flat_width, Flat_weight)
    Flatten( Zn1 N1B C2B C3B C1B N2B Zn2_2 , 0.186575814, Flat_width, Flat_weight)
    Flatten( Zn1 N1C C1C C2C N2C C3C Zn2_1 , 0.913796592, Flat_width, Flat_weight)
    Flatten( Zn1 N1D C3D C1D N2D C2D Zn2_3 , 1.34884244, Flat_width, Flat_weight)

    AI_Anti_Bump(Zn1 , C1C , 2.75 , 10000000000000000)
    AI_Anti_Bump(C2A , C3C , 3.6 , 10000)
    AI_Anti_Bump(C1D , C3A , 3.6 , 10000)
```